4.4.Validation & Verification for Computational Mechanics

Springerより2017年3月に刊行予定の書籍「Validation & Verification for Computational Mechanics」の入稿原稿を添付する。

Validation & Verification for Computational Mechanics

Editors:　Yoshiaki Tamura, Ryuji Shioya and Yasushi Nakabayashi

Preface

This book provides articles on the state-of-the-art validation and verification (V & V) methodology for computational mechanics, especially fluid-structure interaction analyses and related topics.

Computational mechanics has more than fifty years history and in each research field, typically in structural dynamics and fluid dynamics, the analysis methods have been developed and validated. However fluid-structure interaction (FSI) analysis method, that is the combination of these two methods, has not yet been definitive and still a research topic in computational mechanics. There must be several reasons; the analysis methods were independently developed in the corresponding fields even though the basic methods are the same, such as finite element method or finite difference method, the extensions to higher-order accuracy took different approaches, the requirements for spatial and temporal divisions differ in each field, etc. Moreover reliable (experimental) data are few and V & V methodology has not yet been established for FSI.

The Center for Computational Mechanics Research (CCMR), Toyo University was established in 2005 with the grant of "Science Frontier" in Private Universities by the Ministry of Education, Culture, Sports, Science and Technology (MEXT), Japan and has been pursuing methods, applications and V & V of computational mechanics since then. In 2012, CCMR has been adopted for the MEXT-Supported Program for the Strategic Research Foundation at Private Universities with the research title of "Fluid-Structure Coupled Analysis and Its Validation & Verification". The program will last till the end of March 2017. Most of the articles in this book are the results of this program.

One highlight of this book is proposal of the standard problem of FSI for the validation of code. The detailed experimental data are provided along with the computed results by the method also proposed in one of the articles. Not only comparing with experiments, this book covers various V & V approaches, e. g. the experiment–computation fusion for higher accuracy, the error analysis with the Bayesian estimation, the visual V & V, etc. The articles of large-scale FSI analysis are also included.

Finally, representing the authors in this book, I express our acknowledgements to Toyo University, MEXT, Japan Science and Technology Agency (JST) and all those who have supported our activities at CCMR.

February 13, 2017.

Yoshiaki Tamura
Director, the Center for Computational Mechanics Research, Toyo University

Table of Contents

1. Experiment on Oscillating Circular Cantilever for Fluid-Structure Interaction Code Validation (Fujimatsu)
2. Development of Large Scale Fluid-Structure Coupled Analysis Method by the Enriched Free Mesh Method (Nagaoka, Nakabayashi & Yagawa)
3. High Accurate Analysis by Experiment and Simulation Using Bayesian Inference for Corrugated Cardboard (Shimamura & Ezawa)
4. Validation & Verification of Structural Analysis Using Open Source Finite Element Analysis Code and Material Test Data (Fujioka)
5. ICME - Integrated Computational Materials Engineering, from Micro-Scale to FEM (Ashino)
6. Space-Time Simultaneous Visualization in Virtual Reality Environment for Validation and Verification (Tamura)
7. Application of Machine Learning for Computational Mechanics (Masuda & Nakabayashi)
8. High Performance Computing for Large Scale Structural Analysis (Shioya, Kawai and Ogino)
9. Large Scale Numerical Simulation of Water Splash by Moving Particle Simulation Method (Yokoyama & Yagawa)
10. Numerical Study of Adhesion Behavior of Sea-Salt Particles on Concrete Bridge Girders (Tomiyama & Nakabayashi)
11. Numerical Simulation of the Mudcrack Grows (Matsubara & Hirose)
12. Coupled Analysis of Electromagnetic Fields and Temperature Distributions inside the Human Body Using Microwave Therapeutic Devices (Shindo)
13. Hybrid Geometry/Material Monitoring Method for Microcrack Identification (Furukawa)

Experiment on Oscillating Circular Cantilever and Sheet Flutter for Fluid-Structure Interaction Code Validation

Nobuyoshi FUJIMATSU

[1]Department of Mechanical Engineering, TOYO University, JAPAN

fujimatsu@toyo.jp

Abstract

The purpose of this chapter is to provide the reliable experimental results for FSI code validation. We conducted the experiment on the flow-induced vibration of the oscillating cylinder and the sheet flutter and investigated a characteristics of critical flow velocity for oscillation. Three kinds of material of cylinder and of sheet with a different dimensions are used for the present experiment. The oscillation motion and the flutter frequency are measured using the laser-displacement sensor and the high-speed camera. There are differences on characteristics of the flutter in the case of increasing and decreasing the flow velocity. These dependencies on the material properties and the size of experimental model. We discussed from the comparison of the critical flow velocity. The present results showed that the sheet of same material with the short length has the greater critical flow velocity and the sheet of soft material with same length has the smaller critical flow velocity. The frequency of the flutter becomes large when the sheet has the short length. We also conducted the non-dimensional parameter for the classification of critical flow velocity and discussed on the influences to the flutter of the size of experimental model, material property and flow velocity.

Keywords: Flow-induced vibration, oscillating cylinder, sheet flutter, cantilevered flexible plate.

Introduction

The FSI problems is one of fundamental issues in an engineering applications and scientific researches. This topic is concerned with the plural physics. The information obtained by the experimental study is limited in terms of the spatial and the temporal resolutions. Consequently, the physical mechanism of FSI problem is not easy by the restricted information. We hope that the numerical simulation with a plenty of spatial and temporal information is a useful tool to reveal the physics of FSI problem. However, the numerical simulation is usually needed to validate the program code before applying the FSI problems and there are some difficulties from the lack of the experimental results for the FSI problems. There are many researches on the flow-induced vibration in the past and the experimental and numerical studies were conducted [1-6].

Eloy, C., et al.[7] investigated theoretically the linear stability of a variable aspect ratio, rectangular plate in a uniform and incompressible axial flow and could predict the flutter modes, their frequencies and growth rates. They calculated the critical flow velocity of sheet-flutter as a function of the mass ratio and the aspect ratio of the plate. Gjerek, B., et al.[8] studied the airfoil flexibility effect on the flutter behavior in terms of two main dynamic properties of a flexible plate, the flexural stiffness and the areal density and showed that the flutter behavior of a flexible airfoil is characterized by two types of flutter, namely the classical airfoil flutter and the plate flutter. Wu, X., et al.[9] dealt with both linear and nonlinear analyses of sheet flutter in a narrow passage caused by fluid–structure interaction compared the calculated results with previously reported experimental results. In the nonlinear analysis, nonlinear fluid dynamic forces are introduced to simulate the behavior of the sheet, showing the appearance of limit-cycle vibration in high flow speed. In order to modify the underestimation of the critical flutter velocity in the theoretical analysis. Doaré, O., et al.[10] quantified the phenomenon of the flutter by analyzing the effect of the clearance between the plate and the side walls on the flutter instability. Their results showed that the convergence towards the two-dimensional limit is so slow that this limit is unattainable experimentally. Gibbs, S. C. et al.[11] explored cantilevered beam flutter for both clamped and pinned leading edge boundary conditions using a three-dimensional vortex lattice panel method coupled with a classical Lagrangian one-dimensional beam structural model to predict the linear flutter boundary for finite size rectangular plates. They discussed on the change in flutter characteristics as a function of the fluid to structure mass ratio and the structural aspect ratio and confirmed the validity of the three-dimensional vortex lattice aerodynamic model over a subset of mass ratios from the comparison of the aeroelastic experiments. However, those research works were not focused in terms of the classification of flutter frequency.

In the present research work, we conducted two kinds of experiments on the flow-induced vibration. One is an oscillating cylindrical cantilever made of silicone rubber caused by aerodynamic forces. We investigate a characteristics of displacement and oscillating frequency for circular cantilever. The other is an investigation on a sheet flutter used by the metal plate. We research on the relationship of flutter frequency to the flow velocity and the material properties such as Young modulus and propose the non-dimensional parameters of the fluid force to the elastic forces for the estimation of the flutter phenomena. Through these experiments, we provide the reliable data for the code validation on the FSI problems.

Nomenclature

A: cross-section area of rectangular wing, $A=wL_p$ [m^2]
a: amplitude [mm]
D: displacement [mm]
d: diameter of circular cylinder [mm]
E: Young modulus [Pa]
f: oscillating frequency [Hz]
f_n : eigen frequency with n mode [Hz]
I : second moment of area $I=wt^4/12$ [m^4]
L: length of experimental model [mm]
Re: Reynolds number [-]
s_n: non-dimensional frequency with n mode [Hz]
St: Strouhal number [-]
t : thickness of rectangular plate [mm]
U: flow velocity [m/s]
w: chord length of rectangular plate [mm]
λ_n: vibration mode [-]
ν: dynamic viscosity [m^2/s]
ρ_s: density of rectangular plate [kg/m^3]
ρ: density of air flow [kg/m^3]

Subscript

c: cylinder
n: mode number
p: flat plate

Experimental setup

Figure 1 shows the schematic of experimental setup to simulate the oscillating cylinder and the sheet flutter. We conducted the experiments using the blow-down typed low-speed wind tunnel facilities. Area of the cross section of wind tunnel is a 0.3 × 0.3 m^2. Some kinds of material property for the present experiment were selected and we used the silicone rubber and the metal plate with different sizes. Flow speeds were varied from 0 to 45 m/s. We tested to investigate the displacement of oscillation and the frequency of flow induced vibration. The cylinder was supported at the top of that using the clamp and the motion of cylinder was recorded using the high-speed camera from the bottom and the side of the cylinder. The HAS-L1 is used as the digital image storage system produced by the DITECT Co. Ltd. in Japan. The rectangular plate supported by clamp is used in the sheet flutter experiment. We used the combination of the laser-head KG-G500 and the controller KG-G3000 made by KEYENCE Corp. as the LDS. The video image has 800x600 resolutions recorded by 300 fps. The CCD camera and the LDS were located to a downstream of rectangular plate and above the experimental model, respectively. We measured the displacement of the sheet flutter using the LDS. Table 1 shows the specifications of the LDS and the high-speed camera.

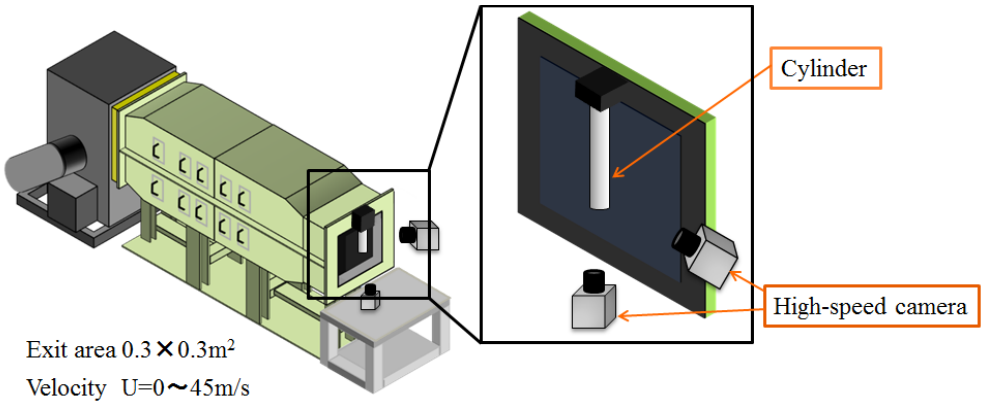

(a) Schematic of experimental setup for oscillating cylindrical cantilever.

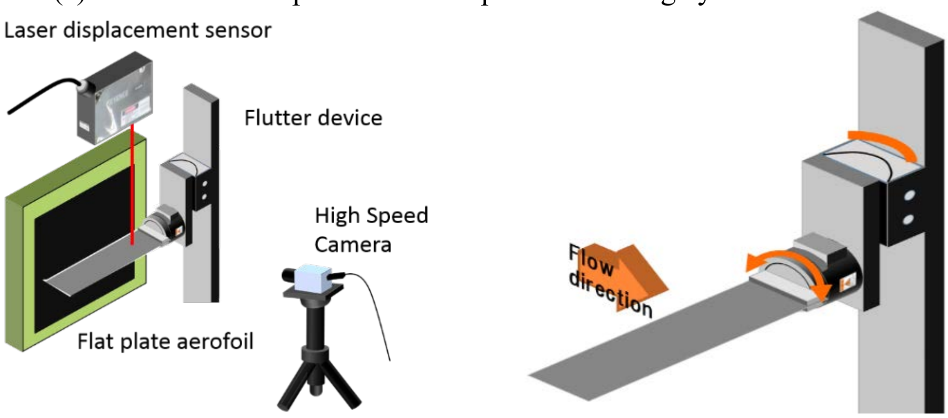

(b) Sheet flutter.

Fig. 1 Schematic of experimental setup for sheet flutter.

Table 1 Specifications of laser displacement sensor and high-speed camera.

Laser displacement sensor KG-G500		High-speed camera HAS-L1	
Installation mode	Diffuse reflection	Frame rate	300 fps
Sampling period [μs]	200	Resolution	800 × 600
Measurement time [s]	120 seconds	Measurement time [s]	30

Experimental results and discussions

Experiment on oscillating cylindrical cantilever

Table 2 shows the material properties and the size of circular cantilever. The cylinder have three kinds of Young modulus with same diameter and length. A50, A60 and A70 means the durometer hardness. The present experiments were conducted from 1.9 to 40.4 m/s of the flow velocity and the motion of cylinder is recorded by the high-speed camera from the bottom and the side views. The recorded time is 30 seconds and the optical images are storage with 9000 flames.

Table 2 Specifications of cylindrical cantilever.

d [mm]	20
L_c [mm]	160
E [MPa]	2.9 (A50)
	4.9 (A60)
	6.8 (A70)

In the wind-tunnel experiments, during the oscillating condition, the experimental model moves slightly over the x-y plane vertical to the cylindrical axis (z-axis). In order to capture the motion of cylinder, we conducted the image processing from the time series of images. Figures 2-(a) and (b) show the instantaneous images of elastic cylinder taken by the high-speed camera from the bottom and the side of the cylinder. From the images of bottom view of cylinder, the center coordinates of experimental model are automatically determined using the binary conversion from the pixel locations with the value of 1 in images[13]. We used herein the following algorithm for the detection of center coordinate: (1) Perform binary conversion of the image. (2) Search the location of arbitrary pixel with the value of 1 and determine the position of one pixel. (3) Search for pixels having the same intensity level around the position of arbitrary pixel with the value of 1. (4) Count the number of pixels having the same value. (5) Compute the total area. (6) Average the coordinates of the pixels having the same value and locate the center coordinate of the experimental model. The above process was applied to the experimental images and we could acquire the center coordinate of cylinder at every time.

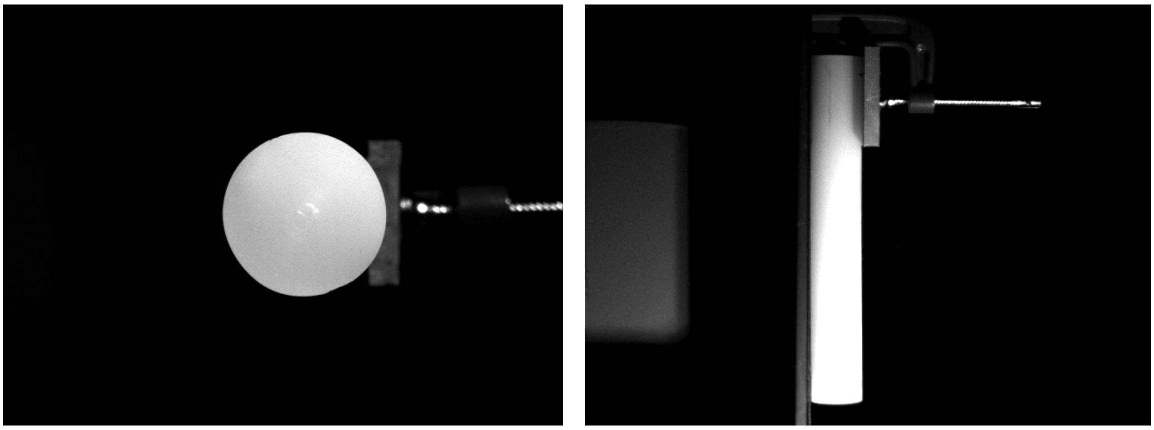

(a) bottom view. (b) side view.

Fig. 2 Instantaneous image of oscillating cylinder (U=18.6m/s).

Figures 3 and 4 showed the time-averaged displacement and the root mean square (R.M.S.) of amplitude for oscillating cylinder, respectively. The x and y components of each quantity are shown in the same figures. The Reynolds number is defined as Re=Ud_c/ν using a diameter of cylinder. The vertical axis means the ratio of each measurement value to the diameter d_c. Maximum value of displacement D_y is less than 3 percentages of a diameter dc and we can be negligible rather than D_x in the present flow condition. Each amplitude for x and y directions gradually becomes large over Re=1×10^4 and is nearly proportional to the Reynolds number. The amplitude a_y perpendicular to flow direction is greater than a_x with streamwise direction. These tendencies do not change to the material properties.

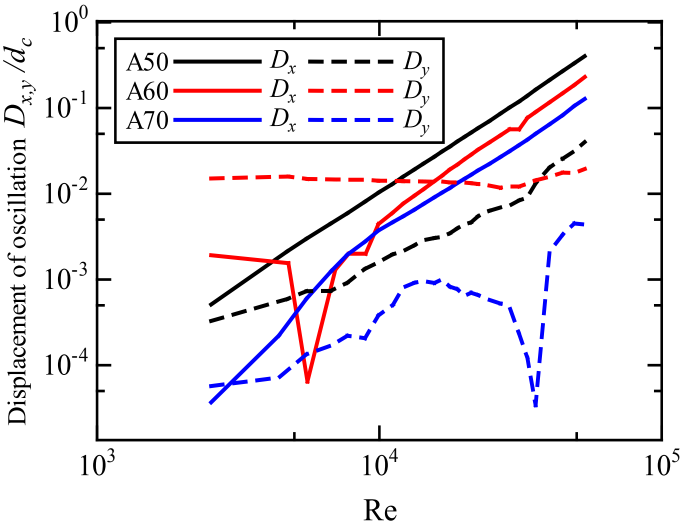

Fig. 3 Time-averaged displacement of oscillating circular cantilever.

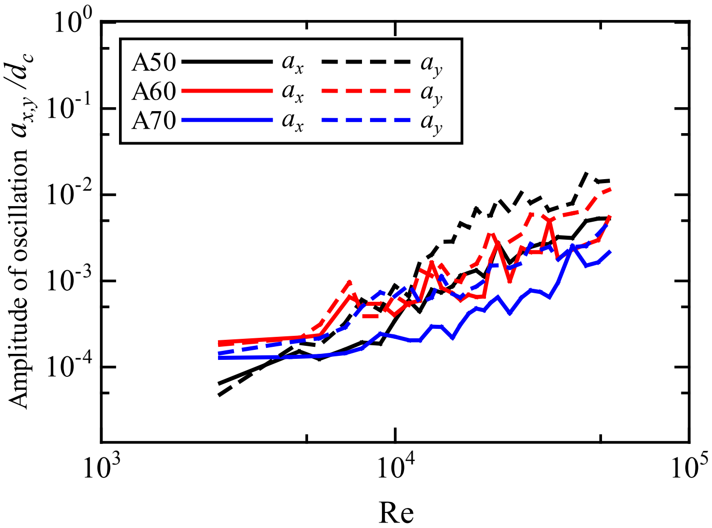

Fig. 4 Root mean square amplitude of circular cantilever.

Figures 5 showed the frequency characteristics of oscillating cylinder. The FFT analysis was applied to capture the power spectrum using 8192 points. The Strouhal number is defined as St=$f_c\, d_c\, /U$. The data points are not shown in Figs. 5 because the oscillating frequency could not successfully captured in the case of the tiny displacement. The Strouhal number decreases to the Reynolds number and the frequency characteristics are almost constant to all the flow conditions and for each material. Table 3 shows the slope of experimental results for the oscillating circular cantilever. These values are computed using the least square method. We did not show the slope of D_y because the y-component of displacement is negligible rather than that of D_x. The gradient of displacement in x-direction corresponds to about 2 in all the cases. The variation rate of amplitude a_x and a_y are slightly large and those values have the range of 1.0 to 1.5. In the only case of A50, the a_x and a_y are greater than 1.5 because the Young modulus is less than those of the other cylinder. The Strouhal number changes with the slope value -1.0 for x and y directions in all the cases.

In this section, we showed the experimental results on the oscillating circular cantilever. Characteristics on the displacement and the frequency are simply changed to Re and are useful to validate the FSI code.

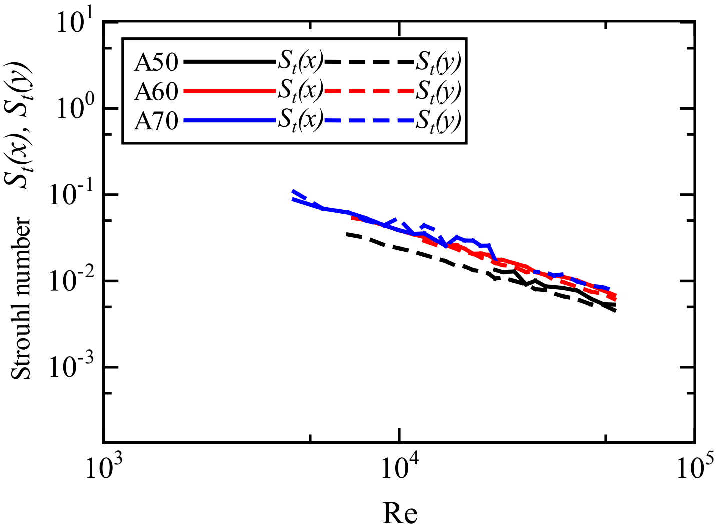

Fig. 5 Oscillating frequency of circular cylinder.

Table 3 Slope of characteristics of oscillating cylinder.

	D_x	D_y	a_x	a_y	S_t (x)	S_t (y)
A50	2.164	-	1.626	1.988	-1.017	-0.985
A60	2.260	-	1.090	1.504	-1.005	-1.046
A70	2.442	-	1.052	1.125	-0.912	-1.042

Experiment on sheet flutter

In this section, characteristics of sheet flutter is discussed on the material properties of the flat plate. We experimented to investigate the critical flow velocity of sheet flutter. The displacement of flat plate under the flutter condition was measured using the LDS. Table 4 shows the material properties and the size of flat plate airfoil. The experimental model is a rectangular plate and has three kinds of metal plate such as aluminum, brass and stainless with 9 kinds of different dimensions. The flow velocity was varied from 1.9 to 42.6 m/s.

Table 4 Specifications of sheet flutter.

w [mm]	40
L_p [mm]	200, 250, 300
t [mm]	0.3, 0.4, 0.5
Young modulus [GPa]	70.6 (aluminum)
	105 (brass)
	210 (stainless)

Figure 6 shows the comparison of flutter velocity to the span length L_p. The flat plate airfoils have 0.3, 0.4 and 0.5 mm thickness with 40mm chord length. The experimental results showed that the flutter velocity to the span length is slightly reduced for the different thickness and the gradient of flutter velocity have almost the same tendencies to the span length. As increasing the thickness of sheet, the flutter phenomena is not easy to occur because of the increment of rigidity. Figure 7 showed the comparison of flutter velocity to the Young modulus. The flat plate has 0.3mm thickness and 40mm chord length. From this figure, the flutter velocity is increased when the strength of material is greater.

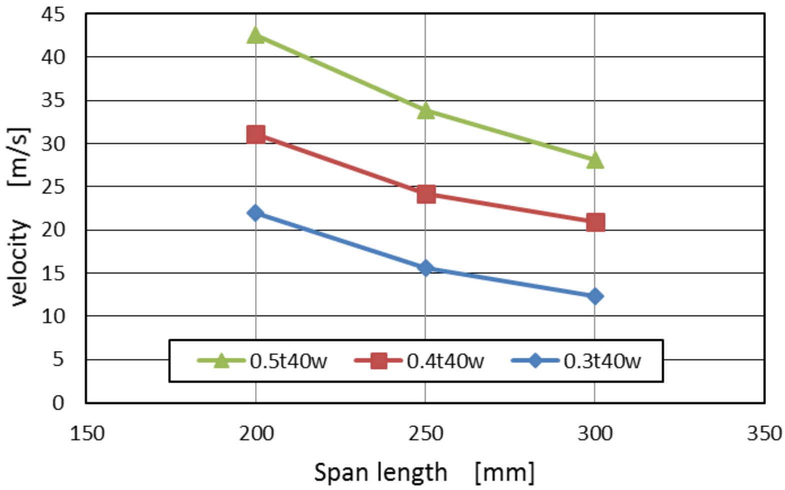

Fig. 6 Comparison of the flutter velocity to span length for the alminum sheet with various thickness.

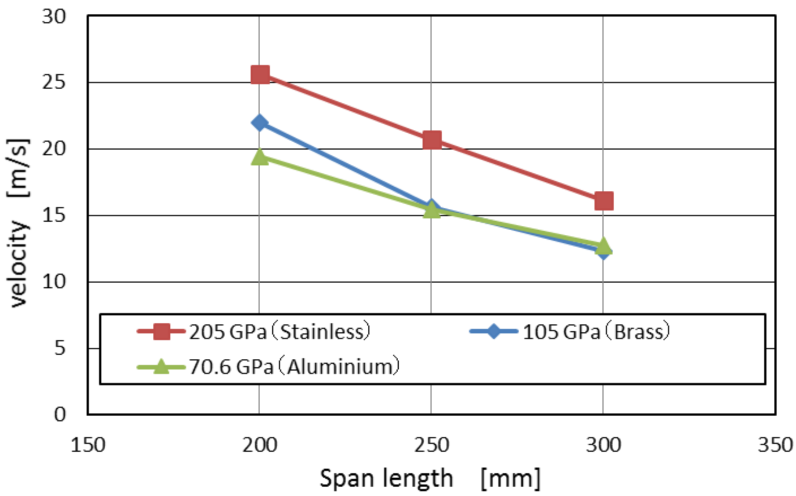

Fig. 7 Comparison of the flutter velocity to span length for various Young modulus (t=0.3mm and w=40mm).

The displacement of the flat plate is measured using the laser displacement sensor under the condition where the flutter phenomena occurs. The measurement point is located at 50mm length from the root of the flat plate. The time history of displacement of the flat plate is recorded for 12 seconds with 5 kHz. The frequency analysis is conducted using the FFT. Figure 8 showed the typical result of aluminum plate under the flutter condition. The peak of power is confirmed at 42 Hz. We classified the characteristics of flutter frequency to the flow velocity for aluminum plate with various size and showed in Fig. 9. The analytical results indicated that the flutter frequency is gradually increasing. Especially, these tendencies depends on the shorter span length with the same thickness.

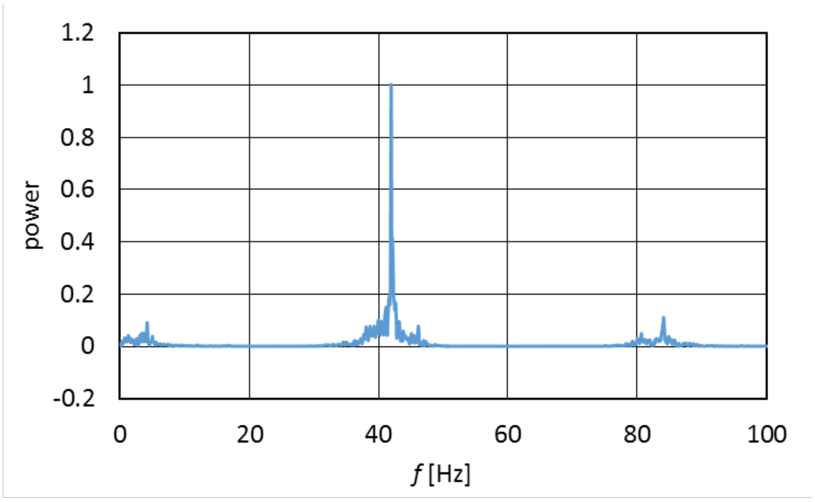

Fig. 8 Flutter frequency for alminum plate which has the dimensions (t=0.3mm, L_p=200mm, w=40mm and U=20m/s).

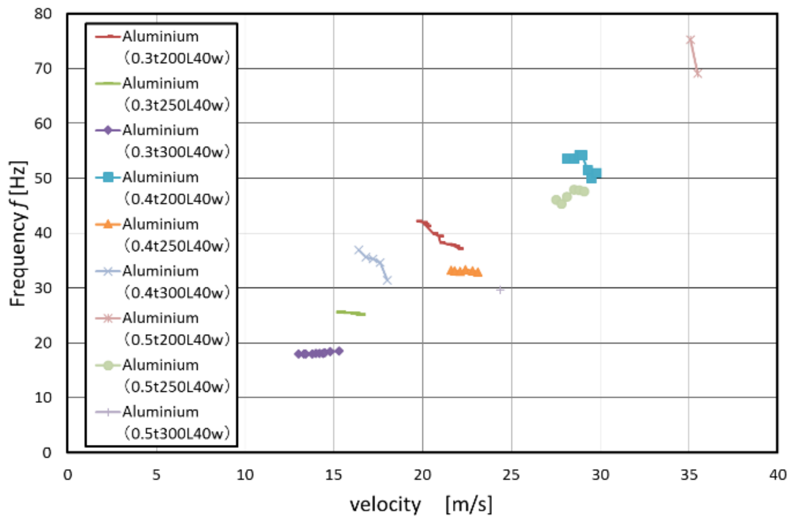

Fig. 9 Flutter frequency to flow velocity.

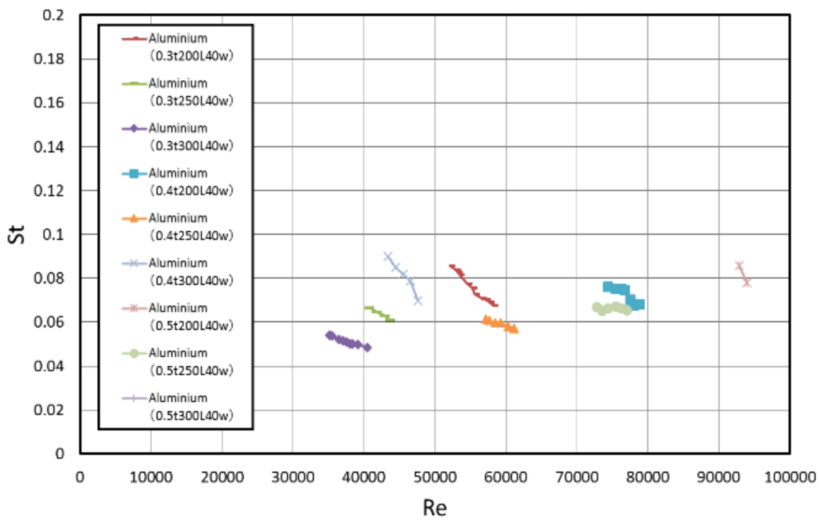

Fig. 10 Characteristics of non-dimensional flutter frequency.

Figure 10 showed the Strouhal number St=$f_p L_p$ /U for flutter frequency to the Reynolds number Re=UL_p /v. The reference length is the chord length 40mm. The experimental results showed that St has the range with in 0.05 to 0.08 for aluminum plate under the flutter condition. However, these results can not be simultaneously arranged for another materials because the Reynolds number does not include the material properties and the flutter frequency depends on the thickness and span length of sheet.
As shown in Fig. 10, we showed that the flutter velocity depends on the cross section area and the Young modulus of flutter sheet. The experimental results is a traditional classification based on the non-dimensional numbers St and Re and is involved for the different size and materials. In order to express the non-dimensional number include with the material properties, we need to incorporate another non-dimensional number from the Buckingham π theorem.
The flat plate is supported as the cantilever and is oscillated by the aerodynamic force. Therefore, we can consider that the flutter frequency is concerned with the eigen frequency for the elasticity of materials. Equation (1) means the eigen frequency with single-supported cantilever.

$$f_n = \frac{\omega_n}{2\pi} = \frac{1}{2\pi}\frac{\lambda_n^2}{L_f^2}\sqrt{\frac{EI}{\rho_s A}} \qquad (1)$$

$$s_n = \frac{f_p}{f_n} \qquad (2)$$

Figure 11 showed the non-dimensional flutter frequency based on Eq. (1). The oscillation mode λ depends on the flow condition. When we substituted 1st, 2nd and 3rd oscillation modes λ_1=1.875, λ_2=4.694 and λ_3=7.854 to Eq. (1), the flutter frequency corresponded to the eigen frequency of the aluminum plate with the 2nd oscillation mode. From the observation study shown in Fig. 12, the flutter patterns in the present experiments indicated the 2nd mode oscillation and we decided λ_2=4.694 is appropriate value used in the non-dimensional. Equation (2) is clear prospects on the discussion of flutter frequency.

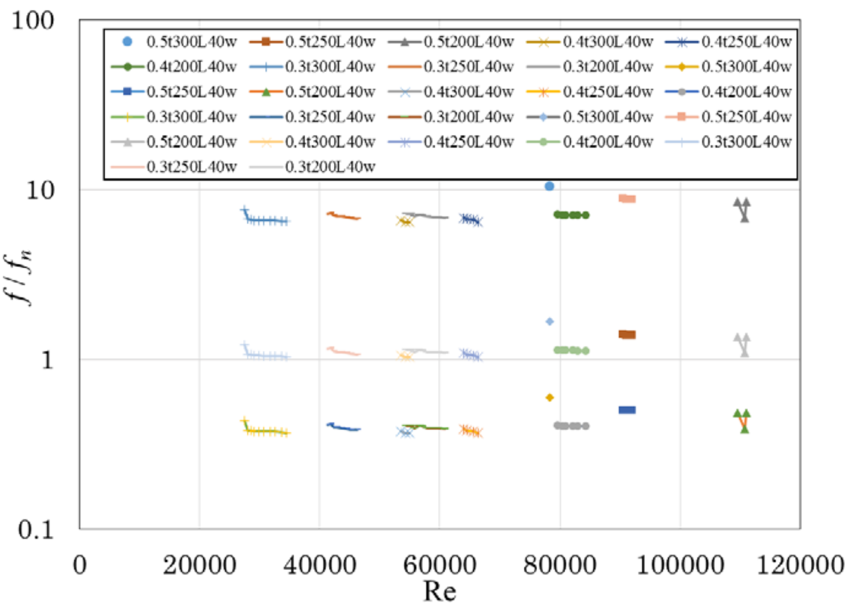

Fig. 11 Characteristics of non-dimensional flutter frequency based on an eigen frequency.

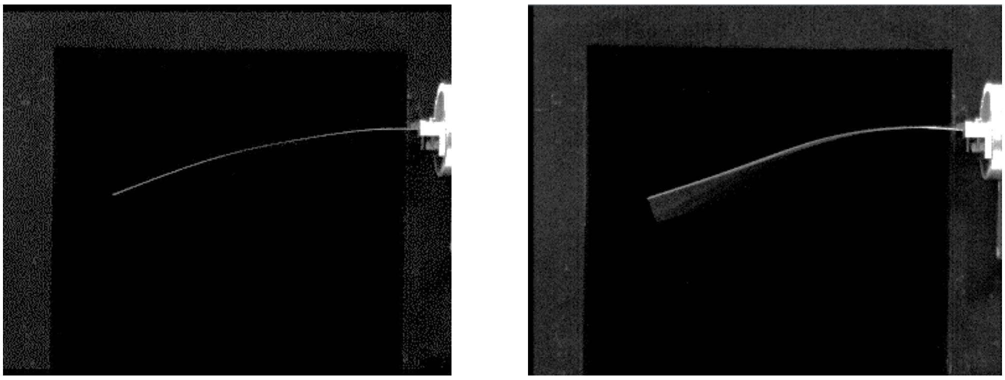

(a) t=0.3, L_p=250, U=15.4m/s. (b) t=0.5, L_p=250, U=27.5m/s.

Fig. 12 Oscillating flat plate with 2nd mode.

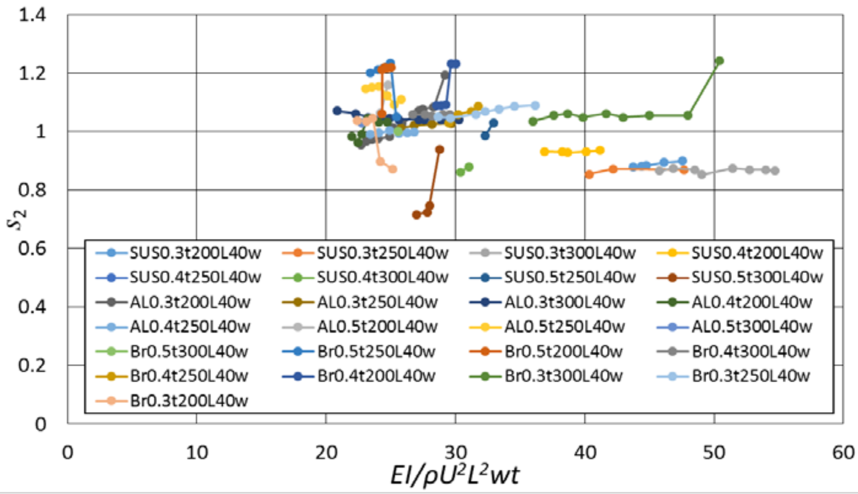

Fig. 13 Characteristics of non-dimensional flutter frequency based on aeroelasticity parameter.

Furthermore, we discuss the relationship of elastic force to aerodynamic force as the remaining problem and propose the non-dimensional number. In the analytic solution of cantilever problem, the displacement of beam under the uniform distributed load q [N/m] has the coefficient EI/qL_p^4 which corresponds to the ratio of moment of force. We consider that this coefficient is also responsible for the displacement of plate in the flutter phenomena and investigate the expression in terms of L_p^4. As the elastic plate is acting to the flat plate, the displacement is caused by the moment of force. The moment of force M is concerned with EI/t. Aerodynamic force is expressed as the dynamic pressure acting to the flat plate. Consequently, the fluid force F has the order of $\rho U^2 wL_p$. The moment of fluid force M is approximately equal to $\rho U^2 wL_p^2$ under the uniformly distributed aerodynamic load. We propose the aeroelastic parameter $EI/\rho U^2 L_p^2 wt$ as the non-dimensional number. Figure 13 show the flutter frequency for the three kinds of materials. These results indicate that the flutter phenomena is occurred in the range of 20 to 55 for the aeroelastic parameter.

Conclusions

We conducted two kinds of experiments for flow-induced vibration. The experimental results on oscillating circular cantilever showed that the displacement and the frequency of cylinder are proportional to the Reynolds number. In the sheet flutter experiment, we introduced the aeroelastic parameter combined with the elastic force to the aerodynamic force and the flutter frequency are classified using the non-dimensional number $EI/\rho U^2 L_p{}^2 wt$ included with the material property. The experimental results in the present research can be useful to validate the numerical code for FSI problems.

References

[1] Blevins, R. D. (1990) *Flow-Induced Vibration*, Krieger Publishing Company.

[2] King, R., Prosser, M. J., and Johns, D. J. (1973) On Vortex Excitation of Model Piles in Water, *Journal of Sound and Vibration* **29**, (2), 169-188.

[3] Kondo, N. (2012) Three-dimensional computation for flow-induced vibrations in in-line and cross-flow directions of a circular cylinder, *International Journal for Numerical Methods in Fluids* **70**, 158-185.

[4] Blake, W. K. (1986) *Mechanics of Flow-Induced Sound and Vibration* - Vol. 1: Gneral Concepts and Elementary Sources, Academic Press, Inc.

[5] Brika, D., and Laneville, A. (1993) Vortex-Induced Vibrations of a Long Flexible Circular Cylinder, *Journal of Fluid Mechanics* **250**, 481-508.

[6] Huerre, P., and Monkewitz, P. A. (1990) Local and Global Instabilities in Spatially Developing Flows, *Annual Review of Fluid Mechanics* **22**, 473-537.

[7] Eloy, C., Souilliez, C. and Schouveiler, L. (2007) Flutter of a rectangular plate, *Journal of Fluids and Structures* **23**, (6), 904-919.

[8] Gjerek, B., Drazumeric, R. and Kosel, F. (2014) Flutter behavior of a flexible airfoil: Multiparameter experimental study, *Aerospace Science and Technology* **36**, 75-86.

[9] Wu, X. and Kaneko, S. (2005) Linear and nonlinear analyses of sheet flutter induced by leakage flow, *Journal of Fluids and Structures* **20**, (7), 927-948.

[10] Doaré, O., Sauzade, M., and Eloy, C. (2011) Flutter of an elastic plate in a channel flow: Confinement and finite-size effects, *Journal of Fluids and Structures* **27**, (1), 76-88.

[11] Gibbs, S. C., Wang, I. and Dowell, E. (2012) Theory and experiment for flutter of a rectangular plate with a fixed leading edge in three-dimensional axial flow, *Journal of Fluids and Structures* **34**, 68-83.

[12] Fujimatsu, N., Tamura, T. and Fujii, K. (2005) Improvement of Noise Filtering and Image Registration Methods for the Pressure Sensitive Paint Experiments, Journal of Visualization **8**, (3), 225-233.

Development of Large Scale Fluid-Structure Coupled Analysis Method by the Enriched Free Mesh Method

Shinsuke NAGAOKA[1]

[1]Center for Computational Mechanics Research, Toyo University, JAPAN.

Abstract

Fluid-Structure interaction phenomenon is becoming a very important issue in recent numerical analysis field. Therefore a lot of new analysis methods are proposed by many researchers. Each approach has various advantages. But crucial analysis method is not proposed yet. We also have been already proposed the new method to obtain highly analysis result. The method is using the SUPG/PSPG stabilized finite element method (FEM) as a fluid analysis method. On the other hand, the Enriched Free Mesh Method (EFMM) is using in structure analysis field. Our approach is combined these two analysis methods. Both methods are using the same type element. For example, linear triangular elements are used for two dimensional analysis. In the case of three dimensional problem, linear tetrahedral elements are used. In short, both methods are using only linear element. Therefore, the handling of the fluid-structure interface becomes simple and accurate. Moreover, these method can be obtained fine analysis result compared with conventional method. Accuracy and parallel efficiency of the SUPG/PSPG stabilized FEM has been already proven by many analysis results so on. Analysis accuracy of the EFMM has been already proven by some analysis results by us. But, EFMM needs special treatment to apply parallel computing. For example, domain decomposition method is different from conventional FEM, communication table will become more complicate compared with conventional parallel computing. Introduced into special treatment for EFMM, parallel efficiency of EFMM is able to obtain very good result. As a written in above features, analysis accuracy and parallel efficiency of our proposed method will become very good. In this study, we describe detail of our proposed analysis method. In addition, analysis result compared with examination result are described to prove of efficiency of our proposed method.

Keywords: Fluid-Structure Interaction Analysis, Large Scale Analysis, Parallel Computing, Enriched Free Mesh Method, SUPG/PSPG Stabilized Finite Element Method.

1. Background

Fluid-structure interaction problem is becoming a very important problem in the recent numerical analysis field. In fact, phenomenon that is occurred around our body is almost interaction phenomenon. Especially, it is very important that to solve fluid-structure interaction problem using numerical simulation in the engineering field.

To solve this fluid-structure interaction phenomenon, a lot of new methods are proposed by many researchers. These new methods have many strongpoint but crucial method is not developed yet.

2. Motivation

The analysis accuracy of the FEM is known to be improved by using higher-order elements with mid-side nodes. If engineers try to improve analysis accuracy without using high-order elements, they usually employ finer finite elements in the analysis domain, which results in the increase of calculation time and memory consumption [1-3].

It is well recognized that, for the FEM-based structural analysis, higher-order elements are generally used to improve analysis results. On the other hand, for fluid analysis, by employing the Streamline Upwind/Petrov-Galerkin (SUPG) [4] method and the Pressure-Stabilizing / Petrov-Galerkin (PSPG) [5-7] method, it is possible to achieve good analysis results without using higher-order elements.

When conducting analysis considering fluid-structure interaction effects, it is desirable that node locations are consistent on the interface between fluid and structure domain as shown in Fig.1. But, when the fluid analysis method using the SUPG/PSPG stabilized FEM and the structural analysis method using higher-order elements are used at the same time, the locations of nodes on the interface between two analysis domain becomes inconsistent (see Fig. 2), because the second-order elements with mid-side nodes are used for the structural field and first-order elements without mid-side nodes for the fluid field, although these elements are both triangular and tetrahedral in the case of the 2D problems and the 3D problems, respectively.

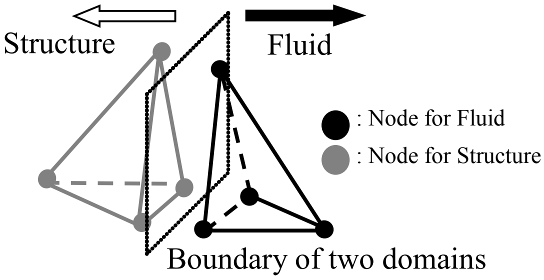

Figure 1. Interface nodes being consistent at the interface between fluid and structure fields

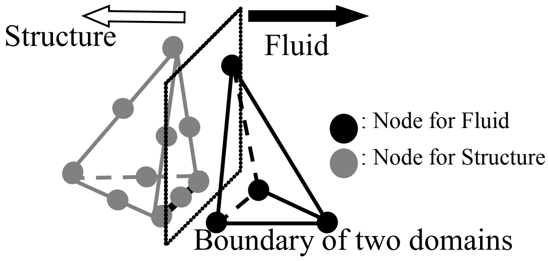

Figure 2. Interface nodes being inconsistent at the interface between fluid and structure fields

Accordingly, when considering the coupling effects of two different fields, it is necessary to interpolate the analysis results between the nodes. Much has been accomplished in 3D computation of practical problems with incompatible meshes at the fluid-structure interface (see, for example [8,9]) and in some cases deliberate use of incompatible meshes might be part of the solution strategy (see, for example [8,9]) and in some cases deliberate use of incompatible meshes might be part of the solution strategy (see, for example [10-13]). Still, using incompatible meshes at the interface complicates the calculation process, influences the coupling accuracy, and unless the solution strategy requires it, should be avoided. Therefore, when we try to perform structure-fluid coupled analysis, it is ideal to adopt an accurate structural analysis method without using the mid-side noded elements.

In order to cope with this problem, the authors propose to use the Enriched Free Mesh Method (EFMM) [14] as the structural analysis part, which is one of the meshless methods of high accuracy. The elements used for the EFMM based analysis are triangular or tetrahedral without mid-side nodes and it has been reported that the method gives solutions as accurate as that of the mid-side noded elements. By combining EFMM with the SUPG/PSPG stabilized FEM, it is possible to accurately analyze fluid-structure interaction problems in which the nodes on the boundaries between the structural and fluid fields are consistent as shown in Fig. 1.

On the other hand, the method has a shortcoming that is too difficult to apply into parallel computing. This issue is caused by algorithm of Enriched Free Mesh Method.

As a motivation, in this study we propose a parallelization algorithm for Enriched Free Mesh Method. And proposed parallelization method apply into our proposed fluid-structure coupled analysis method. Then compared with experimental data to prove effectiveness of our proposed fluid-structure coupled analysis method.

3. Fluid analysis Method

In this chapter, we describe fem that is using as a fluid analysis method. In addition, detail of ALE method is described. The method is the technique to solve moving boundary problem like a FSI problem.

Finally, numerical example that is computed this method is shown to prove validity.

3.1 SUPG/PSPG method

Here, the fluid analysis is conducted with a stabilized finite element formulation based on the SUPG[4] and PSPG[5-7] stabilizations (see [15] for a similar pressure stabilization method) that discretizes the Navier-Stokes equation and the equation of continuity. As the basic equations for incompressible viscous fluid, the dimensionless Navier-Stokes equation and the incompressible continuity equation can be respectively, written as follows,

$$\frac{\partial u_i}{\partial t} + u_j \frac{\partial u_i}{\partial x_j} + \frac{\partial p}{\partial x_i} - \frac{1}{\mathrm{Re}} \frac{\partial}{\partial x_j}\left(\frac{\partial u_i}{\partial x_j} + \frac{\partial u_j}{\partial x_i}\right) = 0 \qquad in \quad \Omega \tag{1}$$

$$\frac{\partial u_i}{\partial \mathrm{x}_i} = 0 \quad in \quad \Omega \tag{2}$$

Where u_i and p represent the velocity and the pressure, respectively. Re is the Reynolds number, and Ω is the analysis domain occupied by fluid. When the SUPG and PSPG method is applied to Eqs. (12) and (13), the following weak form is derived:

$$\begin{aligned}\int_\Omega w_i\left(\frac{\partial u_i}{\partial t} + u_i \frac{\partial u_i}{\partial x_j}\right) d\Omega - \int_\Omega \frac{\partial w_i}{\partial x_i} p d\Omega + \int_\Omega \frac{1}{\mathrm{Re}} \frac{\partial w_i}{\partial x_j}\left(\frac{\partial u_i}{\partial x_j} + \frac{\partial u_j}{\partial x_i}\right) d\Omega \\ + \sum_{e=1}^{n_{el}} \int_{\Omega_e} \tau_s u_k \frac{\partial w_i}{\partial x_k}\left(\frac{\partial u_i}{\partial t} + u_j \frac{\partial u_i}{\partial x_j} + \frac{\partial p}{\partial x_i}\right) d\Omega = \int_{\Gamma_h} w_i h_i d\Gamma\end{aligned} \tag{3}$$

and

$$\int_\Omega q \frac{\partial u_i}{\partial x_i} d\Omega + \sum_{e=1}^{n_{el}} \int_{\Omega_e} \tau_p \left(\frac{\partial u_i}{\partial t} + u_j \frac{\partial u_i}{\partial x_j} + \frac{\partial p}{\partial x_i}\right) d\Omega = 0 \tag{4}$$

Where w_i and q represent the weighting functions of the Galerkin terms of Eqs. (1) and (2), respectively. Γ denotes the boundary of the analysis domain Ω. τ_s and τ_p represent the stabilization parameters of the SUPG and PSPG method, respectively.

Regarding the velocity and the pressure, which are the unknown variables of Eqs. (3) and (4), the interpolation is carried out with the first-order triangular elements. This combination is possible, because the formulation is based on the stabilization finite element method. After discretizing this formulation in the time direction, a system of linear equations is derived with the unknown variables U^{n+1}, V^{n+1}, and P^{n+1} in the two-dimensional case. As the matrices in the above equations are asymmetric, we adopt the Generalized Product type method based on the Bi-CG (GPBi-CG)[16,17] method or the General Minimal Residual (GMRES(m)) method.

3.2 Numerical example

For fluid-structure interaction analysis, it is generally necessary to integrate the Lagrangian structural analysis with the Eulerian fluid analysis. For this purpose, the Arbitrary Lagrangian-Eulerian (ALE[18-23])method is used in this study, in which the Eulerian and the Lagrangian descriptions are combined. By using the finite element mesh moving independently from the motion of fluid, it is possible to track the motion of fluid-structure interface without generating highly distorted elements. In addition, the governing equation for fluid expressed with the ALE method is the same as the Navier-Stokes equation for incompressible flow expressed with the Eulerian method, except that advection velocity is replaced with the relative velocity with respect to mesh moving speed. From these features the method, the ALE method can be considered to be appropriate for analyzing the fluid-structure interaction problems[24].

Here, we discuss a numerical analysis of oscillation of a spring-supported cylinder induced by the Karman vortices in order to demonstrate the effectiveness of the fluid analysis method based on the SUPG/PSPG stabilization FEM. This problem was also studied extensively in [25] by using the DSD/SST formulation [26,27] and a special-purpose meth moving technique [27]. Here we perform this analysis to compare our results to data from a water tank experiment model, with which Anagnostopoulos and Bearma [28-30] succeeded in studying the lock-in phenomenon of the flow with a Reynolds number of around 100. The model used in this analysis is shown in Fig 1. It is assumed that the cylinder is a rigid single-degree-of-freedom spring-mass system. The condition for this analysis are also shown in the figure. The left figure of Fig 2 shows the mesh division at the initial state, while the right figure shows that when the cylinder moves upward due to spring oscillation.

In this analysis, elements are deformed due to the movement of the cylinder as we assume that the entire analysis domain is that of ALE method. In order to avoid an excessive deformation of the mesh during the analysis process, a mesh smoothing method based on the Laplace equation type technique is employed.

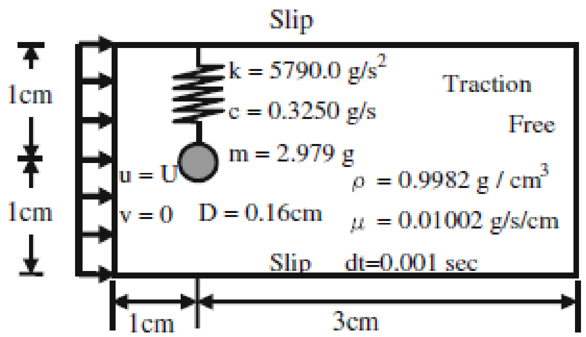

Figure 1. Analysis model

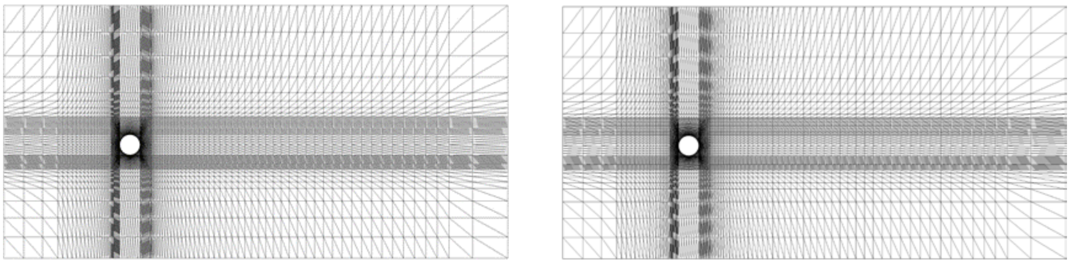

Figure 2. Meshes (Left at initial state, right during oscillation of a cylinder)

The motion of a rigid body can be given by the following equation,

$$m\alpha + c\upsilon + k\delta = X \tag{5}$$

with

$$\upsilon = \frac{d\delta}{dt}, \quad \alpha = \frac{d^2\delta}{dt^2} \tag{6}$$

Where m, c, and k represent the mass, the damping, and the stiffness, respectively. X is the force acting on the body. δ is the displacement of the rigid body. For solving this equation, the Newmark-beta method is used. This analysis is carried out for 4cases of the Reynolds number equal to 100, 110, 120, and 130, respectively.

Figure 3 shows the amplitude of the oscillation of the cylinder and trailing vortex frequency versus Reynolds number, respectively. It is seen from this figure that as upstream flow rate changes, the amplitude of the cylinder oscillation and the trailing vortex frequency change. Especially, when Reynolds number is 110 or 120, vortex frequency is locked at the eigen frequency of the cylinder, whereas the spring amplitude is larger at these Reynolds numbers.

The left figure of Figure 4 shows the streamline around the cylinder with Reynolds number equal to 130, while the right figure shows the case with Reynolds number equal to 110. These indicate that the "lock-in" increases the amplitude of the cylinder oscillation and also causes larger wake flow. It has been reported by the visualization experiment that wake flow widens during the lock-in phenomenon, which indicates that the present result is reasonable.

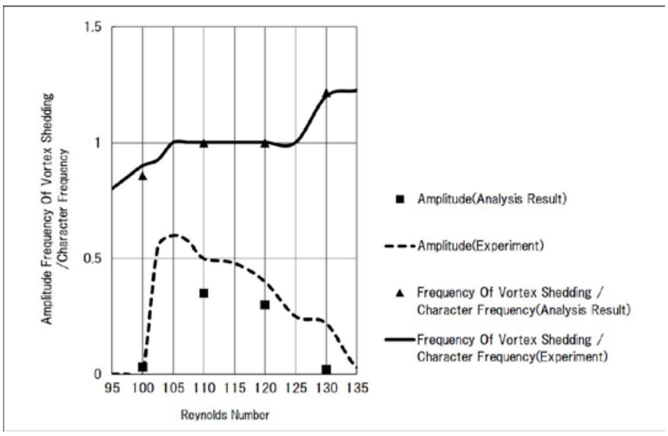

Figure 3. Vibration amplitude and vortex shedding frequency of a cylinder versus Reynolds number

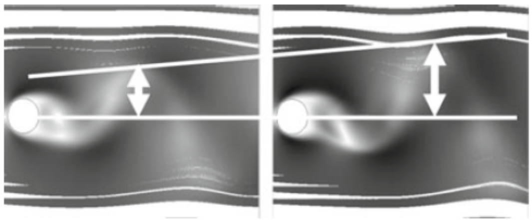

Figure 4. Streamline behind cylinders at lock-in and non-lock-in states (Left Re = 130; At non-locking state, right Re = 110; At locking state)

4. Structure Analysis Method

In this chapter, detail of Enriched Free Mesh Method (EFMM) is described.

4.1 Fundamental Concept of Enriched Free Mesh Method

Enriched Free Mesh Method (EFMM) [14] used for the structure analysis in this study is based on Free Mesh Method (FMM) [31,32], which is one of mesh-less methods. The most important feature of FMM is that it requires only the coordinate date of each node in analysis domains as the input information. Based on the given coordinate date of nodes, a local triangular elements cluster is created at each node. To produce such a local triangular elements cluster, there are a variety of methods including the diagonal comparison method, the gift wrapping method, and the method for developing a Delaunay triangle [33,34] for each central node based on the plannar relative relation between a Voronoi polygon and a Delaunay triangle.

Here, the node located at the center of local triangular elements cluster is called the central node, while nodes located at the edge of the elements cluster are called the satellite nodes (see Fig 5).

The stiffness matrix of this local elements cluster is calculated with the same way as the conventional FEM, and only the row components of the central node of the local trianbular elements cluster are added to the global stiffness matrix. By performing this procedure for all the nodes in the analysis domain, it is possible to obtain the stiffness matrix for the global analysis domain. Then, the resulted final solution becomes equal to that of FEM.

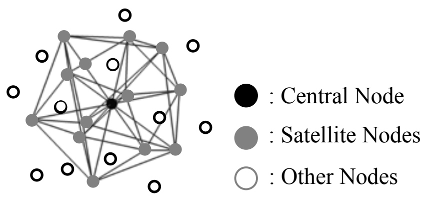

Figure 5. Local triangular elements cluster

4.2 Formulation of EFMM

It is known that FMM has the difficulty in using mid-side noded elements due to its automatic element production algorithm. In order to overcome this problem with FMM, EFMM has been developed, where it is assumed that a local triangular elements cluster has an arbitrary strain field in addition to a displacement field like the conventional FEM or FMM (see. Fig 6).

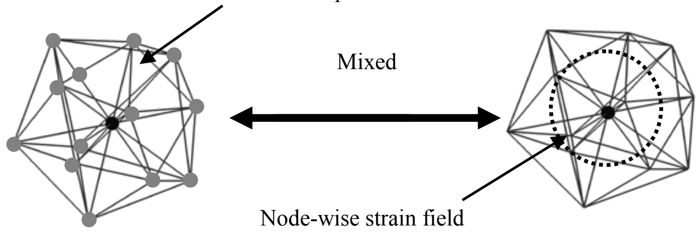

Figure 6. Two independent fields postulated in a local triangular elements cluster

In EFMM, the displacement and the strain fields are, respectively, assumed in independent locations, and these two fields are linked with the Hellinger-Reissner principle [35]. The principle, in which displacement u and strain ε are assumed to be independent variables, is given by

$$\prod(\varepsilon,u)=\int_{\Omega}\{\varepsilon\}^{T}[D]\{\partial u\}d\Omega-\frac{1}{2}\int_{\Omega}\{\varepsilon\}^{T}[D]\{\varepsilon\}d\Omega-\int_{\Omega}\{u\}^{T}\{b\}d\Omega-\int_{S_{\sigma}}\{u\}^{T}\{\tilde{t}\}dS \qquad (7)$$

with

$$\{\partial u\}=[B]\{\overline{u}\},\ \{u\}=[N^{u}]\{\overline{u}\},\ \{\varepsilon\}=[N^{\varepsilon}]\{\overline{\varepsilon}\} \qquad (8)$$

Where $\{\overline{u}\}$ represents the nodal displacement, $\{\overline{\varepsilon}\}$ the unknown parameter of strain, $\{b\}$ the body force, $\{\tilde{t}\}$ the surface force on the boundary S_{σ}, and Ω the analysis domain. $[N_{\varepsilon}]$ is an arbitrary function that determines the strain of a local region, which can be is assumed as

$$[N^{\varepsilon}]=\begin{bmatrix} p^{T} & 0 & 0 & 0 & 0 & 0 \\ 0 & p^{T} & 0 & 0 & 0 & 0 \\ 0 & 0 & p^{T} & 0 & 0 & 0 \\ 0 & 0 & 0 & p^{T} & 0 & 0 \\ 0 & 0 & 0 & 0 & p^{T} & 0 \\ 0 & 0 & 0 & 0 & 0 & p^{T} \end{bmatrix} \qquad (10)$$

where

$$p^{T}=\begin{bmatrix}1 & x & y & z\end{bmatrix} \qquad (11)$$

The stationary condition of Eq. (7) is expressed by

$$\int_{\Omega}\delta\{\varepsilon\}^{T}[D]\left([B]\{\overline{u}\}-[N^{\varepsilon}]\{\overline{\varepsilon}\}\right)d\Omega=0 \qquad (12)$$

and

$$\int_{\Omega} \delta\{u\}^T [B]^T [D][N^{\varepsilon}]\{\bar{\varepsilon}\} d\Omega - \int_{\Omega} \delta\{u\}^T \{b\} d\Omega - \int_{S_\sigma} \delta\{u\}^T \{\tilde{t}\} dS = 0 \quad (13)$$

These equations are written as follows,

$$\begin{bmatrix} -A & C \\ C^T & 0 \end{bmatrix} \begin{Bmatrix} \bar{\varepsilon} \\ \bar{u} \end{Bmatrix} = \begin{Bmatrix} f_1 \\ f_2 \end{Bmatrix} \quad (14)$$

where

$$\begin{cases} A = \int_{\Omega} [N^{\varepsilon}]^T [D][N^{\varepsilon}] d\Omega \\ C = \int_{\Omega} [N^{\varepsilon}]^T [D][B] d\Omega \\ f_1 = 0 \\ f_2 = \int_{\Omega} [N^u]^T \{b\} d\Omega + \int_{\Gamma} [N^u]^T \{\tilde{t}\} d\Gamma \end{cases} \quad (15)$$

Next, Eq. (14) is condensed to the following equation:

$$C^T (A^{-1} C\bar{u}) = f_2 \quad (16)$$

Finally, the local enriched stiffness matrix is derived as

$$[k_{HR}] = C^T A^{-1} C \quad (17)$$

Above enriched stiffness matrix is expected to give more accurate solutions than the usual FEM or FMM with the linear displacement base. The following section demonstrates that EFMM with the use of Eq. (17) is more accurate than the conventional FEM in a simple demonstrative example.

4.3 Numerical example for accuracy check

In this section, describe difference of analysis accuracy computed by EFMM and FEM. Cantilever beam model as shown in Fig. 7 is used for accuracy comparison between FEM and EFMM.

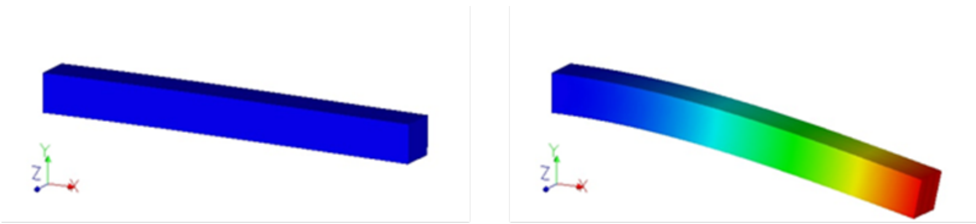

Figure 7. Analysis model and example of analysis result

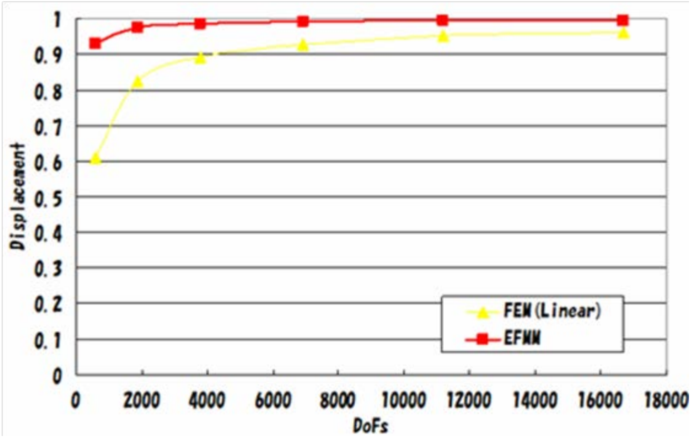

Figure 8. Accuracy comparison with FEM and EFMM

In the Fig.8, x-axis means number of degree of freedoms of analysis model. On the other hand, y-axis means normalized displacement.
From this result, it is obvious that analysis accuracy of EFMM becomes better than conventional FEM.
However, algorithm of EFMM is different from conventional FEM therefore, specific parallelization method for EFMM is needed.
Next chapter, specific parallelization method of EFMM is described.

5. Parallelization Method for Enriched Free Mesh Method

In this chapter, we describe about specific parallelization method for EFMM. In addition, numerical example that to prove a verification of the validity and parallel efficiency of this method are shown.
Incidentally, authors have been already proposed simplified parallelization method for EFMM [36]. This method have strongpoint but it is revealed that this method have some issues. Therefore simplified parallelization method is not able to apply into large scale analysis.
The specific parallelization method that is described in this chapter is able to overcome these problems.

5.1 Fundamental Concept of Parallelization Method

In this section, we describe the specific parallelization method for EFMM. In the case of conventional parallelization method for FEM, analysis domain is divided into some local domains by domain decomposition method, and create communication table. Then communication is done using communication table.
On the other hand, in the case of specific parallelization method for EFMM introduced by us is needed one more process. In particular, node on interface of each local domain have to search node to create correct local elements cluster.
A flowchart of parallelization method for EFMM is as shown Fig. 24.

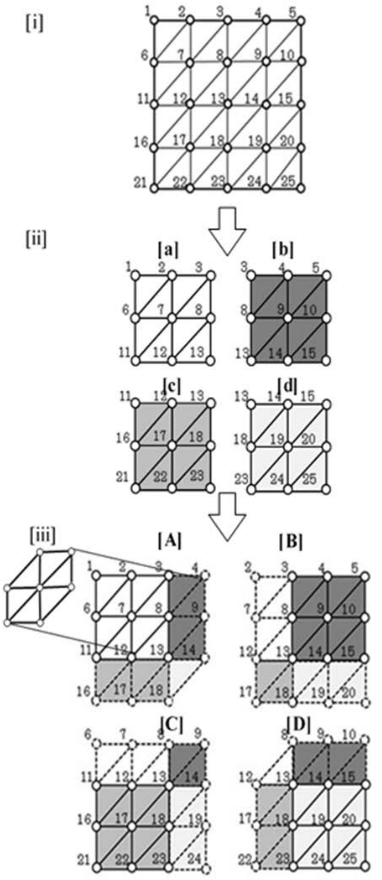

(1) Divide into few local domains by the element based domain decomposition method.

(2) Search nodes which needed to create a correct local elements cluster all of nodes in a whole domain.
*Some nodes are overlapped among with few domains.

(3) Local elements clusters are created without overlapped nodes.

Figure 9. A concept of domain decomposition for parallel EFMM

All node in local domain can create correct local elements cluster by expand local domain as shown in Fig. 9. However additional nodes in the process [iii] can't create correct local elements cluster. Therefore, it can’t be maintained consistency in the whole analysis area. To solve this problem, following communication process is added.

1. Matrix-vector product in each local domain. (All nodes are evaluated in any one of a local domain.)
2. Send computed value of one layer inside node to other domain that compensate for the lack of value. At this time, received value is added.
3. Send and receive value of node on interface between adjacent local domains.
4. Receive computed value of one layer outside node to other domain that compensate for the lack of value. At this time, received value is overwritten.

In short, communication of node data between each local domain will be incompatible. In particular, example of communication table between local domain [A] and [B] is shown in Table 1.
Parallelization of EFMM become possible by above calculation procedure.

Table 1. An example of communication table

	Send	Receive	Send & Receive
Local domain [A]	2,7,12	4,9,14	3,8,13
Local domain [B]	4,9,14	2,7,12	3,8,13

5.2 Evaluation of soundness of algorithm

In this section, describe a verification result of numerical example to prove soundness of proposed algorithm.
Communication tables made for parallel EFMM are different depending on domain decomposition because nodes needed communication are incompatible. Moreover, communication table will become more complicate than conventional parallel FEM.
In this paper, three types of models are used to confirm an evaluation of our proposed parallelization method.

1. Maximum number of adjacent domains : 2
2. Maximum number of adjacent domains : 4
3. Maximum number of adjacent domains : 8

5.2.1 Maximum number of adjacent domain is 2

In this subsection, describe evaluation results using model that is maximum number of adjacent domain is 2. Evaluation model is cantilever beam model shown in Fig 10. Analysis conditions are also written in Fig 10. Number of processers for this numerical example is 2 PEs.

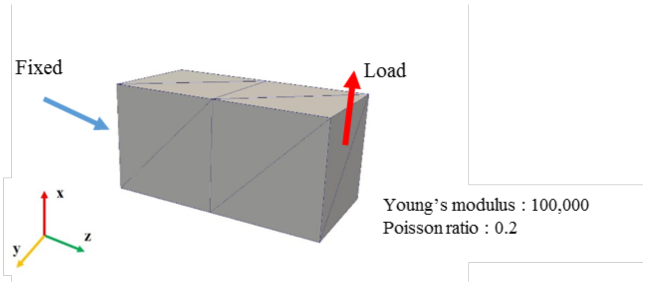

Figure 10. Analysis model

Fig 11 shows analysis results. An analysis result obtained by single computing is shown in left hand side. The other one is an analysis result obtained by 2 parallel computing.

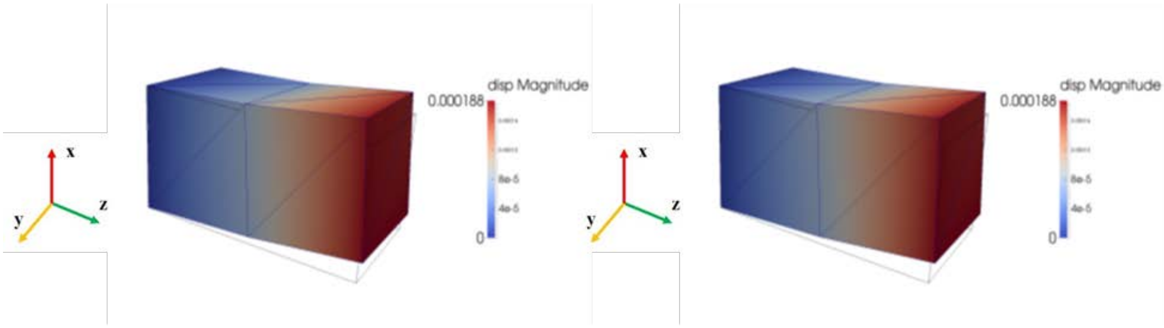

Figure 11. Analysis results (L : Single analysis , R : Parallel analysis)

Obtained maximum displacement of x direction that is computed by single computing and parallel computing is 0.000188. Analysis result obtained by single computing and parallel computing are completely same. From these result, it is revealed that our proposed parallelization method is able to calculate correctly in the case of maximum number of adjacent domain is 2.

5.2.2 Maximum number of adjacent domain is 4

In this subsection, describe evaluation results using model that is maximum number of adjacent domain is 4. Evaluation model is cantilever beam model shown in Fig 11. Evaluation model is simple as same as previous evaluation model but a shape of cantilever beam is little bit different from previous evaluation model. Analysis conditions are written in Fig 12. Number of processers for this numerical example is 4 PEs.

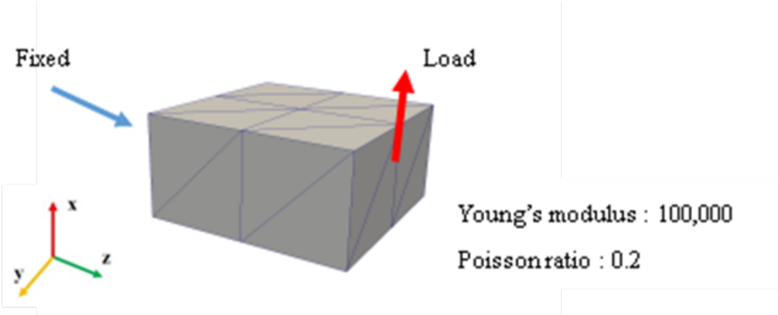

Figure 12. Analysis model

Fig 13 is analysis results obtained by single computing and parallel computing. Single analysis result is shown in (a). (b) is an analysis results computed by 4 PEs.

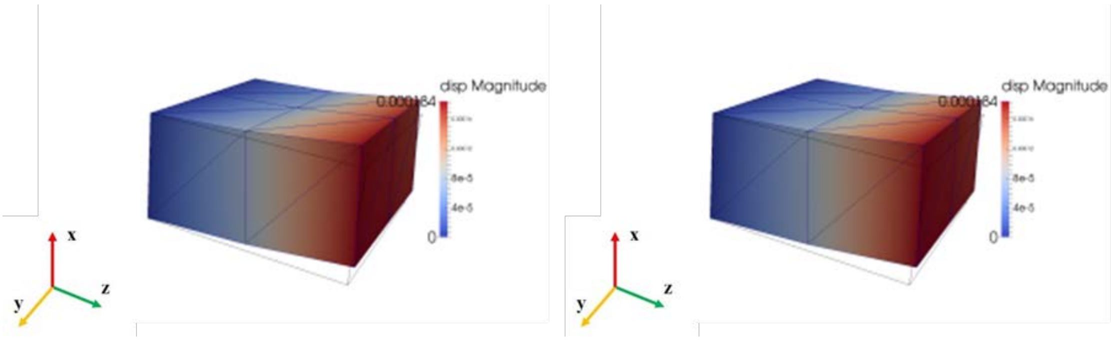

Figure 13. Analysis results (L : Single analysis , R : Parallel analysis)

Obtained maximum displacement of x direction of single analysis and parallel computing are 0.00184. Compared with previous case, communication table becomes more complicate and necessary communication domain is increased but both methods are obtained completely same result. From these results, it is revealed that our proposed parallelization method is able to calculate correctly in the case of maximum number of adjacent domain is 4.

5.2.3 Maximum number of adjacent domain is 8

Finally, in this subsection, describe evaluation results using model that is maximum number of adjacent domain is 8. Evaluation model is simply cantilever beam model as shown in Fig 14. In this case, number of processor that is using for analysis evaluation is 8. Analysis conditions are written in Fig 14.

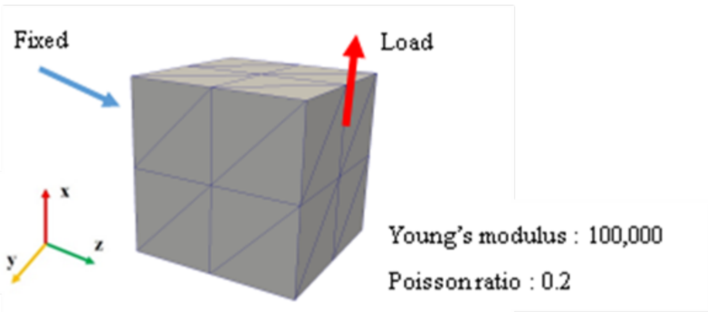

Figure 14. Analysis model

Fig 15 shows analysis results. Single computing result is shown in the left hand side. On the right hand side, parallel computing result is shown.

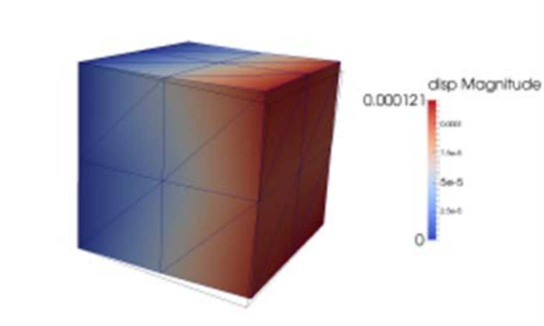

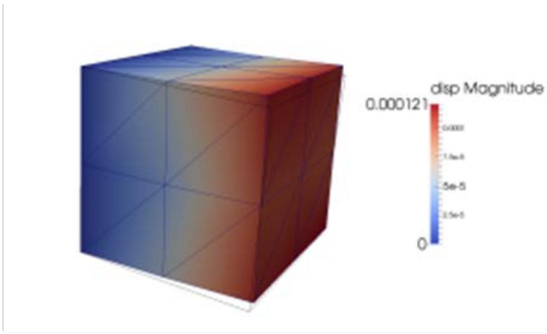

Figure 15. Analysis results (L : Single analysis , R : Parallel analysis)

Obtained maximum displacement of x direction computed by single computing and parallel computing are 0.000121. In short, analysis results are completely same. From this result, it is obvious that our proposed algorithm is able to apply into large analysis that is needed communication between many local domains.

5.3 Numerical Example for accuracy check

As previously described, evaluation of our proposed parallelization method for EFMM is proven. In this section, describe about analysis accuracy of parallelization EFMM. Cantilever beam model shown in Fig 16 are used to prove our proposed parallelization method. Analysis conditions and analysis mesh model are shown in Fig 16.

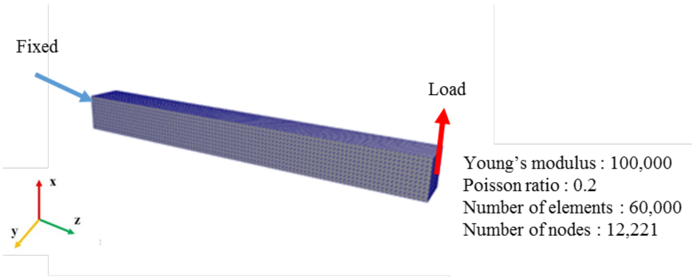

Figure 16. Analysis model

Calculate in accordance with this analysis condition, maximum displacement to tip of cantilever beam is 0.04.
Three types of models are used for evaluation. In particular, single computing, 10 PEs and 20PEs. Detail of analysis mesh data of each case are shown in Table 2.

Table 2. Detail of each local domain

#PE	Number of elements	Number of nodes	Degree of freedoms
1	60,000	12,221	36,663
10	6,000	1,331	3,993
20	3,000	756	2,268

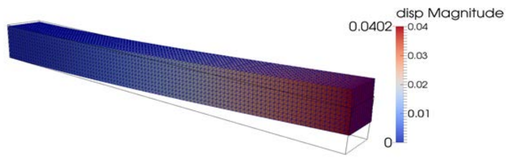

Figure 17. Analysis result

Fig 17 is an analysis result computed by single computing. Obtained displacement of tip of cantilever is 0.0402. From this result, it is obvious that this method can calculate high accuracy because error ratio between numerical result and theory is about 0.05%. Of course analysis results of single computing, 10 PEs and 20 PEs are completely same.

From this result, it is determine that our proposed parallelization method for EFMM is able to calculate correctly.

5.4 Numerical Example for Parallel Efficiency

In this section, describe parallel efficiency of our proposed parallelization method for EFMM. Evaluation model of parallel efficiency is shown in Fig 18. Detail of analysis model and analysis conditions are written in Fig 18.

Parallel efficiency is measured two methods. One is a strong-scaling, the other one is a weak-scaling. Here, this evaluation test is used Kei computer.

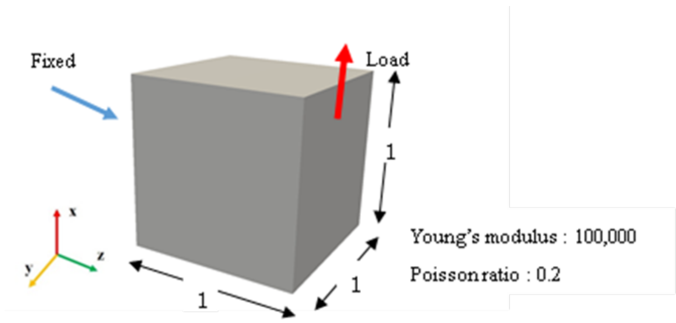

Figure 18. Analysis model

5.4.1 Strong Scaling

First, evaluation result of parallel efficiency that is measured by strong-scaling is shown in this subsection

Table 3 shows detail of whole analysis model that is used for verification of parallel efficiency. Number of elements, number of nodes and degree of freedoms written in Table 4. These are detail of mesh model that is used for each parallel computing.

Table 3. Detail of whole analysis model

Number of elements	7,558,272
Number of nodes	1,295,029
Degree of freedoms	3,885,087

Table 4. Detail of each local domain

#PE	Number of elements	Number of nodes	Degree of freedoms
16	472,392	84,700	254,100
54	139,968	26,011	78,033
144	52,488	10,108	30,324
432	17,496	3,610	10,830

Parallel efficiency that is measured by Kei computer is shown in Table 5. Results of parallel efficiency and speed up are calculated based on 16 PEs.
In addition, whole computing time and time for matrix vector product are calculated in this evaluation. Because, matrix vector product process is needed many time. Therefore, decreasing of calculation time for this process is very important point.

Table 5. Parallel efficiency

#PE	Elapsed [s]		#CG Iter	Speed-Up 16PE			Parallel Efficiency	
	All	mat_vec		All	mat_vec	Ideal	All	mat_vec
16	1,944	1,273	1,375	1.00	1.00	1.00	100.0%	100.0%
54	639	416	1,375	3.04	3.06	3.38	90.1%	90.6%
144	237	151	1,375	8.21	8.41	9.00	91.2%	93.4%
432	90	55	1,375	21.54	23.02	27.00	79.8%	85.3%

Changes in calculation time, acceleration ratio and parallelization ratio are shown in Fig 19, Fig 20 and Fig 21.

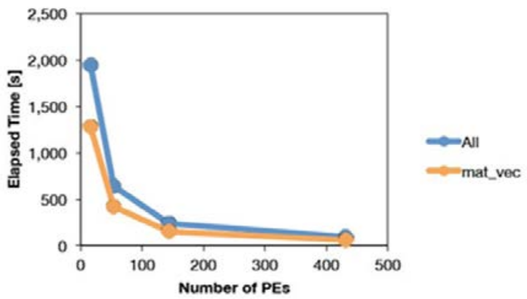

Figure 19. Changes in computing time

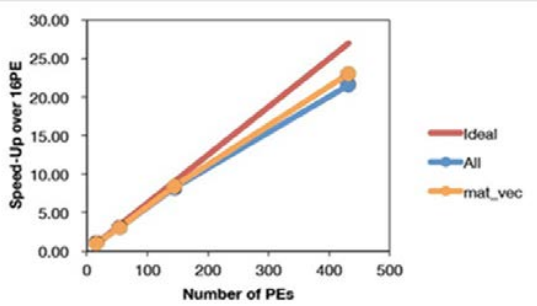

Figure 20. Changes in acceleration ratio

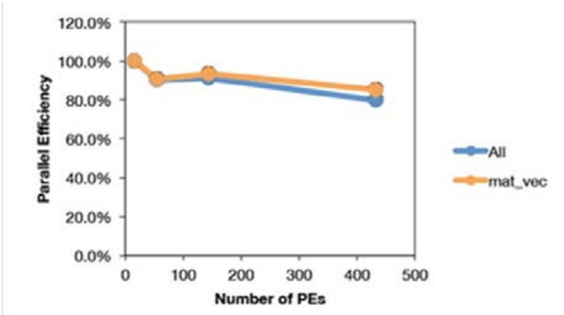

Figure 21. Changes in parallel efficiency

Parallel efficiency becomes worse because percentage of communication time in the whole analysis is increase because calculation scale of each nodes become smaller. This is a feature of strong scaling. However, in view of performance evaluation and calculation scale, it can be said these results are sufficient good performance is obtained.

Moreover, following Table 6 and Fig 22 show a percentage of main routine in the whole computing time. From these table and figure reveal that matrix vector product process occupy 60% in the whole computing time. Therefore, speed up of matrix vector product is very important to obtain more highly parallel efficiency.

Reason of increase of percentage of other process is caused by feature of strong scaling.

In particular, it is considered that amount of communication cost will become increase along with increasing of number of nodes.

Table 6. Detail of each local domain

	4M DoF 16PEs	4M DoF 54PEs	4M DoF 144PEs	4M DoF 432PEs
Matrix vector product	65.51%	65.15%	63.96%	61.29%
Calculation time for making stiffness matrix	30.26%	30.35%	31.01%	31.79%
Others	4.23%	4.50%	5.03%	6.93%

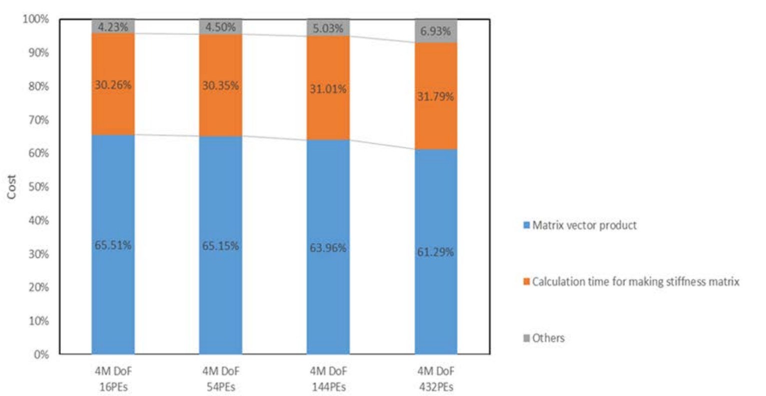

Figure 22. Percentage of primary routine

5.4.2 Weak Scaling

In this subsection, describe an evaluation result of parallel efficiency measured by weak scaling. Detail of analysis model that is used for this evaluation is shown in Table 7. And Table 8 shows a detail of analysis model for each parallel analysis.

Table 7. Detail of analysis model

Number of elements	472,392
Number of nodes	84,700
Degree of freedoms	254,100

Table 8. Detail of analysis model for each parallel analysis

#PE	Number of elements	Number of nodes	Degree of freedoms
16	7,558,272	1,295,029	3,885,087
54	25,509,168	4,330,747	12,992,241
144	60,466,176	10,218,313	30,654,939
432	204,073,344	34,328,125	102,984,375

Parallel efficiency analysis measured by weak scaling that is computed by Kei computer is shown in Table 9. In this table, whole computing time and time for matrix vector product are written.

Table 9. Result of measurement of parallel efficiency

#PE	Elapsed [s]			#CG Iter
	All	mat_vec	1 mat_vec	
16	1,944	1,273	1,375	1,375
54	2,304	1,614	1,375	1,726
144	2,813	2,115	1,375	2,276
432	3,286	2,568	1,375	2,747

Moreover, Fig 23, 24 and 25 show changes in computing time, matrix vector product, number of iterations and time for matrix vector product

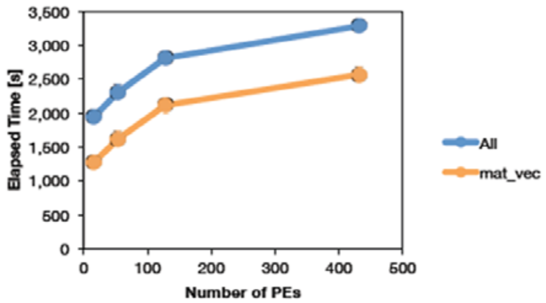

Figure 23. Changes in computing time

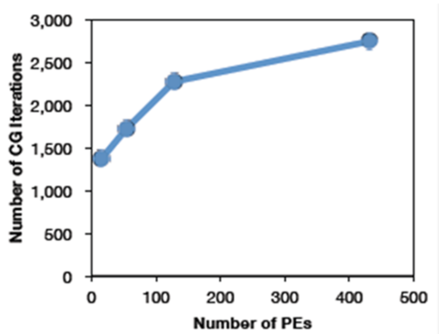

Figure 24. Changes in number of CG iterations

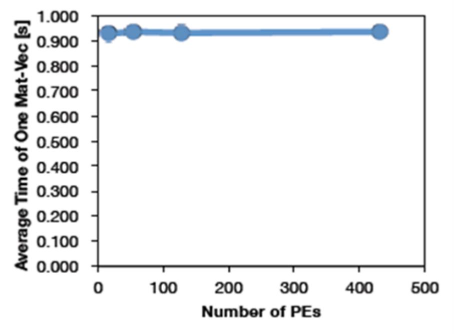

Figure 25. Changes in average time of one matrix-vector product

Number of iterations of CG method will be increased along with increasing of number of degree of freedoms of analysis model. Therefore, total computing time is also increased.

However, computing time for matrix vector product is kept substantially constant. In short, it can be determined that increasing of total computing time is caused by increasing of number of iterations.

Moreover, Table 10 and Fig 26 show a percentage of a computing time of main routine in a total computing time.

From following table and figure, it is obvious that percentage of computing for a matrix vector product time is increased along with increasing of an analysis scale.

In view of results of strong scaling and weak scaling, improvement of process for matrix vector product is very important that to obtain high parallel efficiency using our proposed parallelization method.

However, it is proved that our proposed parallelization method for FMM is able to apply large scale analysis like an about 100 million degree of freedoms from measurement results.

Table 10. Percentage of primary routine

	4M DoF 16PEs	13M DoF 54PEs	31M DoF 144PEs	103M DoF 432PEs
Matrix vector product	65.51%	70.04%	75.21%	78.13%
Calculation time for making stiffness matrix	30.26%	26.08%	21.35%	18.48%
Others	4.23%	3.88%	3.44%	3.39%

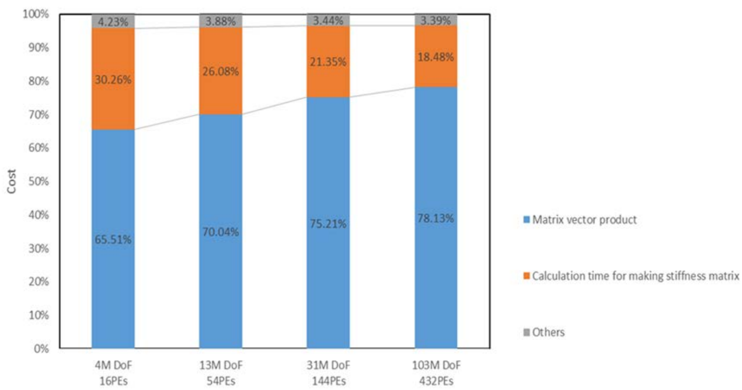

Figure 26. Percentage of primary routine

5.5 Conclusion

In this chapter, parallelization algorithm for EFMM that was too difficult to apply into large scale analysis is introduced and implemented.

Our proposed parallelization method was verified a parallel efficiency by weak scaling and strong scaling. From obtained verified results, it is obvious that speed up of matrix vector

product is very important to obtained higher parallel efficiency by our proposed parallelization method.
However, our proposed method is able to apply into large scale analysis and obtained fine analysis result. Therefore, it can be said that our proposed parallelization method is an effective method from verified results.
From this perspective, EFMM can be expected to be applied into wider field (ex : fluid-structure coupled phenomenon) by our proposed parallelization method.

6. Analysis

In this chapter, outline of our proposed fluid-structure coupled analysis method is described.

6.1 Flow chart

In this section, explain about analysis flow of our proposed method.
Fig 27 is flow chart of our proposed method.

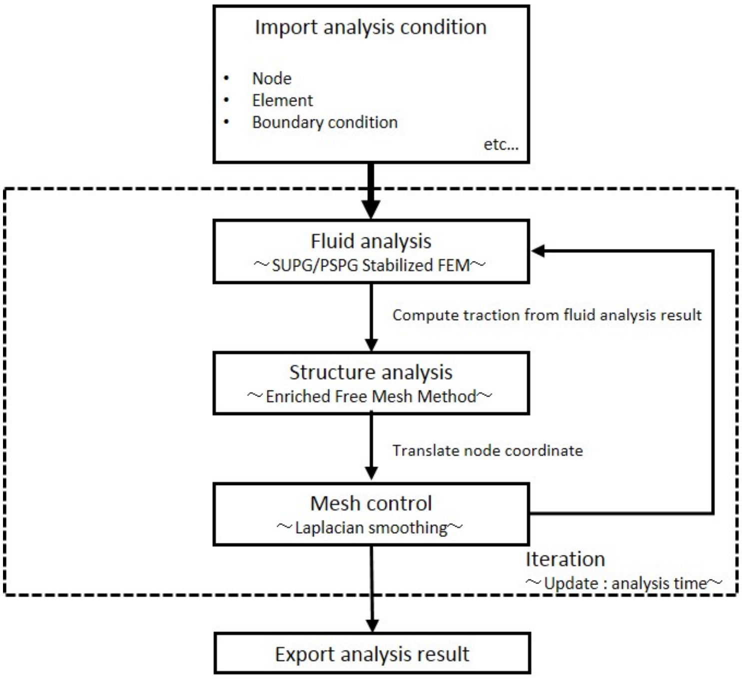

Figure 27. Flow chart of fluid-structure coupled analysis

First, import an analysis model.
Second, solve fluid analysis field by FEM. And calculate traction of fluid-structure interface.
Next, solve structure analysis field using EFMM. At this time traction that is calculated by previous process is used as a load.
Then, coordinate of node is moved according to analysis result.
Iterate above processes to obtain fluid-structure coupled analysis result.
This is the flowchart of our proposed fluid-structure coupled analysis method.

6.2 Numerical Example

In this section, describe a numerical example that is conforming to an experiment.
Fig 28 shows an analysis model that is used for numerical example.

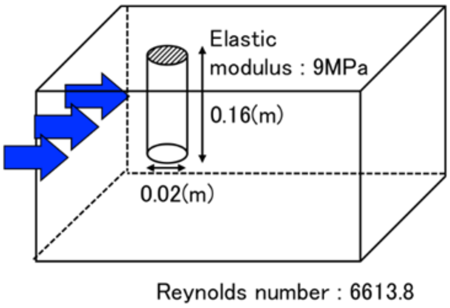

Figure 28. Analysis model

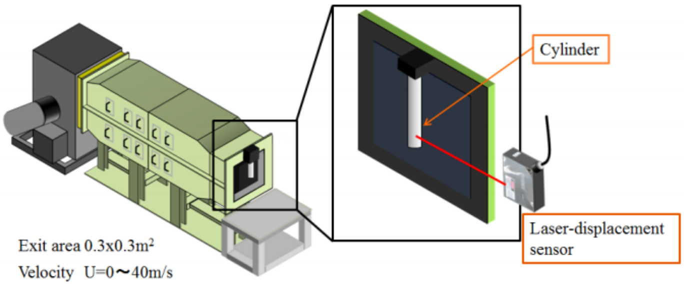

Figure 29. Experiment device

As shown in Fig 28, fluid flow is given to cylinder that is made by rubber. Upper side of cylinder is fixed. As an objective, elucidate difference of cylinder vibrations and relationship between flow velocity and physical properties of cylinder.

This numerical example is calculated accordance with experiment that is using experiment device as shown in Fig 29. Fig 30 is an analysis mesh model.

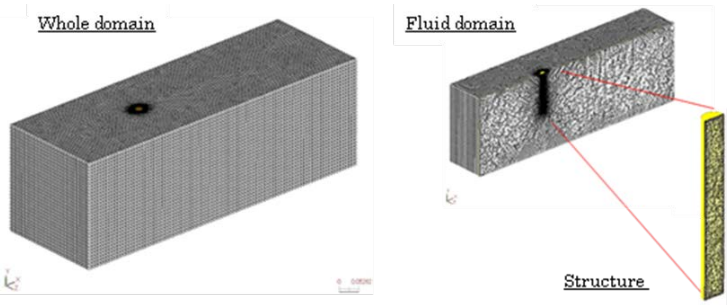

Figure 30. Analysis mesh model

Table 11. Detail of analysis mesh model data

	Fluid	Structure
Number of Nodes	944,121	94,768
Number of Elements	169,321	21,295

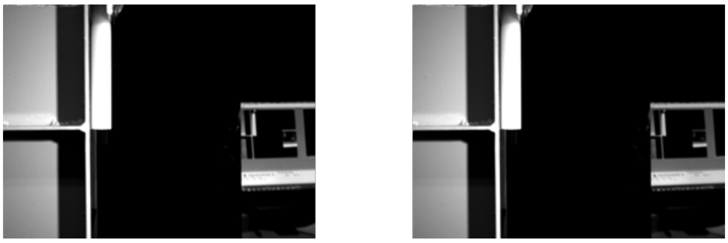

Figure 31. Experimental result (side)

Figure 32. Experimental result (upper side)

Experiment result shows in Fig 31 and 32.

A Cylinder did not vibrate under this experiment condition. As a behavior of cylinder that is simply bended by fluid flow. Observed displacement was very small. In particular, maximum displacement of bottom of cylinder was only 0.0005m.

Next, numerical analysis result is shown in Fig 33. Color contour in this figure means displacement. Obtained displacement is 0.0063m, amount of bending of cylinder is bigger than experiment result.

Error ratio between numerical result and experimental result is about 20%.

Unfortunately, effectiveness of our proposed method can't prove from this numerical result.

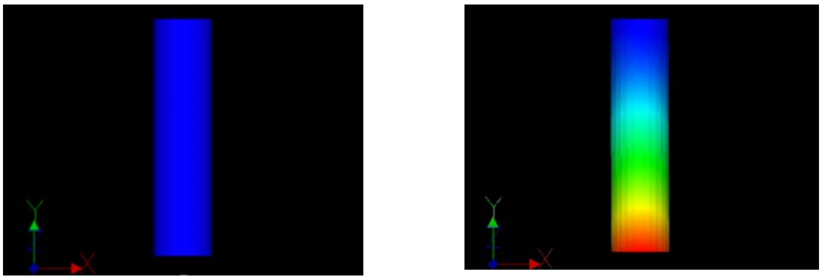

Figure 33. Numerical analysis result (side)

7. Conclusion

In this paper, proposed the new fluid-structure coupled analysis method that is combining SUPG/PSPG stabilized FEM and Enriched Free Mesh Method to solve fluid-structure coupled phenomenon.

Most important issue of this method was parallelization of EFMM. Because EFMM is needed the specific treatment to apply into parallel computing.

In this paper, proposed the specific parallelization method for EFMM and proved an effectiveness of this method. By evaluation result, our proposed method proved that is able to solve about 100 million degree of freedoms problem.

Our proposed method has already proven that can obtain fine analysis result by a qualitative evaluation [37]. But quantitative evaluation result and observation result were significantly different. From obtained result, quantitative evaluation of our proposed method was not able to prove.

As a future work, change experimental condition and continue evaluation to prove soundness of our proposed fluid-structure coupled analysis method.

However, proposed parallel fluid-structure coupled analysis method can be expected to be obtained fine analysis result. Because, the method has proven that to obtain fine analysis result of structure analysis and fluid analysis, moreover, highly parallel efficiency of each analysis field can be obtained.

References

[1] Zienkiewicz OC, Taylor RL (2000) The finite element method, 5^{th} edn. Elsevier, Amsterdam

[2] Hughes TJR (1987) The finite element method: linear static and dynamic finite element analysis. Prentice Hall, New York

[3] Zienkiewicz OC, Taylor RL, Nithiarasu P (2005) The finite element method for fluid dynamics, 6th edn. Elsevier, Amsterdam
[4] Brooks AN, Hughes TJR (1982) Streamline upwind/Petrov–Galerkin formulations for convection dominated flows with particular emphasis on the incompressible Navier–Stokes equations. Comput Methods Appl Mech Eng 32:199–259
[5] Tezduyar TE (1992) Stabilized finite element formulations for incompressible flow computations. Adv Appl Mech 28:1–44
[6] Tezduyar TE, Mittal S, Ray SE, Shih R (1992) Incompressible flow computations with stabilized bilinear and linear equal-orderinterpolation velocity-pressure elements. Comput Methods Appl Mech Eng 95:221–242
[7] Tezduyar TE (2003) "Computation of Moving Boundaries and Interfaces and Stabilization Parameters". Int J Numer Methods Fluids 43:555–575
[8] Tezduyar TE, Sathe S, Keedy R, Stein K (2006) Space-time finite element techniques for computation of fluid-structure interactions. Comput Methods Appl Mech Eng 195:2002–2027
[9] Tezduyar TE, Sathe S (2007) Modeling of fluid-structure interactions with the space-time finite elements: solution techniques. Int J Numer Methods Fluids 54:855–900
[10] Tezduyar TE, Sathe S, Pausewang J, Schwaab M, Christopher J, Crabtree J (2008) Interface projection techniques for fluidstructure interaction modeling with moving-mesh methods. Comput Mech 43:39–49
[11] Tezduyar TE, Takizawa K, Moorman C, Wright S, Christopher J (2010) Multiscale sequentially-coupled arterial FSI technique. Comput Mech 46:17–29
[12] Takizawa K, Moorman C, Wright S, Christopher J, Tezduyar TE (2010) Wall shear stress calculations in space-time finite element computation of arterial fluid-structure interactions. Comput Mech 46:31–41
[13] Takizawa K, Tezduyar TE (2011) Multiscale space-time fluidstructure interaction techniques. Comput Mech. doi:10.1007/s00466-011-0571-z
[14] Yagawa G, Matsubara H (2007) Enriched free mesh method: an accuracy improvement for node-based fem, computational plasticity. Comput Methods Appl Sci 7:207–219
[15] Franca LP, Frey SL (1992) Stabilized finite element methods II. The incompressible Navier–Stokes equations. Comput Methods Appl Mech Eng 99:209–233
[16] Zhang S (1997) GPBi-CG generalized product-type methods based on Bi-CG for solving non-symmetriclinear systems. SIAM J Sci Stat Comput 18:537–551
[17] Thuthu M, Fujino S (2008) Stability ofGPBiCG AR method based on minimization of associate residual. ASCM 5081:108–120
[18] Belytschko T, Flanagan DF, Kennedy JM (1982) Finite element method with user-controlled meshes for fulid-structure interactions. Comput Methods Appl Mech Eng 33:689–723
[19] Huetra A, Liu WK (1988) Viscous flow with large free surface motion. Comput Methods Appl Mech Eng 69:277–324
[20] Huetra A, Liu WK (1988) Viscous flow structure interaction. J Press Vessel Technol 110:15–21
[21] Nitikipaiboon C, Bathe KJ (1993) An arbitrary Lagrangian-Eulerian velocity potential formulation for fluid-structure interaction. Comput Struct 47:871–891
[22] Bathe KJ, Nitikitpaiboon C, Wang X (1995) A mixed displacement- based finite element formulation for acoustic fluid-structure interaction. Comput Struct 56:225–237
[23] Bathe KJ, Zhang H, Wang MH (1995) Finite element analysis of incompressible and compressible fluid flows with free interfaces and structural interactions. Comput Struct 56:193–213
[24] Chakrabarti SK (2007) Fluid structure interaction and moving boundary problems. WIT Press, Southampton
[25] Mittal S, Tezduyar TE (1992) A finite element study of incompressible flows past oscillating cylinders and airfoils. Int J Numer Methods Fluids 15:1073–1118
[26] Tezduyar TE, Behr M, Liou J (1992) A new strategy for finite element computations involving moving boundaries and interfaces – the deforming-spatial -domain/space-time procedure: I. The concept and the preliminary
[27] Tezduyar TE, Behr M, Mittal S, Liou J (1992) A new strategy for finite element computations involving moving boundaries and interfaces – the deforming-spatial-domain/space-time procedure: II. Computation of free-surface flows, two-liquid flows, and flows with drifting cylinders. Comput Methods Appl Mech Eng 94: 353–371
[28] Nomura T (1992) Finite element analysis of vortex-induced vibrations of bluff cylinders. J Wind Eng 52:553
[29] Anagnostopoulos P, Bearman PW (1967) Response characteristics of vortex-exited cylinder at low Reynolds numbers. J Fluids Struct 6:501–502
[30] Koopman GH (1967) The vortex wakes of vibrating cylinders at low Reynolds numbers. J Fluid Mech 28:501–502
[31] Yagawa G, Yamada T (1996) Free mesh method a new meshless finite element method. Comput Mech 18:383–386
[32] Yagawa G,Yamada T (1996) Performance of Parallel computing of free mesh method. In: Proceedings of the 45th National Congress of Theroretical & Applied Mechanics

[33] Berg M, Cheong O, Kreveld M, Overmars M (2008) Computational geometry: algorithms and applications, 3rd edn. Springer, New York
[34] Inaba M, Fujisawa T, Okuda Y, Yagawa G (2002) Local mesh generation algorithm for free mesh method. The Japan Society of Mechanical Engineers [No. 02-9] Dynamic and Design Conference
[35] Zienkiewicz OC, Taylor RL (1996) Matrix finite element method I (Recision new publication) Kagaku Gijutsu Shuppan, Inc
[36] Nagaoka S, Nakabayashi, Y, Yagawa G, (2014) Parallelization of Enriched Free Mesh Method for Large Scale Fluid-Structure Coupled Analysis. Procedia Engineering 90
[37] Nagaoka S, Nakabayashi, Y, Yagawa G, YJ Kim (2011) Accurate fluid-structure interaction computations using elements without mid-side nodes. Computational Mechanics Volume 48 Number 3.

High Accurate Analysis by Experiment and Simulation Using Bayesian Inference for Corrugated Cardboard

Masahiko Shimamura[1], Yoshitaka Ezawa[2]

[1]Department of Mechanical Engineering, Toyo University
[2] Center for Computational Mechanics Research, Toyo University

Abstract
Corrugated cardboards are used in many fields. The design of corrugated cardboard, however, is based on experimentations. The subject of this paper is developing the technique for high accurate analysis of corrugated cardboards. The corrugated cardboard is complicated structures and its property is unknown. Therefore, it is difficult to analyze this structure. We did bending tests of corrugated cardboard and its homogenized analysis using finite elements. We estimated its property by comparing both results. The experimentations include a lot of variation because the sample varies widely. Therefore model verification and validation is necessary. We used Bayesian inference for this purpose. In Bayesian inference, a priori probability is important. We compared three a priori probabilities. The first one is a uniform distribution which means no a priori information. The second one is a normal distribution which indicates a priori information about ambiguous data of the property. The third one is a normal distribution of which mean is the exact property. It is not realistic to use the third one. Numerical results show a uniform distribution is useful for estimating the property. The variance of Bayesian inference using a uniform distribution is wide, but the mean value becomes exact value quickly. The numerical results show the validity of Bayesian inference.

Key words : Corrugated cardboard, Finite element analysis, Data assimilation, Bayesian inference, Equivalent analysis

1. Introduction

Products that use composite materials, such as corrugated cardboard, are used in a wide variety of fields. Therefore, the importance of conducting numerical analysis of composite materials is increasing. When conducting numerical analysis of a composite material structure with anisotropic characteristics, one must give sufficient consideration to the parameters of composite material characteristics; therefore, to conduct a valid numerical analysis, it is important in engineering to calculate physical properties that are unique to the structure. In this study, we approached these issues using corrugated cardboard consisting of composite materials. In recent years, the use of corrugated cardboard has expanded, such as in transportation and cushioning material, and accurate strength design is necessary. However, corrugated cardboard parameters in a numerical analysis are adjusted based on literature and the previous experiences of the designer. Corrugated cardboard is structured by having a wave-shaped corrugating medium sandwiched between two base papers called liners. Since its flute is quite dense, it takes much time and effort to model, and it is unpractical to run the usual finite element analysis as it requires too much cost and time to generate mesh for each flute. Therefore, numerical simulation of corrugated cardboards has not progressed. As such, to analyze subjects for which discretization is difficult with a finite element method due to its analysis domain regularly repeating with a microscopic structure as a unit, and its dense degree of repetition, a study that applies a homogenization technique is being conducted [1].

Therefore, it is quite effective to apply a homogenization technique to corrugated cardboard with the complex and microscopic structure of multiple flute [2][3]. To estimate the material properties of corrugated cardboard, in this study, by incorporating the experimental values of a bending test into numerical analysis using the homogenization technique, we were able to fully utilize the experimental results, and established a method that efficiently obtained the material properties, which are unknown parameters, using the response surface from the results of these numerical analyses. By comparing the results of numerical analysis of material properties with experimental values, we were able to verify its validity. In addition, to obtain material properties, we used experimental values of corrugated cardboards; however, the quality of corrugated cardboard materials is not uniform, and thus the reliability of analytical results obtained for material properties is essential in conducting numerical analysis. As such, the methodology of Model Verification &Validation (V&V) [4] that increases the reliability of analytical results against modeling errors and parameter uncertainties is gaining attention and Bayesian inference [5][6][7] in particular, is considered to be effective. There is no example of obtaining material properties of corrugated cardboard and conducting accuracy validation with the Model V&V. Therefore, we quantitatively evaluated uncertainties for material properties obtained using Bayesian inference, and examined the validity. Also In this paper, we conducted discussion on especially elastic modulus for material property.

2. Corrugated cardboard test method

2.1 Test material

Fig. 1(a) shows the structure of the single corrugated cardboard used for the experiment. Table 1 shows the dimensions, and Fig. 1(b) shows the load direction due to an indenter. In addition, in this study, we used B flute that consists of corrugating medium MC120 and liner LB180 that is compliant to JIS P 3902 and JIS P 3904, and the experiment was performed at a temperature of 11 degrees and humidity of 38%.

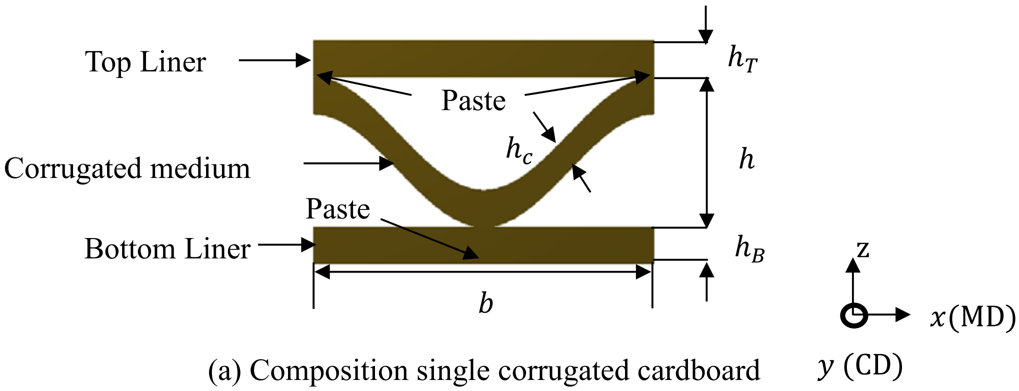

(a) Composition single corrugated cardboard

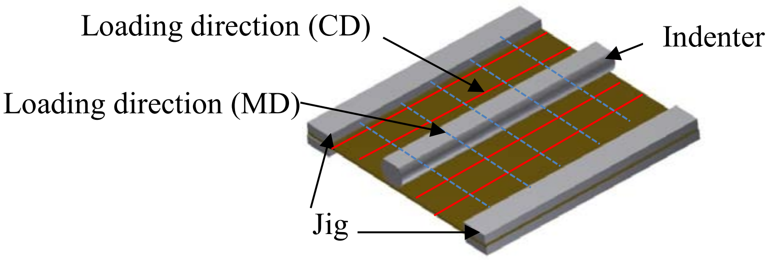

(b) Load direction of Indenter

Figure 1. Composition single corrugated cardboard and loading

Table 1. Size of corrugated cardboard

h_T	h_B	h_c	h	b
0.3	0.3	0.3	2.4	6

(mm)

2.2 Bending test

To measure the flexural strength characteristics of corrugated cardboard, the sample was fixed with jigs and load was applied with an indenter as shown in Fig. 2. At the speed of 10 mm/min, tests were conducted in the CD and MD ten times until the flute was completely crushed. The test fragment was to be changed in each experiment. Load and displacement characteristics of the test results are shown in Fig. 3. It shows that with the maximum load, the bent part of the corrugated cardboard forms a line and buckling develops, confirming a rapid decrease in the load. Furthermore, when comparing each experimental result, there was a difference in the behavior of load and displacement, likely due to systematic errors.

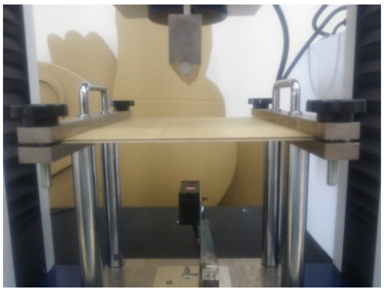

Figure 2. Bending test of corrugated cardboard

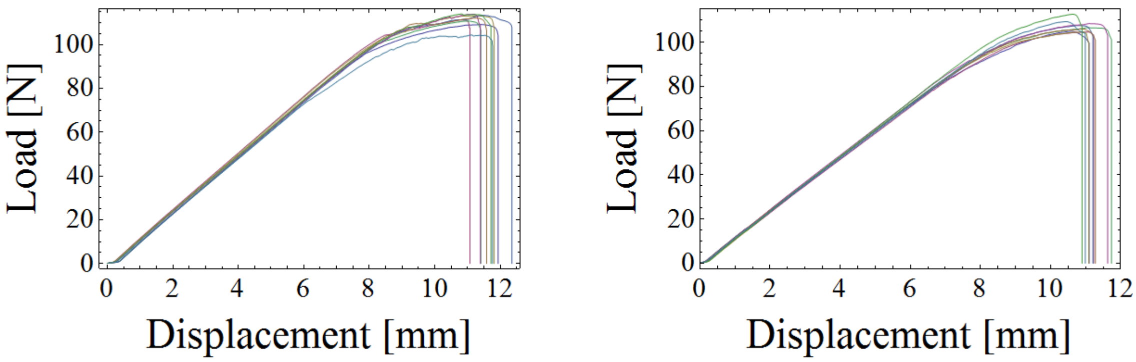

(a) CD (b) MD

Figure 3. Results of bending test

3. Errors and the least square method
3.1 The regression line by the least square

Data obtained from the experiment have errors as long as there are human factors involved. If a theoretical model is applied to such experimental values, one may use the least square method to determine the most appropriate function. If the model function is a primary function, a single regression model can be expressed as follows:

$$f(x) = ax + b \tag{1}$$

If n data $(x_1, y_1), (x_2, y_2), \cdots, (x_n, y_n)$ is obtained:

$$a = \frac{n\sum_{i=1}^{n} x_i y_i - \sum_{i=1}^{n} x_i \sum_{i=1}^{n} y_i}{n\sum_{i=1}^{n} x_i^2 - (\sum_{i=1}^{n} x_i)^2} \tag{2}$$

$$b = \frac{\sum_{i=1}^{n} x_i^2 \sum_{i=1}^{n} y_i - \sum_{i=1}^{n} x_i y_i \sum_{i=1}^{n} x_i}{n\sum_{i=1}^{n} x_i^2 - (\sum_{i=1}^{n} x_i)^2} \tag{3}$$

By obtaining Eq. (2) and (3), the slope of Eq. (1) and the value for the intercept can be obtained. We used the results between displacement 0.5 and 2.0. These result shows linear response.

3.2 Pretreatment for regression line

The value of b of Eq. (1) depends on the setting of the indenter. This value is not important for the analysis. Therefore, we set the value of b at zero as in Eq. (4) to recreate the behavior of experiment values in a numerical simulation. The analysis domain was limited to a linear range (0.5 ≤ displacement ≤ 2.0). Fig. 4 shows regression lines of Eq. (1) obtained from the least square method and Eq. (4) in which the error due to the sample attachment is 0, in both the CD and MD.

$$y = ax \tag{4}$$

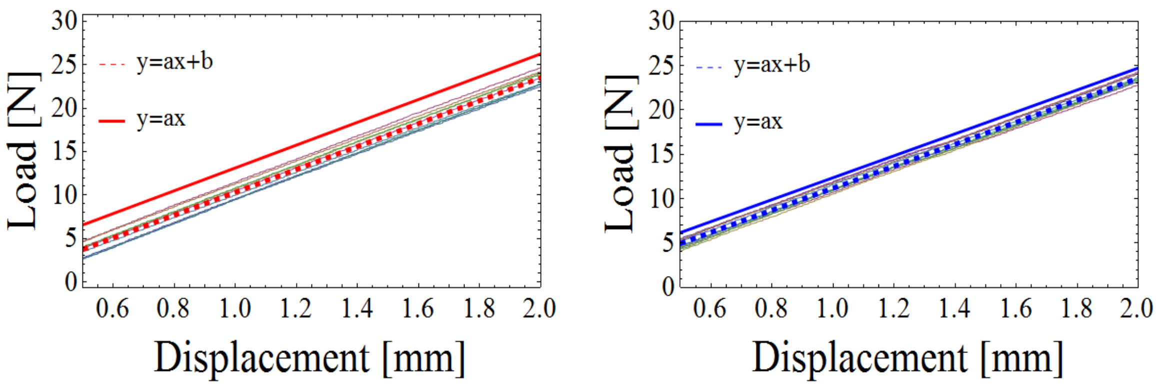

(a) CD (b) MD

Figure 4. Analysis target area

4. Numerical analysis of corrugated cardboard
4.1 The homogenization technique

The homogenization technique [1] substitutes composite material with a microscopic periodic structure with an equivalent homogenous body and reflects the analysis of a microscopic basic structural unit (unit cell), consisting of one period of microscopic period structure, to evaluate macroscopic behavior. It is one of the effective averaging methods, and makes microscopic-macroscopic coupled behavior analysis possible. If we set the coordinate system of a macro structure as x, and the microscopic coordinate system of the unit cell as y, the following equation is established through microstructural parameter μ:

$$y_i = \frac{x_i}{\mu} \tag{5}$$

Assuming body force f that works in the domain Ω and surface force t that works in the domain Γ_t, the work of the virtual principle against the macro-model can be expressed as follows:

$$\int_\Omega D^\mu_{ijkl} \frac{\partial u^\mu_k}{\partial x_i} \frac{\partial v^\mu_i}{\partial x_j} d\Omega = \int_\Omega f_i v^\mu_i d\Omega + \int_{\Gamma_t} t_i v^\mu_i d\Gamma \tag{6}$$

where D^μ_{ijkl} is the elastic tensor. Displacement u^μ of a structure consisting of a microscopic structure with periodicity is asymptotically expanded.

$$u^\mu_i = u^0_i(x) + \mu u^1_i(x,y) + \cdots, y_i = \frac{x_i}{\mu} \tag{7}$$

where the following equation can be established for Y–periodic function $\Psi(y)$:

$$\lim_{\mu \to 0} \int_\Omega \Psi(\frac{x}{\varepsilon}) d\Omega = \frac{1}{|Y|} \int_\Omega \int_Y \Psi(y) dY d\Omega \tag{8}$$

Here, $|Y|$ represents the volume of the unit cell. Eq. (7) is substituted into Eq. (6) and rearranged, and by applying Eq. (8), it can be divided into Eq. (10) that expresses microstructure and Eq. (11) that expresses macrostructure.

$$\frac{1}{\varepsilon^2} \int_\Omega D^\varepsilon_{ijkl} \frac{\partial u_{0k}}{\partial y_l} \frac{\partial v_i}{\partial y_j} d\Omega = 0 \tag{9}$$

$$\frac{1}{\varepsilon} \int_\Omega D^\varepsilon_{ijkl} \left[\left(\frac{\partial u_{0k}}{\partial x_l} + \frac{\partial u_{1k}}{\partial y_l} \right) \frac{\partial v_i}{\partial y_j} + \frac{\partial u_{0k}}{\partial y_l} \frac{\partial v_i}{\partial x_j} \right] d\Omega \ = 0 \tag{10}$$

$$\int_\Omega D^\varepsilon_{ijkl} \left[\left(\frac{\partial u_{0k}}{\partial x_l} + \frac{\partial u_{1k}}{\partial y_l} \right) \frac{\partial v_i}{\partial y_j} + \left(\frac{\partial u_{1k}}{\partial x_l} + \frac{\partial u_{2k}}{\partial y_l} \right) \frac{\partial v_i}{\partial y_j} \right] d\Omega = \int_{\Omega^\varepsilon} f^\varepsilon_i v_i d\Omega + \int_{\Gamma^\varepsilon_i} t_i v_i \tag{11}$$

By applying divergence theorem and Eq. (8) to Eq. (9), the following equation is obtained:

$$u_0 = u_0(x) \tag{12}$$

where u_o only depends on the overall structure. By applying Eq. (8), Eq. (12), and divergence theorem to Eq. (10), and by introducing χ that satisfies Eq. (9), Eq. (14) is obtained:

$$\int_Y D_{ijmn} \frac{\partial \chi_m^{kl}}{\partial y_n} \frac{\partial v_{1i}}{\partial y_j} dY = \int_Y D_{ikjl} \frac{\partial v_{1i}}{\partial y_j} dY \qquad \forall v_1 \in V_Y \tag{13}$$

$$u_{1i} = -\chi_i^{kl}(x, y) \frac{\partial u_{ok}(x)}{\partial x_l} \tag{14}$$

By applying Eq. (8), (12), (14), and divergence theorem to Eq. (11), the virtual principle of the overall structure can be derived.

$$\int_\Omega D_{ijkl}^h \frac{\partial u_{0k}}{\partial y_l} \frac{\partial v_{0i}}{\partial y_j} d\Omega = \int_\Omega \left(\frac{1}{|Y|} \int_Y f_i dY \right) v_{0i} d\Omega + \int_{\Gamma_t} t_i v_{0i} d\Gamma \tag{15}$$

where Eq. (16) is an equation that obtains the equivalent elastic constant in macroscopic structure, and if defined as a homogenization elastic tensor D_{ijkl}^h, we obtain:

$$D\,{}_{ijkl}^{h} = \frac{1}{|Y|} \int_Y \left(D_{ijkl} - D_{ijmn} \frac{\partial \chi_m^{kl}}{\partial y_n} \right) dY \tag{16}$$

In addition, displacement u^ε, strain ϵ^ε, and stress σ^ε that take microscopic structures into consideration can be obtained with the following equation:

$$u_i^\varepsilon = u_{0i}(x) - \varepsilon \chi_i^{kl}(x, y) \frac{\partial_{u0k}(x)}{\partial x_l} + \cdots \tag{17}$$

$$\epsilon_{ij}^\varepsilon = \frac{\partial u_{0i}}{\partial x_j} - \frac{\partial \chi_i^{kl}}{\partial y_j} \frac{\partial u_{0k}}{\partial x_l} + \cdots \tag{18}$$

$$\sigma_{ij}^\varepsilon = \left(D_{ijkl} - D_{ijmn} \frac{\partial \chi_m^{kl}}{\partial y_n} \right) \frac{\partial u_{0k}}{\partial x_l} + \cdots \tag{19}$$

We used the finite element method calculating Eq. (13),(14),(15),(16),(17),(18) and (19).

4.2 Microscopic structure finite element method model

Since flute of corrugated cardboard have periodicity, we prepared a finite element model that uses one flute as a unit cell as shown in Fig. 5. To model corrugating medium, we approximated with Sine wave. Poison ratio was literature [1][8] reference and element decomposition was performed with appropriate number of nodes and elements considering the analysis time. Details are shown in Table 2.

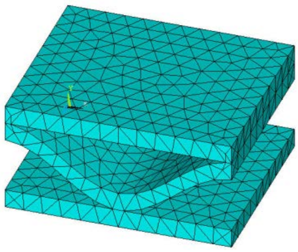

Figure 5. Unit cell finite element method for corrugated cardboard

Table 2. Specifiction of unit cell finite element method

Size(mm)		x=6.0,y=6.0,z=3.0
Element Type		Quadratic element
Number of nodes		6099
Number of elements		2973
Number of materials		2
Material 1		Liner
Material 2		Corrugated medium
Poison ratio	Liner	0.6
	Corrugated medium	0.3

4.3 Overall structure finite element method model

We use the homogenized elastic stiffness obtained in Section4.2. We prepared a finite element method model that uses the test fragment used in the bending test as the overall structure.
Fig. 6 shows the finite element model, and Table 3 shows the details. Boundary conditions are shown in Fig. 6: shown in Fig. 6(a) if analyzing in the CD, cross-directional xyz direction C_1 and C_2 were constant, and -20N was applied in the line z direction on the both L_1 and L_2; shown in Fig. 6(b) if analyzing in the MD, cross-directional xyz direction C_3 and C_4 were constant, and -20N was applied in the line z direction on the both L_3 and L_4.

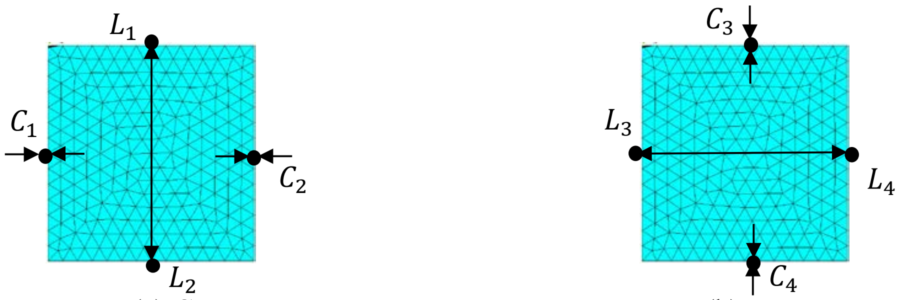

(a) CD (b) MD

Figure 6. Finite element method for corrugated cardboard for macro model

Table 3. Specifiction of finite element method for macro model

Size(mm)	X=250,y=250,z=3.0
Number of nodes	3019
Number of elements	1492

5. Method of calculating material constant
5.1 Formulation of elastic modulus search

In this study, we targeted both the CD and MD of the corrugated cardboard that receives point load as an external force, and numerical simulation searched for elastic modulus that fit the displacement due to known 20 N load from the regression line using the homogenization technique. e_1 represents the liner, while e_2 represents the elastic modulus of the corrugating medium, respectively, and can be formulated as in Eq. (20).

$$im(F_{20})(\{(e_1, e_2) | e_1, e_2 \in \{1000, 2000, 3000, \cdots, 10000\}\}) \tag{20}$$

5.2 Response surface model

Response surface method is technique for continuous carved surface complementary discrete multiple solution, and predictive accuracy and that depend on approximate function and interpolation technique but it have estimating advantage relativity well-approximate equation by low sample number. If analysis point of search $x_i (i = 1, 2, \cdots, n)$ and approximation error as ε, elastic modulus of liner and corrugated medium y can be expressed as Eq. (21).

$$y = f(x_1, x_2, \cdots, x_n) + \varepsilon \tag{21}$$

Fig. 7 shows response surface of CD and MD obtained in this research. Point is result of numerical simulation and curved surface is response surface. There was difference in both numerical simulation and response surface from approximation error as ε. But obtained numerical simulation and response surface are consistent, and the number of sample used here was sufficient enough to give accurate response surface.

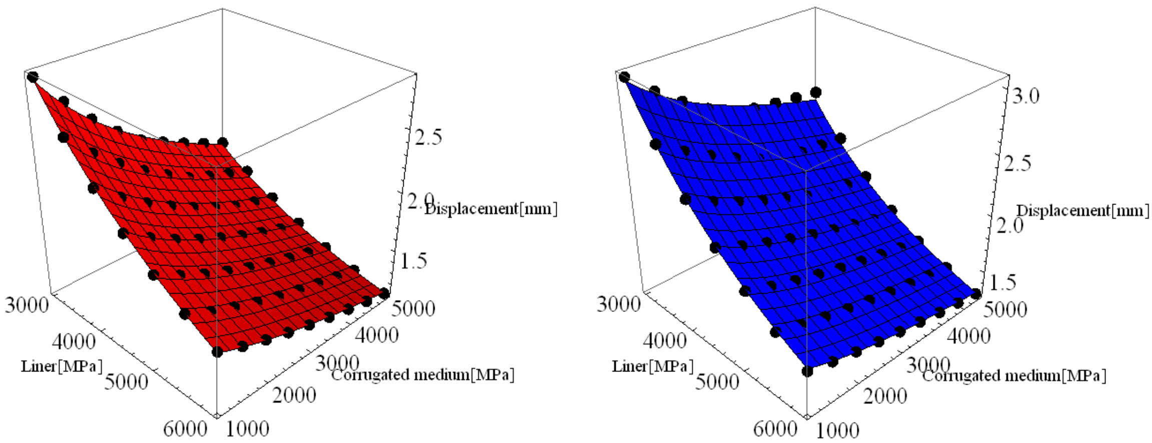

(a) CD (b) MD

Figure 7. Response surface model search for elastic modulus

5.3 Calculation of material constant

We considered the coordinates of CD and MD intersection as shows Fig. 8 by Eq. (22) in solution space of responses surface that the estimated elastic modulus of liner and corrugated medium.

$$(e_1^*, e_2^*) = \underset{(e_1,e_2)}{\operatorname{argmin}}(rs'(data')(e_1, e_2) - rs''(data'')(e_1, e_2))^2 \tag{22}$$

Where e_1^* and e_2^* are the estimated elastic modulus of liner and corrugated medium, rs' and $data'$ are response surface and data used in the response surface of CD, rs'' and $data''$ are response surface and data used in the response surface of MD. Therefore, $rs'(data')(e_1, e_2)$ and $rs''(data'')(e_1, e_2)$ are shows response surface of liner and corrugated medium of CD and MD. In this study, we get intersection coordinate by calculating difference $rs''(data'')(e_1, e_2)$ from $rs'(data')(e_1, e_2)$ as a method of obtaining the coordinate of CD and MD intersection. Material properties of Liner and Corrugated medium calculated by intersection coordinate are shown in Table 4.

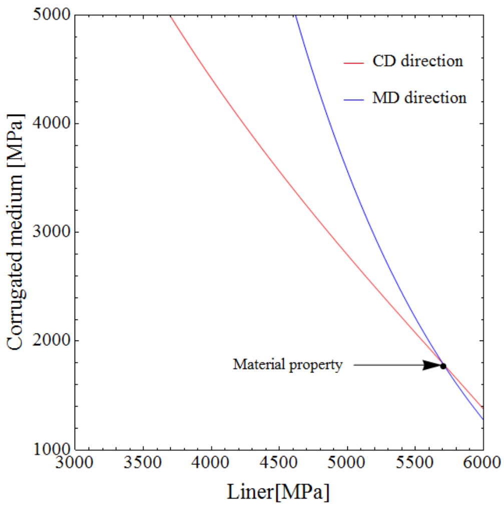

Figure 8. Inference of elastic modulus by intersection of coordinate

Table 4. Elastic modulus by inference

	Liner	Corrugated medium
elastic modulus (MPa)	5700	1850

6. Verification of elastic modulus

We will verify if the elastic modulus obtained in this research are valid. In the verification used elastic modulus both liner and corrugated medium of estimated Table 4 by this research. Fig. 9 shows the results of comparing results of regression lines and numerical analysis by conducting an analysis under the condition of applying a load on a linear range using the homogenization technique as shown in Section 4. In this study, by rationally incorporating displacement data of the regression line into a numerical simulation, elastic modulus were obtained. Therefore, both in the CD and MD, results are consistent with regression line values, confirming the validity of elastic modulus.

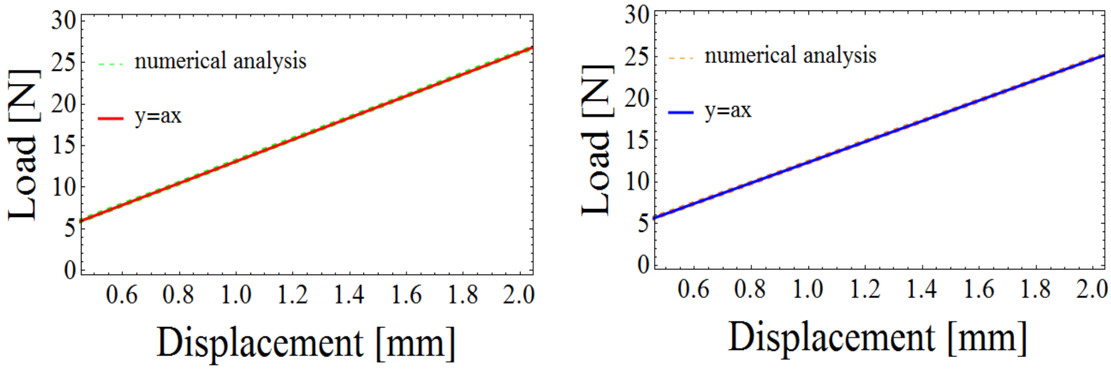

(a) CD (b) MD

Figure 9. Comparison of between regression line and numerical analysis

7. Reducing uncertainty

7.1 Posterior distribution estimation method

Bayesian inference determines posterior distribution by uploading observational data to parameters of prior distribution, which consist of information already obtained and the prior knowledge of the analyst. Bayes theorem can be expressed with Eq. (23). Assuming the parameter the elastic modulus of liner and corrugated medium as θ and observational data as d, posterior distribution $p(\theta|d)$ can be obtained from the product of likelihood $f(d|\theta)$, which is probability of obtaining observation data as a condition for elastic modulus has particular value.

$$p(\theta|d) \propto f(d|\theta)p(\theta) \tag{23}$$

In other words, posterior distribution is proportional to prior distribution and likelihood, and can be considered to be the conditional probability of parameters when data were obtained. Since Bayesian inference can actively utilize prior distribution, even if the number of samples is low, it allows for estimation of unknown parameters that include uncertainties. In this study, we estimated parameter elastic modulus of liner and corrugated medium using

7.2 Bayesian updating

As shown in the Fig.10, Bayesian inference improves the accuracy of estimation by sequential updating estimated posterior distribution using observed data.

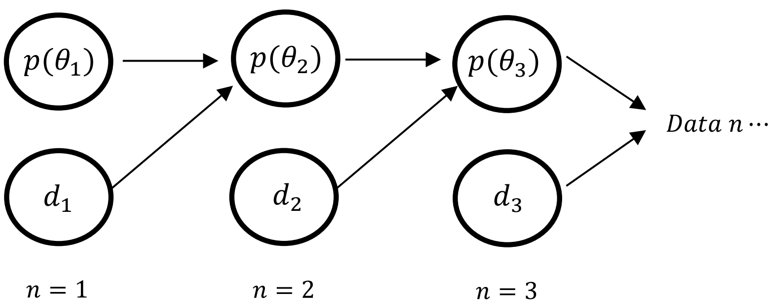

Figure 10. Bayesian updating

7.3 Likelihood

We calculate probability distribution by using Bayesian inference. This method does not calculate fixed parameters unlike maximum likelihood method. Considering elastic modulus of liner and corrugated medium follows normal distribution of Eq. (24), we estimate parameter μ, σ^2 of elastic modulus by observed data x.

$$N[x|\mu,\sigma^2] = \frac{1}{\sqrt{2\pi}\sigma}\exp\left\{-\frac{\{x-\mu\}^2}{2\sigma^2}\right\} \tag{24}$$

where μ is average and σ^2 is variance. Therefore the likelihood for complete experimental data is Eq. (25), (26).

$$p(u'|e_1,e_2,\mathrm{MD}) = \mathrm{N}\left[u'\middle|rs'(data')(e_1,e_2), var\left(rs'(data')(e_1,e_2)\right)\right] \tag{25}$$

$$p(u''|e_1,e_2,\mathrm{CD}) = \mathrm{N}\left[u''\middle|rs''(data'')(e_1,e_2), var\left(rs''(data'')(e_1,e_2)\right)\right] \tag{26}$$

where *u* is a displacement as observed data and *var* is a function for calculating the variance. In this study, we calculate posterior distribution, multiplying those likelihood by prior distribution.

7.4 Setting prior distribution

Prior distribution can reflect the analyst's subjective information. Fig. 11 shows used prior distributions and its details are shown in Table 5. In Case A, uniform distribution considers all parameters uniform when there is no prior knowledge, and in Case B, though it is unclear based on past experience, the range of model parameter values is roughly understood. Therefore, to reflect model parameter uncertainties as effectively as possible, we applied Gaussian distribution that has been through engineering study to this information. In Case C, we applied isotopic Gaussian distribution that reflects detailed information using the estimated model parameter values.

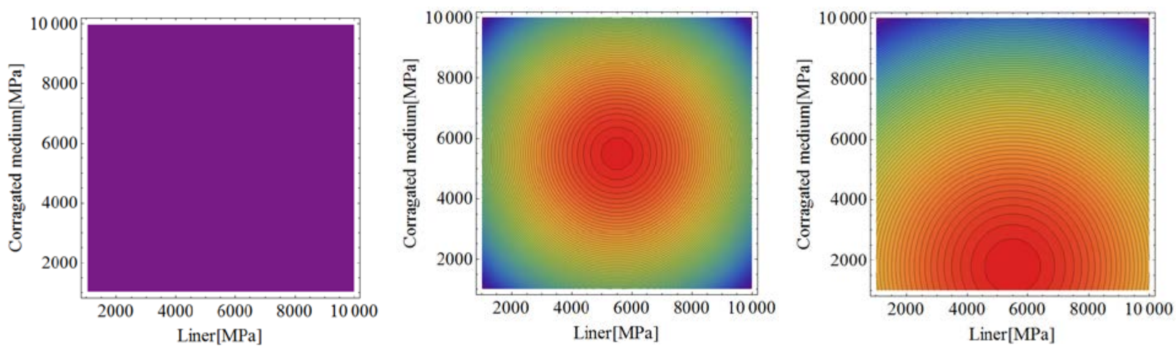

Case A Case B Case C

Figure 11. Prior distribution

Table 5. Prior distribution value

		Case A	Case B	Case C
Average	Liner	5500	5500	5500
	Corrugated medium	1800	5500	1800
Variance	Liner	1.0×10^{10}	10000	10000
	Corrugated medium	1.0×10^{10}	10000	10000

7.5 Reducing uncertainty in posterior distribution

In this study, to examine reduction of uncertainty, we made a ten-step observation where the total of two types of data (one in the CD and one in the MD) were represented as one step in order to make confirmation. Fig. 12 shows the posterior distribution results of first step and final step. In addition, Table 5 shows mean and variance of ten steps. According to Fig. 10 and table 5, in Cases A and B, with the number of data used in this research, it is difficult to say that uncertainty has been reduced to the point to guarantee the validity of elastic modulus. In Case B, results were biased toward prior distribution due to the impact of variance of prior distribution set for the estimated mean values. Thus, it was shown to be strongly influenced by prior distribution. In Case C, uncertainty was reduced even with a small number of data by reflecting more accurate prior information. Therefore, knowing more accurate prior information obviously contributes to gaining a valid value more quickly. In addition, while incomplete prior information has a negative impact on the estimation of mean value, in Case A without prior information, by using Bayesian inference, though reduction of uncertainty is slow, estimated mean value reaches a valid value quickly.

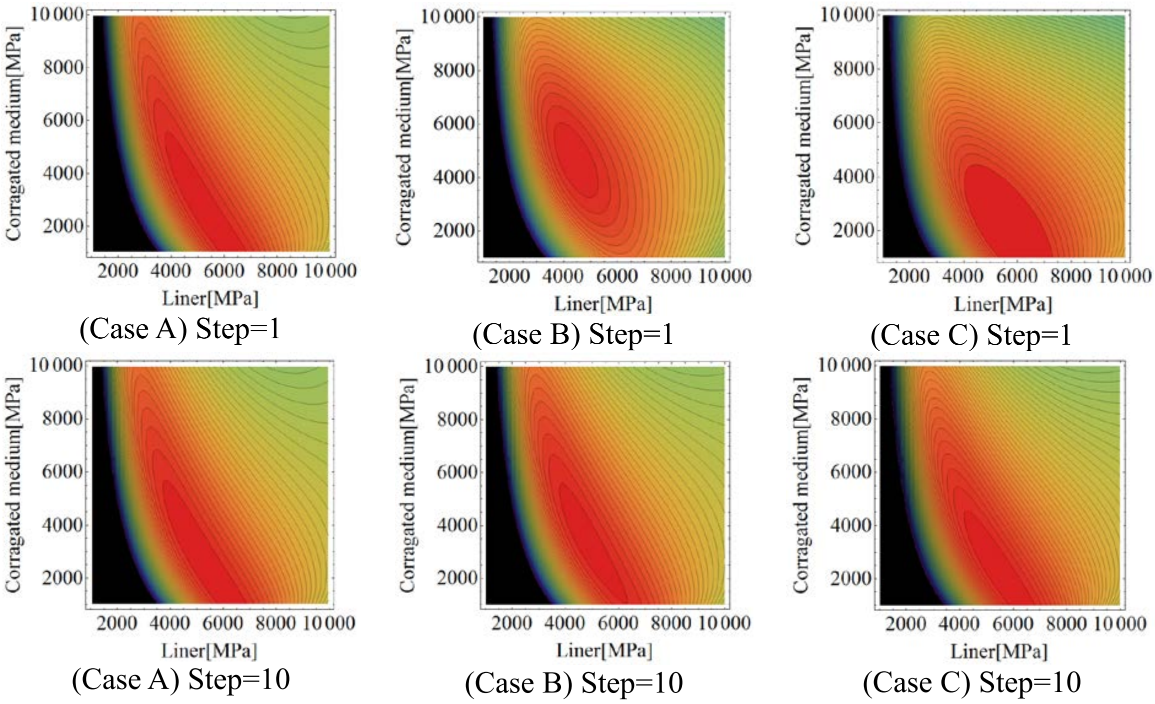

Figure. 12 Posterior distribution

Table 6. Comparison of posterior distribution

		Case A	Case B	Case C
Average	Liner	5494.9	4760.53	5629.13
	Corrugated medium	2211.7	3491.87	2001.32
Variance	Liner	6892.2	1046.41	2492.13
	Corrugated medium	16070	3342.29	5470.91

8. Conclusion

In this study, we proposed a method of obtaining elastic modulus from a response surface prepared by using numerical analysis with a homogenization technique that focuses on the periodicity of corrugated cardboard and a bending test. Additionally, we then made a comparison with experimental values in order to confirm its validity. To reduce uncertainty in the obtained elastic modulus values, we conducted a quantitative evaluation using posterior distribution obtained using Bayesian estimation and conducted examination and validation. We present our findings below.

1. In a conventional finite element analysis, it took time and effort to prepare the model. In addition, since mesh is generated for each flute, the calculation cost is extremely high and inefficient. We focused on the periodicity of the corrugated cardboard, and used a flute of corrugated cardboard as a unit cell in order to conduct homogenization analysis of the test fragment as the overall structure. In this manner, by only preparing a model of the microstructure and simplified overall structure, and substituting the flute with a uniform material, analysis that takes microstructure into consideration was possible. This allows for a significant reduction in calculation cost, indicating that this is a useful method in analyzing corrugated cardboards.

2. We incorporate displacement of experimental value into numerical analysis of CD and MD, and created response surface by that result of analysis. Calculated material properties of liner and corrugated medium by the intersection of these response surface, displacement of numerical simulation analysis using calculated elastic modulus was compared with displacement of regression line. Result shows elastic modulus calculated by method proposed in this research is consistent with regression line values, confirming the validity of elastic modulus.

3. To reduce uncertainty of model parameters with Bayesian inference, posterior distribution was quantitatively examined. When more accurate prior distribution was used, even with a small number of samples, reduction in uncertainty was confirmed. However, with other prior distributions, such reduction was not confirmed. By using prior distribution for which analysts examined uncertainty, a valid posterior distribution was obtained. However, even when there is no prior information, by using Bayesian inference, though reduction of uncertainty is slow, estimated mean value reached a valid value quickly.

Reference

[1] Kawashima, Y., Nishimura, F. and Tezuka, A., Research on Structural Analysis of Paper Ware, Gifu Prefectural Research Institute of Manufacturing Information Technology Report, Vol. 2, (2000), pp.29-34

(in Japanese).
[2] Terada, K., Yuge, K. and Kikuchi, N., Elasto-Plastic Analysis of Composite Materials Using the Homogenization Method, 1st Report, Formulation, Japan Society of Mechanical Engineers, vol. 590, (1995), pp.2199-2205 (in Japanese).
[3] Terada, K. and Kikuchi, N., Introduction to Homogenization Technique (2003), Maruzen.
[4] Alvin, K. F., et al., Uncertainty Quantification in Computational Structural Dynamics: a new paradigm for model validation, Society for Experimental Mechanics, Inc, 16th International Modal Analysis Conference, Vol. 2, (1998), pp.1191-1198.
[5] Watanabe, S., Theory and Method of Bayesian Inference (2012), Corona Publishing Co.
[6] Fukasawa, K. and Sumiya, T., Let's Start! Data Analysis with Bayesian Inference, Japanese Journal of Ecology, Vol. 59, (2009), pp.207-216 (in Japanese).
[7] Nishio, M. and Fujino, Y., Baysian Inference Based Uncertainty Quantification and Calibration of Numerical Models of Existing Structures, JSCE A2 (Applied Mechanics), Vol. 69, (2013), pp.711-718 (in Japanese).
[8] Ishibuchi, H., Nagasawa, S., Yoshizawa, A. and Yoshitani, Y., Three-Dimensional Bending Stress Analysis for Corrugated Fibreboard Sheet, Japan Society of Mechanical Engineers, vol. 60, (1994), pp.2774-2781 (in Japanese).
[9]Hirohata, K., Kawakami, T., Mukai, M., Kawamura, N., Yu., Q. and Shirai, M., Proposal for Structural Reliability Design Method Based on the Response Surface Methodology and Bayes theory, Japan Society of Mechanical Engineers, Vol. 660, (2001), pp.1297-1304 (in Japanese).
[10]Christopher, M. B., Pattern Recognition and Machine Learning (2006), pp.137-156, Springer.
[11]Steffen, L. L., Graphical Models (1996), pp.4-26, Oxford University Press Inc.

Validation and Verification of Structural Analysis Using Open Source Finite Element Analysis Code and Material Test Data

†Terutaka Fujioka[1]

[1] Department of Mechanical Engineering, Faculty of Science & Engineering, Toyo University, Japan
†Corresponding author: fujioka@toyo.jp

Abstract

Quality management of most commercial finite-element analysis solvers is conducted by the software vendors themselves. Therefore, users do not need to know the source codes. Validation and verification (V&V) of open-source solvers, on the contrary, is accomplished by the users, who can access the source codes. When a user attempts V & V of an open-source solver, they should compare their analytical results with reference test data. This study presents a V & V example of non-linear analyses using the open-source finite-element solver Code_Aster. The outputs are compared with simple tensile test data produced by a ubiquitous material test machine.

Keywords: Stress Analysis, Finite Element Method, Open Source, V & V, Material Test.

Introduction

The importance of validation and verification (V&V) of computer-aided engineering (CAE) software is widely recognized. CAE software, especially structural finite element analysis (FEA) solvers, are widely used in various industries, as its user-friendliness and reliability. Most of these commercial solvers are black box software whose source codes are not disclosed to ordinary users. Nonetheless, regular users of such software can perform proper analyses under technical support of the software vendors.

However, the strength and safety of structures designed using CAE software, particularly those that pose a public safety risk, must be evaluated to promote public acceptance and understanding of the technologies. Open-source CAE may mitigate this concern. In V & V of a finite element solver, the analytical results should be compared with corresponding test data. The tests themselves should be accessible to the public and easily performed without requiring costly and specialized experimental equipment.

This paper demonstrates a V & V of non-linear finite element analyses. The analyses were performed by the open-source FEA solver *Code_Aster* [1], developed by the French organization EDF (Électrocité de France). The results were compared with those of a conventional tensile test using a ubiquitous material test machine. The selection of tensile curves and analytical options are also discussed. The analyses dealt with material non-linearity and geometrical non-linearity.

Reference Test Data

The reference test data were acquired in a simple tensile test using a round-bar-type specimen constructed from low-alloy steel (2.25Cr–1Mo Steel), as reported in [2]. This material was one of the test materials for creep datasheet provided by the National Institute of Materials Science (NIMS). The chemical composition of the steel is shown in Table 1 [3]. The dimensions and configurations of the test specimen are shown in Figure 1.

The test was conducted at room temperature. In the commonly employed standard test procedures, the strain is measured until the stress slightly exceeds the 0.2% proof strength level. To obtain a widely applicable stress–strain curve, the strain in the present study was measured up to maximum loading. The ultimate and 0.2% proof strengths were 636 and 426 MPa, respectively. Figure 3 plots the nominal stress–strain curve obtained in this test.

Table 1. Chemical compositions of the tested material (2.25Cr–1Mo Steel) [3]

Element	Requirement*)	Analyzed	Element	Requirement*)	Analyzed
C	≤ 0.17	0.12	Cr	1.88-2.62	2.20
Si	≤ 0.50	0.29	Mo	0.85-1.15	0.99
Mn	0.27-0.63	0.29	Cu	——	0.07
P	≤ 0.030	0.015	Al	——	0.018
S	≤ 0.030	0.007	N	——	0.0095
Ni	——	0.05		——	

(mass percent) *) JIS G 4109-1987

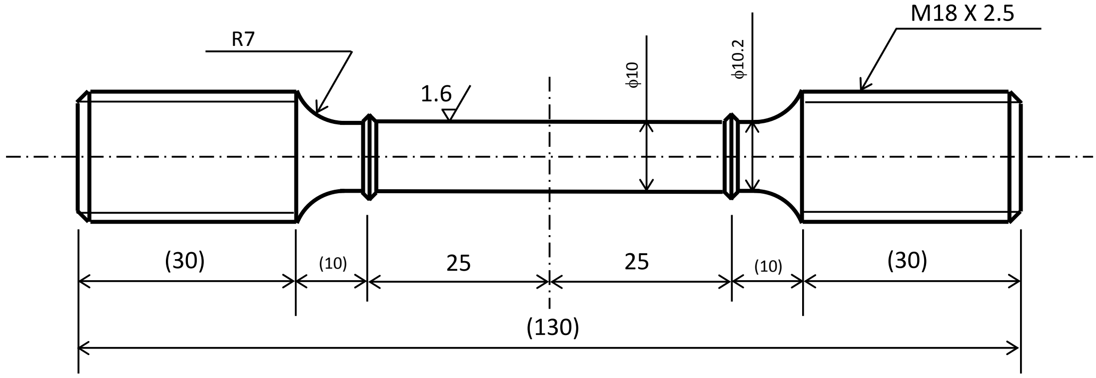

Figure 1. Round-bar-type specimen for the tensile tests

Analysis Methods

Code_Aster & Salome_Meca

The analyses were performed by *Code_Aster* (Ver. 11.3.0). Pre- and post-processing were performed by the integrated CAE package *Salome_Meca* (2013.2). *Code_Aster* and *Salome_Meca* are downloadable from the *Code_Aster* website [1].

Finite element model and boundary conditions

Excluding the gripping portions in the specimen, the analytical model was axisymmetric. The round bar was subdivided into simple uniform square meshes for easy comparisons with various solvers. The axisymmetric construction and mesh subdivisions are shown in Figure 2. The element was an eight-node iso-parametric quadratic full integration element. Necking at the specimen center was induced by a slight initial imperfection (1/1000 of the bar radius).

To define the multi-point constraints on the top-edge nodes, the model was subjected to displacement-controlled loading using the operator LIAISON_UNIF. The loading was incremented by equal time steps. Because we were evaluating the actual performance of the non-linear analysis, we omitted automatic loading step adjustment.

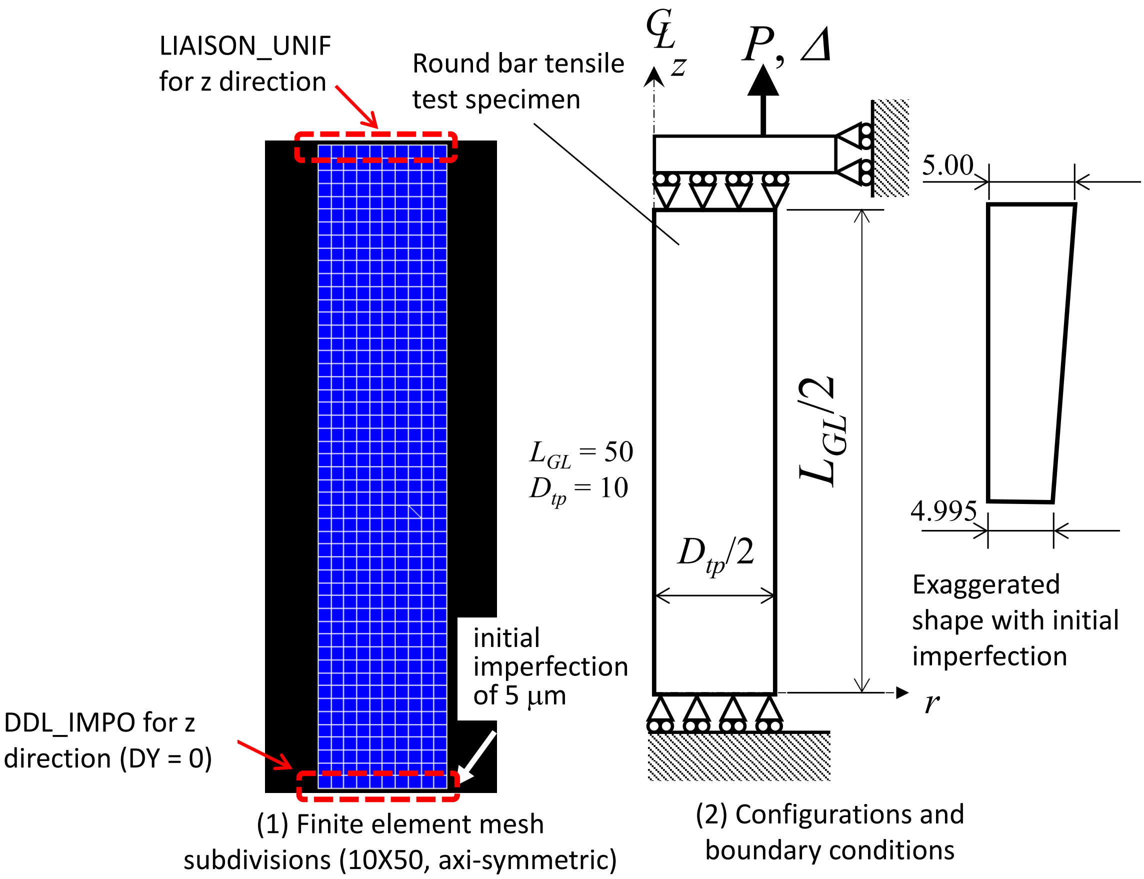

Figure 2. Finite element mesh model of the specimen and boundary conditions

Material properties

The results were compared against the nominal and true stress–strain curves, as shown in Figure 3. The test data were approximately fitted to the left-hand side of the nominal stress–strain curve, and the right-hand side (beyond the maximum load point) was assumed as a horizontal straight line (see Figure 3). The true stress–strain curve was expressed by the Ramberg–Osgood law

$$\varepsilon = \frac{\sigma}{E} + \kappa\left(\frac{\sigma}{\sigma_Y}\right)^m, \tag{1}$$

where ε is the strain, σ is the stress, and σ_Y, κ, and m are material constants. The constants were selected to fit the true stress and strain data converted from the test data between the zero and maximum loading points. Beyond the maximum load point, the stress was extrapolated by a power law. The constants are tabulated in Table 2.

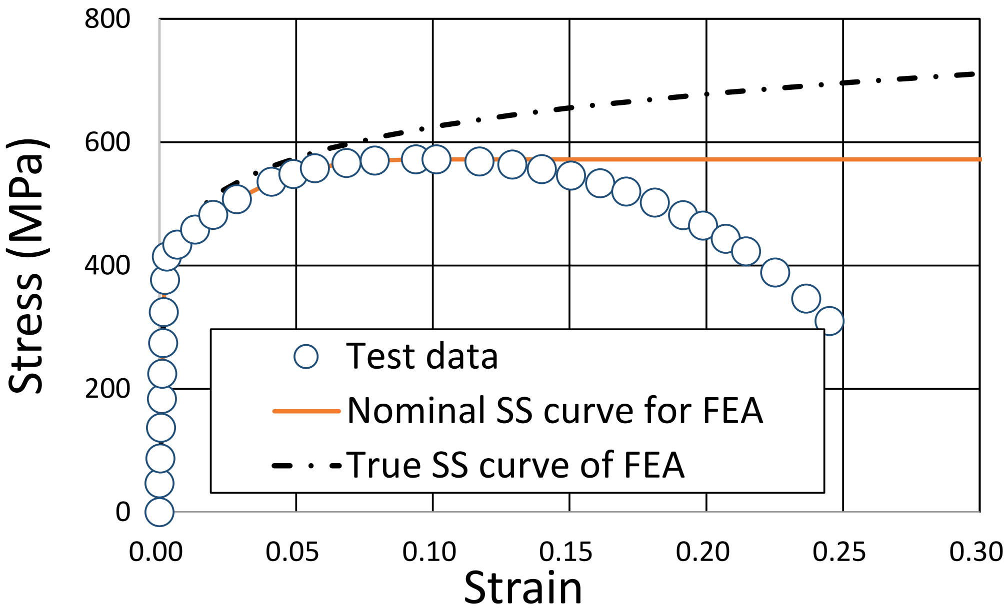

Figure 3. Comparisons between stress–strain curves for FEA and tensile test data

Table 2. Constants related to material properties

Elastic modulus	E = 204.1 GPa	Reference yield strength	σ_Y = 426 MPa
Poisson's ratio	ν = 0.3		
Coefficient for plasticity	κ = 3.582 x 10^{-3}	Yield strength for elastic, perfectly-plastic body	σ_u = 636 MPa
Stress exponent	m = 8.607		

Treatment of geometric non-linearity

Many of the theoretical studies on plasticity, such as path independence of the elastic–plastic J-integral, have assumed small deformation. Limit analysis, which can replace the elastic FEA-route stress classification in pressure vessel design codes [4], is based on the small deformation theory. For these reasons, large deformation analysis is not always appropriate.

Some users consider that the true stress–strain curves are mandatory in elastic–plastic FEA. Although the true stress–strain is appropriate in large deformation analyses, where the nodal coordinates change step by step, the nominal stress–strain curve is suitable for small deformation analyses. The present study investigates unsuitable combinations for comparison purposes.

Small and large deformation analyses were performed with the operators DEFORMATION = "PETIT" and DEFORMATION = "SIMO_MIEHE," respectively. The various combinations of stress–strain curves and operators are tabulated in Table 3.

Table 3. Cases in the geometric non-linearity analyses

	Stress-strain curve	Geometrical non-linearity
Case 1	Nominal curve	Small deformation (PETIT)
Case 2	Nominal curve	Large deformation (SIMO_MIEHE)
Case 3	True curve	Small deformation (PETIT)
Case 4	True curve	Large deformation (SIMO_MIEHE)

Results and Discussion

The reaction forces and displacements obtained in the elastic–plastic FEA were converted into nominal stresses and strains. The resultant stresses and strains are compared with the test data in Figure 4. The most accurate case, Case 4, well agreed with the tensile curve throughout the test, including the loading decline after the maximum load point. Case 1 accurately estimated the maximum load (tensile strength). The results of Cases 2 and 3 differed from the test data.

Necking was observed in the cases analyzed with SIMO_MIEHE. A typical deformation, along with the distribution of equivalent plastic strain in the time step near the specimen rupture (roughly 25% of the nominal strain), is shown in Figure 5.

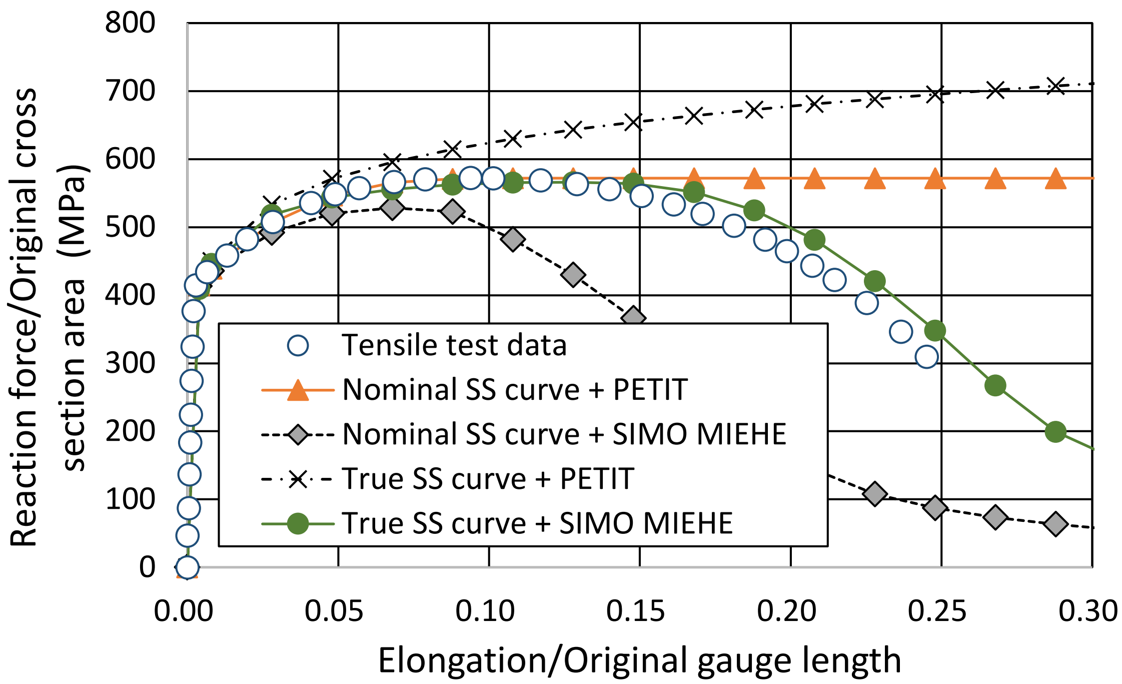

Figure 4. Comparisons of analysis results and tensile test data

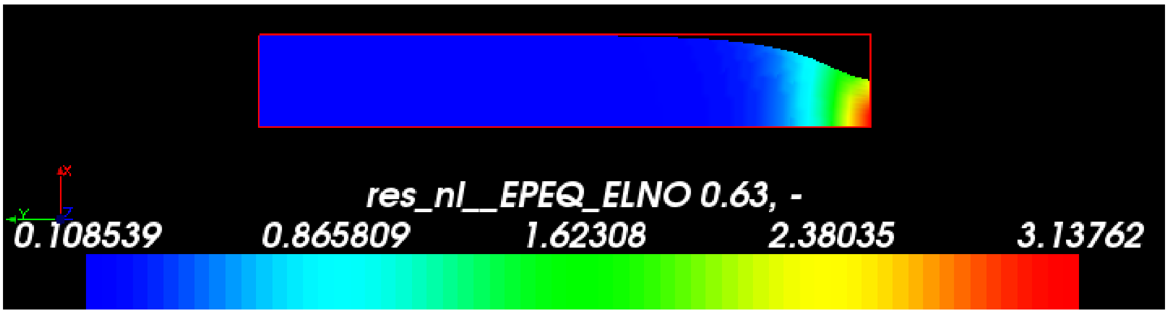

Figure 5. Deformation (top, actual size) and distribution of equivalent plastic strain (bottom)

Conclusions

This study presented a V & V of an open-source finite element structural analysis solver. The validated phenomena were material non-linearity and geometrical non-linearity. The reference test was a simple tensile test using a ubiquitous test machine. By following this example, users can perform their own V&Vs.

Appropriate stress–strain curves in FE analyses were also discussed, and the analytical results were compared with actual data. It was confirmed that large deformation FEAs should use the true stress–stain curve, whereas small deformation FEAs can assume the nominal stress–strain curve.

Similar V & V examples should be publicized in future. Small punch tests, including friction and contact, and other simple material tests, are useful and easily performed and are suitable for this purpose.

References

[1] http://www.code-aster.org/
[2] Fujioka, T., et al. (2012) Analytical Replication of Room Temperature Small Punch Test of 2.25Cr-1Mo Steel (STBA24) and Its Application to Load-Stress Conversion of Small Punch Creep Test, Proceedings of the Annual Meeting of JSMS, Vol. 61, Okayama, JSMS, pp. 77-78. (in Japanese)
[3] NIMS (1997), Creep Data Sheet, 2.25Cr-1Mo (Plate) JIS SCMV 4 NT 11B, NIMS, Tokyo.
[4] European Commission Joint Research Centre and EPERC (1999) The Design-by-Analysis Manual, EUR 19020 EN.

ICME: Integrated Computational Materials Engineering - From Micro Structure to FEM

T. Ashino[1]

[1]Department of Regional Develpment Studies, Toyo University, Japan

ashino@toyo.jp

Introduction

Integrated Computational Materials Engineering (ICME) is a kind of materials and products design methodology by integrating micro to macro scale data and simulation[1]. Materials performances, such as strength, creep and fatigue are critical for designing articacts. They depend on many phenomena, crystal structure, micro structure, dislocation and others, hence, combining, integrating many types of data and models are essential and obtained materials properties are essential inputs for computational fluid dynamics, heat transfer and finite element models.

ICME is expected to accelerate design and delopment process of products if the framework has been established and relevant models are modularized, freely combined each together for problem solving. Since there are no established rules how to combine these data and models, it becomes important to accumulate use cases as many as possible. It requires heterogeneous information integration, i.e. common data representation, unified vocabulary and definition of terms are fundamental. In this section, ICME data and models hierarchy and ontology based information integration for such heterogeneous data and models are discussed.

Hierarchy of Data and Models

Fig. 1 shows one of relation schematizations between substances, computational models, data and properties for materials design. It starts left side from atomic level and moving to right, crystal structure, interaction energy of atoms, thermodynamics e.g. phase transition and properties are estimated. Also, in lower part, dislocations and other deformation mechanisms are introduced.

This diagram for virtual experiment[3] is mainly focusing on materials design and property prediction, in ICME concept, it is trying to apply more realistic product design and manufacturing process, this schema is extended to macro scale and connected to computer simulation like computational fluid dynamics (CFD), heat transfer and finite element method (FEM), Since there are so many proprietary and open source software tools developed for each stage of simulation models, general idea of ICME platform is to modularize such simulation codes by wrapping or data conversion, and connect these modules with a workflow engine[4][5][6].

But all software tools are developed independently, they requires original input and output data formats, sometimes only controllable from GUI, “integration” requires conversion of data format, structure, representation and terms. In order to solve this kind data exchange and metadata description issues, the Semantic Web provides generic framework and many software tools.

The Semantic Web and Materials Data and Knowledge

The Semantic Web is an activitiy of W3C which intends to introduce semantics into the Web which just provides simple links of data, web pages, images and query[7]. It is basically a kind of knowledge representation framework for knowledge base for machine reasoning. There are

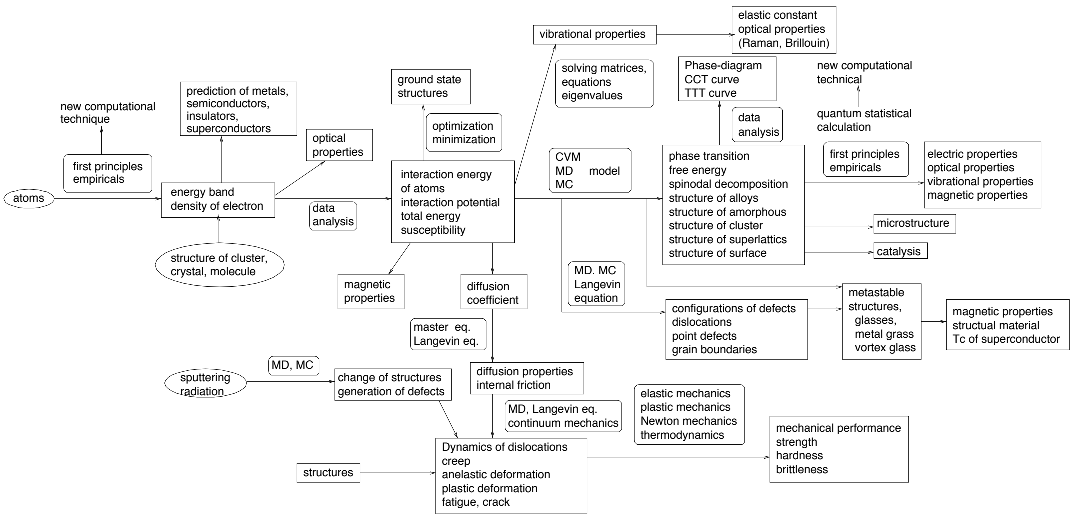

Figure 1: Conceptual diagram related to modeling and simulation for materials[2].

several building blocks, one is URI, Unified Resource Identifier, which identifies a concept or object on the Web.

Data is usually written as semi-structured data, i.e. text data which is annotated by tags defined in eXtensible Markup Language (XML). It enables much more flexbile description of data structure compared with relational model which is a data model widely used for database management system and also provides a method to exchange metadata - data which describes data. After introduction of XML and XML Scehma, a W3C standard of XML based data schema definition language have been published, it became general to use XML for defining standard data schema definition and exchanging data in specific domain.

Resource Description Framework (RDF) standard provides a way to write the relationship between two objects like a simplest sentence, object, verb and subject. In many cases, objects and subjects are identified by URI, defined the meaning of them by RDF network. In application of materials data, RDF is used for describe a meaning of materials data in the context of other data resources.

RDF is a simple building block just describe a one to one relationship, but there is a set of verbs usualy used for knowledge representation, e.g. “is a”, “equivalent” and “part of”. RDF Schema (RDFS) and Web Ontology Language (OWL) are standards which define the sets of verbs for constructing network of concepts called ontology.

In information science field, ontology is used for namings of concepts and their definition of types, attributes, and description of relationships of them. With OWL, the meaning of a concept can be defined on the basis of relationships between other concepts. Information resources assigned same OWL entity are considered as the same meaning. In other words, ontology can work as common structured dictionary for data interpretation and translation.

Ontology for Materials Science and Engineering

Ontology which describes knowledge about specific domain is called domain ontology and there are several trials defining domain ontology in materials science and engineering[8].

One of them is Materials Ontology[9][1], which is written in Web Ontology Language (OWL), the W3C standard for ontology construction. It consists of four core ontologies and three peripheral ontologies as follows.

- Core Ontologies
  - Substance - defines elements and materials taxonomy
  - Process - descriptions of materials processing
  - Property - names of properies and their classification
  - Environment - environment of measurement and operation
- Peripehearl Ontologies
  - Materials Information - class definitions for aggregation of materials data entry
  - Unit Dimension - measurement units and dimensions
  - Physical Constant - a list of URI's of physical constant

The categories of four core ontologies are selected from the viewpoint of orthogonality of the concepts.

As an example of this ontology definition, the basic structure of property ontology is illustrated in Fig. 2. Class "Property" has properties (attributes), its name (PropertyName) and value (Value). The value is a measured value and contains corresponding maximum, minimum, unit and dimension. Subclasses "Chemical", "Thermal" and "Mechanical" are classification of properties, by tracking this tree, specific materials property and its definition can be found.

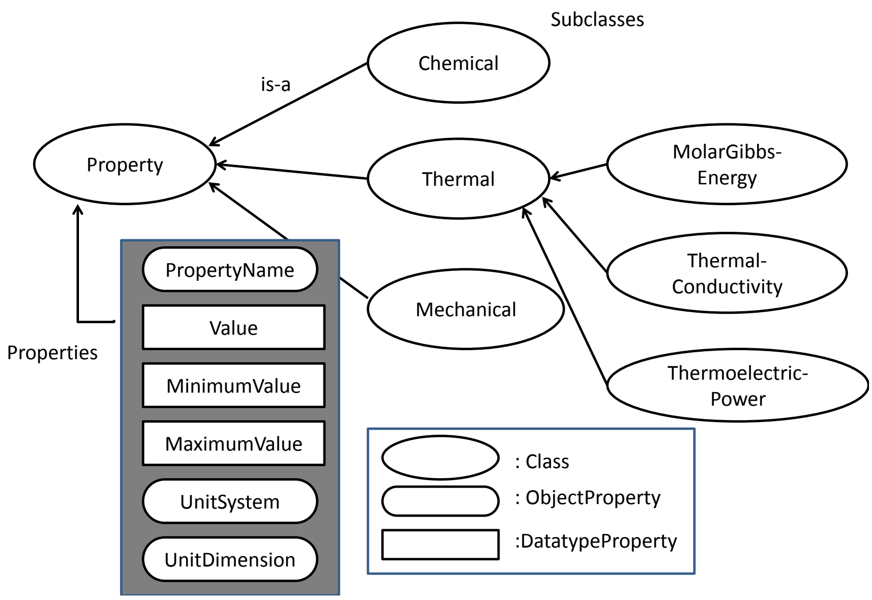

Figure 2: Definition and classification of materials properties in Materials Ontology.

[1]OWL definitions and examples of Materials Ontology can be obtained from the web site, http://www.codata.jp:8080/.

Since there are huge number of related concepts about materials science and engineering, property ontology focuses on thermophysical properties, but four core ontologies consists over 600 class definitions, it is regarded not realistic to define whole domain ontology for materials science and engineering by pure top down style.

ICME concept requires data integration, for example, experiment data, the output of simulation models and empirical equations. One idea of how to integrate such heterogeneous information resources is ontology based integration, information resources are described by using standards of the semantic web, and the vocabularies used in these descriptions are selected from the common ontology.

The architecture for materials data and knowledge integration based on the Semantic Web framework is shown in Fig. 3. Data and knowledge are written in XML format. For example, experimental data are in XML Schema, reference of articles are in RDF and mathematical objects are in OpenMath, which is a standard for representing the semantics of mathematical objects[10]. For materials performance estimation, mathematical knowledge, e.g. empirical equations and constitution equations are very valuable, therefore, such equations are stored as OpenMath library for processing by symbolic mathematics system, and variables estimated from experimental data are stored as RDF data.

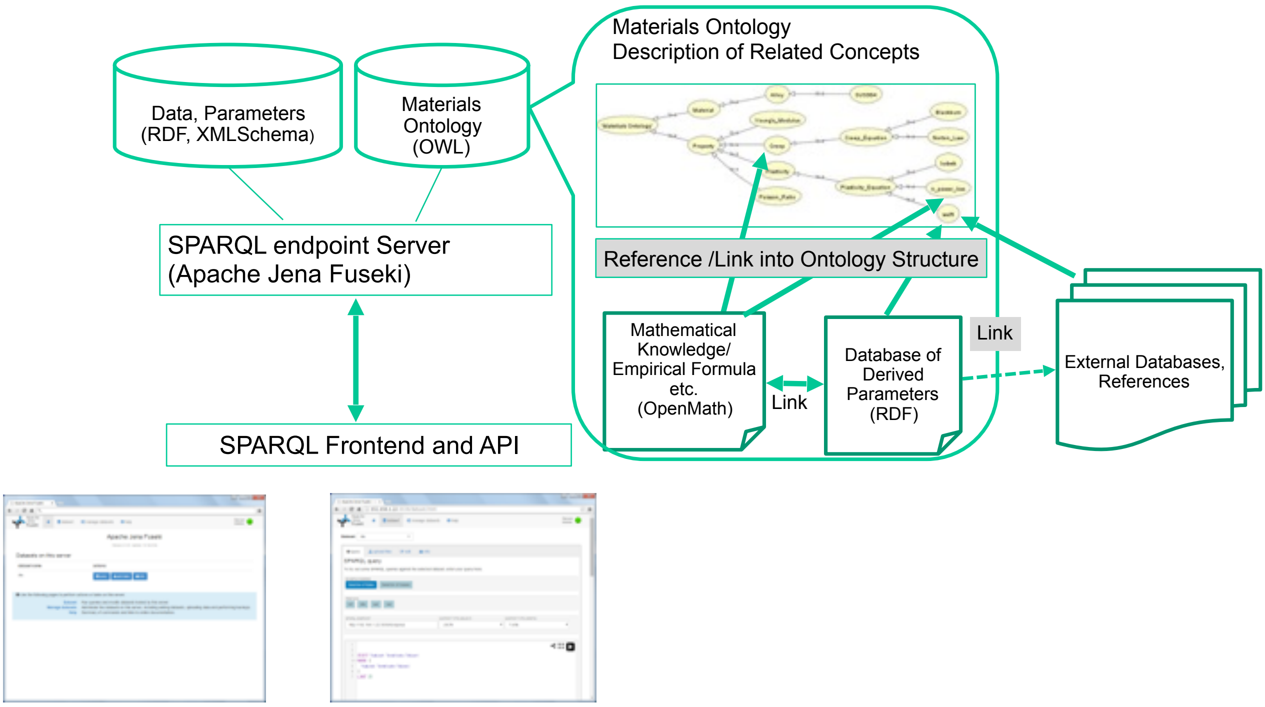

Figure 3: Data and knowledge integration by Materials Ontology.

These all data share Materials Ontology as a common vocabulary, it enables to identify same data from these heterogeneous data resources and process them. RDF query language, SPARQL Protocol[11] and RDF Query Language (SPARQL) endpoint stores these data and provides interface to retrieve these data and knowledge.

Conclusions

ICME platform is designed as an total product and component design environment which consists of materials selection, materials process design, structural calculation and other data, simulation models. Each data and simulation models are connected by workflow but data interchange requires standardized data and metadata. Constructing domain ontology for materials science and engineering is key to integrate heterogeneous data resources, but it requires huge efforts, novel idea and collaboration between information scientists, materials scientists and engineers is required.

References

[1] National Research Council (2008) *Integrated Computational Materials Engineering: A Transformational Discipline for Improved Competitiveness and National Security*, The National Academies Press, USA.

[2] Shichijo, N. (1999) Modular simulation technique for virtual experiment of complex phenomena in materials (Doctorial dissertation), Retrieved from National Diet Library of Japan. (DOI. 10.11501/3162796)

[3] Iwata, S., Shichijo, N. and Ashino, T. (2001) Modular simulation technique for virtual experiment of complex phenomena in materials, *Materials & Design*, **22**, 77–79.

[4] Schmitz, G. J. (2016) Microstructure Modeling in Integrated Computational Materials Engineering (ICME) Settings: Can HDF5 Provide the Basis for an Emerging Standard for Describing Microstructures?. *Journal of Materials*, **68(1)**, 77–83.

[5] Jacobsen, M. D., Benedict, M. D., Foster, B. J., & Ward, C. H. (2015) An Integrated Collaborative Environment for materials research. Proceedings of the 3rd World Congress on Integrated Computational Materials Engineering, John Wiley & Sons, 285–292.

[6] Arnold, S., Frederic, H. and Bednarcyk, A. (2014) Robust Informatics Infrastructure Required for ICME: Combining Virtual and Experimental Data, *55th AIAA/ASME/ASCE/AHS/ASC Structures, Structural Dynamics, and Materials Conference, National Harbor, Maryland.*, (DOI. 10.2514/6.2014-0460)

[7] Berners-Lee, T., Hendler, J., & Lassila, O. (2001) The semantic web, *Scientific american* **284(5)**, 28–37.

[8] Zhang, X., Zhao, C., & Wang, X. (2015) A survey on knowledge representation in materials science and engineering: An ontological perspective, *Computers in Industry*, **73**, 8–22.

[9] Ashino, T. (2010) Materials Ontology: An Infrastructure for Exchanging Materials Information and Knowledge, *Data Science Journal*, **5**, 52–63.

[10] Buswell, S., Caprotti, O., Carlisle, D. P., Dewar, M. C., Gaetano, M., & Kohlhase, M. (2004) *The open math standard. version 2.0*, Technical report, The Open Math Society, http://www. openmath. org/standard/om20

[11] Yu, L. (2014) A Developer's Guide to the Semantic Web, Second Edition, *Springer*

Space-Time Simultaneous Visualization in Virtual Reality Environment for Validation and Verification

†Y. Tamura[1 2]

[1]Center for Computational Mechanics Research, Toyo University, Japan.
[2]Department of Information Sciences and Arts, Toyo University, Japan.

†Corresponding author: tamura@toyo.jp

Abstract

A novel space-time simultaneous visualization system using virtual reality (VR) technology is developed. Visualization is one of useful tools for validation and verification (V & V) of computational mechanics. In the literature, many scientific visualization systems were developed, including ones for V & V purpose. They were typically intended to compare computed results with experiments visually. VR, on the other hand, was invented as an extension of computer graphics (CG) or interactive media, and merely applied to scientific visualization. In the present article, VR technology is applied for V & V of computational mechanics, especially fluid-structure coupled analyses, displaying the computed and the experimental results at the same location and time. We name it "space-time simultaneous visualization". The present system shows the potential for V & V in VR space.

Keywords: Scientific visualization, Virtual reality, Fluid-structure coupled analysis, Stereovision.

Introduction

Scientific (computer-aided) visualization has long history back in 1963 when E. E. Zajac made a movie of the motion of a satellite [1]. In those years, one did not have a graphics monitor but used a printer or a film recorder to make computer graphics (CG) images. In 1980's, NASA Ames research center developed a visualization system called "PLOT3D" [2] which visualizes computed results of flow fields. PLOT3D created three-dimensional (3D) images of computed results in wireframe initially and later had capability of 3D surface rendering with light and shade. PLOT3D made a great success and created a lot of followers.
The present author had started his carrier of visualization in late 1980's and he developed his own visualization system called "Post-kun" in 1989 [3] when PLOT3D was not available outside of U. S. A. The uniqueness of Post-kun is that it has a feature to simulate visualization process in experiment, such as the shadowgraph and the schlieren photograph [4]. This must be one of typical visual V & V (validation and verification) tools.
In 1990's and after, visualization systems were shifted to commercial ones, such as "Field View", "Techplot" or "AVS". They have sufficient functions and capability to visualize the computed results till now. However visual V & V is becoming more difficult because of the complexity of computation caused by detailed representation of objects, by the targeted flow field itself and by the nature of multi-physics.
Virtual reality (VR) is rather a new technology and its potential is expected for scientific visualization but very few papers have been published. Kageyama and his group of the National Institute for Fusion Science in Japan tried to visualize 3D vector data in VR facility [5][6]. The present author also tried to visualize 3D flow field in VR environment [7]. Both of them had clear objectives to use VR. One is to use the stereovision technique to see 3D field as it is. One could see objects in font of him and walk around them and even touch them (virtually). Also he could see the detail of objects simply by coming closer to them. He didn't need to scale the objects. In other words, the human interface of visualization is very natural in VR space. Their trial might make a certain success but the counterarguments have always converged with indispensability of 3D view or virtual reality experience. VR is expensive and the argument if VR is worth paying the price for scientific visualization is still an open question.

In the present article, we propose a novel idea of using VR for visual V & V. We name it "Time-Space Simultaneous Visualization" and try to visualize computed results and corresponding experimentally-obtained images at the same time, at the same location in VR space in order to demonstrate the potential of VR for scientific visualization.
In the section 2, VR is briefly reviewed to clarify the present situation of VR in the field of scientific visualization. In the section 3, the basic idea and the practical procedure of the present VR system are described. Some examples are shown in the section 4 to demonstrate the capability of the present system, followed by the discussions and conclusions.

Virtual Reality (VR) for Visualization

The purpose of this article is not to explain VR itself but a brief history of VR is reviewed here in order to discuss the possibility of VR for scientific visualization.
VR has a couple of ancestors and one of them is the "ultimate display" developed by I. E. Sutherland [8]. This type of device is currently called a head mounted display (HMD) or more simply a headset. Two small monitors are in front of viewer's eyes and show two images for the left and the right eyes respectively to realize stereovision. Also HMD has a device to detect the location and the orientation of the viewer's head to generate proper CG images for the both eyes. This technology is called "head tracking". Nowadays head tracking is realized by an acceleration sensor (gyro sensor) though it was mechanical in the ultimate display. HMD, however, had a weak point that the graphics power of the computer is required to catch up the movement of a head. Otherwise the viewer feels strange feeling that the image drops behind the motion, and that may lead to a motion sickness. A low resolution of monitors in HMD is also a problem that reduces the reality of images. To overcome these problems, Cruz-Neira et al. developed a four-screen VR system called CAVE [9]. This type of system is called an immersive display or an immersive projection technology (IPT). IPT uses one or more numbers of large screens surrounding viewers. A viewer wears stereo glasses and sees the stereo images on the screens. The location and the orientation of the viewer are detected, usually by the visible markers or by the magneto-electric source attached to the stereo glasses. IPT has some advantages to HMD. As IPT uses multi-screens surrounding a viewer, the field of view is sufficiently wide and thus images displayed on the screens might change less than the image of HMD with the motion of the head. This relaxes the requirement of the computer power. As each screen is large compared to the display of HMD, higher resolution is possibly achieved. Moreover the viewer can see himself in IPT, but not with HMD. This also helps to increase the reality of the virtual image. Only the drawback of IPT is the cost and the space for construction, as easily imagined. CAVE was later commercially released, followed by many similar systems. The present author has been using IPT systems called CABIN [10], CANVAS [11] and currently HoloStage® Mini [12] (Holostage, in short). All of them are general-purpose VR systems and the present author has been applying them to scientific visualization. Figure 1 shows CABIN and a snap shot of visualization. CANVAS images are shown in fig. 2. Even with one screen, we could see a virtual 3D image.

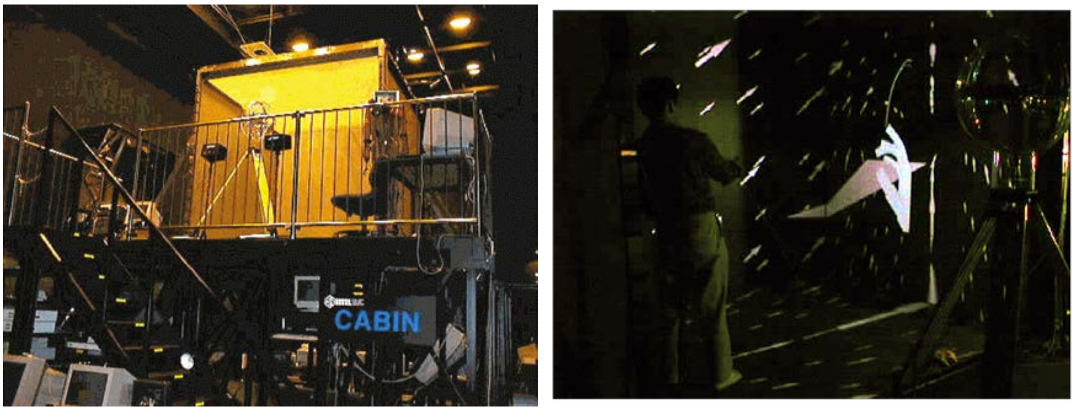

Figure 1. CABIN. Left: overview of CABIN, which has five screens, namely top, bottom, front, left and right. Right: flow field visualized in CABIN. Arrows indicate flow velocity vectors.

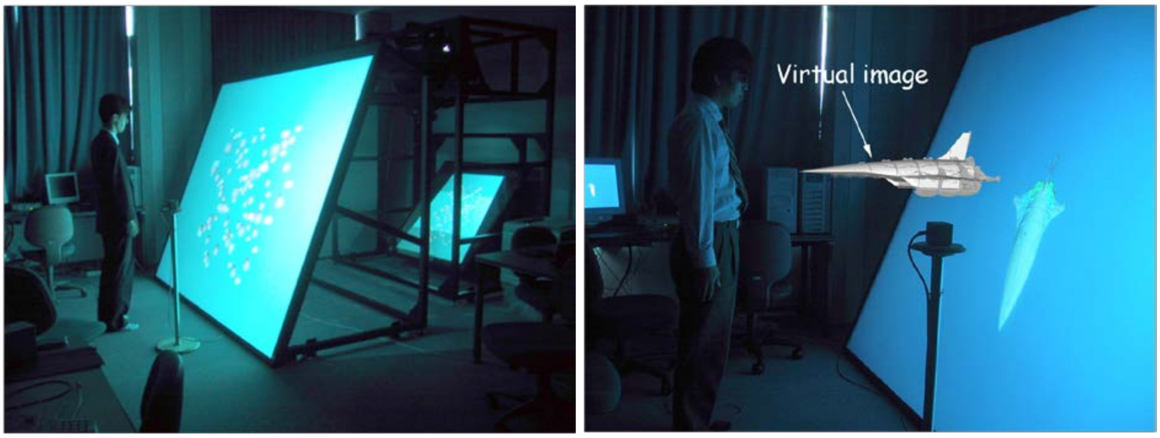

Figure 2. CANVAS having one large slant screen. Left: observing molecules. Right: flow around a spaceplane.

For scientific visualization, important factors for observing computed results in VR space are that we can see the results from every direction, that we can come up as close as we want and that we can see the object of its real scale. They are believed to help a viewer to recognize 3D conformation of the results.

Idea and Process

When an analysis is three-dimensional (3D), we want to see the visualized image in 3D. It is realized with stereovision or VR. When an experiment is recorded or shot in 3D, we also want to see it in 3D. After a certain post process, the experimentally recorded images can also be displayed in VR space, thus can be viewed with stereovision.

A visualization system of VR, that can handle both computed and experimental results, was developed as shown in fig. 3.

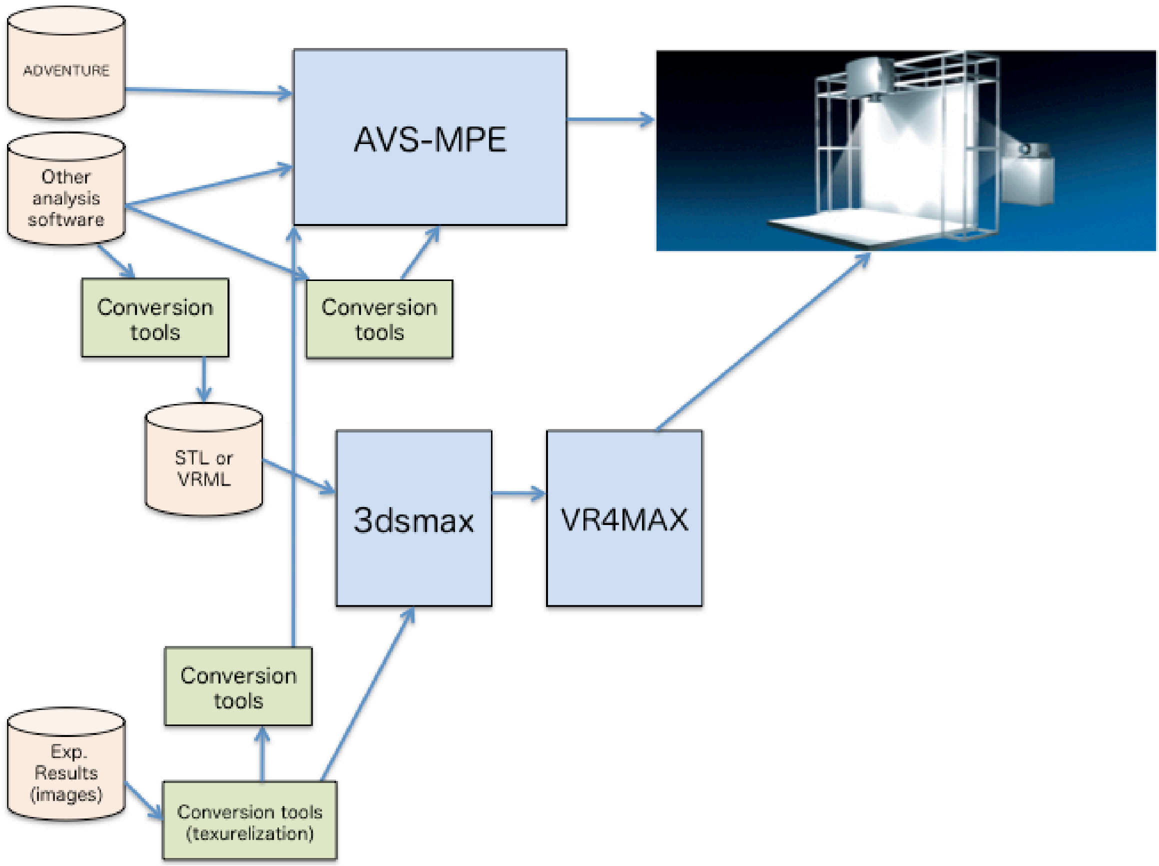

Figure 3. The design of the space-time simultaneous virtual reality visualization system. Bigger square boxes are software, smaller boxes are in-house conversion tools and cylinders represent data.

The upper-right picture is HoloStage and there are two routes to reach HoloStage. One is AVS/Express MPE [13] (AVS-MPE). It is a multi-screen version of AVS/Express (AVS), which is commercial scientific visualization software for all kinds of computational mechanics. AVS visualizes the data of several formats for a finite element method (FEM), a finite difference method, a particle method, and more. The other is VR4MAX [14], which is a computer graphics (CG) software for VR. AVS-MPE is the main path that allows results of ADVENTURE [15] software and other computational mechanics analysis as well as two-dimensional video images. Experimental 2D videos are mapped onto a rectangular panel with a specially developed AVS module in AVS-MPE. The video is firstly converted to sequentially numbered still images. The time steps of a computed result and an experimental video must be matched manually in advance.
Two network modules of AVS are shown in fig. 4. The left figure is for the computed results and the right for video images. The two network modules are linked with other AVS modules in order to synchronize the two results both in time and space. In time, the sequential number of the experimental data is counted up while the time step of the computed results advances together. The location, the orientation and the scale of the computed results and the video images are also controlled together, typically by the controller input (fig. 5).

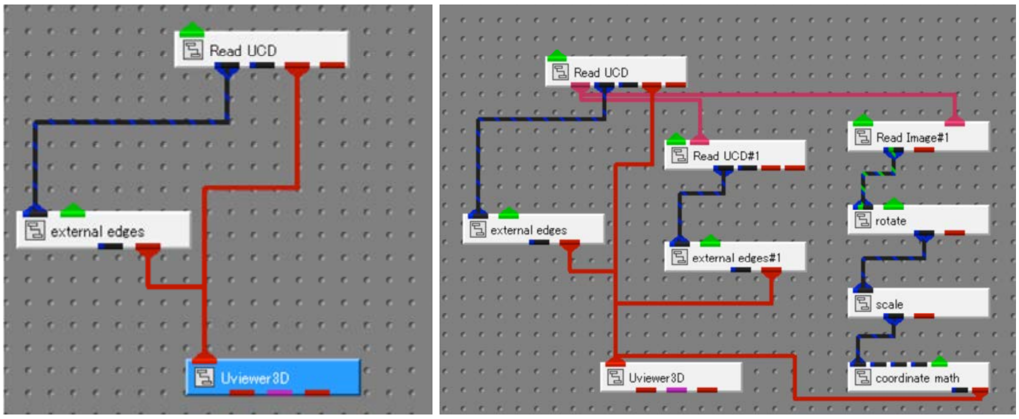

Figure 4. Parts of AVS network module. Left: for computed results. Right: for sequentially numbered images.

Figure 5. The controller and the stereo glasses. Four balls attached to the controller and the glasses are the markers for a visual motion capture system.

Figure 6 illustrates a whole module network of AVS-MPE even though the detailed explanation of AVS is out of scope of this article.

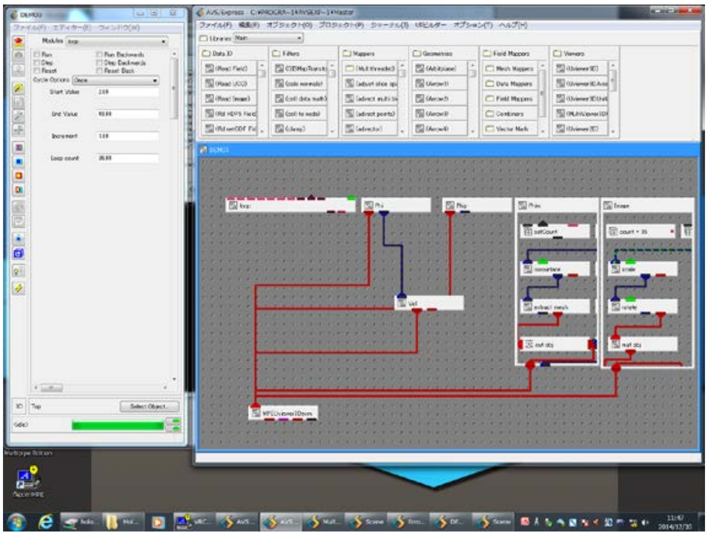

Figure 6. A whole module network of AVS-MPE.

The other types of data are displayed with VR4MAX. As described above, VR4MAX is CG software but does not have modeling functions. Thus 3ds Max [16], which is standard CG software, is used to make CG models. As analysis software, in general, does not output data for 3ds Max directly, here data for visualization is created by our in-house post-process software and converted into VRML format, which is supported by 3ds Max. Experimental videos can be displayed as a texture of a CG object.

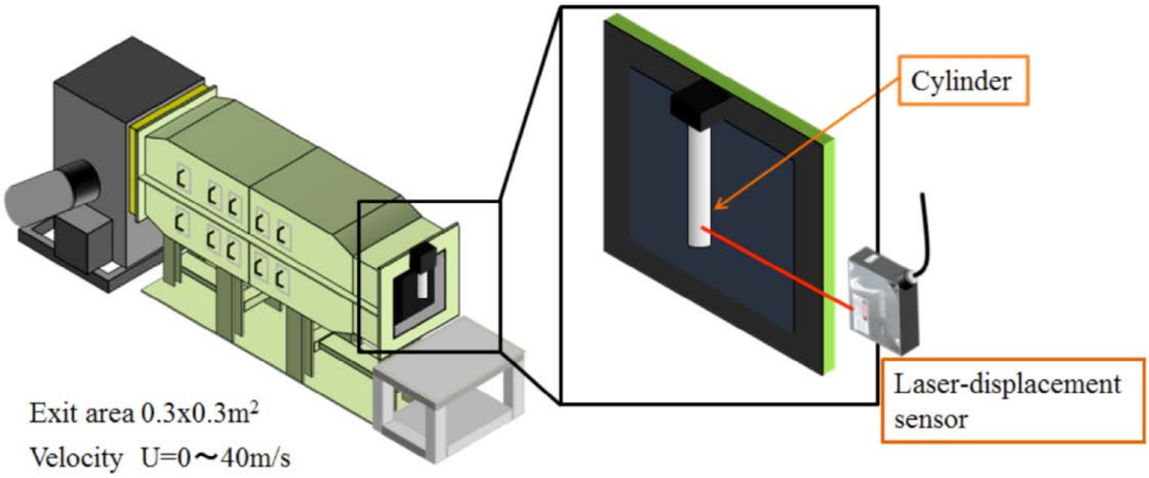

Figure 7. Schematic picture of the experimental setup.

Results and Discussions

In this section, an example of visualization by the present VR system is described. The so-called standard problem of fluid-structure coupled analysis proposed in this book (see the chapter of "Experiment on Oscillating Circular Cantilever for Fluid-Structure Interaction Code Validation") is applied. Figure 7 schematically shows the setup of the experiment. The low speed wind tunnel gives uniform flows of 10 - 40 m/s to hit a cylinder that is fixed at the top wall and that is deformed or is vibrated according to the condition of the flow and the material properties of the cylinder. High-speed video cameras, which are not illustrated in the figure, are located so as to obtain the views from the side and the bottom of the cylinder. Snap shots of the movies are shown in fig. 8. In the left figure, the cylinder slightly deforms by the flow from the left to the right.

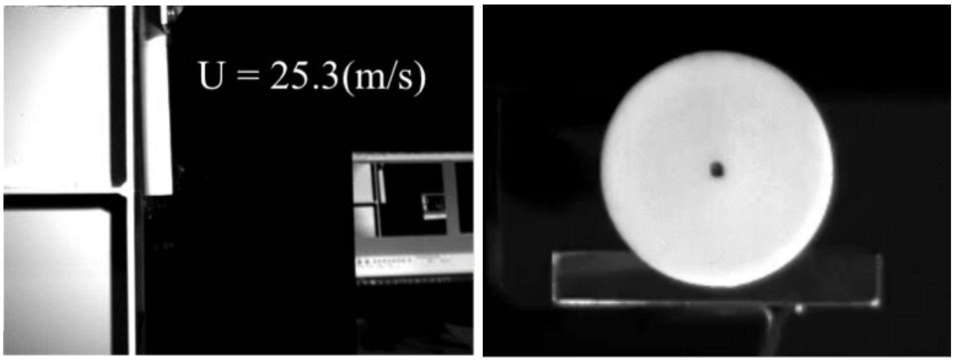

Figure 8. Snap shots of experiment. Left: side view. Right: bottom view.

Computation is done by our in-house fluid-structure analysis code also described in this book (see the section of "Development of Large Scale Fluid-Structure Coupled Analysis Method by the Enriched Free Mesh Method"). Both the flow field and the cylinder are discretized with a sort of FEM. More accurately, the flow field is computed with the SUPG-PSPG stabilized FEM [17] and the structure of the cylinder is analyzed with the enriched free mesh method (EFMM) [18]. Both results of the flow field and the structure of the cylinder are output as the format of ADVENTURE, and thus directly visualized with AVS-MPE.

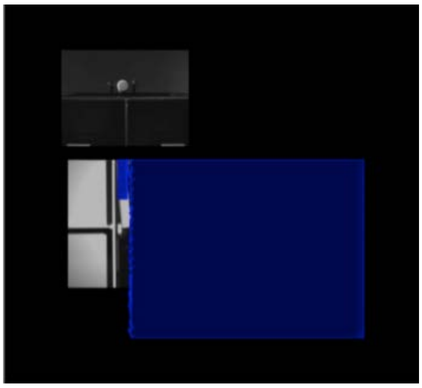

Figure 9. A monitor image of AVS showing two experimental video images and the corresponding computed result onto one of these videos.

Figure 9 shows the monitor image of the computed and the experimental results visualized with AVS (not AVS-MPE). One of the two video images (the side and the bottom views) is overlapped with the computed result. As expected, it is not easy to compare the computation and the experiment results. A usual side-by-side arrangement might be better for the comparison on a monitor display.

On the other hand, In VR space, two results are separately recognized even if they are overlapped each other. Especially in the present case, the video image is 2D and the computed result is 3D. Then changing the view angle simply highlights their difference. Figure 10 shows a picture of VR space showing two experimental video images and the corresponding computed result at the same location, the same orientation and the same scaling of one of the videos. The side view video and the computed result are overlapped. You can see doubled images in this figure, but because of the stereovision.

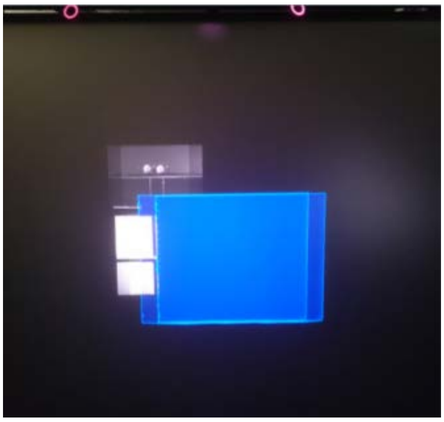

Figure 10. Space-time simultaneous visualization in VR space. Experimentally obtained video images and the corresponding computed result are displayed at the same time on the same location with the same scaling. As to stereovision, images of the left and the right eyes are doubly displayed. Two red circles on the top are infrared cameras to detect the viewer's location and orientation.

Figure 11 shows images from the viewer's eyes. In fig. 11 (a), the video from the side and the corresponding computed result are displayed side by side. This is a typical arrangement for comparison. You might recognize the difference of the two results but there is no significant difference in VR space and on a standard monitor. On the other hand, the video from the bottom and the corresponding computed results are overlapped in fig. 11 (b). In VR space, the difference of the two results must be clearly observed.

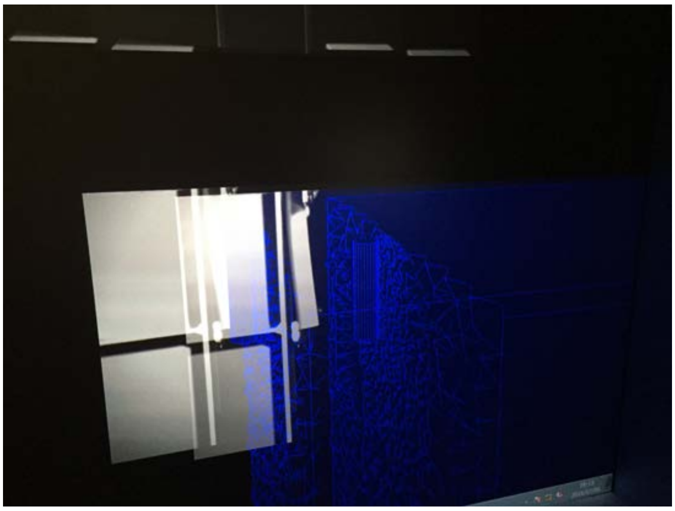

(a) The side view of the video is placed aside of the computed result. A typical arrangement for comparison.

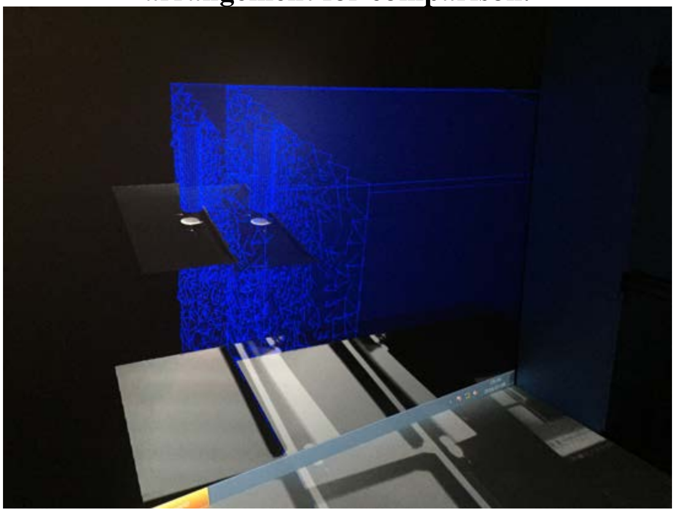

(b) The bottom view of the video is placed almost coinciding with the computed result. An example of the space-time simultaneous visualization.

Figure 11. An image from viewer's eyes.

Compared with the previous systems on CABIN and CANVAS, the possibility of the present system becomes clear. In CABIN or CANVAS, only computed results are visualized. We could enjoy the stereovision and experience the virtual world, but CABIN and CANVAS did not show the capability for V & V more than visualization on a computer monitor. The present system apparently shows the capability of visual comparison for V & V.

One of current problems of the present system is a manual control of the location and the size of the two results in order to be perfectly overlapped. Also the video image includes the distortion of the lens, resulting in degrade of accuracy. These spatial matching problems are crucial, especially in the present particular situation that the deformation of cylinder is small. In the computation, the deformation can be numerically enlarged, for example ten times of the original values, but not in the experiment. If we want to enlarge the deformation in experimental images, some special techniques of image processing might be necessary. It is left for future works as well as the stereovision video shooting in experiment.

In this article, the example with AVS-MPE is described. The other route with VR4MAX has another possibility. VR4MAX as well as 3ds Max is pure CG software and they have various

functions for CG expressions. They can create photo-realistic images of VR space, such as those of laboratories or of any other places, which might give us more immersive environment. The present system was developed for IPT but HMD is less expensive and tends to become common lately. The present author has a little experience of Oculus Rift [19] (Oculus) and Oculus and other similar devices have well-designed developer's tools, such as Unity [20]. A disadvantage of HMD that HMD couldn't follow a rapid head motion is mostly overcome thanks to the progress of graphics power of PC. There other disadvantages are still left, namely a heavier headset, a narrower eyesight, etc. Despite them, HMD seems to have possibility to widen applications of VR for scientific visualizations.
This article mainly deals with VR. There is a similar technology called augmented reality (AR) which superimposes CG images onto the real world, typically used for instruction, navigation, planning, etc. with see-through glasses or a computer monitor with a webcam or a smartphone. The present system has possibility to extend to AR in which a computed result is superimposed onto the corresponding experiment, being conducted just in front. This system is not a pure V & V but will be useful for "augmenting" the analysis.

Conclusions

A novel space-time simultaneous visualization system using VR technology is developed. The hardware for VR is HoloStage® Mini and the software is AVE-MPE, both are commercial products. On this VR system, some tools (AVS modules) are developed to display computed and experimental results. The present example of the fluid-structure coupled analysis and the corresponding experiment proves the possibility and usefulness of the present system.
There are some problems left, e.g. matching of the precise location of two results, causing the deficiency of quantitative evaluation. VR is now becoming common and expected to be a new scientific visualization tool.

References

[1] Zajac, E. E. (1964) Computer-made perspective movies as a scientific and communication tool, *Communications of the ACM* **7**, 169-170.
[2] Buning, P. G. and Steger, J. L. (1985) Graphics and flow visualization in computational fluid dynamics, AIAA Paper 85-1507-CP.
[3] Tamura Y. and Fujii, K. (1989) Use of graphic workstation for computational fluid dynamics, *A Collection of Technical Papers International Symposium on Computational Fluid Dynamics Nagoya*, 197-202.
[4] Tamura Y. and Fujii K. (1994) Simulation of experimental visualization methods for computational fluid dynamics research, *International Journal of Computational Fluid Dynamics* **2**, 309-333.
[5] Kageyama, A., Tamura, Y. and Sato, T (2000) Visualization of vector field by virtual reality, *Progress of Theoretical Physics Supplement* **138**, 665-673.
[6] Tamura Y., Kageyama, A., Sato T., Fujiwara, S. and Nakamura H. (2001) Virtual reality system to visualize and auralize numerical simulation data, *Computer Physics Communications* **142**, 227-230.
[7] Yano, H., Hirose, M., Ogi, T. and Tamura, Y. (1999) Haptization of flow field using vibroglove, *Transaction of Information Processing Society of Japan* **40**, 414-421 (in Japanese).
[8] Sutherland, I. E. (1965) The ultimate display, Proceedings of IFIP Congress, 506-508.
[9] Cruz-Neira, C. Sandin, D. J. and DeFanti, T. A. (1993) Surround-screen projection-based virtual reality: the design and implementation of the CAVE, *SIGGRAPH '93 Proceedings of the 20th annual conference on Computer graphics and interactive techniques*, 135-142.
[10] Hirose, M. (1997) CABIN-A multiscreen display for computer experiments, *Proceedings of Virtual Systems and MultiMedia 1997*, 78-83.
[11] Tamura Y. (2002) Development of an immersive display system for flow visualization, *Japan Korea Computer Graphics Conference 2002*, 7.
[12] Christie HoloStage® Mini - spatially immersive environment, https://www.christiedigital.com/en-us/3d/products-and-solutions/standard-projection-solutions/christie-holostage-mini (last access 5 Jul. 2016).
[13] AVS/Express MPE, URL: http://www.cybernet.co.jp/avs/products/mpe/ (last access 9 Feb. 2017).
[14] VR4MAX, URL: http://www.tree-c.nl/products/vr4max/ (last access 5 Jul. 2016).

[15] Yoshimura, S., Shioya, R., Noguchi, H. and Miyamura, T. (2002) Advanced general-purpose computational mechanics system for large-scale analysis and design, *Journal of Computational and Applied Mathematics* **149**, 279-296.
[16] 3ds max, URL: http://www.autodesk.com/products/3ds-max/overview/ (last access 14 Feb. 2017).
[17] Tezduyar, T. E. (1992) Stabilized finite element formulations for incompressible flow computations, *Advances in Applied Mechanics* **28**, 1-44.
[18] Yagawa, G. and Matsubara, H. (2007) Enriched free mesh method: an accuracy improvement for node-based FEM, *Computational Plasticity* **7**, 207-219.
[19] Oculus Rift | Oculus, URL: http://www.oculus.com/en-us/rift/ (last access 8 Jul. 2016).
[20] Unity, URL: https://unity3d.com/unity/ (last access 13 Feb. 2017).

Application of Machine Learning for Computational Mechanics

†Masato Masuda[1] and *Yasushi Nakabayashi[2]

[1]Center for Computational Mechanics Research, Toyo University, Japan
[2] Faculty of Information Sciences and Arts, Toyo University, Japan

†mst.masuda@gmail.com
*nakabayashi@toyo.jp

Abstract

In this research, it aims to predict the degree of analysis results without analysis, by using a large amount of analysis results obtained by the computational mechanics.

First, the ultimate goal of this research is the analysis result prediction intended for the fluid-structure interaction analysis. But, for the sake of simplicity, the problem is dealing with the vibration problem of a two-dimensional cylinder with moving boundary problem in the fluid analysis. The initial conditions and the results of the numerical analysis are collected as teacher data, and given to the learning machines. We performed a numerical fluid analysis using ADVENTURE_Fluid, mesh were smoothed using the velocity Verlet method. Analysis was calculated until the steady state.

In this study, machine learning is a neural network. Networks are constructed Multi-Layer Perceptron (MLP), modular network Self-Organizing Map (mnSOM) and Deep MLP using Auto-encoder of pre-process type. MLP is a very simple configuration of three layers with input layer, hidden layer and output layer. mnSOM is a general configuration using MLP to the module.

Benchmark problems using techniques respectively were solved. And we checked these prediction accuracy.

Then analysis result of our target is predicted. As the prediction result, the mnSOM and Deep MLP are clearly better than the MLP. In addition, Deep MLP and mnSOM was almost the same prediction performance. However, Deep MLP was obtained high prediction accuracy even though a small number of neurons.

Deep MLP can be better prediction with tuning. In summary, we propose a network that changed the module of mnSOM to Deep MLP.

Keywords: Machine Learning, Deep Learning, Neural Network, Perceptron, Self-Organizing Map.

Introduction

In recent years, computer improves the increasingly performance, the top of the super computer was got the calculation speed of 93PFLOPS in 2016 June[1]. This is a factor that became high speed of vector calculation by progress in generalization of GPU (Graphics Processing Unit). "Kei" computer in Japan recorded the performance of 10 PFLOPS. Against this background, Computational mechanics has become super large scale. Analysis of complex shapes and phenomenon are possible by the large-scale computing.

Experimental analysis is costly to make the modeling, experimental environment and maintenance for one analysis. The simulation can be easily analyzed for multiple conditions. If there is an assurance of analysis accuracy, the cost is lower than the experiment.

In fact, numerical analysis becomes high accuracy by creating a fine grid[2]. In addition, fluid-structure interaction analysis technique also has enabled highly accurate analysis by the large-scale computation[3]. In our CCRM team, we have been the variety analysis of fluid-structure interaction and large-scale[4][5][6].

On the other hand, mechanical learning is dramatically improved image recognition technology such as "Google's cat" [7][8]. A boom of artificial intelligence happens by these technology breakthroughs, and machine learning has achieved further development. Convolutional Neural Network (CNN), Recurrent Neural Network (RNN) and Multi-Layer Perceptron (MLP) etc. are being the mainstream of mechanical learning in the present day.

Arthur Lee Samuel proposed machine learning in 1959 as “Field of study that gives computers the ability to learn without being explicitly programmed.”[9]. And, Mechanical learning was defined closely by Tom M. Mitchell as "A computer program is said to learn from experience E with respect to some class of tasks T and performance measure P, if its performance at tasks in T, as measured by P, improves with experience E." in 1999[10].

Research target of this paper is coupled analysis. We will develop a system to predict the analysis results from the initial conditions of the analysis. Analysis is directed to a vibration phenomenon of a two-dimensional cylindrical problem. The analysis is dealing with a moving boundary problem of fluid analysis for the sake of simplicity.

In this paper, machine learning is a neural network, and the techniques of Multi-Layer Perceptron (MLP) and modular network Self-Organizing Map (mnSOM) are used. And, Deep MLP using the technology of Deep Learning was constructed.

Each neural network solves the benchmark problems, and operation check was performed. We compare the respective prediction results, and show the advantage of a prediction by Deep Learning.

Numerical Analysis

In this present study, we aim to analyze the results prediction of fluid-structure interaction analysis. However, we deal with the vibration problem of fluid analysis intended for the two-dimensional cylindrical problem for simplicity. In addition, input and output for use as teacher data is defined in this chapter.

Analysis Model

Analysis model was elastically support the two-dimensional cylinder with a spring damper model in a direction perpendicular to the flow. A schematic diagram of the analysis model is shown Fig. 1. The influx gives a uniform flow from the left side of Fig. 1. Cylinder is vibrated up to down by the fluid force.

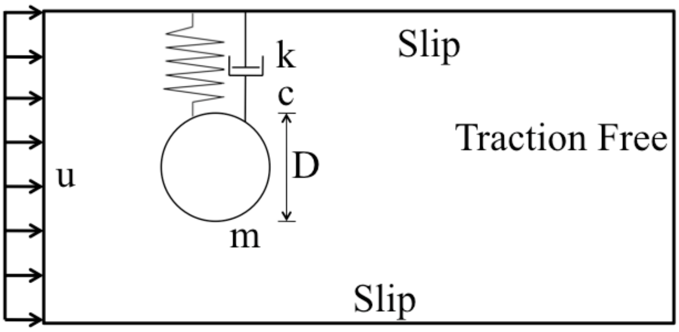

Figure 1. Model of Analysis

Fluid analysis uses the ADVENTURE_Fluid of ADVENTURE_system [11].

DVENTURE_Fluid is a large-scale parallel incompressible fluid analysis module by the finite element method. There are hexahedron code and tetrahedral code. Hexahedral code as based on the Q1-P0 element, is memory saving and high speed by one point integration. Also stabilization by BTD method is applied. Tetrahedral code as based on the P1-P1 element, is stabilized by SUPG / PSPG method. These codes are parallelized using MPI. ADVENTURE_Fluid can cooperate with other modules of the ADVENTURE system and perform efficiently large-scale parallel analysis by domain decomposition method

In this paper, a coupled analysis of the incompressible viscous fluid and two-dimensional rigid cylinder using tetrahedral code of ADVENTURE_Fluid is performed. Weak form of the finite element method is expressed as follows.

$$
\begin{aligned}
&\int_{\Omega} w_i \cdot \rho\left(\frac{\partial u_i}{\partial t} + u_j u_{i,j} - f_i\right) d\Omega + \int_{\Omega} w_{i,j}\sigma_{ij} d\Omega + \int_{\Omega} q u_{i,j} d\Omega \\
&\quad + \sum_e \int_{\Omega^e} \tau_{SUPG} u_j w_{i,j} \left[\rho\left(\frac{\partial u_i}{\partial t} + u_k u_{i,k} - f_i\right) - \sigma_{ik,k}\right] d\Omega \\
&\quad + \sum_e \int_{\Omega^e} \tau_{PSPG} \frac{1}{\rho} q_i \cdot \left[\rho\left(\frac{\partial u_i}{\partial t} + u_k u_{i,k} - f_i\right) - \sigma_{ik,k}\right] d\Omega \\
&\quad = \int_{\Gamma_h} w_i h_i d\Gamma
\end{aligned} \tag{1}
$$

An algebraic equation obtained by discretizing this equation becomes asymmetric matrix. Since the pressure diagonal terms become nonzero by PSPG term, this equation can be solved directly. In practice, Bi-CGSTAB method is used in conjunction with the diagonal scaling pre-processing.

Mesh smoothing is used to grid control in accordance with the movement of the cylinder. And moving boundary using the ALE method is expressed. The weak form of SUPG / PSPG stabilized finite element method of ALE notation is shown below.

$$
\begin{aligned}
&\int_{\Omega} w_i \cdot \rho\left(\frac{\partial u_i}{\partial t} + \bar{u}_j u_{i,j} - f_i\right) d\Omega + \int_{\Omega} w_{i,j}\sigma_{ij} d\Omega + \int_{\Omega} q u_{i,j} d\Omega \\
&\quad + \sum_e \int_{\Omega^e} \tau_{SUPG} u_j w_{i,j} \cdot \left[\rho\left(\frac{\partial u_i}{\partial t} + \bar{u}_k u_{i,k} - f_i\right) - \sigma_{ik,k}\right] d\Omega \\
&\quad + \sum_e \int_{\Omega^e} \tau_{PSPFG} \frac{1}{\rho} q_i \cdot \left[\rho\left(\frac{\partial u_i}{\partial t} + \bar{u}_k u_{i,k} - f_i\right) - \sigma_{ik,k}\right] d\Omega \\
&\quad = \int_{\Gamma_h} w_i h_i d\Gamma
\end{aligned} \tag{2}
$$

$$
\bar{u} = u - \hat{u} \tag{3}
$$

Here, $\hat{u}$ is a moving speed of the mesh.

Vibration of the cylinder by the results obtained by integrating the traction around a cylinder at each time step, perform a mesh smoothing and move the position of the cylinder. Moving position and the moving speed of the cylinder is determined by the velocity Verlet method. The formula is indicated below.

$$
x(t+\Delta t) = x(t) + v(t)\Delta t + \frac{1}{2}a(t)\Delta t^2 \tag{4}
$$

$$
v(t+\Delta t) = v(t) + \frac{1}{2}\left[a(t+\Delta t) + a(t)\right]\Delta t \tag{5}
$$

Here, x, v, a and t are the position, speed, acceleration of the cylinder and time step of the fluid analysis. Fig. 2 shows the flow of analysis.

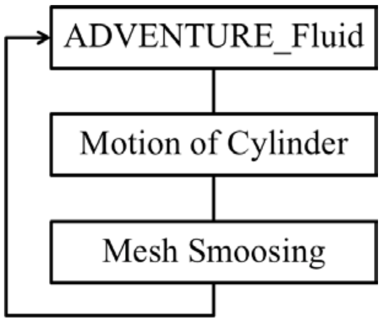

Figure 2. Flowchart of Fluid-Ridged Coupled Analysis

The mesh of the numerical analysis is shown in Fig. 3. Mesh is 256 points in the circumferential direction, and 64 points in the normal direction. Minimum grid width is 0.0003D, and cylinder around holds a sufficient mesh resolution. Furthermore, ADVENTURE_Fluid is a 3-dimensional analysis code, and the analysis was pseudo two-dimensional analysis as the two nodes and 1 element. One example of analysis conditions is shown in the Table 1, the lift coefficient and drag coefficient is shown in Fig. 4. And the time history of the cylinder center position is shown in Fig. 5. The drag coefficient indicates a slightly higher value, but the vibration frequency and the lift coefficient were obtained generally satisfactory values.

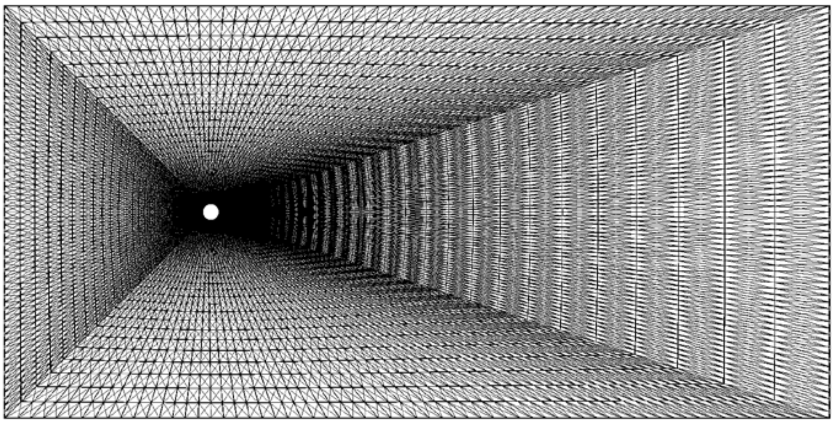

Figure 3. Mesh of 2-Dimentional Cylinder Model

Table 1. An Example of Calculation Condition

Time Step	1.0×10^{-3}	[s]
Flow Velocity	1.0	[m/s]
Cylinder Diameter	1.0	[m]
Reynolds Number	100	[-]
Cylinder Mass	1.0	[kg]
Spring Constant	1.0	[kg/s^2]
Dumper Constant	0.0	[kg/s]

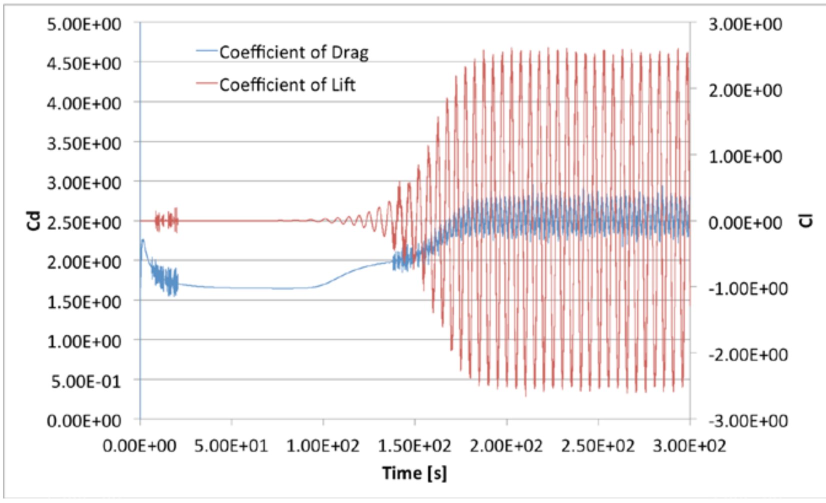

Fig.4 Coefficient of Lift and Drag at Reynolds Number 100

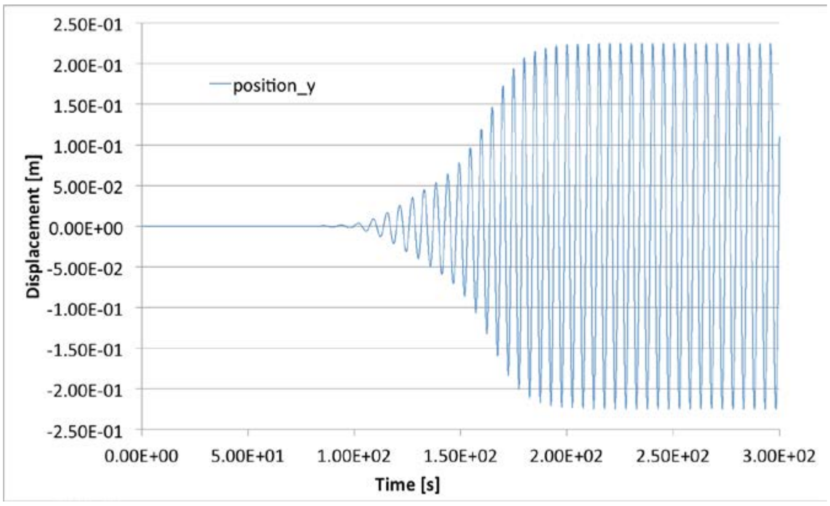

Fig.5 Displacement of Cylinder

Generation of Teacher Data

Next, we show how to create a teacher data. Aforementioned fluid-motion interaction analysis is analyzed until a steady state. The initial conditions of numerical analysis are the mass of cylinder, the spring constant, the damping coefficient, the velocity of the uniform flow, the Reynolds number and the natural frequency of cylinder. The lift coefficient, drag coefficient, the amplitude and frequency of the analysis result are obtained as Fig. 4, 5. In addition, the Strouhal number is also obtained.

Input and output items of teacher data are summarized in Table 2.

Input items are the following six. 1: Mass of Cylinder, this is the mass of the cylinder, using two types of 0.5kg and 1.0kg. 2: Spring Constant, this is a spring constant of the spring to support the cylinder, using two of 0.5kg/s and 1.0kg/s. 3: Dumper, this is the damping coefficient of the damper for suppressing the motion of the cylinder to damp the kinetic energy of the cylinder. If with damper, damping coefficient is 0.01kg/s^2. 4: Flow Velocity, this is uniform flow velocity from the inlet, flow velocity are two of 0.5m/s and 1.0m/s. 5: Reynolds Number, Reynolds number is a dimensionless quantity that is defined as the ratio of inertial forces to viscous forces. Reynolds number that is adjusted the kinematic viscosity coefficient, 100, 500, 1000 uses 3 ways. 6: Natural Frequency of Cylinder, this is the natural frequency of the cylinder. This value is determined from the mass and the spring constant of the cylinder.

Table 2. Input and Output Items for Machine Learning

Inputs	Symbols	[Unit]	Ways
Mass of Cylinder	m	[kg]	0.5 1.0
Spring Constant	k	[kg/s]	0.5 1.0
Dumper	c	[kg/s^2]	0.0 0.01
Reynolds Number	Re	[-]	100 500 1000
Natural Frequency of Cylinder	f_N	[Hz]	-
Outputs			
Amplitude of Cylinder	Ac	[m]	-
Frequency of Cylinder	f_C	[Hz]	-
Maximum Coefficient of Lift	C_L	[-]	-
Strouhal Number	St	[-]	-
Average Coefficient of Drag	C_D	[-]	-

Output items are five of the following obtained from the analysis results. 1: Amplitude of Cylinder, which is the largest amount of displacement when the cylinder vibrates. 2: Frequency of Cylinder, this is the frequency of the cylinder to oscillate regularly in the steady state. 3: Maximum Coefficient of Lift, this represents the coefficient of the maximum lift that cylinder receives from fluid. 4: Strouhal Number, Strouhal number is the vortex shedding frequency of Karman vortex that is released from the cylinder. 5: Average Coefficient of Drag, which is the average drag coefficient in the steady state.

Teacher data is 48 dataset, the number of combinations of input. Furthermore, we prepared 22 datasets for verification. The input items of verification data are shown in Table 3.

Table 3. Input Items of Verification Data

No.	mass	k	c	u	Re
1	0.750	1.000	0.000	1.000	100.000
2	0.500	0.750	0.000	1.000	100.000
3	0.500	1.000	0.005	1.000	100.000
4	0.500	1.000	0.000	0.750	100.000
5	0.500	1.000	0.000	1.000	300.000
6	0.500	1.000	0.000	1.000	750.000
7	0.750	0.750	0.000	1.000	100.000
8	0.750	1.000	0.005	1.000	100.000
9	0.750	1.000	0.000	0.750	100.000
10	0.750	1.000	0.000	1.000	300.000
11	0.750	1.000	0.000	1.000	750.000
12	0.500	0.750	0.005	1.000	100.000
13	0.500	0.750	0.000	0.750	100.000
14	0.500	0.750	0.000	1.000	300.000
15	0.500	0.750	0.000	1.000	750.000
16	0.500	1.000	0.005	0.750	100.000
17	0.500	1.000	0.005	1.000	300.000
18	0.500	1.000	0.005	1.000	750.000
19	0.500	1.000	0.000	0.750	300.000
20	0.500	1.000	0.000	0.750	750.000
21	0.750	0.750	0.005	0.750	300.000
22	0.750	0.750	0.005	0.750	750.000

The flow velocity of verification data is fixed to 1.0m/s. Other input items are intermediary value of the values of the teacher data. Location marked with the color of the Table 3 is an intermediate value. Numerical analysis for verification was also calculated until the steady state.

The verification data are given to network after learning by using the 48 data. The output results were compared with the results actual numerical analysis, and the error was calculated.

Multi-Layer Perceptron

In this chapter, Multi-Layer Perceptron (MLP) is described. MLP is a common approach of the neural network. We explain the Simple Perceptron, and describe the MLP.

Simple Perceptron

Simple Perceptron is such a structure of Fig.1.

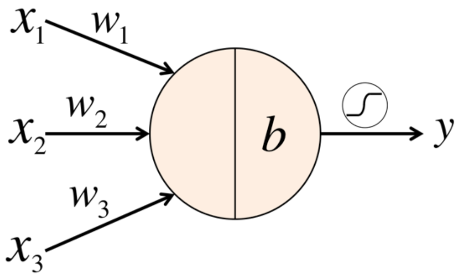

Figure 6. Simple Perceptron

Simple Perceptron is learning with the teacher data. The weight w_i is modified based on teacher data using the forward propagation method and gradient descent method. Forward propagation determines the output of the network as in the following expression.

$$y = f\left(\sum_i x_i w_i + b\right) \tag{6}$$

Here, b is a bias, $f(\cdot)$ is a transfer function. And the subscript i is the index of i-th input. Mean square error E is calculated from the output of teacher data and output of perceptron by the Eq. (6).

$$E = \sum \frac{(t-y)^2}{2} \tag{7}$$

Here, t is the output of the teacher data. Weights are modified by Back propagation by using the E. Formula conversion is omitted, but modified formula of weight is as below.

$$w_i = w_i + \Delta w_i \tag{8}$$

$$\Delta w_i = -\alpha \frac{\partial E}{\partial w_i} \tag{9}$$

$$\frac{\partial E}{\partial w_i} = (t-y) f'(x_i) \cdot x_i \tag{10}$$

The α is the learning rate, given a value less than 1. When the function $f(\cdot)$ is a sigmoid function, modified formula of weight is Eq. (11).

$$\Delta w_i = -\alpha(t-y)y(1-y)\cdot x_i \tag{11}$$

The update equation is repeated enough times. The method of optimizing the weights so as to satisfy the teacher data is perceptron. The process to modify the weight is called learning.

Multi-Layer Perceptron

The Multi Layer Perceptron is a network that formed a simple perceptron hierarchical, commonly called the neural networks. A schematic diagram of an MLP is shown in Fig. 7.

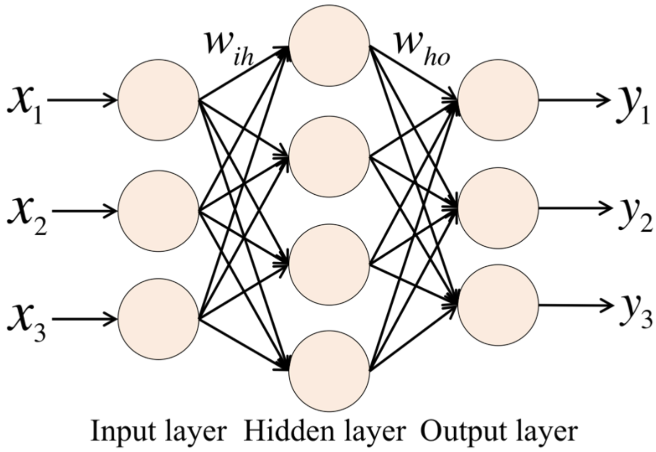

Figure 7. Multi-Layer Perceptron

w_{ih} is the weight that connects the input layer and the hidden layer, w_{ho} is the weight that connects the output layer and the hidden layer. The learning method calculates the loss function by forward direction calculation at first like a simple perceptron. In Forward propagation, an output of the perceptron is given as input for Perceptron of the next layer. An expression of the o-th output vector is Eq. 12.

$$h_o = f\left(\sum_j f\left(\sum_i x_i w_{ih,i} + b_j\right) w_{ho,j} + b_o\right) \tag{12}$$

Subscripts are i-th input vector, the number of j-th neurons in the hidden layer, and the o-th output vector. Weights are modified by the Back Propagation method. When the function $f(\cdot)$ is the sigmoid function, the weight w_{ho} connecting the hidden layer and output layer is updated by the following equation.

$$w_{ho} = w_{ho} + \Delta w_{ho} \tag{13}$$

$$\Delta w_{ho} = -a(t_o - h_o)h_o(1-h_o)h_h \tag{14}$$

The weights w_{ih} connecting the input layer and hidden layer are updated by Eq. (15).

$$w_{ih} = w_{ih} + \Delta w_{ih} \tag{15}$$

$$\Delta w_{ih} = -\alpha \sum_j \left(w_{ho\,j}(t_o - h_o)h_o(1-h_o)\right)h_h(1-h_h)x_i \tag{16}$$

The h_h is the output of hidden layer. MLP is learned by solving the Eq. (12), (14) from the output side.

modular network Self-Organizing Map

This chapter describes the mnSOM. First, self-organizing map (SOM) is explained. mnSOM is a technique that is advanced SOM. SOM is a classification machine, and there is a function of grouping the input. mnSOM becomes prediction machine from classification machine by introducing module into SOM. In addition, SOM, mnSOM have functions of clustering the teacher data on the map and interpolating between the teacher data.

Self-Organizing Map

Self-Organizing Map (SOM), which is one of neural networks and was proposed by T. Kohonen[12], is a two-layered unsupervised competitive learning model that does not have a hidden layer. In the learning algorithm of SOM, the characteristics of input data are learned through neighborhood learning. A map is formed so that similar kinds of data are located in the neighborhood and other data are located at distant places. Accordingly, it is possible to visualize high-dimensional vector data, and understand the relations among data intuitively.

SOM has a map with the M×N grid, and weighted units exist (Fig.8).

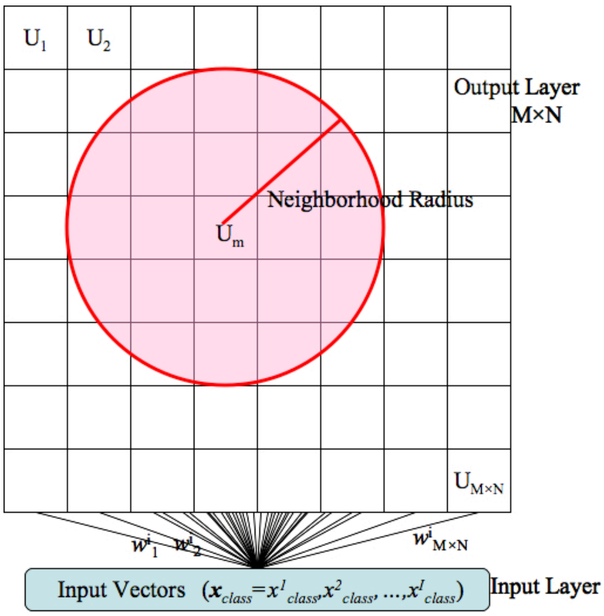

Figure 8. Conceptual Diagram of SOM
(U is map unit, m and n are unit number, w is uniting weight, X is input signal)

Unit weights are updated in neighborhood learning. The algorithm of SOM is as follows:

Step 1. Initialize the weight vector w of units.

Step 2. Input the vector $\boldsymbol{x}_{class} = (x^1_{class}, x^2_{class}, x^3_{class}, \cdots, x^I_{class})$ into input layer. Here, "*class*" represents the number of input vectors, and "*I*" denotes the dimension of the input vector.

Step 3. Calculate the Euclidean distance "*Dist*" between an input vector and the weight vector of a unit in the map layer (competitive layer).

$$Dist_m = \sqrt{\sum_i \left(x^i_{class} - w^i_m\right)^2} \tag{17}$$

Step 4. Define the unit that minimizes the Euclidean distance obtained at Step 3 as the winning unit BMU (Best Matching Unit).

$$BMU = \arg\min_m Dist_m \tag{18}$$

Step 5. Update the weights of the winning unit and surrounding units only.

$$\Delta w_m^i = h\left(l\left(BMU, m\right)\right)\left(x_{class}^i - w_m^i\right) \tag{19}$$

$$h(l) = \alpha \exp\left(\frac{l^2}{2\sigma^2}\right) \tag{20}$$

Step 6. Repeat Steps 2 to 5 sufficiently.

Here, l represents the distance between the winning unit and the unit whose weight is updated. $h(\cdot)$ and σ denote the neighborhood function and the range of the influence of the neighborhood function (neighborhood radius), respectively. This is decreased according to learning steps. α is learning coefficient, ranging from 0 to 1. The learning coefficient α decreases as learning steps proceed.

modular network Self-Organizing Map

The modular network Self-Organizing Map (mnSOM)[13] replaces the unit of SOM to the module as shown in Fig. 9. Module is generally used for MLP. Competitive learning of mnSOM is learning by using the output of the module.

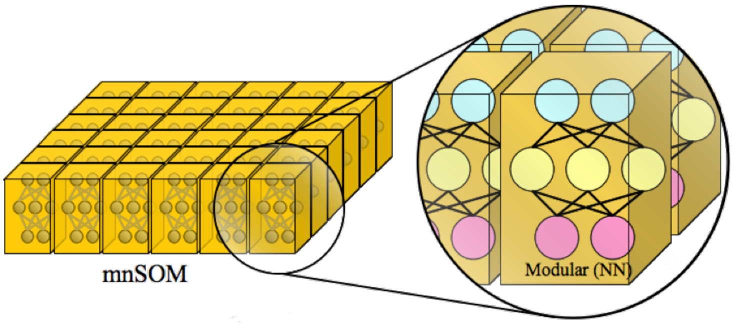

Figure 9. Image of mnSOM

The algorithm of mnSOM is shown below.

Step 1. Initialize the weight vector w of modules.

Step 2. Input the vector $\boldsymbol{x}_{teacher} = (x_{teacher}^1, x_{teacher}^2, x_{teacher}^3, \cdots, x_{teacher}^I)$ into input of modules. Here, "*teacher*" represents the number of input vectors, and "*I*" denotes the dimension of the input vector.

Step 3. Calculate the output vector $\boldsymbol{y}_{teacher} = \left(y_{teacher}^1, y_{teacher}^2, y_{teacher}^3, \cdots, y_{teacher}^J\right)$ of modules. "*J*" is the dimension of the output vector.

Step 4. Calculate the error E between output of module and output of teacher data.

$$E_{teacher} = \frac{1}{J}\sum_{j=1}^{J}\left(T_{teacher}^j - y_{teacher}^j\right)^2 \tag{21}$$

Step 5. Define the module that minimizes the error E obtained at Step 4 as the winning module BMM (Best Matching Module).

$$BMM_{teacher} = \arg\min_{m} E_{teacher} \quad (22)$$

Index "m" is number of module.

Step 6. Update the weights of the winning module and surrounding modules.

$$\Delta w = -\varepsilon \sum_{teacher}^{TEACHER} h_{teacher}(l) \frac{\partial E_{teacher}}{\partial w} \quad (23)$$

$$w^{new} = w^{old} + \Delta w \quad (24)$$

Here, is learning rate. Updating of the weights for 1 step is repeated enough times when the *h* and are fixed.

Step 7. Repeat Steps 2 to 6 sufficiently.

Deep Learning

Since the Deep Learning is a term that refers to the neural network of deep hierarchy, there is no learning machine named Deep Learning. Deep Learning solved the gradient loss (explosion) problems in the back-propagation method that occurs when the neural network is a multilayered. Furthermore, the network is solved complex problem by multilayered.

Deep Learning commencing with the Deep Belief Network[14] optimize the weight of the MLP by pre-processing. The network is aimed at high learning accuracy by this optimization. In this approach, the learning process by the back propagation is called fine-tuning, and the pre-processing is called pre-training. The pre-training calculates the weight of the MLP to reproduce the input vector using a Restricted Boltzmann Machine (RBM) or an Auto-encoder (AE)[15] and etc. The pre-training is unsupervised learning. The weights of the network are the value extracted the feature of the input vector. The weight optimized by pre-training is used, so the learning precision of the network is the mechanism to improve. Because the weight optimized by pre-training is used, the learning precision of the network is the mechanism to improve.

As a feature of Deep Learning, each layer of the neural network is processed independently. Thus, gradient loss problems caused by multi-layered is solved, and super multi-layer of the network is constructed. Further, the network corresponding to different prediction problems, by solving each layer with different approach.

For example, the image recognition mainly uses Convolutional Neural Network (CNN) [16]. Pixel of the image is given to the network as the input vector, and the input vector is compressed and feature is extracted. Since pixels in the image have a continuity of the data, compression of the data by the convolution is valid.

In speech recognition, primarily Recurrent Neural Network (RNN) [17] is used. Speech data is given the input of the sound in the time series, and the word is inferred from past information and current information. Recently, speech recognition can accurately recognized using a Long Short Term Memory (LSTM) [18].

Our Deep Learning technique is the MLP pre-processed using the AE. There is no continuity in the analysis conditions given as an input vector. Analysis conditions do not handle as in the image data. And the data is not the time sequence data. Therefore, CN and RNA are inconsistent with our purpose. We expect to improve the learning accuracy by the feature extraction from the input data by the AE. This technique is called Deep MLP.

Deep MLP

In this chapter, Deep MLP which is a network performed pre-training by the AE is explained. Deep MLP was tested a handwritten digit recognition as a benchmark problem.

Network Structure

Deep MLP performs pre-training and fine-tuning as Fig. 10. There are two ways in the fine-tuning. One is a method to perform fine-tuning in the whole network. The other one is the way to perform fine-tuning several layers of the output side.

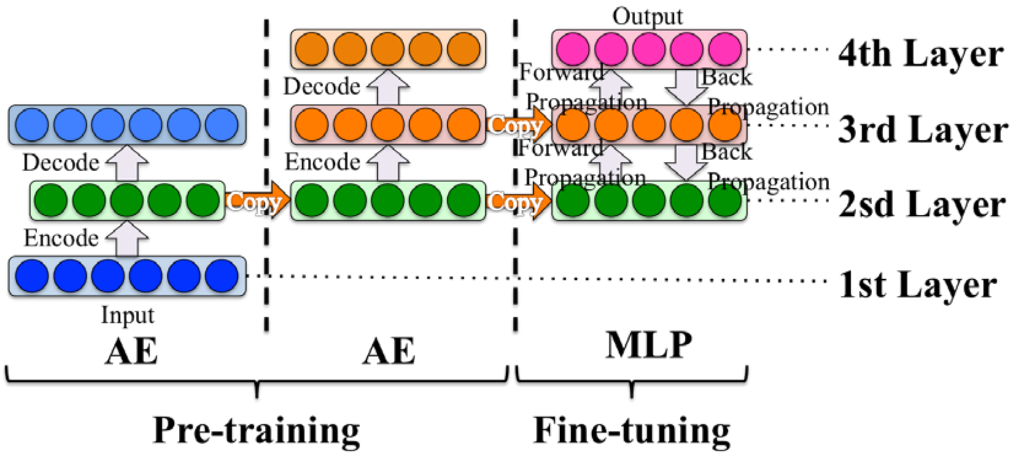

Figure 10. Image of Deep MLP

The encode formula and decode formula of AE are as follows:

$$encode: \quad y = f\left(Wx + b\right) \tag{25}$$

$$decode: \quad z = f\left(W'y + b'\right) \tag{26}$$

Here, $f(\cdot)$ is sigmoid function. W and b are weight and bias. W' is used transpose of W (tied weight). The amounts obtained by differentiating the loss function with respect to weight and bias are used for each modify amount.

Benchmark Test of Deep MLP

As a benchmark problem, handwritten digit recognition is done. Learning data uses the MNIST [19]. The digits data are images of 28×28 pixels and are labeled with one-hot.

Network was simple configuration of 4-layers. The pre-training by AE in two layers from the input layer is performed, and MLP is learned in three-layer from the output layer. The results of the benchmark got a good result with a score of 85.1 percent. Correct answer rate is expected to further rise by learning of the deeper layers.

Learning Results

In this chapter, the result of numerical analysis is predicted using machine learning. In addition, Prediction results for MLP, mnSOM and Deep MLP are compared and summarized. In this case, the learning coefficient is fixed at 0.01 and the iteration of learning is fixed at 10,000 steps. Training data is given six input of analysis condition and the five output of analysis result as shown in the Table 2. Learning is used 48 datasets as Training data. Verification is used 22 datasets of unlearned data.

MLP is constructed of three layers, and the number of neurons of the intermediate layer is 900. Module of mnSOM is the 3-layered MLP. The number of neurons in the hidden layer is 50. Map size is 10×10. Deep MLP is a network of five layers. The hidden layers are 3 layers. The number of neurons in respectively layers is 50. Result is shown in the Table.6 when given validation data after learning.

Table 6. Error Rate of Learning Result

	MLP	mnSOM	Deep MLP
Average error	73.5 %	51.3 %	53.1 %
Maximum error	230.3 %	214.1 %	227.3 %
Number of Neurons (hidden)	900	50 / module	50×3Layers

Error Rate is defined by the following equation.

$$Error = \sum_{o} \left(\frac{\| NN - correct \|}{correct} \right) \tag{27}$$

$$average = \frac{\sum_{data} Error}{DATA} \tag{28}$$

$$maximum = \underset{data}{\operatorname{argmax}} \left(Error \right) \tag{29}$$

Here, *NN* is the output of the neural network, *correct* is the value of the analysis result. Subscript o is the number of output items, and data is represents the number of datasets.

From Table 6, the average error of mnSOM and Deep MLP were clearly better than the MLP. Maximum error was not much difference in all networks. Maximum error was recorded when given the same dataset to all learning machine. Predictions of 21-th and 22-th of validation data were insufficient. It is due to the weak network to unknown input. However, when comparing the number of neurons, Deep MLP is the smallest number of neurons in these methods. Learning accuracy of Deep MLP is the same as the mnSOM even if the number of neurons is small. In order to increase the prediction accuracy in this network, it is necessary to learn using more teacher data and to tune the network. Tuning is to increase the number of layers and number of neurons. By doing so, learning accuracy will be improved.

Conclusions

Neural network that predicts analysis results was constructed using MLP and mnSOM and Deep MLP. In each method, learning accuracy and the number of neurons were compared. The results are summarized below.

- By building the neural network of the five-layer, capacity to deal with problem was raised. Thereby prediction accuracy of Deep MLP is clearly better than MLP.
- Even if number of neurons is small, the same prediction result as mnSOM is obtained by increasing layers.

The Deep MLP is a network without tuning. Therefor, we think that it is possible to improve the prediction accuracy by tuning. By Increase the number of layers and neurons, prediction accuracy will be more improvement.

Finally, although not summarized in this paper, we are thinking the Deep mnSOM that changes mnSOM module to Deep MLP. In view of the fact that mnSOM and Deep MLP has clearly improved accuracy more than the MLP, we believe that Deep mnSOM gives great result better than the Deep MLP and mnSOM.

References

[1] Super Computer Top500, https://www.top500.org (as of 31 July, 2016)

[2] Masao Ogino, Ryuji Shioya, Parallel Finite Element Analysis of 100 Billion DOFs based on the Hierarchical Domain Decomposition Method, Proceedings of the Conference on Computational Engineering and Science 18, 4p, 2013, in Japan

[3] Yuri Bazilevs, Kenji Takizawa, Tayfun E. Tezduyar, 流体−構造連成問題の数値解析，森北出版株式会社

[4] Kohei Murotani, Seiichi Koshizuka, Eiichi Nagai, Toshimitsu Fujisawa, Akira Anju, Hiroshi Kanayama, Satoshi Tanaka, Kyoko Hasegawa, Large-Scale Tsunami Run-Up Analysis Using Particle Method, High-Performance Computing for Structural Mechanics and Earthquake / Tsunami Engineering (Springer Tracts in Mechanical Engineering), Springer, pp.157-177, 2015

[5] Hiroshi Kawai, Masao Ogino, Ryuji Shioya, Shinobu Yoshimura, Fundamentals of High-Performance Computing for Finite Element Analysis, High-Performance Computing for Structural Mechanics and Earthquake / Tsunami Engineering (Springer Tracts in Mechanical Engineering), Springer, pp.1-21, 2015

[6] Shinsuke Nagaoka, Yasushi Nakabayashi, Genki Yagawa, Fluid-Structure Coupled Analysis Using Enriched Free Mesh Method, Key Engineering Materials, Vols. 462-463, pp.1238-1243, 2011

[7] Quoc V. Le, Marc'Aurelio Ranzato, Rajat Monga, Matthieu Devin, Kai Chen, Greg S. Corrado, Jeff Dean, Andrew Y. Ng, Building High-level Features Using Large Scale Unsupervised Learning, Appearing in Proceedings of the 29th International Conference on Machine Learning, Edinburgh, Scotland, UK, 2012

[8] IMAGENET Large Scale Visual Recognition Challenge 2012 (ILSVRC2012), http://image-net.org/challenges/LSVRC/2012/results.html (as of 31 July, 2016)

[9] Arthur Lee Samuel, Some Studies in Machine Learning Using the Game of Checkers, IBM Journal, Vol.3, No.3, p.535-554, 1959

[10] Tom Michael Mitchell, Machine Learning, McGraw Hill. ISBN 0-07-042807-7, 1997

[11] ADVENTURE Project, http://adventure.sys.t.u-tokyo.ac.jp/jp/ (as of 31 July, 2016)

[12] T. Kohonen, Self-Oganizing Maps, Springer-Verlag, 1995

[13] T. Furukawa, K. Tokunaga, K. Morishita and S.Yasui, Modular network SOM (mn- SOM) : From vector space to function space, Proceeding of International Joint Conference on Neural Networks, pp.1581-1586, 2005

[14] Geoffrey E. Hinton, Simon Osindero, Yee-Whye Teh, A Fast Learning Algorithm for Deep Belief Nets, Massachusetts Institute of Technology, *Neural Computation*, No.7, vol.18, pp.1527–1554, 2006

[15] G. E. Hinton; and R. R. Salakhutdinov, Reducing the Dimensionality of Data with Neural Networks, Science vol.313, pp.504–507, 2006.

[16] Y. LeCun, L. Bottou, Y. Bengio, P. Haffner, Gradient-Based Learning Applied to Document Recognition, *Proc. IEEE*, 1998

[17] Tomas Mikolov, Martin Karafiát, Lukas Burget, Jan "Honza" Cernocký, Sanjeev Khudanpur, Recurrent neural network based language model, Proceedings of the 11th Annual Conference of the International Speech Communication Association (INTERSPEECH 2010), 2010

[18] Felix A. Gers, Nicol N. Schraudolph, Jürgen Schmidhuber, Learning Precise Timing with LSTM Recurrent Networks, Journal of Machine Learning Research, 3, pp.115-143, 2002

[19] Yann LeCun, "The MNIST database of handwritten digits", http://yann.lecun.com/exdb/mnist/ (as of 31 July, 2016)

High Performance Computing for Large Scale Structural Analysis

R. Shioya[1], Hiroshi Kawai[2], M. Ogino[3]

[1]Faculty of Information Sciences and Arts, Toyo University, JAPAN
[2] Faculty of Engineering, Tokyo University of Science-Suwa, JAPAN
[3]Information Technology Center, Nagoya University, JAPAN

Introduction

In November 2016, TOP500 [1] List of the world's top supercomputers reported that the world's fastest supercomputer is Sunway TaihuLight, NRCPC, China with 93 Peta Flops (PFlop/s) of maximal LINPACK performance and in June 1993 when the first list of TOP500 was released, it was CM-5/1024, Los Alamos National Laboratory, United States with 59.7 Giga Flops (GFlop/s). Therefore, it is about 1,500,000 times faster in these 23 years, that is, about 1.9 times faster per year. According to the Moore's law [2], it is 2 times per year. With such speed-up, in 2020, it will achieve over 1 Exa Flops (EFlop/s), so called post petascale speed.

To use such high performance computers in the post generations of petascale supercomputer, developing system software technologies as well as related systems is very important. More concretely, research and development of system software enable us to exploit maximum efficiency and reliability from supercomputers which will be composed of general purpose many-core processors as well as special purpose processors, so called GPGPU. In addition to the system software such as programming languages, compilers, runtime systems, operation systems, communication middleware, and file systems, application development support systems and ultra-large data processing systems are important targets for research and development.

In such situation, we have been developing open source system software, ADVENTURE [3], which is a general-purpose parallel finite element analysis system and can simulate a large scale analysis model with supercomputer like the Earth Simulator or K-computer. In the system, HDDM (hierarchical domain decomposition method), which is a very effective technique to large-scale analysis, was developed. The aim of our project is to develop a numerical library based on HDDM that is extended to pre and post processing parts, including mesh generation and visualization of large scale data, for the post petascale, that is, exa scale simulation (Fig. 1).

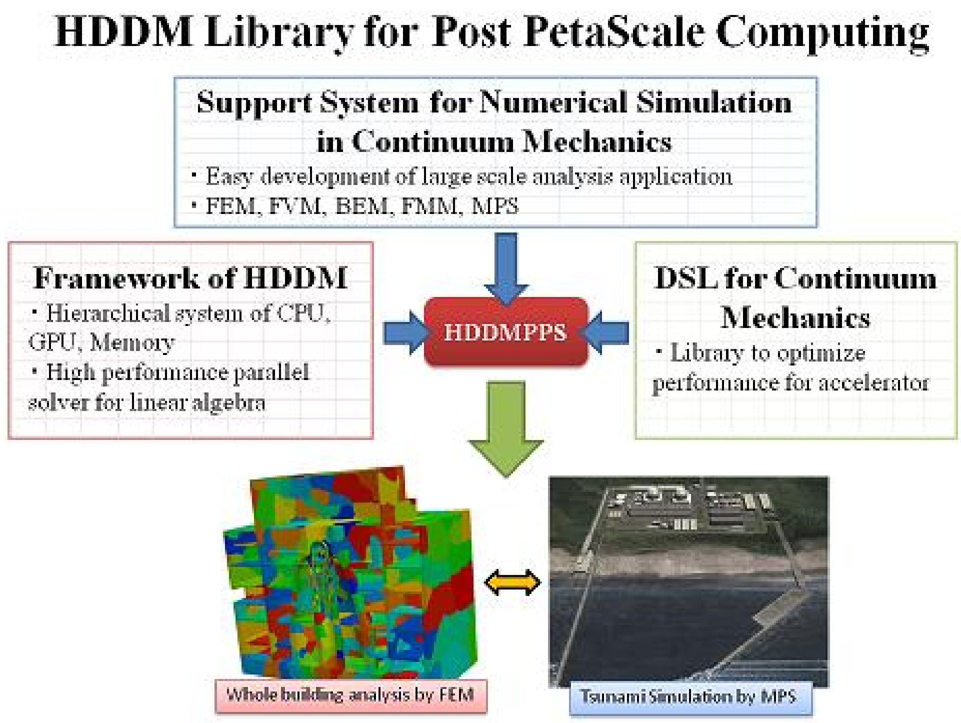

Fig.1: HDDM Library for Post Petascale Computing.

1. Overview of ADVENTURE SYSTEM

Various general-purpose computational mechanics systems have been developed in the last three decades to quantitatively evaluate mechanical / physical phenomena such as deformation of solid, heat transfer, fluid flow and electromagnetics. Nowadays such systems are regarded as infrastructural tools for the present industrialized society. The existing systems, however, cannot be used with massively parallel processors (MPPs) with the order of 100-10,000 processing elements (PEs), which are about to dominate the high-performance computing market in this century, as they were developed for single-processor computers, which took leadership an age ago. Neither can the current systems be used in heterogeneous parallel and distributed computing environments such as the Grid. Owing to the fact, they can deal with only medium scale problems with millions degrees of freedom (DOFs) at most.

The ADVENTURE project [3, 4] was one of the research projects in the "Computational Science & Engineering" field selected for the "Research for the Future (RFTF)" Program sponsored by the Japan Society for the Promotion of Science (JSPS) [5] during 1997-2002. The project is continuously going on as an open source software development project. In the project we have been developing an advanced general-purpose computational mechanics system named ADVENTURE since August 1997. The system was designed to be able to analyze a three-dimensional (3D) finite element model of arbitrary shape over 100 million DOF mesh, and additionally to enable parametric and non-parametric shape optimization. The first version of the ADVENTURE system has been released from the project website as open source software since March 2002 [3]. About 1,320 registered users in academia and industries are now using the programs, while one private company has developed and released its commercial version named ADVENTUREcluster [6, 7].

Domain-decomposition-based parallel algorithms are implemented in pre-processes (domain decomposition), main processes (system matrix assembling and solutions) and post-process (visualization), respectively. Especially the hierarchical domain decomposition method with a

preconditioned iterative solver (HDDM) [8-10] is adopted in two of the main modules for solid analysis and thermal conduction analysis, named ADVENTURE_Solid and ADVENTURE_Thermal. The employed pre-conditioner is the Balancing Domain Decomposition (BDD) type method [11-18]. To efficiently solve a coarse space problem derived from equilibrium conditions for singular problems associated with a number of subdomains appeared in the BDD formulation, an incomplete factorization based parallel direct solver is employed. The ADVENTURE_Solid has been successfully implemented on a single PC, PC clusters and supercomputer such as the Earth Simulator or K-computer.
The ADVENTURE system consists of pre-, main- and post-processing modules and design modules that can be used in various kinds of parallel and distributed environments. The system employs HDDM based massively parallel algorithm as one of the major solution algorithms in order to handle a huge-scale finite element model over 100 million DOFs efficiently. The system employs module-based architecture and consists of 19 modules. The pre-process modules include the surface patch generator which converts geometry model data into a collection of triangular surface patch data, named ADVENTURE_TriPatch, a tetrahedral mesh generator [19, 20], i.e. ADVENTURE_TetMesh, an attachment tool of boundary conditions and material properties onto the mesh, i.e. ADVENTURE_BCtool, and a domain decomposer of a finite element model, i.e. ADVENTURE_Metis. The kernels of the ADVENTURE_Metis are a graph partitioning tool METIS and its parallel version ParMETIS developed in the University of Minnesota [21, 22]. The main process modules, i.e. solvers include an implicit elastic-plastic analysis module named ADVENTURE_Solid [9-10, 18] which enables large-deformation and implicit dynamic analyses, a thermal conductive analysis module named ADVENTURE_Thermal, a thermal-fluid analysis module named ADVENTURE_Fluid, a magnetic analysis module named ADVENTURE_Magnetic [23], an explicit impact analysis module named ADVENTURE_Impact, and a rigid plastic analysis module named ADVENTURE_Forge. The post process module named ADVENTURE_Visual is for parallel visualization of analysis results [24]. Common functions related to finite elements are programmed as class libraries named libFEM. Figure 2 shows the configuration of the ADVENTURE modules.

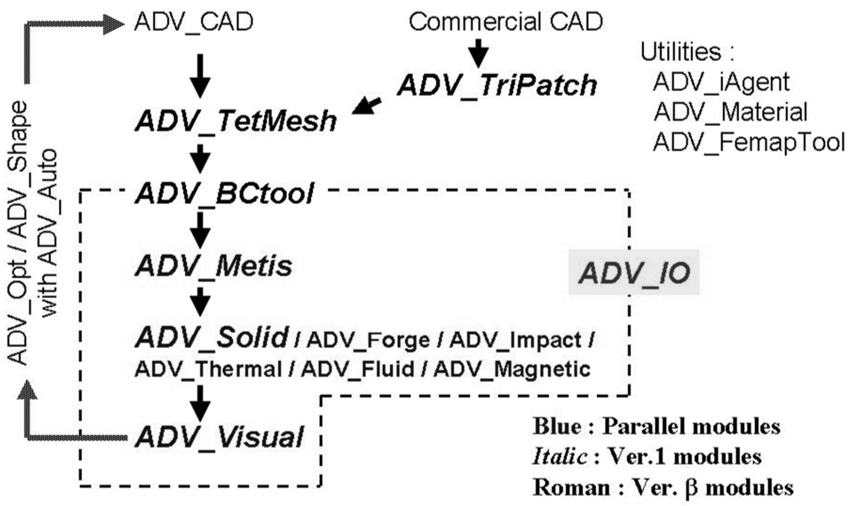

Fig.2: Configuration of ADVENTURE modules.

2. Hardware

A typical modern supercomputer consists of many computational nodes. They are connected each other by high-speed network interconnect. Each computational node holds one or a few processor chips and its associated memory chips, thus forming a distributed memory parallel computer. As a result, both intra-node and inter-node performance are important for the performance design of simulation code. Here in this section, these hardware components are explained briefly.

2.1 Processor and memory

Nowadays, a processor can issue multiple instructions and execute multiple floating point operations for each clock cycle. For example, a pair of multiplication and addition, or a set of multiply-add pairs packed in one SIMD instruction. It is called Instruction-Level Parallelism (ILP). For example, if a processor can handle 8 double precision (DP) floating-point operations per clock, and it runs with 2 GHz, its DP peak performance is 8 x 2 = 16 GFLOPS. In real code, however, it is very likely that only a small portion of these computational resources is utilized. It is so-called "ILP wall" problem, and it is gradually widening the gap between the ideal, peak performance of the hardware and the actual, sustained performance when running real application code on the hardware.

In recent years, the number of cores in a chip had also increased. Here, "core" means "processor" in a traditional sense. Until recently, one processor corresponds to just one chip, or sometimes to multiple chips in case of very complicated processor design. But nowadays, because of Moore's law, one processor chip can hold multiple processors. To avoid ambiguity, the keyword "processor" is renamed to "core". Thus, it is called "multi-core". Currently, a typical scalar processor has 2, 4, 8 or 16 cores in one chip, although there are some "many-core" chips having more than twenty cores. They can be regarded as a shared memory computer in one chip. Either MPI or OpenMP can be used for parallel programming.

Even if the processor can perform multiple operations per clock, in reality, it is no meaning if data cannot be supplied from the memory system into the processor in enough speed. Memory access pattern is the important keyword to understand the performance characteristics of the memory system. Let's imagine the memory access patterns in a loop. It can be sequential, stride or random. In case of random access, actually it may be indirect index access.

Cache memory is very important in the design of modern scalar processors, and it is related to a memory access pattern called data locality. In short, the cache memory is a fast but small special memory region, and it is separated from the main memory. When the processor tries to read a small amount of data from the main memory, the fetched data is once copied into the cache memory automatically. Then, suppose this small data becomes necessary again. If the data still remains on the cache memory, instead of reading the original data again from the slow main memory, it is sufficient to access this copy from the fast cache. This means, it is better to keep using this small amount of data as much as possible. If the size of frequently used data is larger than the size of the cache, however, it doesn't work in this way. While reading it, most of data are kicked out of the cache, and it ends up virtually accessing to the main memory. Thus, the cache mechanism works only if "a relatively small amount of data is accessed repeatedly, repeatedly and repeatedly".

Then, how can we utilize such tricky cache mechanism? There is a well-known technique called blocking or tiling. In cache blocking, a big data region is divided into many small data blocks first. For example, in case of a matrix, it is decomposed into multiple sub-matrices. They look like tiles. Using associated blocking algorithm, once a small block is read from the main memory, it is utilized repeatedly before the next one is needed.

However, if any blocking algorithm cannot be devised, how come? In this case, sadly, you have to directly tackle against the slowness of the main memory. Now, memory bandwidth becomes a serious issue. To consider the memory bandwidth problem, it is useful to understand the keyword, B/F ratio. B/F ratio measures how much data can be read / write from / to the main memory for each execution of floating-point operation. This ratio typically assumes a specific numerical algorithm. If the actual B/F ratio value is no less than the value originally required by the algorithm, it is OK. Otherwise, there is memory bandwidth bottleneck.

The recent rapid growth of the raw computational power of a processor chip in terms of floating point operations, caused by the increase of both the number of processor cores and the number of SIMD ways, has made this memory bandwidth issue more serious and desperate. Thanks to Moore's law, the growth pace of the FP capability is far exceeding that of the memory bandwidth. While each core has its own cache memory (roughly speaking), the path to the main memory is basically shared among all the cores, because it is "shared memory". As a result, only the algorithms which can take advantage of cache mechanism can keep up with the growth of the computational power, while B/F ratio will drop further.

2.2 Network interconnect

In modern supercomputing, distributed memory parallel architecture is the primary hardware architecture. A supercomputer is composed of multiple computational nodes. Each of them has its own memory space. A computational node cannot directly access memory owned by other nodes. Instead, it has to send / receive data to / from others through this high-speed network interconnect.

As the architecture of the network interconnect, nowadays torus or fat tree is utilized for a high-end supercomputer, while for low-end HPC environment like a PC cluster, switching hardware is used. The fat tree can be said to be cascade of switches. On the other hand, in case of the torus architecture, each node has very high bandwidth connection directly, but to only a few neighbouring nodes. To communicate to any node other than these neighbour nodes, data has to be relayed through one or a few intermediate nodes. It is typically used to connect relatively large number of nodes.

To use such a distributed memory parallel computer, care must be taken about communication patterns. Because some of the communication patterns are either inherently efficient or strengthened by additional hardware mechanism, the use of these special patterns should be considered first in the design of parallel software.

Global communication, such as barrier, broadcast and reduce operations are frequently used in various kinds of parallel programs. High-speed interconnect supports those patterns directly in hardware level. Therefore, if these communication patterns are recognized in your code, instead of ordinary send / receive protocol, the corresponding special communication API or directives should be used. They are the only routes to take advantage of the special network hardware mechanism.

On the other hand, neighbour communication is another important pattern. To understand it, let's consider the difference between bus and switch. Suppose there are four nodes, A, B, C and D. In case of the bus architecture, node C and D cannot communicate while node A and B are talking. In case of the switching architecture, however, communication of A-B and C-D can work simultaneously. It can be easily extended to the case of many, many nodes. A-B, C-D, E-F, G-H, and so on. All of them can be invoked at once. Instead, if node A wants to receive data from more than one, for example, node B and C, there will be conflict.

The neighbour communication pattern is very important in case of macro-scale, continuum mechanics-based simulation. In this type of simulation, the whole analysis domain can be decomposed into multiple subdomains. Typically, communication between neighbouring subdomains frequently occurs. It can be represented as the neighbour communication pattern. Thus, well-designed code for the continuum mechanics field can easily scale on a supercomputer.

As for the neighbour communication pattern, it is better to understand the keyword, volume to area ratio. This means the ratio between amount of calculation per subdomain as a volume, and that of the associated interface boundaries as an area. As the problem size grows, this ratio is expected to grow also, because of comparison between volume N^3 and area N^2. That means, the bigger the problem size is, the easier to parallelize. You can always enjoy good parallel efficiency, if you specify the problem size big enough. Of course, there are some issues, too long execution time and lack of memory.

3. Software

In the previous section, the hardware architecture of modern supercomputers is described. It is also necessary to mention about more software-related topics, especially, the software development process and environment of supercomputing applications. In this section, starting from basic programming models, programming languages, compilers, libraries and tools are explained.

3.1 Programming model

To consider the software design for modern supercomputing applications, there are some special programming models. Each model covers a specific HPC hardware architecture. Here, we introduce two important programming models, hybrid parallel and data parallel.

Suppose if a supercomputer is based on multi-core scalar processors, there are two choices in programming models, flat MPI and hybrid parallel. In case of flat MPI, it is just sufficient to re-use your MPI-based code without modification, but you need to set the number of MPI ranks as same as the number of total cores using. On the other hand, the hybrid parallel programming model is needed mainly for two reasons. One is, to obtain the maximum parallel efficiency. The other one is, to utilize processor cores of sub-million order or more.

Theoretically, it is better to utilize OpenMP for intra-node communication, while MPI is used for inter-node one. In reality, it depends on applications and problems. Typical trend is, when the problem size is relatively small while the number of cores used is many, hybrid parallel programming model works well. If the parallel efficiency is already good enough with the current flat MPI implementation, however, the additional gain obtained from the hybrid parallel approach is marginal. In case of domain decomposition-based approaches, because of the volume to area ratio, explained before, the bigger the problem size is, the better the parallel efficiency is also.

On the other hand, if luckily you have a chance to utilize a world-class supercomputer, then unluckily you will be forced to adopt the hybrid parallel programming model, simply because the flat MPI model does not work in this environment. Currently, no MPI implementation seems to work well more than ten thousand MPI processes. The combination of MPI and OpenMP is the only way to utilize millions of cores available on such a top-end supercomputer.

Data parallel programming model, or SIMD, is the programming model useful for GPU, and also for SIMD instruction in modern scalar processors. SIMD is Single Instruction Multiple Data. It usually involves the use of either compiler directives, such as SIMD vectorization and OpenACC, or extension to existing programming languages, such as CUDA and OpenCL. In the former cases, a loop is annotated by compiler directives with additional information necessary to parallelize. In case of CUDA and OpenCL, the loop body of a loop is extracted as a GPU-local routine, which is associated to a thread when running on the GPU.

3.2 Programming language and compiler

To port your simulation code onto a supercomputer, more or less some amount of code modification effort will be required. It typically involves inserting special compiler directives such as vectorization, OpenMP and OpenACC into the code, and calling functions / subroutines of HPC-related libraries such as MPI and BLAS. In the worst case, instead of keep using ordinary programming languages such as Fortran, C and C++, special programming languages dedicated for specific HPC environments might have to be employed, and the code would be re-written completely from scratch.

If the hybrid parallel programming model, explained before, is employed, OpenMP is the primary choice for intra-node parallelization. OpenMP is mainly a set of compiler directives designed for thread-level parallelization on shared memory parallel environment. It fits well on modern multi-core or many-core scalar processors. Programmer specifies OpenMP compiler directives on each loop which can be parallelized. Instead, if your code is relatively simple and also you are lucky, the automatic parallelization capability of compiler may also work well.

Recently, the impact of SIMD instructions is becoming more and more important for the performance design in supercomputing. To utilize the SIMD instructions, there are three ways. One is, of course, directly use assembly language. Most of people, including us, would want to ignore the first choice. Then, the second option is, to use SIMD intrinsic functions / subroutines. Still, this option is very tedious. Therefore, the third option, compiler-driven vectorization, is more practical for the most of programmers.

Compiler-driven vectorization technique for SIMD is very similar to the so-called "vectorization" in the vector supercomputer age. The idea itself has been very simple, inserting compiler directives just before loops which can be vectorised. However, there is one big difference between the current SIMD vectorization (also called, short vectorization) and the old predecessor. While the vector processor can aggressively read / write data from / to main memory, the SIMD mechanism of the modern scalar processor is effective only to data on cache memory. That means, before considering the use of SIMD instructions, first, you need to put your data on cache.

We also need to mention about accelerators. The use of accelerators such as GPU and many-core chip is gradually starting. On these environments, special programming languages or extension to existing languages, such as CUDA and OpenCL, may have to be utilized. Directive-based programming models such as OpenACC, which require much less work, are also becoming available.

3.3 Library

Some HPC-related libraries are available. They may have to be employed into your code if necessary.

Assuming the use of a modern distributed memory parallel supercomputer, for inter-node parallelization, MPI (Message Passing Interface) is the primary choice. It is a message passing-based communication library among computational nodes. In case of macro-scale simulation, domain decomposition is required. Especially in case of unstructured grid or mesh-free / particle, identifying the boundary region between subdomains is a bit complicated task. Instead of this really tedious approach, some people have started using PGAS languages also. Using these special languages, programmer can parallelize code in much similar way as shared memory environments like OpenMP.

In addition, the knowledge of linear algebra is often required. It is very useful if matrix and vector-related libraries are available. Linear algebraic solver and eigenvalue solver libraries are also important.

BLAS (Basic Linear Algebraic Subroutines) is one of the famous libraries for matrix and vector operations in the basic and fundamental level, such as various kinds of vector-vector, matrix-vector and matrix-matrix operations. The scene behind the fact that recently this library becomes very important is, however, because nowadays highly tuned versions of this library prepared by hardware vendors themselves are available. Especially, level-3 BLAS routines, which are related to matrix-matrix operations, are really important. Usually, inside the vendor-provided library, these routines are implemented as cache-aware and SIMD-vectorised. And, by using these optimized routines, high peak ratio can be easily obtained. Although BLAS is designed for dense matrix, recently, its sparse matrix version becomes also available.

As for the linear algebraic solver, variety of libraries is available. LAPACK contains direct solvers for dense and banded matrices [1]. ScaLAPACK is also available for MPI-parallel environments. In case of sparse solvers, some are direct and others are iterative. SuperLU, MUMPS, PARADISO and WSMP are examples of sparse direct solvers, while PETSc is an example of iterative solver libraries.

3.4 Supporting environment and tools

Other than compiler, the most important programming tool for supercomputing is, profiler. This tool can be used to identify hot spot of the code. Finding the hot spot is vital in performance-centric software design, described before. Moreover, the profiler can measure how fast your code runs on the supercomputer. That means, measuring FLOPS values.

4. Design and Implementation of Finite Element Code

The finite element method (FEM) is one of the famous approximation methods for solving partial differential equations. Starting from structural mechanics, it has mainly been applied to macro-scale problems in the continuum mechanics field.

As for the history of FEM on supercomputers, until recently, it used to be just enough to tune only the direct solver part of the FE code. With sufficiently large problem size, either band or skyline solver can be easily vectorised on vector processor, or parallelized on shared memory environment.

With the emergence of distributed memory parallel supercomputers, however, things have been drastically changed. Numerical schemes adopted in the applications running on PC cluster and MPP are mainly dominated by either static / implicit time marching schemes using iterative solver as the linear equation solver, or explicit time marching schemes. The whole analysis domain has to be domain-decomposed into multiple subdomains. The use of sparse direct solvers on such a distributed memory parallel environment has just begun recently with a relatively limited number of computational nodes.

Here in this section, related to the implementation of FE code on supercomputers, four topics are explained. Starting from element-by-element (EBE) approaches, some issues about linear algebraic solver are described, followed by The Domain Decomposition Method (DDM) as a parallel processing scheme. Finally, the issue of pre- and post-processing in supercomputing applications is briefly described.

4.1 Element-by-element (EBE)

Although the typical performance bottleneck, or the hot spot, of a FE code is its linear algebraic solver, the part of forming element-wise matrices and vectors can also be another weak point. In case of an explicit code, this part typically dominates. Even in an implicit or a static code, it can occupy a significant portion of execution time, if non-linearity is strong and stress integration involves relatively heavy calculation, or some of the terms in the weak form are explicitly evaluated. The performance tuning effort of element-by-element (EBE) operations is at least not negligible.

As for the performance optimization of the EBE routines, it is easy to parallelize them. Because they are namely element-by-element operations, each of them can be done

independently. The granularity of parallelization can be any, because there will be millions, or perhaps billions of elements to be processed.
In addition to parallelization, what else? Intra-core optimization remains. For example, SIMD vectorization. Assuming that there is no major IF/THEN branch in forming an element-wise value, evaluation of this quantity in multiple elements or multiple integration points in an element can be performed not only in parallel, but also in exactly the same way. This fact naturally leads to SIMD. SIMD / short vectorization can be applied. SIMD implementation on GPU is also possible if a sufficient number of elements, for example, thousands or more, can be allocated in each GPU.

4.2 Linear algebraic solver

Unless the scheme of your FE code is purely explicit, it is necessary to prepare a linear algebraic solver to handle the matrix equation [A] {x} = {b}. The matrix [A] may be represented as band, skyline or sparse. Here, sparse means storing only non-zero components in a certain way, such as CRS (Compressed Row Storage) format or block CRS one.
If no iterative solver can be employed to solve the linear equation, because the matrix [A] is highly ill-conditioned or some other reasons, direct solver is the only choice. In this case, however, you'd better give up using a supercomputer. Even a small-scale PC cluster may have difficulty in scaling, unless the problem size is really huge. Currently, it can be said that it is very difficult or even impossible for direct solver to take advantage of distributed memory parallel architecture. As for a typical modern supercomputer with hundreds or thousands of computational nodes, either implicit code employing iterative solver or explicit code using EBE operations predominantly is the choice.

It can be said that iterative solver works fine on massively parallel environment, if domain decomposition is properly performed [2]. At least, the matrix-vector product, which is the main body of iterative solver, can be easily parallelized on any parallel environment, from SIMD, share memory to MPP. However, this is the case without pre-conditioner. In some problems, without efficient pre-conditioner, the convergence ratio is very bad. Then, the question is, are there any parallel pre-conditioners available? Currently, not so many pre-conditioners are ready. It is because, the stronger and the more effective the pre-conditioner is, the more it looks like a kind of direct solver. As we explained just before, it is very difficult to parallelize direct solver. Currently, finding a good parallel pre-conditioner is on-going challenge in this research field. Some parallel pre-conditioners based on hierarchical domain decomposition, in a similar way as that of sparse direct solver, are available. Also, multi-grid approaches are effective. Either geometrical multi-grid or algebraic multi-grid (AMG) solver may be used. The third way is, domain decomposition method (DDM), described in the next section.

4.3 Domain decomposition method (DDM)

The domain decomposition method (DDM) is a way to solve partial differential equation, by solving each subdomain problem separately [3]. The solution of each subdomain problem requires assumed boundary condition. With the repetition of this process, this, initially assumed boundary condition along subdomain interface gradually converges to the true one. In this sense, it is a kind of iterative method. DDM is inherently parallel, because each subdomain local problem can be solved independently [4] [5]. To solve the subdomain local problem, either iterative or direct solver may be used.
Anyway, DDM is different from just decomposing a mesh into multiple subdomains. This type of domain decomposition reduces the communication cost in matrix-vector product operations, which is typically found in parallel iterative solver and explicit code. Instead, DDM is an independent numerical scheme originated from the mathematical field of partial

differential equation. Sometimes, it is also called as Schur complement method or iterative sub-structuring method in the field of iterative solver.

DDM is a kind of hybrid method between iterative solver and direct one. The global view of DDM is iterative, and pre-conditioner may be required in the similar way as the case of iterative solver. Coarse grid solver is typically employed as pre-conditioner. In this case, the coarse grid is derived from the graph structure of domain decomposition itself, and it can be said to be a kind of two grid version in multi-grid solver. To solve the coarse problem and the subdomain local problems, direct solver may also be utilized.

4.4 Pre- and post-processing: where and how?

When a supercomputer is employed to solve a huge-scale problem, its input and output data, namely, the mesh and the result data of such a huge-scale analysis can also be very huge. Then, the pre- and post-processing becomes a critical issue.

The mesh generator might have to be ported onto the supercomputer side. That means, it also has to be fully parallelized. Unfortunately, the development of highly parallel automatic mesh generator is still the on-going research topic. To overcome the issue, instead, mesh refiner may be utilized [6]. This tool simply refines the given initial mesh into half. Speaking more exactly, in case of 3-D solid / volume element, each element is divided into 8 elements, by adding a mid-node on each edge. One step refinement increases the number of elements 8 times. Uniform mesh refinement itself can be easily parallelized. Because the refiner can be invoked on the supercomputer, it is sufficient to create an initial coarse mesh on your desktop PC and send it to the supercomputer through slow network.

About the visualization of the result data, however, things are more complicated. One obvious answer is, generate images and movie data on the supercomputer side [7]. Not only this post-processor simply runs on the supercomputer, it should also be parallelized. Assuming the analysis domain is already decomposed into subdomains, it is possible for each subdomain to generate its own result image independently, and to gather these images and compose a single image, by image convolution techniques. These processes can be parallelized. This software rendering process can be contained as a part of the main analysis process. After a job is completed, you can obtain not only the result data, but also their images and movies. While waiting for the download of the huge result data, you can quickly browse these images and movies.

5. Parallel Algorithms Implemented in ADVENTURE System

One of the key technologies of the ADVENTURE System is the HDDM, which enables parallel finite element calculations on various kinds of computing environments. Basically in the HDDM, force equivalence and continuity conditions among subdomains are satisfied through iterative calculations such as the Conjugate Gradient (CG) method. Therefore it is indispensable to reduce the number of iterations by adopting some appropriate preconditioning technique especially for solving large-scale ill-conditioned problems. The Neumann-Neumann algorithm (N-N) [11] is known as efficient domain decomposition preconditioner for unstructured subdomains. However, its convergence deteriorates with the increasing number of subdomains due to lack of a coarse space problem which takes care of global propagation of error. The Balancing Domain Decomposition (BDD) based N-N algorithm proposed by Mandel [12] shows that the equilibrium conditions for the singular problems on subdomains result in simple and natural construction of a coarse space problem and that its construction is purely algebraic. The BDD has been applied to solve various phenomena [13-15]. There are also several researches on parallelization of the BDD and also the FETI (Finite Element Tearing and Interconnecting) [26-32]. However, most problems solved there are still medium scale ones such as sub-millions to one million DOFs. As the DOFs of the coarse space problem is directly related to the number of subdomains, it is indispensable to consider the parallelization of the solution process of the coarse space problem as well when solving large-scale problems. The Salinas system [33], which employed the FETI-DP method [32], is succeeded in solving large-scale problems such as over 100 million DOF mesh of optical shutter model [34]. It shows good performance but does not seem to include load-balancing techniques. In the present study, an incomplete parallel direct method and the HDDM are adopted.

5.1 Hierarchical Domain Decomposition Method (HDDM)

In Domain Decomposition Methods (DDM), an analysis model, i.e. a finite element mesh with boundary conditions and material properties, is subdivided into a number of subdomains. The HDDM employs a hierarchical technique to implement the DDM on various parallel computers. In the HDDM, a group of processing elements (PEs) are subdivided into the following three subgroups: one Grand Parent PE (Grand), several Parent PEs (Parent or Parents), and many Child PEs (Child or Children). At the same time, the analysis model is subdivided into some 'parts' whose number is the same as the number of the Parents. Each part is further subdivided into a number of subdomains, the number of which can be much larger than that of the Children. Figure 3 shows a 35 million DOFs mesh for an Advanced Boiling Water Reactor (ABWR) model, generated by the ADVENTURE_TriPatch and the ADVENTURE_TetMesh. Figure 4 illustrates an example of the hierarchically decomposed mesh generated by the ADVENTURE_Metis.

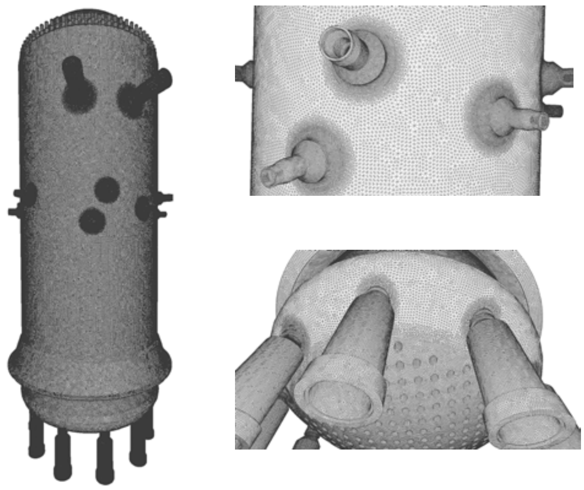

Fig.3: 35 million DOF mesh of ABWR model.

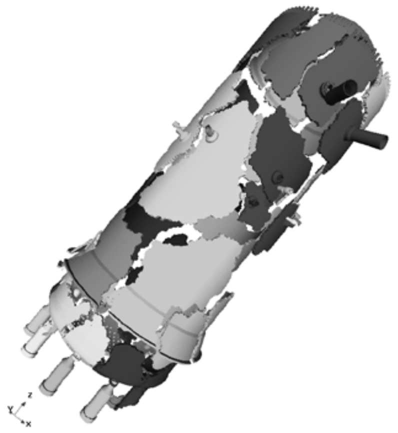

Fig.4: Part decomposition of ABWR vessel model.

Owing to the HDDM algorithm, large-scale analysis data can be easily handled by increasing the number of the Parents. The main roles of the three kinds of processors are summarized as follows. The Grand manages all PEs, i.e. synchronization and calculation of the sum of vectors spread over a number of Children. Each Parent stores mesh data and material properties of subdomains, sends / receives subdomains data to / from Child, and iterates loops of the CG method. Each Child performs finite element calculations of the subdomains received from the Parent, and sends analyzed data back to the Parent. Figure 5 shows the schematic data flow among PEs.

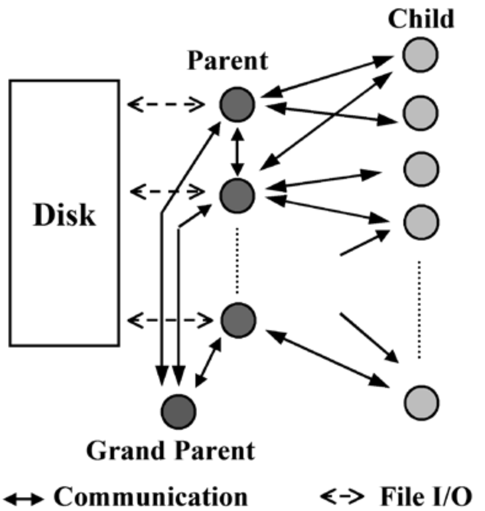

Fig.5: Schematic data flow in h-mode.

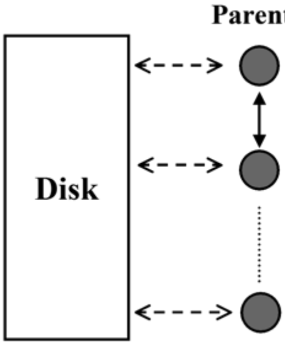

Fig.6: Schematic data flow in p-mode.

According to the design concept of the HDDM, most computation is assigned to the Children, while most communication occurs in between Parents and Children. Varying the number of Parents and Children for different kinds of parallel computers, the present HDDM-based system can easily achieve high performance. In the HDDM architecture, thanks to the dynamic load balancing technique among Child processors, high parallel performance can be achieved even in heterogeneous computer environments. However in this mode, an amount of data communication between Child and Parent tends to be large. To reduce such data communication among Children and Parents, it is useful to assign all balance becomes static. This analysis mode shown in Figure 6 is called in parallel processors mode (p-mode), while the original analysis mode as shown in Figure 5 is named hierarchical processors mode (h-mode).

5.2 Balancing Domain Decomposition (BDD)

The BDD algorithm is based on the DDM with a preconditioned iterative solver. After eliminating interior DOFs of local subdomain matrices, the problem to be solved is reduced onto the interface DOFs of subdomains. The reduced matrix is so-called Schur complement. The reduced problem is also called the interface problem, and is to be solved by a preconditioned iterative method. There are two main methods as such preconditioner, i.e. local subdomain correction and coarse grid correction in a coarse space.

5.3 Performance Optimization of ADVENTURE System

As optimization approaches of structural analysis code, ADVENTURE Solid, one example for The Earth Simulator 2 is described. In this case, we have chosen two approaches. One is to optimize the ADVENTURE Solid code within the range of the existing design, by varying a few selected performance-sensitive parameters. The other is to apply more drastic design changes, such as the local Schur complement approach.

Here, the performance design issues of ADVENTURE Solid are briefly explained. ADVENTURE Solid is based on the hierarchical domain decomposition method (HDDM). In HDDM, a whole analysis domain is subdivided into many small subdomains. The parallelization of ADVENTURE Solid code is primarily based on subdomain-wise FEM calculation. On the FE analysis of each subdomain, a linear system of the subdomain stiffness matrix is solved. A skyline solver is employed for the solution of the relatively small system. In the current version of ADVENTURE Solid, this subdomain-wise skyline solver is identified as a hot spot. The inner-most loop of the hot spot is the double loop in forward and back substitution of the skyline solver. Its loop length, which means the band width of the skyline matrix, is not so large. It is usually about several hundreds.

As for the former approach, we selected average subdomain size of the domain decomposition method as the most performance-sensitive parameter. This parameter controls the effective vector length of inner-most loops of ADVENTURE Solid. By varying the subdomain size parameter in the input data files through the analysis of 245 million DOF Pantheon model, about 15 % of peak performance was achieved. In this case, vector operation ratio was 98.57 %. Using 512 processors, 6.5 T flops was obtained. The analysis of this Pantheon model took 18.6 minutes, using 4.1 TB memory. The number of DDM iterations was 277. Each DDM iteration took 2.48 seconds.

As the latter approach, the local Schur complement (LSC) of each DDM subdomain is explicitly formed. An LSC matrix is a symmetric full matrix. In each DDM iteration, simply a matrix vector product using the LSC is performed for each subdomain. The last year, the performance of this approach itself has already been investigated fully using the extracted hot spot code from ADVENTURE Solid. About 40 % of the peak performance was obtained through the hot spot code. This year, the new LSC-based performance design was verified within the single process code of ADVENTURE Solid. Scalar version of this new LSC implementation achieved about twice faster than the existing implementation using skyline solver for the DDM subdomain local solver on PC. This means the total number of floating point operations, or the number of I/O requests to memory system can be halved by this approach.

5.4 Developing mesh refinement function for ADVENTURE Metis

A mesh refinement function for ADVENTURE_Metis was implemented, since the huge size models must be generated because of the huge analyses in post petascale simulation. We have succeeded to generate the refined mesh models of more than tens-of-billions DOF scales from the coarse mesh models in parallel computers at short times (Fig.7).

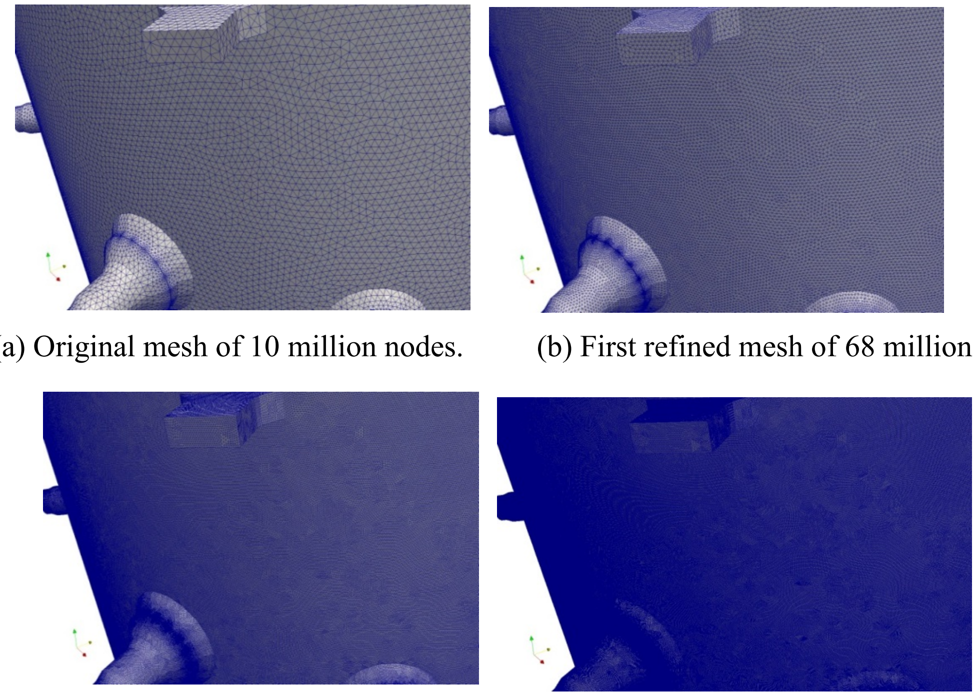

(a) Original mesh of 10 million nodes. (b) First refined mesh of 68 million nodes.

(c) 2nd refined mesh of 480 million nodes. (d) 3rd refined mesh of 3,600 million nodes.

Fig. 7: Refined mesh generating system.

The generated elements by the mesh refinement function can be geometrically fitted on surfaces of CAD models by shape functions of finite element method, as shown in Figure 8. Additionally, to generate mesh model of the same scale size by memory-saving mode using only one CPU, this system can be flexible for computer environment.

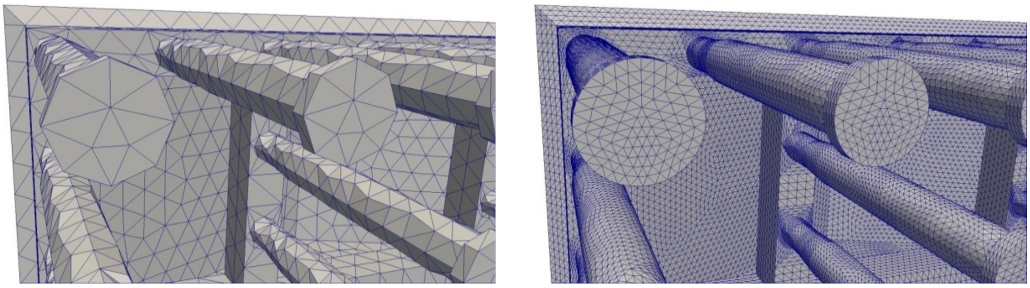

(a) Initial mesh (b) Twice refined mesh by Geometry fitting

Fig. 8: Geometry fitting function.

5.5 Numerical Analysis of Pressure Vessel Model

The ADVENTURE_Solid is implemented on the Earth Simulator (ES) consisting of 256 nodes, i.e. 2,048 PEs with 4TB of main memory, whose theoretical peak performance is 16 TFLOPS. The second problem is an elastostatic stress analysis of a simplified pressure vessel model with 100 million DOFs unstructured mesh. Its mesh size is listed in Table 1. As a boundary condition, the bottom surface of the vessel is fixed, and a static gravitational force is applied to the vessel in the horizontal direction, being similar to the previous problem.

Table 1: Mesh size for a simplified vessel model.

Number of elements	25,084,456
Number of nodes	34,772,634
Total degrees of freedom	104,195,500

Although we do not show convergence histories of relative residual, (1) HDDM with BDD and N-N preconditioner (denoted as BDD) and (2) HDDM with BDD and diagonal-scaling preconditioner (denoted as BDD-DIAG) demonstrate excellent performance in convergence. By considering the performance results, it is concluded here that the diagonal scaling is sufficient as local subdomain correction in the BDD method. The analysis model is divided into 34,816 subdomains and then the number of DOFs of its coarse space is 208,896. The LU factorization of the coarse grid operator is calculated in only 20 seconds. As the result, the present system successfully achieved 5.1TFLOPS, which is 31.8% of the peak performance. The calculation time is only 8.5 minutes. Parallel ratio over 99.9% is achieved, and then parallel efficiency exceeds 80% not only for computation time per iteration but also for total computation time.

Conclusions

We have been developing an advanced general-purpose finite element analysis system, named ADENTURE, which is designed to be able to analyze a model of arbitrary shape over 100 million DOF mesh. The ADVENTURE_Solid has been successfully implemented on a single PC, PC clusters and supercomputers such as K computer.

To perform our systems on the post petascale supercomputers with high efficiencies, we are developing a numerical library based on HDDM [35, 36] that is extended to pre and post processing parts, including mesh generation and visualization of large scale data, for the post petascale simulation.

References

[1] J. J. Dongarra et al., Numerical Linear Algebra for High-Performance Computers, SIAM, 1998.
[2] Y. Saad, Iterative Methods for Sparse Linear Systems, SIAM, 2003.
[3] B. Smith et al., Domain Decomposition: Parallel Multilevel Methods for Elliptical Partial Differential Equations, Cambridge Univ. Press, 2004.
[4] Bhardwaj et al., Salinas: A scalable software for high-performance structural and solid mechanics simulations, Proceedings of SC02, 2002.
[5] M. Ogino, R. Shioya, H. Kawai and S. Yoshimura, Seismic response analysis of full scale nuclear vessel model with ADVENTURE system on the Earth Simulator, J. Earth Simulator, Vol. 2, pp. 41-54, 2005.
[6] K. Murotani, S. Sugimoto, H. Kawai and S. Yoshimura, Hierarchical domain decomposition with parallel mesh refinement for billions-of-DOF-scale finite element analyses, Int. J. Comput. Methods, DOI: 10.1142/S0219876213500618, 2013.
[7] H. Kawai, M. Ogino, R. Shioya and S. Yoshimura, Vectorization of polygon rendering for off-line visualization of a large scale structural analysis with ADVENTURE system on the Earth Simulator, J. Earth Simulator, Vol. 9, pp. 51-63, 2008.

[8] The Top500 List: http://www.top500.org
[9] Gordon E. Moore, Cramming more components onto integrated circuits, Electronics Magazine, Vol. 38, No. 8 (1965).
[10] ADVENUTRE System: http://adventure.sys.t.u-tokyo.ac.jp
[11] S. Yoshimura, R. Shioya, H. Noguchi and T. Miyamura, Advanced general-purpose computational mechanics system for large-scale analysis and design, Journal of Computational and Applied Mathe-matics, Vol. 49 (2002) 279-296.
[12] Report on Computational Science and Engineering, JSPS-RFTF Program 2001-2002, (2002).
[13] M. Suzuki, H. Akiba, S. Yoshimura and G. Yagawa, Analysis of stress intensity factor of piping using large scale analysis code AD-VentureCluster, Trans. 16th SMiRT, G05/5, Washington D.C., CD-ROM, (2001).
[14] M. Suzuki, T. Ohyama, H. Akiba, H. Noguchi and S. Yoshimura, Development of fast and robust parallel coarse-grid based CG solver for large scale finite element analyses, Trans. JSME, 68A-671 (2002) 1010-1017 (in Japanese).
[15] G.Yagawa and R.Shioya, Parallel finite elements on a massively parallel computer with domain decomposition, Computing Systems in Engineering, 4 (1994) 495-503.
[16] R.Shioya and G.Yagawa, Parallel finite elements of ten-million DOFs based on domain decomposition method, WCCM IV Computa-tional Mechanics -New Trends and Applications- IV 11 (1998) 1-12.
[17] T. Miyamura, H. Noguchi, R. Shioya, S. Yoshimura and G. Ya-gawa, Elastic-plastic analysis of nuclear structures with millions of DOFs using the hierarchical domain decomposition method, Nuclear Engineering & Design, 212 (2002) 335-355.
[18] Y. H. DeRoeck and P. LeTallec, Analysis and test of a local domain decomposition preconditioner, 4th International Symposium on Do-main Decomposition Methods (1991) 112-128.
[19] J. Mandel, Balancing domain decomposition, Communications on Numerical Methods in Engineering, 9 (1993) 233-241.
[20] P. LeTallec and M. Vidrascu, Generalized Neumann-Neumann preconditioners for iterative substructuring, 9th International Sympo-sium on Domain Decomposition Methods, (1996) 413-425.
[21] P. LeTallec, J. Mandel and M. Vidrascu, A Neumann-Neumann domain decomposition algorithm for solving plate and shell problems, SIAM J. Number. Math., 35 (1997) 836-867.
[22] J. Mandel and C. R. Dohrmann, Convergence of a balancing do-main decomposition by constraints and energy minimization, Numer. Lin. Alg..
[23] R. Shioya, H. Kanayama, D. Tagami and M. Ogino, 3D large scale structural analysis using a balancing domain decomposition method, Trans. JSCES, 2 (2000) 139-144 (in Japanese).
[24] R. Shioya, M. Ogino, H. Kanayama and D.Tagami, Large scale finite element analysis with a balancing domain decomposition method, Key Engineering Materials, 243-244 (2003) 21-26.
[25] T. Miyamura and S. Yoshimura, Parallel stress analyses of ancient architecture Pantheon on PC cluster, Trans. Architectural Institute of Japan, 55 (2001) 95-102 (in Japanese).
[26] G. Yagawa, S. Yoshimura and K. Nakao, Automatic mesh generation of complex geometries based on fuzzy knowledge processing and computational geometry, Integrated Computer-Aided Engineering 2 (1995) 265-280.

[27] S. Yoshimura, H. Nitta, G. Yagawa and H. Akiba, Parallel auto-matic mesh generation of nuclear structures with ten-million nodes, Trans. 15th SMiRT, Seoul, II (1999) 21-28.
[28] G. Karypis and V. Kumar, Multilevel k-way partitioning scheme for irregular graphs, Technical Report TR 95-064, Department of Computer Science, University of Minnesota, (1995).
[29] G. Karypis and V. Kumar, Parallel multilevel k-way partitioning scheme for irregular graphs, Technical Report TR 96-036, Department of Computer Science, University of Minnesota, (1996).
[30] H. Kanayama, R. Shioya, D. Tagami and M. Saito, Numerical analysis of 3D eddy current problems by the hierarchical domain de-composition method, Trans. JSCES, 3 (2001) 151-156 (in Japanese).
[31] S. Shoui, S. Yoshimura, H. Akiba, T. Ohyama and G. Yagawa, Parallel visualization of finite element solutions with ten million DOFs using PC cluster, Proceedings of European Congress on Computational Methods in Science and Engineering (ECCOMAS2000), Balcelona, CD-ROM, (2000)
[32] http://www.es.jamstec.go.jp/
[33] M. Vidrascu, Remarks on the implementation of the generalized neumann-neumann algorithm, 11th International Conference on Do-main Decomposition Methods, (1998) 485-493.
[34] P. R. Amestoy, I. S. Duff, J. -Y. L'Excellent and P. Plechac, PARASOL. An Integrated programming environment for parallel sparse matrix solvers, High-Performance Computing, (1999) 79-90.
[35] J.-M. Cross, A preconditioner for the Shur complement domain decomposition method, 14th International Conference on Domain Decomposition Methods (2002)
[36] P. Goldfeld, Balancing Neumann-Neumann for (in)compressible linear elasticity and (generalized) stokes-parallel implementation, 14th International Conference on Domain Decomposition Methods, (2002)
[37] F.-X. Roux and C. Farhat, Parallel implementation of the two-level FETI method, 9th International Conference on Domain Decomposition Methods, (1997)
[38] J. Mandel, R. Tezaur and C. Farhat, A scalable substructuring method by lagrange multipliers for plate bending problems, SIAM Journal of Numerical Analysis, 36 (1999) 1370-1391.
[39] M. Lesoinne and K. Pierson, FETI-DP : An efficient, scalable and unified dual-primal FETI method, 12th International Conference on Domain Decomposition Methods, (1999) 421-428.
[40] http://endo.sandia.gov/9234/salinas
[41] M. Bhardwaj, K. Pierson, G. Reese, T. Walsh, D. Day, K. Alvin, J. Peery, C. Farhat and M. Lesoinne, Salinas : A scalable software for high-performance structural and solid mechanics simulations, Technical Papers of SC2002, (2002).
[42] H. Kawai, M. Ogino, R. Shioya and S. Yoshimura, Large Scale Elasto-Plastic Analysis Using Domain Decomposition Method Optimized for Multi-core CPU Architecture, Key Eng. Materials, 462-463 (2011) 605-610.
[43] M. Ogino, R. Shioya, A Scalable and High Performance Implementation of the Domain Decomposition Method, The 4th International Conference on Computational Methods (ICCM2012), 160.pdf, (2012) 1-8.

Large-Scale Numerical Simulation of Water Splash by Particle Method

†Masao Yokoyama[1], Genki Yagawa[2]

Abstract

Numerical simulation of water splash, which is one of the free surface flows, was performed using the high-performance Moving Particle Simulation (MPS) method.
The MPS method is an effective method for calculating fluid with free surface, but the conventional simulation results of splash have not been sufficiently expressed and compared with experimental results. This is because the model of the interaction force between water particles and solid particles was insufficient. Therefore, we performed a highly accurate calculation using the MPS method and validated the models for expressing the slip effect and interfacial tension. The numerical simulation of the splash by falling solid sphere, milk-crown, and water drip spilling from the edge of the cup were carried out. The obtained simulation results of splash are in much better agreement with the experimental results than the conventional results. This indicates the appropriateness of our proposed approach.

Keywords: Splash, Milk crown, Water drip, Surface condition, High-performance computing, Moving Particle Simulation method.

Introduction

In our daily lives, we often see many splash phenomena such as droplets on a puddle during the rain, sea spray by an advancing ship or splash when a frog plunges into a pond. The earliest research on splash form was done by Worthington in 1882 [1], who noted that the form of a splash made by a plunging sphere depends on the surface roughness or wetness of the sphere. Among the various splash phenomena, the milk drop coronet seems to be an interesting fluid phenomenon, which occurs when a droplet of milk falls into a tank filled with milk, producing a beautiful shape that has attracted many researchers (Peregrine[2]). This "milk crown" phenomenon was first filmed by Harold Edgerton in the 1930s (Deegan et al.[3]).

In the field of numerical simulation, splash simulation is often performed as a typical example of Fluid–Structure Interaction (FSI). On the other hand, the sloshing problem is taken as another important issue of FSI (Manservisi and Scardovelli[4]). Rebouillat et al.[5] performed a comparative simulation of liquid splashing in a container and the wall adhesion of a droplet using the finite-element, finite-difference, and smoothed-particle hydrodynamics (SPH) methods (Saksono and Perić[6], Angeles et al.[7]).

In the research on preventing natural disasters, the coupled problems of alluvion and floating object (Koshizuka et al.[8]) and the destruction of a structure by tsunami or flood (Kanamori, et al.[9], Mader[10], Imamura[11]) are very significant issues.

One of the earliest numerical simulation in splash studies was that of the collision of a drop using the Marker-and-Cell method by Harlow and Shannon[12].

Subsequently, more results were published, including simulation with a falling square object (Idelsohn et al.[13]) and the drop simulation considering the wetness using the contact angle by the phase-field method (Do-Quang and Amberg[14]).

A splash on a plate was simulated by the volume of fluid (Yokoi et al.[15], Pasandideh-Fard[16]), Lattice Boltzmann (Tanaka et al.[17]), and moving particle simulation (MPS) methods (Xie et al.[18]). The relation between the impact velocity of a drop and tip number of the tip of the crown splash, called the splash finger, was simulated (Bussmann et al.[19]) and that between the depth of a liquid film and height of a splash was revealed through the SPH method (Nishio et al.[20]).

The accuracy of the splash simulations of a drop improved with the introduction of surface tension or wetness (Nomura et al.[21], Caboussat[22], Alam et al.[23]). However, the details of the splash are yet to be well calculated because the treatment of surface conditions or the surface tension of an object is insufficient.

The splash patterns strongly depend on the surface conditions of a solid object such as hydrogel or acrylic resin (Yokoyama et al.[24]). For this problem, we proposed a model for splash calculation considering the slip condition or electric condition of the surface of a falling object.

In this paper, we discuss the modeling of surface condition and splash simulation by a falling object, the high accuracy calculation of milk crown by large-scale parallel computing, and the simulation of water dripping from the edge of a cup or dish.

Governing equations and particle method by high-performance computing

Here, we describe the outline of the method of discretizing the Navier–Stokes equation by the MPS method. In this study, we simulate the 3D Navier–Stokes equation as shown in Eq.1 using the Explicit Moving Particle Simulation (EMPS) method (Murotani et al.[25]).

$$\frac{D\vec{u}}{Dt} = -\frac{1}{\rho}\nabla P + \nu\nabla^2\vec{u} + \vec{F} \quad (1)$$

Here, ρ is the density of the fluid, P is pressure, v is the kinematic viscosity, and vector u is the velocity of flow. F is an external force term, including gravity G and surface tension T that will be described later.

For calculating the step k+1, u*, which is intermediate velocity, is explicitly calculated from viscosity and the external force in the Navier-Stokes equation except for the pressure as follows:

$$\vec{u}^* = \vec{u}^k + \Delta t\left(\nu\left[\nabla^2\vec{u}\right]^k + \vec{F}\right) \quad (2)$$

where the vector u^k is velocity at step k, and Δt is time step.

The EMPS method differs from the conventional MPS method because when solving pressure P using the former method, the Poisson's equation is not solved implicitly. Instead, pressure P_i for each particle is calculated using Eq. 3, and the correction velocity u' in Eq.4 is calculated using the pressure gradient, which differs from the previous MPS.

$$P_i = c^2\rho^0\frac{n_i - n^0}{n^0} \quad (3)$$

$$\vec{u}'_i = -\frac{\Delta t}{\rho}\left[\nabla P_i\right]^{k+1} \quad (4)$$

Here, ρ^0 is the initial density of liquid particle, n_i is the particle density for particle number i, and n_0 is the particle density for the initial allocation. c is a parameter, which is determined as the Courant condition is satisfied (Oochi et al.[26]).

Then, u' is added to u*, then the velocity u at step k+1 is obtained as follows:

$$\vec{u}^{k+1} = \vec{u}^* + \vec{u}' \quad (5)$$

Moreover, the splash is a physical phenomenon in which the surface tension is dominant. Therefore, in this study, we adopted a surface tension model using the potential force between particles (Kondou et al.[27]).

$$\vec{f}_{ij} = -\frac{\partial\Phi}{\partial r_{ij}}\frac{\vec{r}_{ij}}{r_{ij}} \quad (6)$$

Here, Φ represents the potential energy, and $f_{ij,}$ is the potential force acting from particle j to particle i in radius r_s (valid radius when calculating surface tension). For $r_{s,}$ here, we used the 2.6 r_0 (initial particle distance) used by Kondou et al.[27]. For the external force F in Eq.1, the force acting on particle i is the sum of the potential force from peripheral particle j,

$$\vec{T}_i = \sum_{j\,in\,r_s}\vec{f}_{ij} \quad (7)$$

The potential energy is calculated as

$$\Phi(r_{ij}) = C\phi(r_{ij}) \tag{8}$$

$$\phi(r_{ij}) = \begin{cases} -\frac{1}{3}(r_{ij} - \frac{3}{2}r_0 + \frac{1}{2}r_s)(r_{ij} - r_s) & (r_{ij} < r_s) \\ 0 & (r_{ij} >= r_s) \end{cases} \tag{9}$$

Here, C is the adjusted value.

The computer used for the simulation was a Fujitsu PRIMEHPC FX100 from Nagoya University, with the following specifications:

Processor name: Fujitsu SPARC64 XIfx
Clock Rate: 2.2 (GHz)
Cores/CPU: 32
The Number of Nodes: 2,880

For the method of domain decomposition with parallel computing, we used a two-level hierarchical domain decomposition.

Surface condition for different material

In this section, the numerical simulation of splash considering a surface condition is described.

Effect of surface condition of object on splash's form

When simulating the splashes by a solid object plunging into the water, the major issue is how to model the properties of the wall of the object. The wall is usually assumed in numerical simulations so that the water does not permeate into the object, and the boundary condition between the object and the water is no-slip. It is well recognized that the above assumptions cannot distinguish the qualities of the surface of the iron and those of the skin of an animal in the water. In other words, the simulated pattern of the splash by the hydrogel object and that by the acrylic resin object becomes the same.

The importance of consideration of the surface properties in the splash formation can be seen in the experimental results as shown in Fig. 1. Fig. 1 A shows the crown-type splash generated by a hydrophilic object (hydrogel), and Fig. 1 B shows the column-type splash generated by an object of weaker hydrophilicity (acrylic resin). These figures show that the splash patterns strongly depend on the surface conditions of the objects.

To calculate the splash, the large geometry change of the free surface of water needs to be solved. However, past research works have ignored surface properties related to different materials, so the effects of a surface on the splash formation remain to be clarified.

In this section, we describe the effect of the surface condition of an object and propose a method distinguishing the difference in materials in the particle method.

The purpose of the present paper is

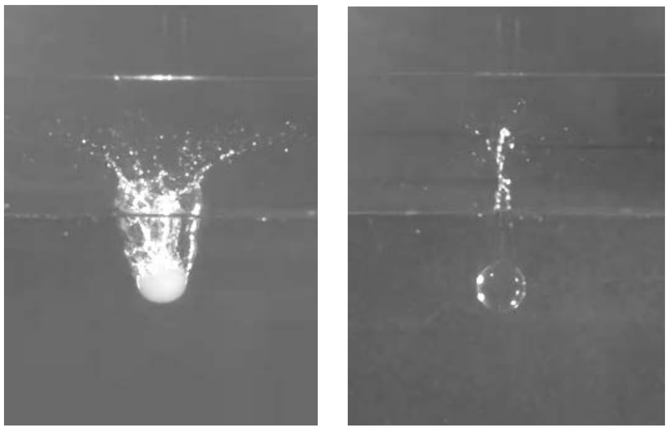

(A) Hydrogel (Agar) (B) Acrylic resin

Figure 1. Comparison of splash patterns between hydrogel and acrylic resin (Radius of sphere=10 mm and Impact velocity=2.21 m/sec).

to discuss the effects of the difference in surface conditions when we solve a splash caused by a sphere diving into water with the particle method. The proposed method describes the wall conditions, considering the effect of the slip such as hydrophilicity and the attractive force or electrostatic force.

Surface condition and slip ratio

We show here how we can introduce the influence of the slippery wall seen, for example, in the case of the skin of a frog into the calculation in a heuristic manner. We take a diving sphere made of agar as the hydrophilic material, which consists of cross-linked structure by polymer called agarose, and plenty of water molecules between the polymer structures to make the solid surface slippery. The velocity distribution of water flow near the surface of the acrylic-resin versus that of the agar-gel is called "slip ratio." Here, the slip ratio α is defined as follows,

$$\alpha = \tau' / \tau \qquad (10)$$

where τ is the wall shear stress under the no-slip condition, and τ' is the wall shear stress under the slippery condition. The wall shear stresses are obtained experimentally from the flow velocity near the wall as follows:

$$\tau = \mu \frac{du}{dy}\Big|_{y=0} \qquad (11)$$

where μ is the kinematic viscosity, and u the flow velocity. Figure 2 shows the experimental relations between the swelling ratio S and the slip ratio α for the agar-gel and the carrageenan-gel, respectively, where the swelling ratio S is defined as follows [20]:

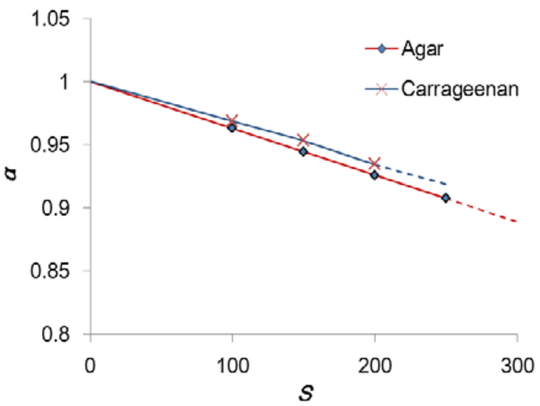

Figure 2. Relationship of swelling degree *S* and slip ratio *α*.

$$S = (m_{\mathrm{water}} + m_{\mathrm{gel}}) / m_{\mathrm{gel}} \qquad (12)$$

where m_{water} is the mass of the water, and m_{gel} is the mass of the solid gel. S increases with the amount of the water contained in the solid gel. Agar employed in this study is a kind of hydrogel. Figure 2 suggests that α can be expressed as:

$$\alpha = 1 - \beta S \qquad (13)$$

where β is a constant value estimated to be 1.2×10^{-3} in the case of the agar. This relation indicates that larger S gives more slip on the surface.

The above relation is taken into consideration in the vicinity of the solid wall in the viscous term of the Navier-Stokes equation. Since the shear force acting between the wall and the fluid is presumed to be directly related to the viscosity term of the Navier-Stokes equation, we modified the discretized form of the viscosity term as follows:

$$\nabla^2 u = \frac{2d}{\lambda n^0} \sum_{i \neq j} \left[(u_j - u_i) \kappa_H (|\vec{r}_j - \vec{r}_i|) \right] \tag{14}$$

with

$$\kappa_H(r) = \alpha \kappa(r) \tag{15}$$

where i denotes the water particles near the hydrogel wall, and j denotes the surface particles of the hydrogel wall. α is set effective only near the hydrogel wall because the effect of the slip is important only near this area.

Validation – comparison with experimental result

The comparison of the MPS simulation result with S = 100 and the experimental one is shown in Fig. 3, where the radius of the sphere R is 10 mm, and the sphere is dropped from the height h = 50R in both the simulation and experiment. The left hand side of Fig.3 shows the simulation result (top) and the snap-shot of the experiment (bottom) at t = 0.02 second after the sphere touches the surface of the water, respectively. On the other hand, the figures on the right hand side are those at t = 0.03 second. The first splash, which is observed just after the hydrogel sphere is dropped into water, is called the primary splash. It is noted that the patterns of the crown-type splash and the air cavity by the present simulation are similar to the experimental ones and that the above crown-type form and the occurrence of the air cavity are not seen in the case of the acrylic resin sphere.

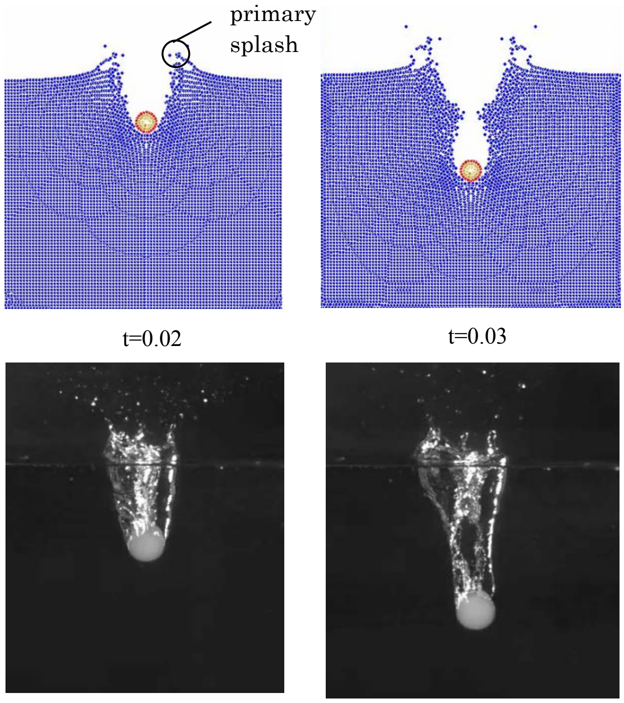

Figure 3. Crown-type-splash of hydrogel (S = 100) by experiment and simulation, where primary splash (t=0.02) and air cavity (t=0.03) are shown.

Figure 4 shows the crown-type splashes and the representative path trajectories of particles for the different swelling ratios. The blue solid lines are the path trajectories of particles when S is 50 or α = 0.94, whereas the red lines are those when S is 350 or α = 0.7. It is seen from the figure that the splashes spread widely with a larger value of S or α, or the velocity of the water near the wall is larger with the swelling ratio, which causes the earlier exfoliation, creating the wider primary splash.

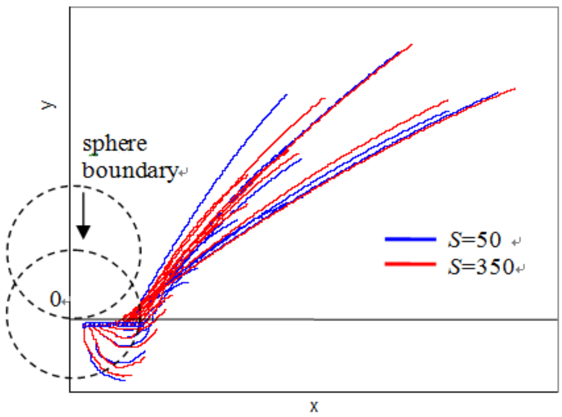

Figure 4. Path lines of a virtual water particle near the impact point hydrogel sphere plunging, during T = 0 to 0.045sec. The particles started from the surface of water at x = 0 to R. Blue line: S = 50, Red line: S = 350. The particle of S = 350 moved wider than that of S = 50.

Simulation of splash in 3D

We performed the large-scale simulation using the distributed memory parallel computers, employing the two-level domain decomposition (Yagawa and Shioya[28]). The first level domain decomposition is performed in order to keep the balance in the number of particles among nodes, and the second level domain decomposition is performed in order to keep the balance in the number of particles among the threads in each node.

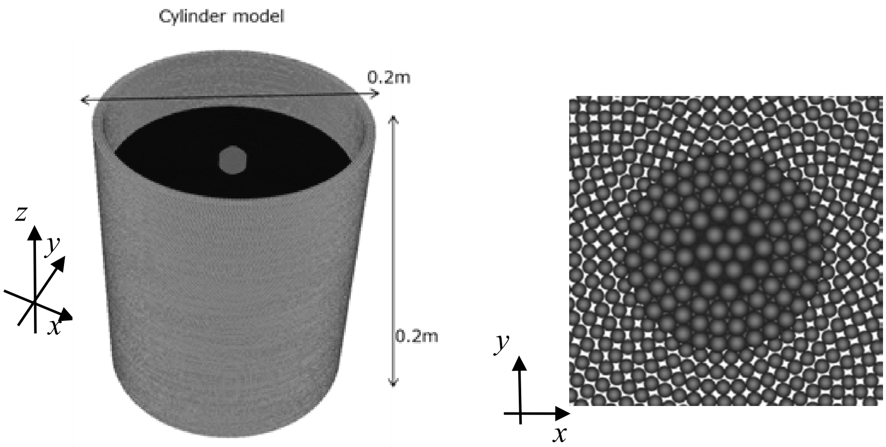

Figure 5. Analysis domain for 3D splash simulation (left figure) and arrangement of particles of hydrogel sphere and water viewed from the top (right figure). Figure 6.

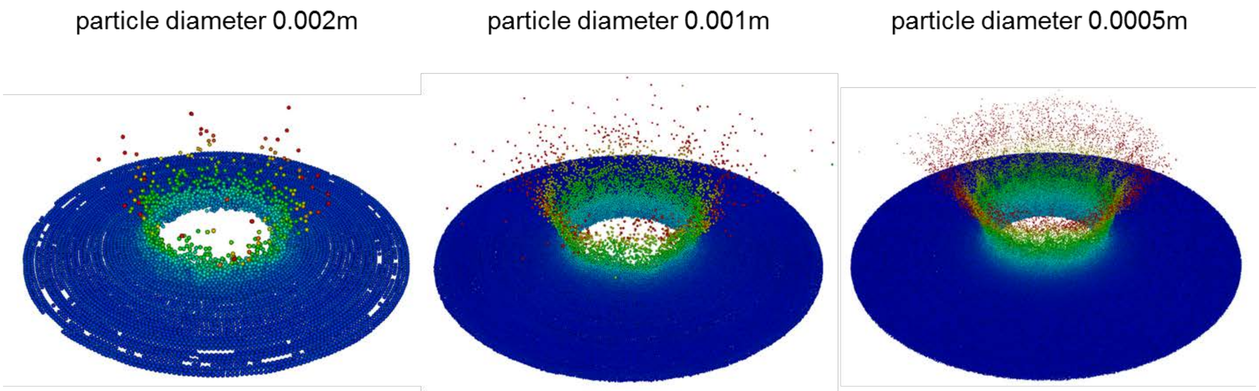

Figure 6. Comparison of splash patterns with the different initial distances of water particles l_0 (S = 100, r_e=4.1 and t=0.03 sec.)

Figure 5 shows the simulation setup for splash by a ball. The initial locations of particles are arranged concentrically, and the water tank is a circular cylinder. Figure 6 shows the simulation result of our 3D calculation, which is in good agreement with the experimental result as shown in Fig.1, where the crown-type splash, the air cavity and the droplets scattering are expressed well in the condition of particle diameter 0.0005 m. It is observed that the particle diameter, which is described as the initial distance of particle l_0, influences the pattern of the splash. In other words, l_0 becomes smaller and the total number of particles is larger, and hence, the splash pattern is expressed more clearly. But as we could not simulate the finger or the spike in the crown-type splash as seen in the experimental result, we need a larger scale computing.

3D simulation of milk crown by large-scale simulation

The “milk crown” is formed when a milk droplet falls and collides with the surface of the thin milk tank (Fig. 7). We calculated the condition when the spherical droplets with a diameter of 4 mm collided with the milk in a tank having a depth of 1 mm at a speed of 1.71 m/s. The 4 mm sphere was selected as it was the approximate size of the maximum diameter droplet that falls freely through the air. The collision speed of 1.71 m/s was equivalent to falling from a height of 15 cm. The depth of 1 mm was selected to match the experimental result [29]. The property of the fluid was water, with a viscosity of $\nu=1.0\times10^{-6}$ m^2/s, and the coefficient of surface strength C in Eq. 8 was set to 0.02361 N/m, in accordance with Kondou et al.

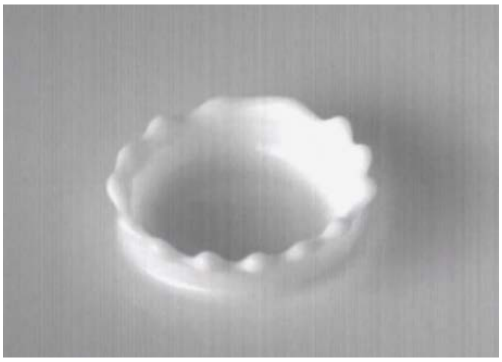

Figure 7. Milk crown by high speed camera. Milk droplet is dropped from 15 cm height.

In order to evaluate the influence of the particle diameter and confirm suitable particle diameter, the particle diameter was changed to 0.2 mm, 0.1 mm, 0.05 mm, and 0.025 mm.

Table 1 Particle spacing and number of particles for calculation

Particle spacing (mm)	Number of particles	Time for calculation	Number of Node (FX100, Nagoya Univ.)
0.2	787,670	0.3 h	12
0.1	4,526,320	2.3 h	24
0.05	29,273,448	12.6 h	96
0.025	208,465,245	53.2 h	384

The number of particles and the number of nodes in the calculation conditions for the respective particle diameters are shown in Table 1. For the particle spacing at 0.2 mm and 0.025 mm, the number of fluid particles was calculated at 7.8 M at 200M, respectively. Fig.8 to Fig.11 show the simulation results with the particle diameters at 0.2 mm, 0.1 mm, 0.05 mm, and 0.025 mm, and the colors in the figures represent the velocity of each particle. The analysis of particle diameters of 0.2 mm in Fig.8 and 0.1 mm in Fig. 9 showed the occurrence of unrealistic phenomena such as holes in the wall of the milk crown because the necessary surface tension to tether the particles was not sufficient. This is because the diameter of the particle is too large, and a sufficient number of particles could not be allocated in the direction of the thickness of crown’s wall.

On the other hand, the simulation result of particle diameter 0.05 mm in Fig.10 and 0.025 mm in Fig.11 shows the successful results in generating milk crowns. From the above results, we should use particles with a diameter of at least 0.1 mm, and if possible, a particle diameter of 0.05 mm should be used.

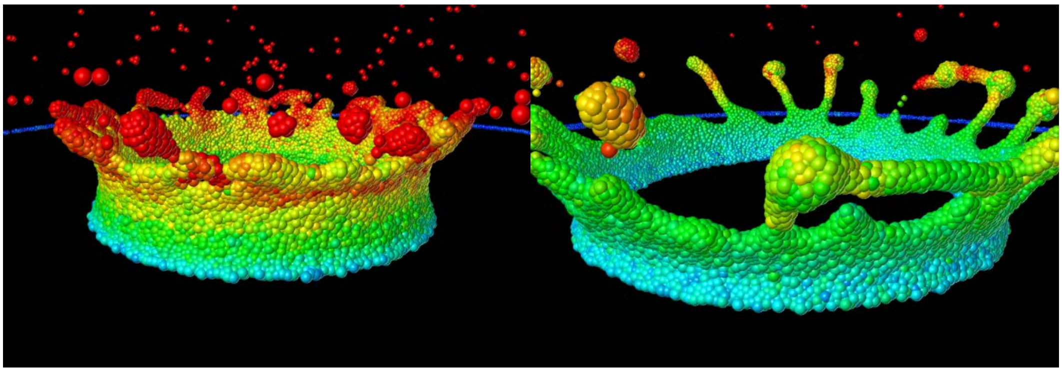

(a) 10 ms (b) 24 ms

Figure 8. Particle Diameter 0.2 mm Analysis

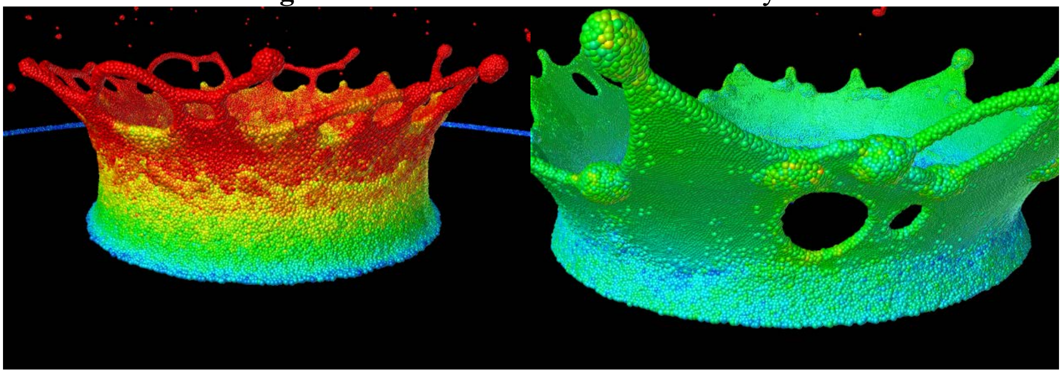

(a) 10 ms (b) 24 ms

Figure 9. Particle Diameter 0.1 mm Analysis

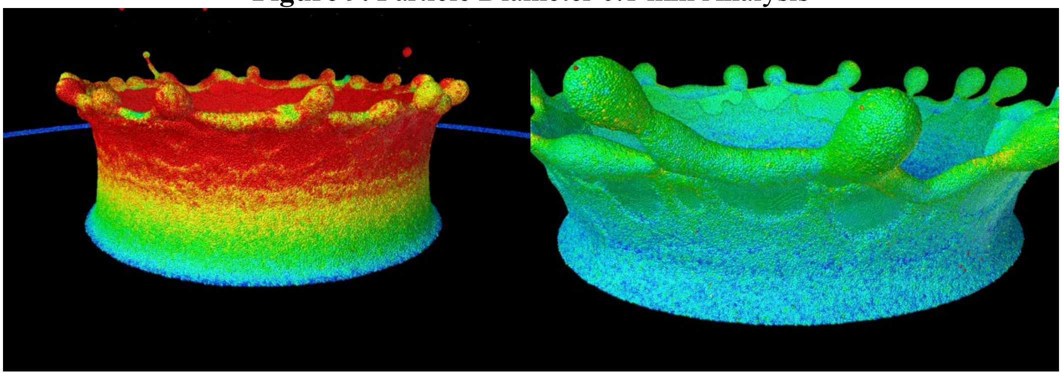

(a) 10 ms (b) 24 ms

Figure 10. Particle Diameter 0.05 mm Analysis

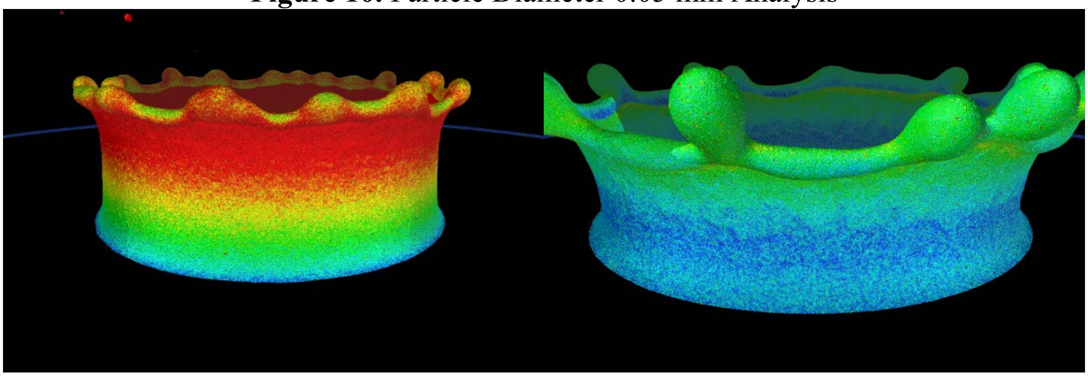

(a) 10 ms (b) 24 ms

Figure 11. Particle diameter 0.025 mm Analysis

Mechanism of water drip

We have stimulated water dripping, which is a phenomenon of droplet, as an issue of FSI.

This phenomenon occurs when we pour water or any other liquid by a cup or pot, causing the adherence of the liquid to the wall of the cup or pot and making them dirty, which is an annoying problem for us.

Therefore, the experimental observation was carried out by recording movies with a high-speed camera, and we observed the flow from the various edges of the cup made using a 3D printer.

Three patterns of the cup, i.e., square edge, circle edge, and 45-degree slope edge, were made of polylactic resin. The experiment was carried out in various settings with the angle of the cup ranging from 0 to 30 degree. The movie was recorded from the beginning of pouring

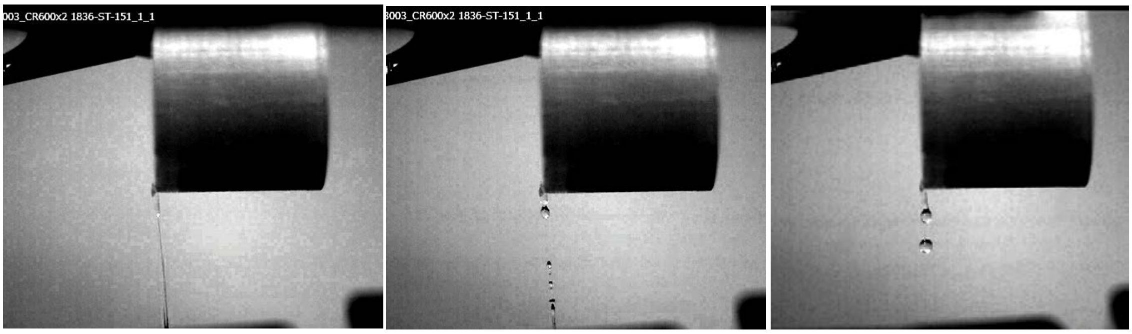

(a) (b) (c)

Figure 12. Experimental result of water drip from square edge of cup

water, which was poured by a pipette at the rate of 3 ml/sec, to the end when the last water dripped. Figure 12 shows the snapshots of water dripping from square edge set at 0 degree. As the droplets are seen on the edge of the cup in Figs. 12 (b) and (c), this indicates the wall of the cup gets dirty by the adhesion.

On the other hand, the simulation result of water dripping is shown in Fig. 13. The contact angle model by Kondo et al. was used as the model of wetness between wall and liquid, and we set the value of contact angle to be 45 degrees in this calculation. In Fig.13, the edge of the cup was square, and the cup was set at 0 degree as in the experiment.

We found some differences between our simulation and experimental results. The distance from the edge to the point where the adhesion of droplet on cup's wall appeared was longer than that in the experimental result, and the flux of water was larger than that of the experimental result.

To improve this disagreement with the experimental result, the calibration of contact angle and flux are needed, and these problems were adjusted.

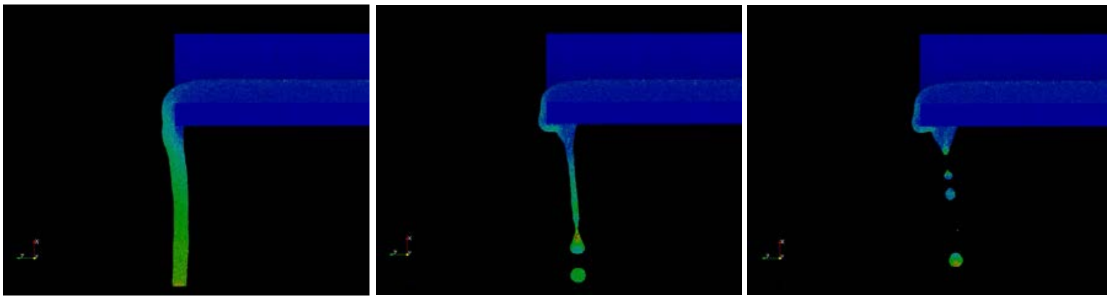

(a) (b) (c)

Figure 13. Simulation result of water drip from square edge of cup

Conclusions

In this study, we performed a large-scale calculation of the splash phenomenon using the MPS method. We focused on the importance of the object's surface properties, such as the slip wall, by hydrophilicity of hydrogel and proposed a new intuitive model using slip ratio to express the splash by an object with slip surface properties. Using our large-scale calculation, the projection of the milk crown and its tips such as spikes could be expressed more precisely. Our simulation result was in good agreement with the experimental result in the form of spike and width of a splash. As one of the FSI problem, the simulation of dripping water from the edge of the cup was carried out, and we showed the simulation result of expressing water adhesion by introducing the wetness model of the wall.

References

[1] Worthington A. M. (1882) On Impact with a Liquid Surface. Proceedings of the Royal Society of London, 34, 217-230.
[2] Peregrine, D. H. (1981) The fascination of fluid mechanics. Journal of Fluid Mechanics, 106, 59-80.
[3] Deegan, R. D, Brunet, P. and Eggers, J. (2008) Complexities of splashing. Nonlinearity, 21(1), C1.
[4] Manservisi S., Scardovelli R. (2009) A variational approach to the contact angle dynamics of spreading droplets. Computers & Fluids, 38, 406-424.
[5] Rebouillat S., Liksonov D. (2010) Fluid–structure interaction in partially filled liquid containers: A comparative review of numerical approaches, Computers & Fluids, 39, 739-746.
[6] Saksono P. H., D. Perić (2006) On finite element modeling of surface tension Variational formulation and applications–Part I: Quasistatic problems, Computational Mechanics, 38(3), 265-281
[7] Angeles J. and Thomson M. (1989) Profile determination of a drop of liquid under surface tension, gravity and centrifugal forces, Computational Mechanics, 4(5), 329-344.
[8] Koshizuka, S., Nobe, A., and Oka, Y. (1998) Numerical analysis of breaking waves using the moving particle semi-implicit method. International Journal for Numerical Methods in Fluids, 26(7), 751-769.

[9] Kanamori H. (1972) Mechanism of tsunami earthquakes. Physics of the earth and planetary interiors, 6(5), 346-359.
[10] Mader C.L. (1973) Numerical simulation of tsunamis. Hawaii Institute of Geophysics, University of Hawaii, 1973.
[11] Imamura F., Goto, K., and Ohkubo S. (2008) A numerical model for the transport of a boulder by tsunami. Journal of Geophysical Research, 113(C1), C01008.
[12] Harlow, F. H. and Shannon, J. P. (2004) The splash of a liquid drop. Journal of Applied Physics, 38(10), 3855-3866.
[13] Idelsohn S.R., Onate E and Pin F.D. (2003) A Lagrangian meshless finite element method applied to fluid structure interaction problems. Computers & Structures 81:655-671.
[14] Do-Quang, M., and Amberg, G. (2009) The splash of a solid sphere impacting on a liquid surface: numerical simulation of the influence of wetting. Physics of Fluids (1994-present), 21(2), 022102.
[15] Yokoi, K., Vadillo, D., Hinch, J. and Hutchings, I. (2009) Numerical studies of the influence of the dynamic contact angle on a droplet impacting on a dry surface. Physics of Fluids (1994-present), 21(7), 072102.
[16] Pasandideh‐Fard, M., Qiao, Y. M., Chandra, S. and Mostaghimi, J. (1996) Capillary effects during droplet impact on a solid surface. Physics of Fluids (1994-present), 8(3), 650-659.
[17] Tanaka Y., Washio Y., Yoshino M. and Hirata T. (2011) Numerical simulation of dynamic behavior of droplet on solid surface by the two-phase lattice Boltzmann method. Computers & Fluids 40, 68-78.
[18] Xie, H., Koshizuka, S. and Oka, Y. (2004) Modelling of a single drop impact onto liquid film using particle method. International journal for numerical methods in fluids, 45(9), 1009-1023.
[19] Bussmann M., Chandra S. and Mostaghimia J. (2000) Modeling the splash of a droplet impacting a solid surface. Physics of fluids, 12, 3121-3132.
[20] Nishio, N., Yamana, K., Yamaguchi, Y., Inaba, T., Kuroda, K., Nakajima, T., Fujimura, H. (2010) Large - scale SPH simulations of droplet impact onto a liquid surface up to the consequent formation of Worthington jet. International journal for numerical methods in fluids, 63(12), 1435-1447.
[21] Nomura K., Koshizuka S., Oka Y., Obata H. (2001) Numerical Analysis of Droplet Breakup Behavior using Particle Method. Journal of Nuclear Science and Technology, 38, 1057-1064.
[22] Caboussat A. (2006) A numerical method for the simulation of free surface flows with surface tension. Computers & Fluids, 35, 1205-1216.
[23] Alam A., Kai H. and Suzuki, H. (2007) Two-dimensional numerical simulation of water splash phenomena with and without surface tension. J Mar Sci Technol, 12, 59-71.
[24] Yokoyama M., Kubota Y., Kikuchi K., Yagawa G. and Mochizuki O. (2014) Some remarks on surface conditions of solid body plunging into water with particle method, Advanced Modeling and Simulation in Engineering Sciences, 1, 9.
[25] Murotani K., Koshizuka S., Tamai T., Shibata K., Mitsume N., Yoshimura S., Tanaka S., Hasegawa K., Nagai E. and Fujisawa T. (2014) Development of Hierarchical Domain Decomposition Explicit MPS Method and Application to Large-scale Tsunami Analysis with Floating Objects, Journal of Advanced Simulation in Science and Engineering (JASSE), October 31, , pp.16-35 .
[26] Oochi, M., Yamada, Y., Koshizuka, S. and Sakai, M. (2011) Validation of Pressure Calculation in Explicit MPS Method Transactions of the Japan Society for Computational Engineering and Science, Vol. 2011, P 20110002.

[27] Kondo, M., Koshizuka, S., Suzuki, K., and Takimoto, M. (2007). Surface tension model using inter-particle force in particle method. In ASME/JSME 2007 5th Joint Fluids Engineering Conference, American Society of Mechanical Engineers, 93-98.
[28] Yagawa G and Shioya R. (1994) Parallel finite elements on a massively parallel computer with domain decomposition, 4, Comput. System Eng. 4, 495-503.
[29] Gunji H., Ishii H., Saitoh A. and Sakai T. (2003) http://www2.nagare.or.jp/mm/2003/gunji/index_ja.htm, The Japan Society of Fluid Mechanics.

Numerical Study of Adhesion Behavior of Sea-Salt Particles on Concrete Bridge Girders

†Jun Tomiyama[1], *Yasushi Nakabayashi[2]

[1]Department of Civil Engineering and Architecture, University of the Ryukyus, Japan.
[2] Department of Information Sciences and Arts, The University of Tokyo, Japan

*Presenting author: jun-t@tec.u-ryukyu.ac.jp
†Corresponding author: nakabayashitoyo.jp

Abstract

The deterioration rate of concrete structures caused by salt attack differs according to each member and site of these structures. One proposed reason for this is the difference in amount of airborne salt adhering to individual members and sites. In fact, some concrete structures in coastal areas suffer serious salt damage. Therefore, the quantification of airborne salt adhesion on these surfaces is key for the appropriate maintenance of concrete structures. We have proposed a numerical approach for airborne salt transportation and adhesion to concrete surface based on the random walk method which is a particle diffusion method. In this study, measurements and simulations obtained for an existing concrete bridge are compared to validate the proposed method. These results agree well qualitatively, validating this method.

Keywords: Concrete structure, Salt damage, Airborne salt adhesion, Random walk method, Maintenance

Introduction

Located in a subtropical area and surrounded by sea, Okinawa Prefecture is subjected to a hot and humid climate that inherently produces a corrosive environment.

The deterioration rate of concrete structures caused by chloride attack differs at their individual members and sites because of variations in the amount of adhered airborne salt on these components and area. In particular, airborne salt inflicts serious salt damage to some concrete structures in coastal areas. Therefore, an estimate of airborne salt adhesion on these surfaces is essential for the proper maintenance of concrete structures.
Numerous studies have been performed to evaluate salt damage caused by airborne salt spray [1].

These studies focused on the spatial distribution of the deterioration rate and environmental factors, such as temperature, humidity, rainfall, isolation, and airborne salt for individual components and area of the same structure. Moreover, they underlined the importance of environmental action on these deterioration rates.
We have proposed a simulation method to assess airborne salt transportation and adhesion to concrete surfaces using the random walk method, which is a particle diffusion method. In this study, the analytical and numerical results obtained for an existing concrete bridge are compared in order to determine the validity of the proposed method.

Simulation Method

Outline of Simulation method

The proposed method comprised two stages (Fig. 1). First, the wind velocity field in the analytical domain was calculated using the finite element method. Second, airborne salt particle transport and their adhesion to concrete surfaces were simulated by the random walk method using the calculated wind velocity data.
The flowchart of the proposed method is shown in Fig. 1.

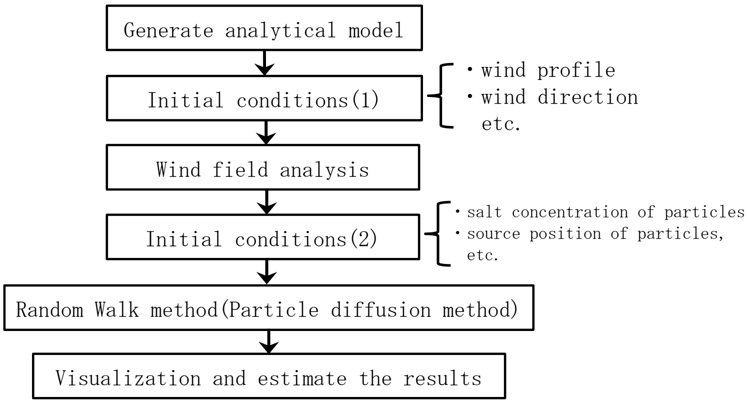

Fig. 1 Flowchart of the proposed method

Wind Field Analysis

The wind field around the structure was analyzed using the three-dimensional (3D) large-scale incompressible fluid finite element code ADVENTURE_Fluid [2].

This analysis considered the following velocity–pressure formulation of the Navier–Stokes equations governing incompressible flows:

$$\nabla \cdot u = 0 \tag{1}$$

$$\rho\left(\frac{\partial u}{\partial t} + u \cdot \nabla u - f\right) - \nabla \cdot \sigma = 0, \tag{2}$$

where u is the velocity,   is the density, f is a body force vector, is the stress tensor,   is the differential operator, and t is the time.

The incompressible fluid analysis code for tetrahedral P1-P2 elements ADVENTURE_Fluid [2] was stabilized using streamline-upwind/Petrov–Galerkin (SUPG) and pressure-stabilized/Petrov–Galerkin (PSPG) methods.

The Crank–Nicolson method was chosen for time discretization, and the velocity and pressure fields are determined simultaneously using asymmetric solvers.

Finite element equations based on the combined SUPG/PSPG method are written as

$$\begin{aligned}(M + M_\delta)\frac{\partial u}{\partial t} + (N + N_\delta)u \\ + Ku - (G + G_\delta)p = 0\end{aligned} \tag{3}$$

$$G^T u + M_\varepsilon \frac{\partial u}{\partial t} + N_\varepsilon u + G_\varepsilon p = 0, \tag{4}$$

where matrices M, N, K, and G are the mass, convection, diffusion, and gradient, respectively. The subscripts   and   identify the SUPG and PSPG contributions, respectively.

Particle Diffusion Method[3]

The 3D random walk [3] was used to model the advection–diffusion of airborne salt particles. Here, individual particles in a 3D space was assumed to be transported by turbulence and mean flow.
(1) Particle position
Salt particle positions in the Cartesian coordinate system were updated using their velocities:

$$x_j^{i+1} = x_j^i + u_j^{i+1} \Delta t \tag{5}$$

where i is the number of analytical steps, j is the number of 3D coordinates, and is the time step. xi and ui are the particle position and velocity at the ith step, respectively.

The particle velocity at step i+1 is written as

$$u_j^{i+1} = U_j^{i+1} + \alpha u_j^i + \lambda_j^{i+1} \tag{6}$$

where U_j^i is the mean wind velocity in the analytical domain calculated using ADVENTURE_Fluid, λ_j^{i+1} is the turbulence statistic, and α is the Lagrangian correlation function.The particle random velocity was assumed to conform to a normal distribution of mean value zero.

The static turbulence is expressed as

$$\lambda_j^{i+1} = \left(1 - \alpha^2\right)^{1/2} \sigma_j \cdot \eta_j^{i+1} \tag{7}$$

where η_j^{i+1} is a standard normal random variable and σ_j is the standard deviation of the particle velocity representing the particle diffusion properties. In addition, σ, which is assumed to obey a Fick-type diffusion, was defined as

$$\sigma = \sqrt{2Kt} \;, \tag{8}$$

where K is the particle speed-dependent turbulent diffusion coefficient. K is written as

$$K = \frac{\beta}{3}\left(u^2 + v^2 + w^2\right) \cdot t \tag{9}$$

where β is an analytical coefficient.

(2) Determination of salt particle adhesion
Modeling particle adhesion to concrete surfaces is important for evaluating the amount of airborne salt on these surfaces. However, the mechanism of this adhesion is unclear.

Therefore, the full adhesion model, in which all particles reaching the surface and adhered to it, was adopted in this study.

(3) Saline concentration and dropping velocity of particles
The saline concentration and dropping velocity of particles have been previously assumed to exhibit variable distribution values[3]. However, because of the small calculation domain, these values were considered constant in this study.

Experimental Investigation of a concrete bridge

Salt adhesion on the surface of a concrete bridge superstructure[4] was evaluated to estimate the distribution of the environmental impact of airborne salt. For comparison purposes to simulation results, this investigation addressed the central portion of the main girders.

Bridge outline and wind conditions

Opened to traffic in March 2011, the subject bridge is located on Northern Okinawa Island (Fig. 2). As shown in side and cross-sectional views (Fig. 3), this three span post-tension prestressed concrete bridge comprises five main girders.

Salt adhesion was assessed in areas N, M, and S of the bridge positioned in the central region of the girders (Fig. 3). In addition to airborne salt, areas N and S were affected by sea spray. Wind direction and velocity are treated as key factors influencing the amount of airborne salt. Weather data for the Northern Okinawa Island were retrieved from the Izena station between January 2008 and December 2012. The percentage of each accumulative wind direction at Izena station is shown in Fig. 4.

As mentioned above, environmental conditions clearly promote severe chloride attacks in winter because of the north monsoon. Therefore, the bridge was assumed to be subjected to a vertically oriented wind presenting a high airborne salt content.

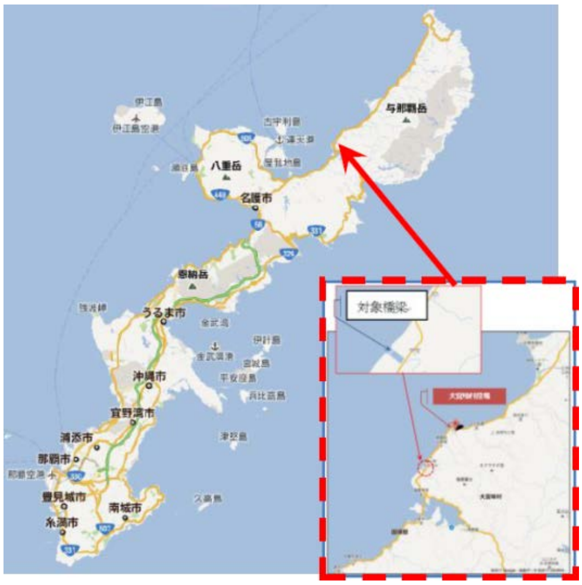

Fig.2 Bridge location

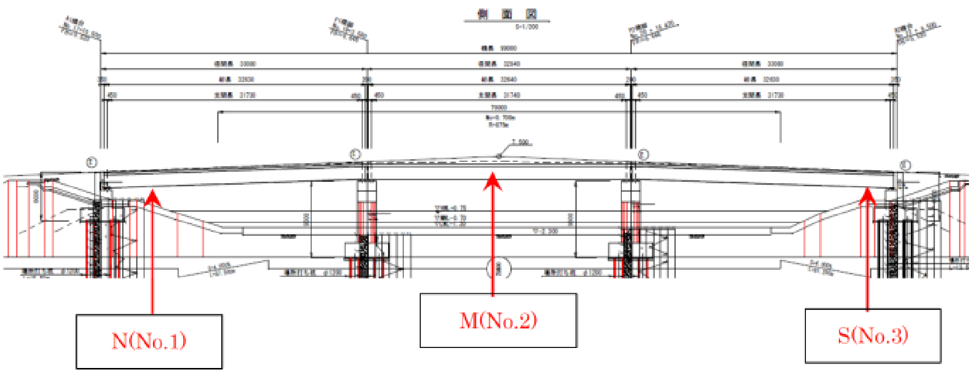

(1) Side view

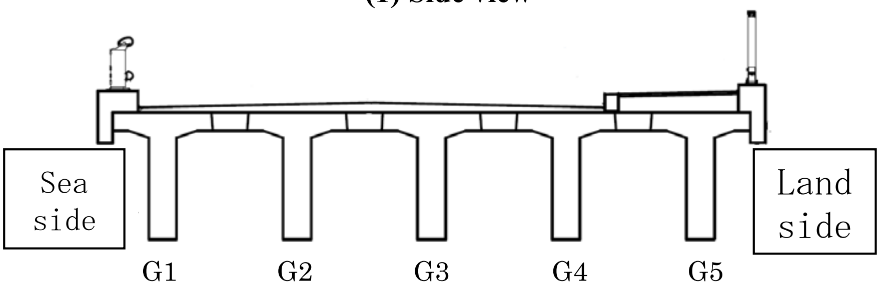

(2) Cross-sectional view
Fig.3 Bridge outline

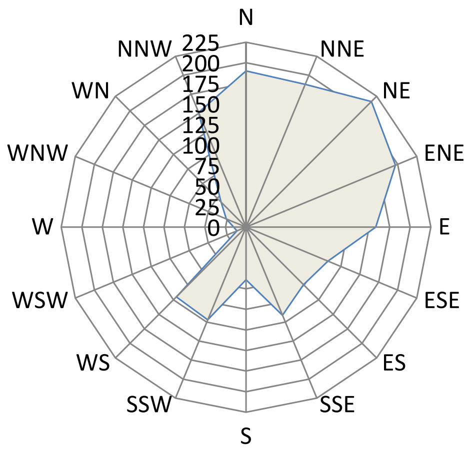

Fig.4 Percentage of each accumulative direction

Gauze swab method

Airborne salt adhesion on main girder surfaces was measured by the gauze swab method [5]. In this method, a 20 cm × 20 cm area was swabbed using moist gauze (Fig. 5) and analyzed using a chloride detector tube. Measurement points #1, #2, #3 #4, and #5 at each main girder are shown in Fig. 6.

Fig.5 Image showing the gauze swab sampling step

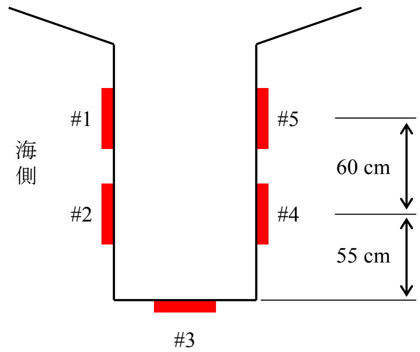

Fig.6 Measurement positions each main girder

Measurement results

Fig. 7 and Fig. 8 show the measurement positions along the main girder surfaces and their corresponding adhered salt content, respectively. These results indicated that airborne salt tended to adhere to the underside of the girders. Moreover, salt adhesion was more significant on the seaside portion of the second girder (G2) than that of the first girder (G1), suggesting that salt adhesion varied within the same structure.

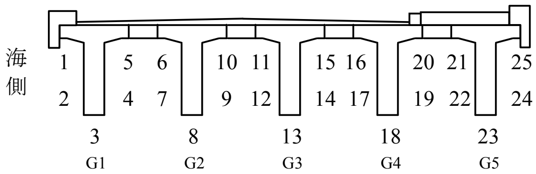

Fig.7 Measurement positions on the main girder surface

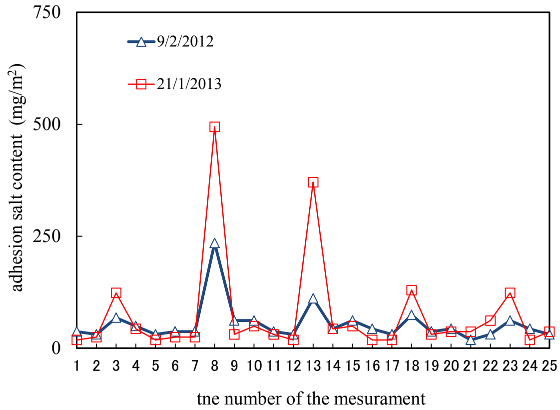

Figu.8 Slat adhesion on the main girder surfaces

Simulation of airborne salt adhesion

In this section, measurements and numerical results of the Northern Okinawa Island concrete bridge were compared to validate the proposed method.

Numerical model and simulation conditions

Fig. 9 shows the analytical domain around the bridge superstructure. A uniform wind velocity was initially set to 5 m/s using mean wind data from the Izena station as a reference.

Fig. 10 shows the mesh division around the bridge superstructure. This mesh consisted of 1,009,795 elements and 174,434 nodal points. The parallel calculation is performed using the Center for Computational Mechanics Research (CCMR) cluster at Tokyo University.

Boundary conditions are established by introducing nonslip velocity conditions in the structure surface and slip velocity conditions in another surface.

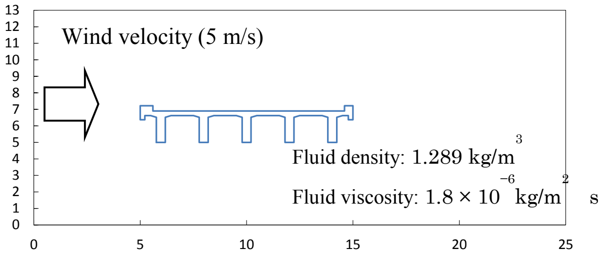

Fig. 9 Analytical domain around the bridge superstructure

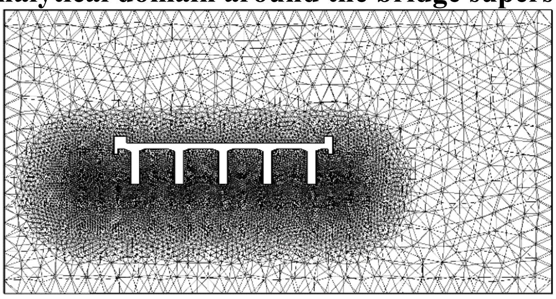

Fig. 10 Mesh division around the bridge superstructure

Numerical results

Wind field and particle advection–diffusion are analyzed by the random walk method and these results are compared with the measurements.

(1) Wind field analysis
Fig. 11 shows the wind velocity obtained from analysis method around the bridge superstructure.

As a boundary conditions, it was assumed that wind velocity of 5m/s is the uniform flow from windward side (sea side). From these results, at first, it was observed that Kármán's vortex was generated at downwind side (land side) of the bridge cross-section, also, wind velocity field in the domain shifted to small eddies from large eddies generated between the main girders.

The wind velocity map after 0.5 s (Fig. 10b) was used in the random walk simulation of particle advection–diffusion because it exhibited the largest eddy between the main girders.

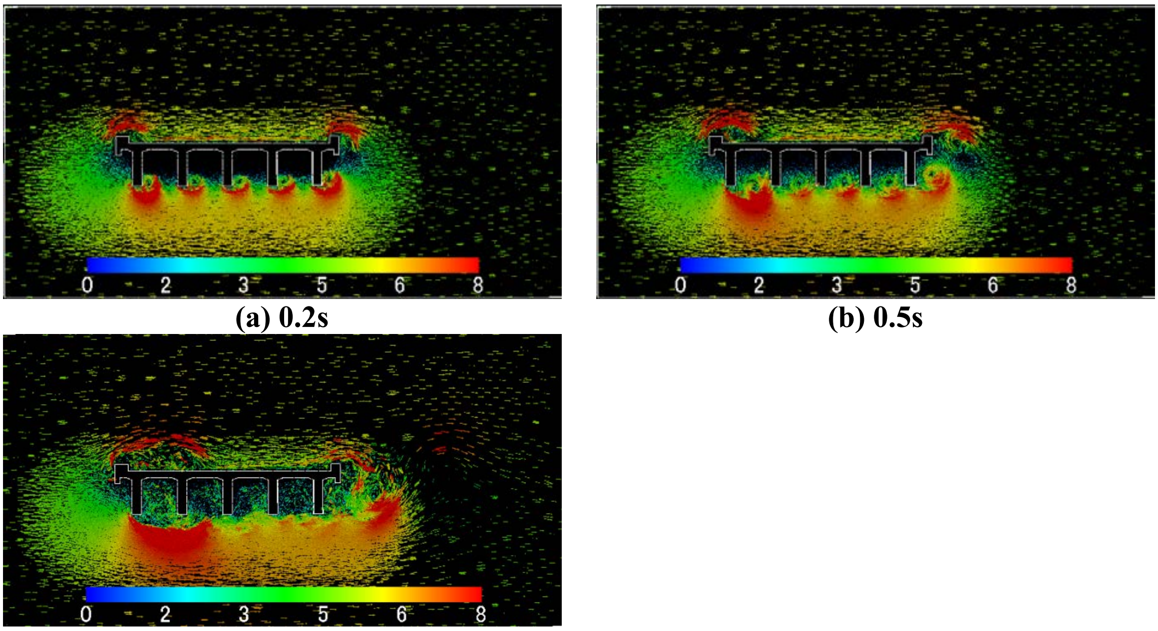

(a) 0.2s **(b) 0.5s**

(c) 0.8s

Fig. 11 Wind velocity vectors

(2) Simulation of salt particle adhesion
The random walk simulation of the particle advection–diffusion–adhesion was conducted using the wind field obtained at 0.5 s (Fig. 10b).

This simulation was performed using 20,000 particles for 3000 steps of 0.01 s. Moreover, the parameter β was defined by preanalysis. Although the simulation was 3D, the particle advection–diffusion–adhesion is considered as a two-dimensional problem because the wind field calculated by ADVENTURE_fluid is like two-dimensional.

Fig. 12 and Fig. 13 show the initial particle position with respect to the bridge and simulated particle advection–diffusion–adhesion at different times, respectively. These results demonstrate that the advection, diffusion, and adhesion of airborne salt particles on the structure surface can be reproduced in response to wind field.

Fig. 14 shows the simulated salt particle adhesion at different positions on the main girder surface. These results are expressed in terms of number of particles per unit area. These numerical results indicated that airborne salt adhesion preferably occurred on the underside of the girders and varied within the same structure, which were consistent with the measurements shown in Fig. 7.

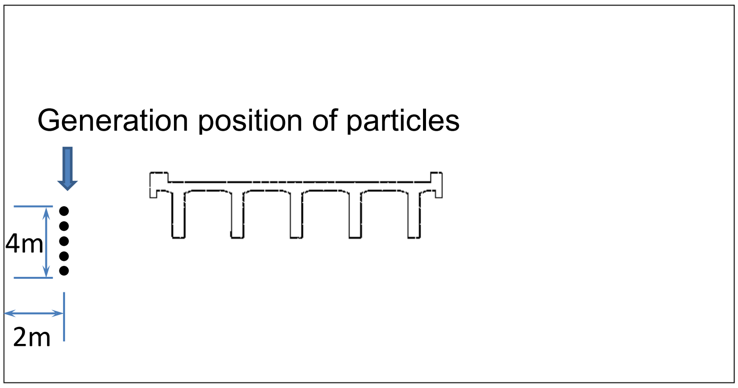

Fig. 12 Initial particle position with respect to the bridge

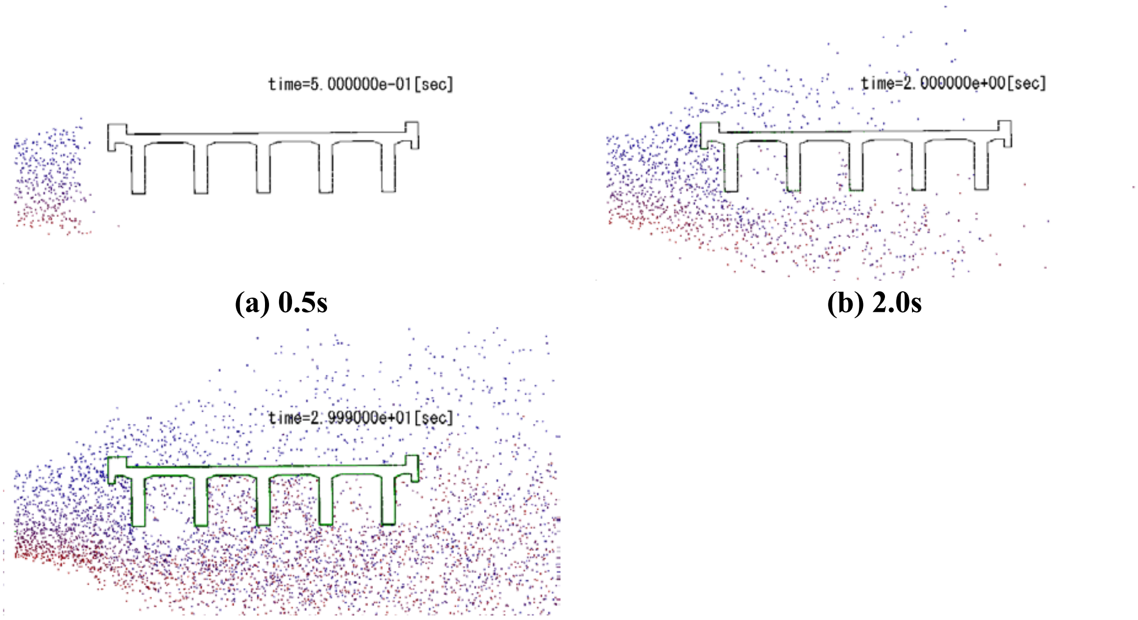

(a) 0.5s

(b) 2.0s

(c) 30s

Fig.13 Random walk simulation of the particle advection-diffusion-adhesion

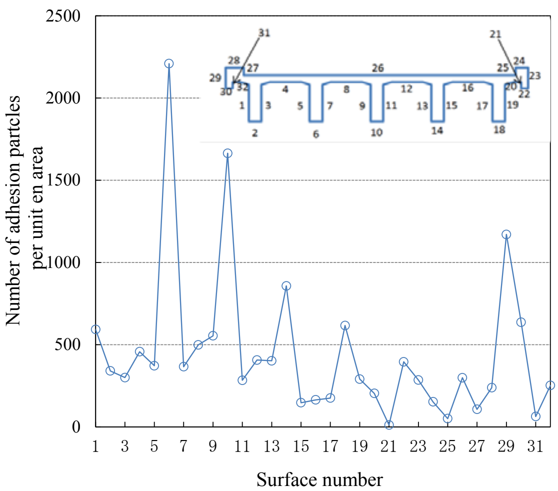

Fig. 14 Simulated salt particle adhesion at measurement positions on the main girder surface.

(3) Correlation between numerical results and measurements

To correlate the numerical results and measurements, which are expressed in different units, surface values were normalized by the value for the underside of girder G2, which exhibited significant salt particle adhesion. Fig. 15 compares these normalized quantities. This comparison clearly showed that numerical results were similar to the measurements.

Correlation diagrams for all data and data recorded on the underside of the main girders are plotted in Figs.16a and b, respectively. These diagrams showed that numerical results and measurements were well correlated. In particular, the values obtained for the underside of the main girders displayed an excellent correlation between simulation and experiment (R2 = 0.9482). Although the values recorded for the main girder sides presented a slightly weaker correlation, the simulation results was the value of the safety side in comparison with the measurements.

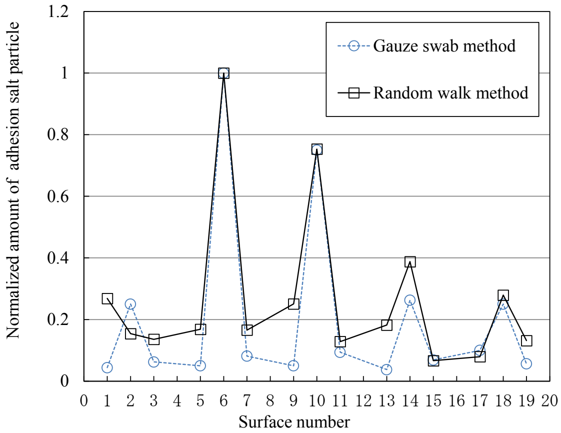

Fig. 15 Normalized amounts of simulated and measured adhered salt particles

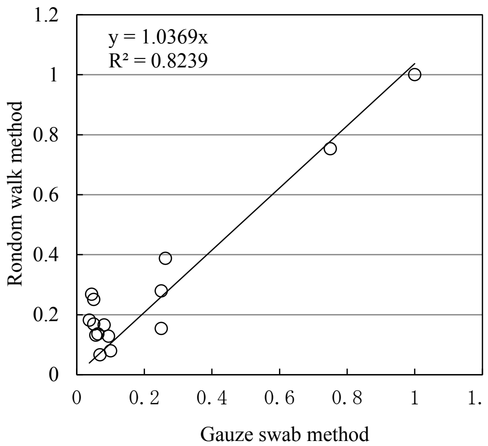

(a) Correlation diagram for all data

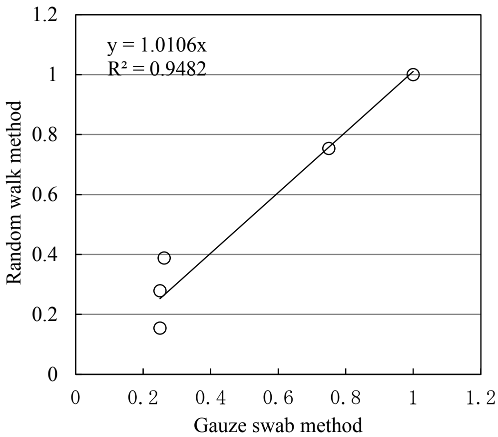

(b) Correlation diagram for data collected on the underside of the main girders

Fig. 16 Correlation between simulated and measured amount of adhered salt particles

Conclusions

The findings of this study are summarized as follows:

(1) Measurements indicated that airborne salt adhesion preferably occurred on the underside of girder G2 positioned seaside and varied within the same structure.

(2) The behavior of airborne salt transported from sea to landside was analyzed using the random walk method.

(3) Simulation results exhibited similar trends to measurements.

(4) A good correlation was observed between the results of the random walk and gauze swab methods, validating the proposed method.

ACKNOWLEDGEMENTS

We thank the Center for Advanced Engineering Structural Assessment and Research (CAESAR) of Japan's Public Works Research Institute (PWRI) for the concrete bridge investigations by the gauze swab method. We also acknowledge valuable discussions on the numerical simulation results with members of the Subcommittee on Priority in Maintenance and Management of Deteriorated Concrete Structures (JSCE-342, the Japan Society of Civil Engineering) and the Research Committee on Long-term Durability Simulation for Concrete Structures (Japan Concrete Institute). Numerical calculations were performed using the CCMR personal computer cluster.

References

[1] Japan Society of Civil Engineers Midterm report of subcommittee on priority in maintenance and management of deteriorated concrete structures, (2012), (In Japanese).
[2] ADVNETURE Project, http://adventure.sys.t.u-tokyo.ac.jp/jp/
[3] Tanaka, T., et al., "Application of random walk method to the airborne salt simulation", Japan Concrete Institute, Vol. 26, No. 1, pp. 789-794 (2004), (In Japanese).
[4] Matsuura, A., et al., "Study on the amount of adhered salt on surface of concrete bridge by using gauze swab method", Japan Society of Civil Engineers Annual Meeting, V-496, pp.991-992,(2013), (In Japanese).
[5] Japan Road Association, "Manual of Steel Road Bridge Painting & Corrosion Prevention (Appendix)", pp.119-120,(2006), (In Japanese).

Numerical Simulation of Mudcrack Grows

†Hitoshi Matsubara[1] and Kosaburo Hirose[2, 3]

[1]Department of Civil Engineering and Architecture, University of the Ryukyus, Japan.
[2]Graduate School of Engineering and Science, University of the Ryukyus, Japan.
[3]Technical Division of Faculty of Engineering, University of the Ryukyus, Japan.

†Corresponding author: matsbara@tec.u-ryukyu.ac.jp

Abstract

The fracture patterns of mud-pastes show significantly complex patterns in nature. The mud-pastes initially have fluid-like properties, but gradually change from "fluid" to porous "solid" in their drying process. The mudcrack phenomena in nature, therefore, is one of the complex physical phenomena of interest in material sciences. However, although it has been considered that mudcrack may be induced by the friction caused by the differences between shrinkage ratios of soil skeletons, the mechanical details remain unknown.

In this work, we describe a novel numerical model based on three dimensional finite element method for mudcrack growth in/on mud-pastes. This model is newly description for mudcrack simulation based on the techniques of three dimensional solid simulations. In order to validate the proposed model, Hausdorff fractal dimension of the numerical fracture patterns is compared with those of the experiments. As a result, the numerical results showed fracture patterns reasonably, and the fractal dimension of the cracking pattern by numerical simulation was almost consistent with the experimental results.

Keywords: Mudcrack, Crack propagation simulation, Digital image correlation, Maximum principal stress/strain, Fractal dimension.

Introduction

The dry shrinkage cracking phenomena of mud-pastes (hereinafter, "mudcrack") is a fracture process commonly observed on surface of farms, tidelands, etc. in nature as shown in Figure 1. Under some multiple physical processes such as wet-drying interactions or changing of material properties, the fracture morphologies show significantly complex patterns [1]-[3]. In addition, the mud-pastes composed of numerous microscopic soil-particles and solvents initially have fluid-like properties, but gradually change from "fluid" to porous "solid" in their drying process. The mudcrack phenomena in nature, therefore, is one of the complex physical phenomena of interest in material sciences. Recently, it has been clarified that mudcrack generated in the ancient Earth may affect the modern geological structures [4]. Therefore, to establish some evaluation techniques for mudcrack patterns would be useful for assessing the natural rock failures such as block or flexural toppling in nature, which is one of the natural disasters. Hence, understanding the mechanism of mudcrack patterns become increasingly important for the geoengineering fields.

Figure 1. Mudcrack pattern in Nature

We often observe geometric patterns of mudcracks having many joints with angles close to 90° or 120° in nature as shown in Figure 1 [2][5]. Ito and Miyata [6] showed experimentally that the joint angles depend on the thickness and the friction between the drying paste and container. Also, they reported that the amount of cracks decreases as the content of coarse sand is increased [6]. Mudcracks are induced by the friction caused by the differences between the shrinkage ratio of the paste and the container. In the case of thin paste samples, Müller [7] and Weinberger [8] used cornstarch pastes to show that the crack propagation speed decreases as the paste thickness becomes less. In addition, they observed plumose morphologies on the surface, and conducted some pattern analyses for these plumose morphologies and clarified that the crack propagation speed on the paste surface is larger than that in the bottom part of the samples [9][10].

On the other hand, in the case of thick paste samples, polygonal blocks are generated as the drying process zones grow from the paste surface in the depth direction [11]-[13]. In these experiments, because the water content and the volume contraction rate of the pastes are positively correlated, it was considered that the mudcracks are induced by the friction caused by the differences of the shrinkage ratios inside the paste samples.

It is interesting that wetted pastes can remember the direction of vibration and flow that were given before the drying process [14]-[16]. The key physical parameter of this imprinting memory in pastes may be the shear stress caused by external vibrations that partially and regularly exceeds the shear yield strength of the paste [15]. Therefore, a strong resistant function may be developed against the fracture process in adequately controlled wetted pastes. In recent viewpoints, it has been considered that the “imprinting memory” in pastes is one of the most important parameters to prevent separation and flaking on the walls of buildings [17].

The fractal analysis is an effective evaluation method for the fracture patterns of mudcracks, and many researchers have attempted to understand the patterns by using this geometric approach [18]-[21]. In most recent literatures, some researchers have proposed a three-dimensional fractal evaluation approach that uses digital images captured by computed tomography and laser scan systems [22][23]. These researchers reported a positive relationship between the porosity of pastes and their fractal dimensions. In this regard, a relationship could exist between the fractal dimensions, the fracture patterns, and the crack propagation in drying pastes. Also, in numerical approaches, the fracture pattern of mud pastes were described by using a simple three dimensional model called as spring network model [24]. However, we have not obtained such complicated patterns in modern three dimensional solid simulations.

Under above situation, however, although it has been considered that mudcrack may be induced by some physical phenomena such as friction caused by the differences between shrinkage ratios of soil skeletons, the mechanical details remain unknown indeed regarding the mechanical evaluation. Also, regarding the morphological evaluation, there are many strange phenomena in mudcrack patterns. In this work, we describe a novel numerical model based on three dimensional finite element method for mudcrack growth in/on mud-pastes. This model is based on the experimental results of digital image correlation, and is newly description for mudcrack simulation based on the techniques of three dimensional solid simulations. In order to validate the proposed model, Hausdorff fractal dimension of the numerical fracture patterns is compared with those of the experiments.

Distribution of principal strain based on Digital image correlation

Digital image correlation (DIC) is a full-field image analysis method, and has been performed with many types of object-based patterns, including lines, grids, dots and random arrays [25]. The greatest feature of this technique is that the measurable strain range could be extremely wide though it depends on the resolution. Therefore, it would be useful to obtain the dynamics of strain distributions for the mudcrack propagation because the mud-pastes would largely shrink in their drying process. The theoretical details of the DIC technique could be followed in the reference [25].

In this work, we observed actual crack propagation process by using a DIC system. In this system, mud-pastes with mottled patterns are captured by 2 cameras as shown in Figure 2. After capturing, we may analyze the distribution of their principal strain by using the dataset of the deformation of mottled patterns. In Figure 3, the mottled pattern on the paste is shown where all of the patterns should be irregular.

Figure 4 shows the experimental cracking patterns with mudcrack propagation. In the experiment, each one crack occurs and propagates independently, and subsequently the cracks are connected to each other with angles closed to 90°. Figure 5 illustrates the distribution of maximum principal strain. From this figure, the cracking on mud-pastes obviously occurs at the point of maximum principal strain. This means that we may use the maximum principal stress/strain theory as a fracture criterion for the mudcrack phenomena.

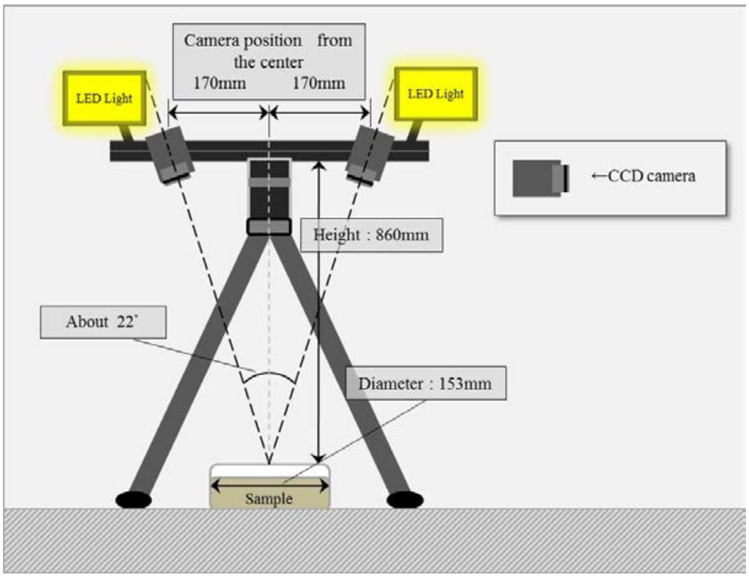

Figure 2. Digital Image Correlation system

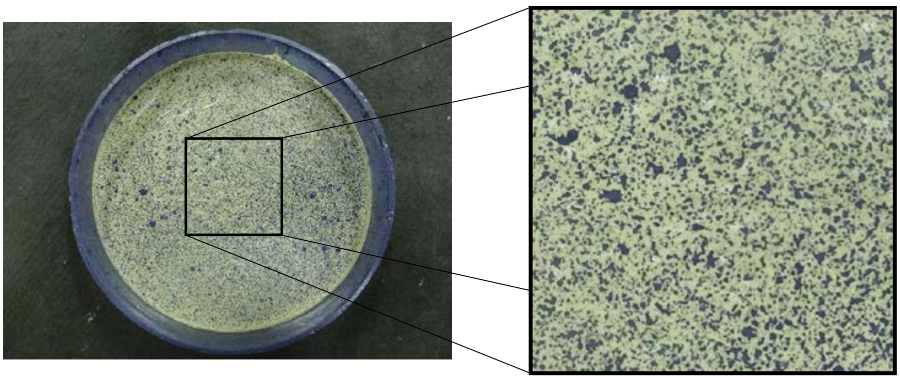

Figure 3. Mud-paste sample with mottled patterns

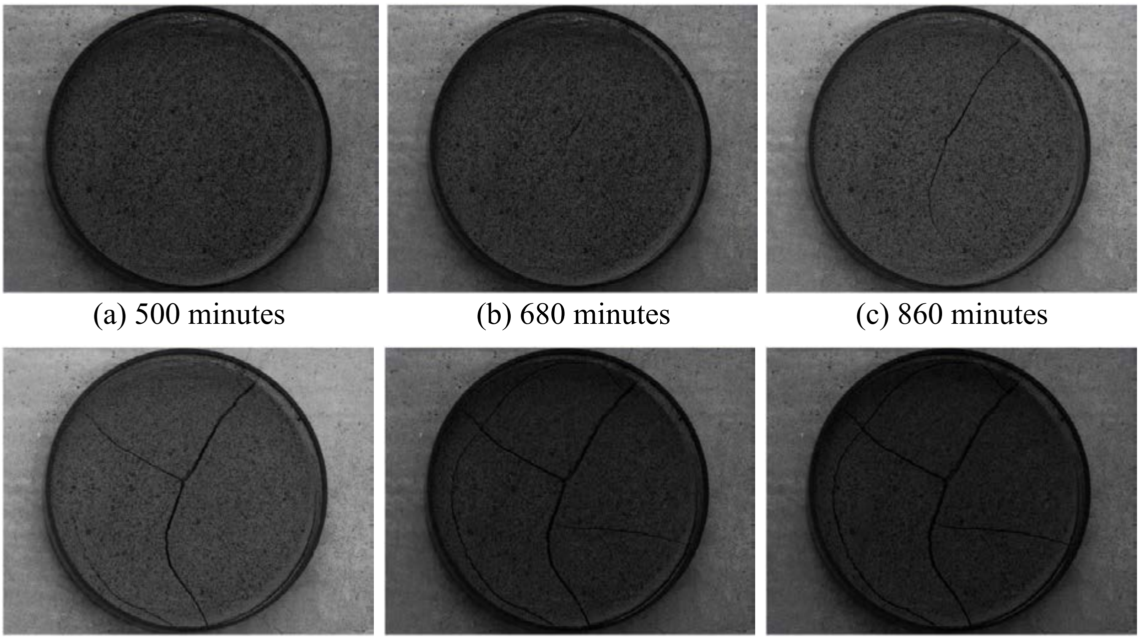

(a) 500 minutes (b) 680 minutes (c) 860 minutes

(d) 1040 minutes (e) 1220 minutes (f) 1400 minutes

Figure 4. State of the mudcrack propagation

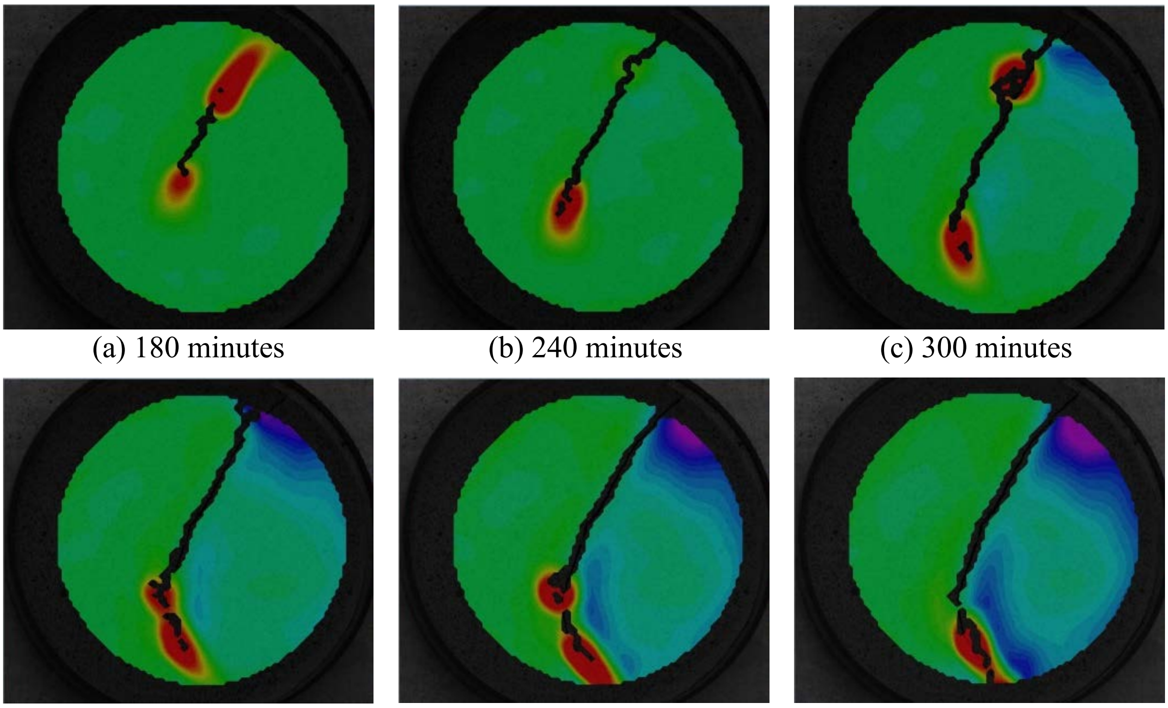

(a) 180 minutes (b) 240 minutes (c) 300 minutes

(d) 360 minutes (e) 420 minutes (f) 480 minutes

Figure 5. State of the mudcrack propagation

Mathematical modeling for mudcrack grows

Finite element formulation

The following governing equation for non-fractured finite element is employed.

$$\int_{\Omega} \mathbf{B}^T \mathbf{D}_e \mathbf{B} \mathbf{u} d\Omega = \int_{\Omega} \mathbf{B}^T \mathbf{D}_e \boldsymbol{\varepsilon}_s d\Omega \tag{1}$$

where **B** is the strain-displacement matrix, $\mathbf{D}_e$ is the elastic stress-strain matrix, **u** is the nodal displacement, Ω is the volume of an element and ε_s is the shrinkage strain. In this work, normal element of ε_s is assumed by the following equations:

$$\varepsilon_s = -\left(\frac{\exp(-\beta \cdot t) - 1}{\exp(-\beta) - 1} \right) \; ; \; t = \frac{z}{z_{\max}} \tag{2}$$

where β is the positive coefficient, t is the normalized thickness of mud-pastes, $z_{\max}$ is the thickness of mud-pastes and z is the distance from bottom. The distribution of ε_s is shown in Figure 6. The distribution shows that the surface drying becomes strong as the β becomes large, or vice versa.

Regarding the stress-strain matrix, **D**, we used the smeared crack model [26]. This model is conceptually and computationally quite simple, but this model is very effective in capturing essential fracture behavior in various materials. This model would be useful for mud-pastes cracking system because it has been found that the crack propagations in paste-like materials may be suppressed by the stress relaxation occurring around crack tips rather than by singularity of crack tip stress [27].

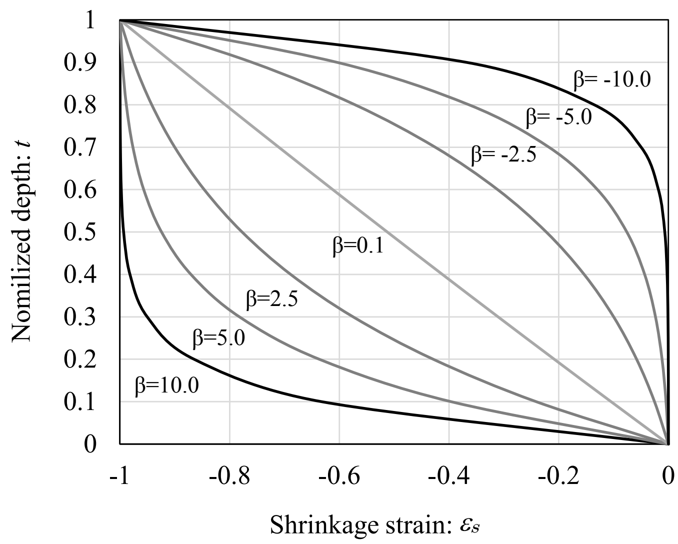

Figure 6. Assumed shrinkage strain distribution

The smeared crack model could be categorized into fixed and rotating crack models. With a fixed crack model, the orientation of the crack is fixed during the entire computational process, whereas a rotating crack model allows the orientation of the crack to co-rotate with the axes of the principal strain. In this work we used the fixed crack model, and employed the following equation for fractured finite elements:

$$\int_{\Omega} \mathbf{B}^T \mathbf{T}^T \mathbf{D}_{cr} \mathbf{B} \mathbf{T} \, \mathbf{u} d\Omega = \int_{\Omega} \mathbf{B}^T \mathbf{T} \, \mathbf{D}_{cr} \boldsymbol{\varepsilon}_s d\Omega \tag{3}$$

where **T** is the transformation matrix for the stress and the strain, which are reflecting the orientation of the crack.

Crack propagation algorithm

In the non-increment-type of the smeared crack model, just one element with the maximum value of the following r is assumed to be a smeared fractured element:

$$r = \frac{\sigma_{1,\max} - f_t}{f_t} \tag{4}$$

where $\sigma_{1,\max}$ is the maximum value of maximum principle stresses, and f_t is the material tensile strength. We used just one criterion of equation (4); that is, only Mode I was assumed in all finite elements based on the experimental results in the previous section.

The calculated physical values **p** (displacement, stress and strain) of all elements are modified by the following equations:

$$\mathbf{p}_{\mathrm{mod}} = \frac{1}{1+r}\mathbf{p} \tag{5}$$

where $\mathbf{p}_{\mathrm{mod}}$ is the modified physical value. In this approach the element is fractured one-by-one, and therefore all we need do is repeat the continuum analysis with some fractured elements. Hence, the cracks propagate slowly but steadily, so that we can observe some localized fracture areas on the screen.

Numerical simulation and its discussion

The three dimensional models with a 50×50×2 (long × wide × height) specimen is simulated. In this numerical example the Poisson's ratio ν of 0.3, Young's modulus E of 40 ± 40 N/mm^2 with random manner, and the tensile strength f_t of 0.02 ± 0.025 N/mm^2 with random manner are set up as the material constants. In the smeared crack model we employed the 4-node tetrahedral element, and the number of elements and nodes were 481,107 and 96,390 respectively. In advance of the calculation, we prepared two analytical models with a different β in equation (2); β = 3.0 and β = -3.0.

The crack propagation results for each case are shown in Figures 7 and 8. From these figures, we can observe that some "crack seeds" that initially occurred in the entire analytical region are interlocked with one another, and some grown-up cracks propagated locally to the various direction with increasing analytical steps.

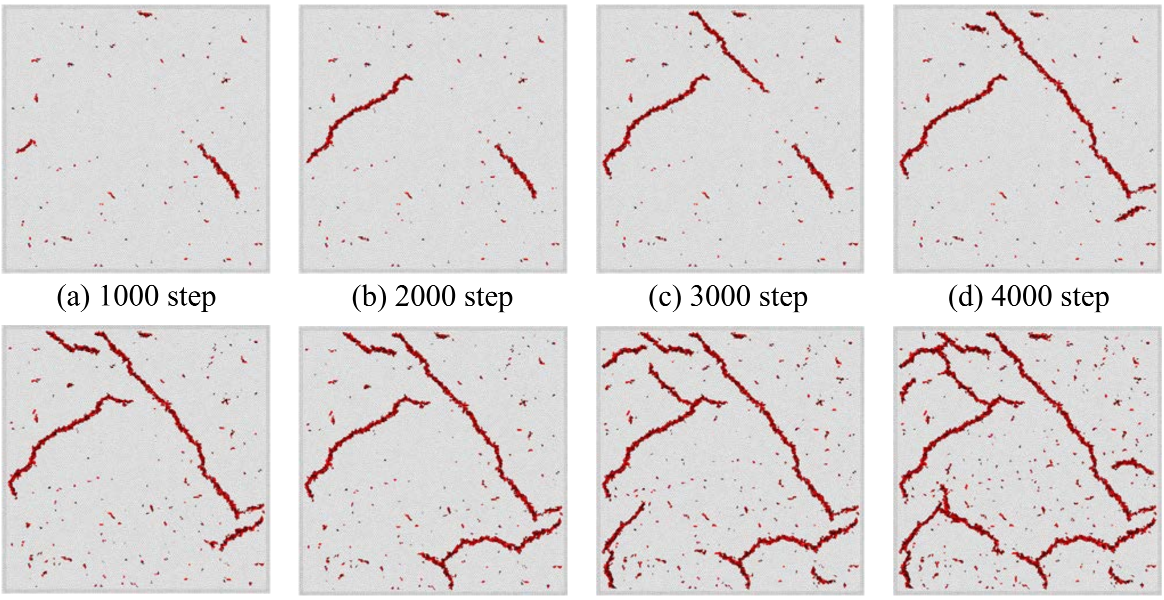

(a) 1000 step (b) 2000 step (c) 3000 step (d) 4000 step

(e) 5000 step (f) 6000 step (g) 8000 step (h) 10000 step

Figure 7. Crack propagation pattern (β = 3.0)

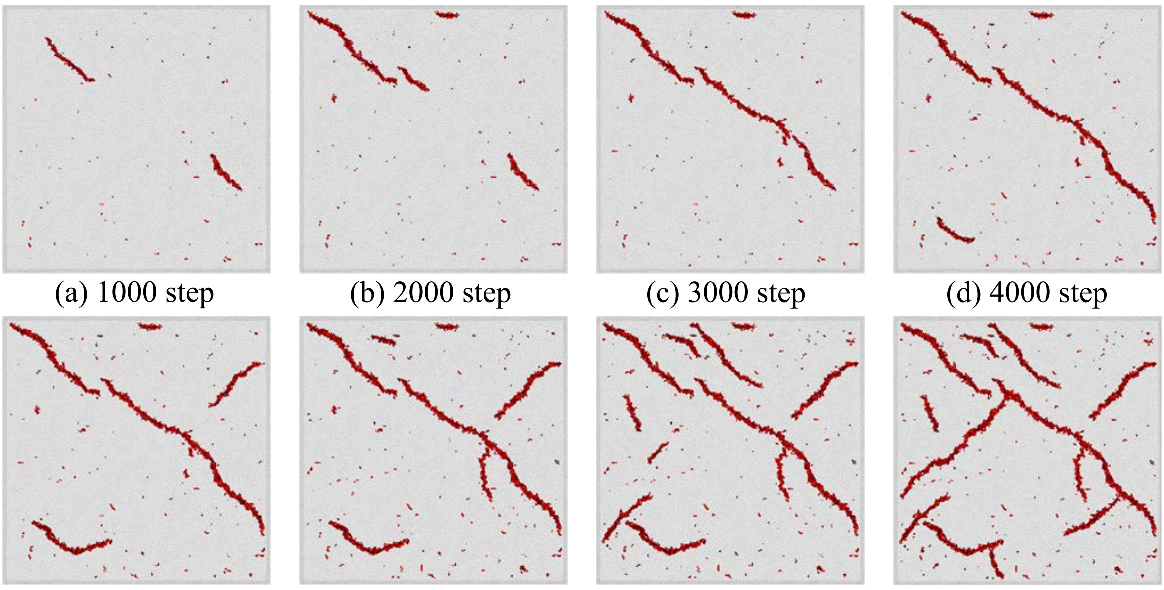

(a) 1000 step (b) 2000 step (c) 3000 step (d) 4000 step

(e) 5000 step (f) 6000 step (g) 8000 step (h) 10000 step

Figure 8. Crack propagation pattern (β = -3.0)

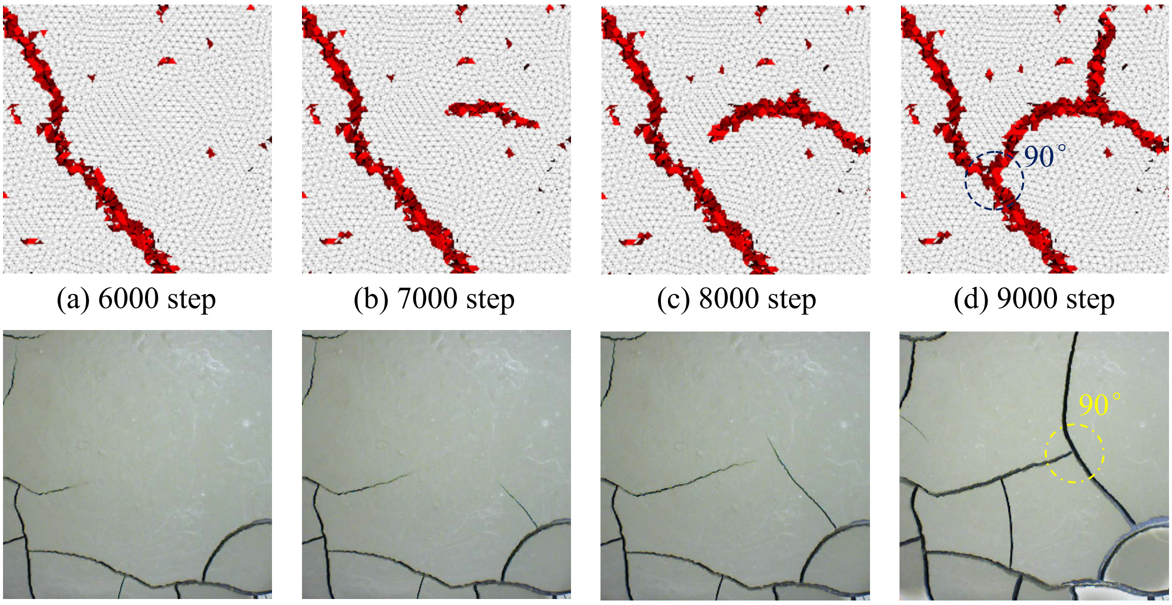

(a) 6000 step (b) 7000 step (c) 8000 step (d) 9000 step

(e) 500 minutes (f) 540 minutes (g) 558 minutes (h) 770 minutes

Figure 9 T-type cracking pattern ((a)-(d): Numerical, (e)-(h): Experimental)

Finally, these cracks connected each other with angles close to 90° or 120° regardless of the value of β. Also, these T- and Y-pattern joints can be seen in nature as shown in Figure 1. Figures 9 and 10 show some comparison images between numerical and experimental results for T- and Y-cracking patterns, respectively. From Figure 9, a crack propagates in direction to another crack surface, and subsequently the cracks connect each other with angle closed to 90°. On the other hand, from Figure 10, a crack branches to two cracks with angle closed to 120°.

Additionally, the cracks in the case of β = 3.0 is concentrated more than those of β = -3.0. These results indicate that many sparse cracks may be generated under the strong drying condition, whereas many dense cracks may be generated under the gentle drying condition. In

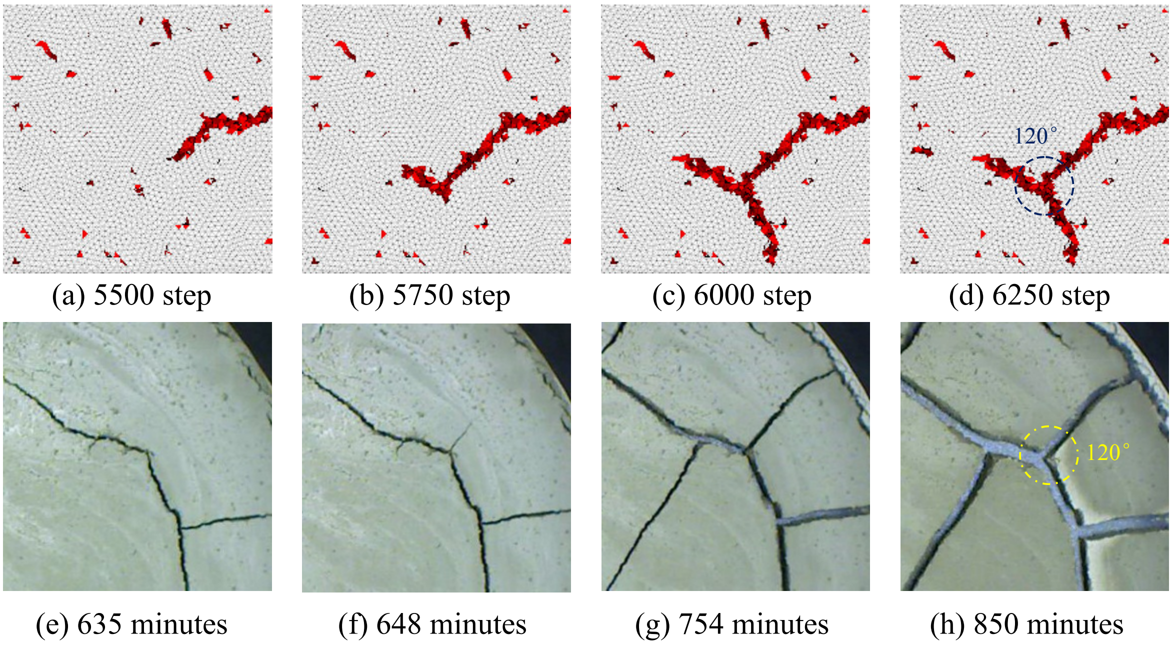

Figure 10 Y-type cracking pattern ((a)-(d): Numerical, (e)-(h): Experimental)

nature, we also observe many sparse cracking patterns and many dense cracking patterns, so that the differences may be caused by atmospheric temperature and humidity.

Figure 11 shows the relationship between fractal dimension and analytical step. The fractal geometry provided exact dimensions to morphologies that could not be quantified in Euclidean geometric analyses [28]. A fractal is generally defined as having a morphology exhibiting self-similarity, such as a coastline, rock surface or crack. Also, it is well known that pattern analysis by fractal dimension is useful for characterizing the crack propagation phenomena in wetted pastes [19] [29]. In this work, the fractal dimensions (Hausdorff dimensions, F_d) of mudcrack are determined by the box counting probability method [19]. Specifically, to calculate F_d, a digital image of the analytical objects is overlaid with boxes of side length d, and the number $N(d)$ of boxes required to cover the object is counted and plotted against d on a double-logarithmic graph. The slope of tangent to this plot is taken as the fractal dimension, F_d. That is,

$$\log\left(N(d)\right) = F_d \log(d) \qquad (6)$$

In this study we assumed the following cases of d: 2, 3, 4, 6, 8, 12, 16, 32 and 64 pixels.

From Figure 11, the fractal dimensions of numerical cracking pattern increased gradually as the analytical step increased, and they converged towards approximately 1.5, regardless of the value of β. Figures 12(a) and 12(b) show the fracture pattern and the relationship between fractal dimension and elapsed time in drying mud, respectively. In the

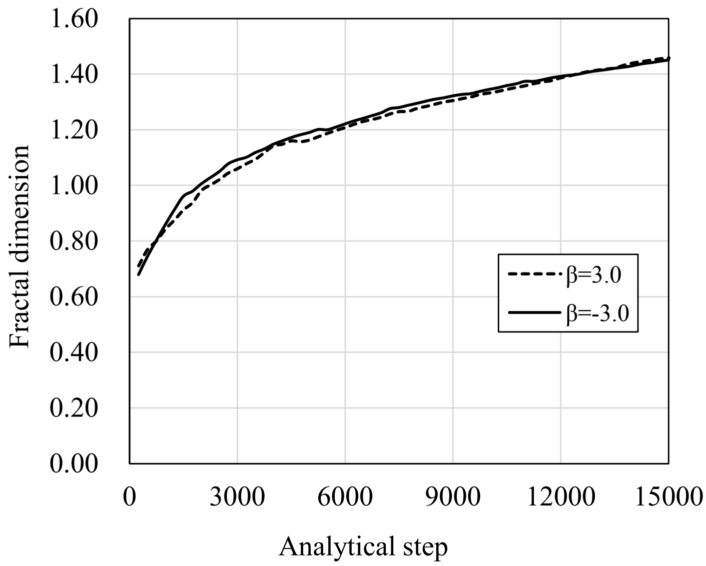

Figure 11. Fractal dimension vs Analytical steps

experiment, the sample was set in a thermostatic device for 24 hours to remove the influence of a changing temperature. In the device, the temperature and humidity were kept constant at 25 °C and 37%, respectively. From Figure 12(b), we understand that the fractal dimensions of mud-paste converged towards approximately 1.46. This tendency and the fractal dimension value is almost consistent with the numerical results in Figure 11.

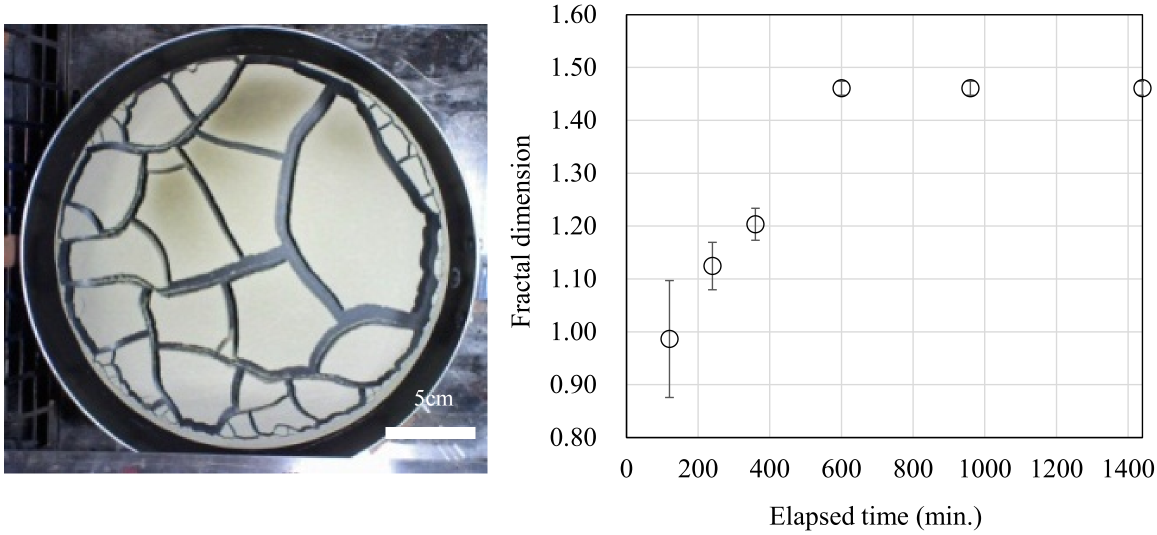

(a) Mudcrack pattern (b) Fractal dimension vs Elapsed time

Figure 12. Change in experimental fractal dimension

Concluding remarks

The three dimensional numerical simulation for mudcrack pattern were described and validated. Our interpretation of the results is summarized as follows:

(1) According to the Digital image correlation analyses, the cracking on mud-pastes occurs at the point of maximum principal strain, and propagates to other cracking surface with the drying process.

(2) The simplified crack propagation algorithm is a powerful computational technique for solving the crack propagation phenomena of mud-pastes. By using this technique, we can determine the carious fracture patterns of mud-pastes.

(3) The cracks in numerical simulations connected each other with angles close to 90° or 120°. These joint-patterns can be seen in nature.

(4) From numerical simulation results, we found that the differences fracture pattern in nature may be caused by atmospheric temperature and humidity.

(5) The fractal dimensions of numerical cracking pattern converged towards approximately 1.5 that was almost consistent with the experimental value of mud-paste, 1.46.

Acknowledgements

A part of this research was supported by the JSPS Grant-in-Aid for Young Scientists (B) Grant Number 26790079.

References

[1] Zhang, Z.B., Zhou, H., Zhao, Q.G., Lin, H. and Peng, X. (2014) Characteristics of cracks in two paddy soils and their impacts on preferential flow, *Geoderma* **228-229**, 114-121.

[2] Sletten, R.S., Hallet, B. and Fletcher, R.C. (2003) Resurfacing time of terrestrial surfaces by the formation and maturation of polygonal patterned ground, *Journal of Geophysical Research: Planets* **108**(E4), 8044.

[3] Aydin, A. and Degraff, J.M. (1988) Evolution of polygonal fracture patterns in lava flows, *Science* **239**, 471-476.

[4] Zhao, Z.Y., Guo, Y.R., Wang, Y., Liu, H. and Zang, Q. (2014) Growth patterns and dynamics of mud cracks at different diagenetic stages and its geological significance, *International Journal of Sediment Research*, **29**, 82-98.

[5] Kerfoot, D.E. (1972) Thermal contraction cracks in an arctic tundra environment, *Arctic Institute of North America*, **25**(2), 142-150.

[6] Ito, H. and Miyata, Y. (1988) Experimental study on mud crack patterns, *Journal of Geological Society of Japan*, **104**, 90-98.

[7] Müller, G. (2001) Experimental simulation of joint morphology, *Journal of Structural Geology*, **23**(1), 45-49.

[8] Weinberger, R. (2001) Evolution of polygonal patterns in stratified mud during desiccation: The role of flaw distribution and layer boundaries, Geological Society of America Bulletin, 113(1), 20-31.

[9] Weinberger, R. (1999) Initiation and growth of cracks during desiccation of stratified muddy sediments, *Journal of Structural Geology*, **21**, 379-386.

[10] Müller, G. and Dahm, T. (2000) Fracture morphology of tensile cracks and rupture velocity, *Journal of geophysical research*, **105**(B1), 723-738.

[11] Toramaru, A. and Matsumoto, T. (2004) Columnar joint morphology and cooling rate: A starch-water mixture experiment, *Journal of Geophysical Research*, **109**, B02205.

[12] Goehring, L. and Stephen, W. M. (2006) An Experimental investigation of the scaling of columnar joints. *Physical Review E*, **74**, 036115.

[13] Goehring, L. (2013) Evolving fracture patterns: columnar joints, mud cracks, and polygonal terrain, *Philosophical Transactions of Royal Society A*, **371**, 20120353.

[14] Nakahara, A. and Matsuo, Y. (2005) Imprinting the memory into paste and its visualization as crack patterns in drying process, *Journal of the Physical Society of Japan*, **74**(5), 1362-1365.

[15] Nakahara, A. and Matsuo, Y. (2006) Transition in the pattern of cracks resulting from memory effects in paste, *Physical Review E*, **74**, 045102.

[16] Nakayama, H., Matsuo, Y., Ooshida, T. and Nakahara, A. (2013) Position control of desiccation cracks by memory effect and Faraday waves, *European Physica Journal E*, **36**, 1.

[17] Carpinteri, A., Lacidogna, G. and Niccolini G. (2009) Fractal analysis of damage detected in concrete structural elements under loading, *Chaos, Solitons and Fractals*, **42**, 2047-2056.

[18] Velde, B. (1999) Structure of surface cracks in soils and muds, *Geoderma* **93**, 101-124.

[19] Baer, J.U., Kent, T.F. and Anderson, S.H. (2009) Image analysis and fractal geometry to characterize soil desiccation cracks, *Geoderma* **154**, 153-163.

[20] Preston, S., Griffiths, B.S. and Young, I.M. (1997) An investigation into sources of soil crack heterogeneity using fractal geometry, *European Journal of Soil Science* **48**, 31-37.

[21] DeCarlo K.F. and Shokri N. (2014) Effects of substrate on cracking patterns and dynamics in desiccating clay layers, *Water Resources Research*, **50**(4), 3039-3051.

[22] Perret, J.S., Prasher, S.O. and Kacimov, A.R. (2003) Mass fractal dimension of soil macropores using computed tomography: from the box-counting to the cube-counting algorithm, *European Journal of Soil Science* **54**, 569-579.

[23] Velde, B (2001) Surface cracking and aggregate formation observed in a Rendzina soil La Touche (Vienne) France, *Geoderma* **99**, 261-276.

[24] Nishimoto, A., Mizuguchi, T. and Kitsunezaki, S. (2007) Numerical study of drying process and columnar fracture process in granule-water mixtures, *Physical Review E*, **76**, 016102.

[25] Michael A. Sutton, Jean-José Orteu and Hubert W. Schreier (2009) Image Correlation for Shape, Motion and Deformation and Deformation Measurements, Springer.

[26] Rots, J.G. (1970) Computational modelling of concrete fracture, Ph.D. diss., *Delft University of Technology*.

[27] Kitsunezaki, S. (2009) Crack propagation speed in the drying process paste, *Journal of the Physical Society of Japan*, **78**(6), 064801.

[28] Mandelbrot, B.B. (1982) The fractal geometry of nature, *W.H. Freeman and Co.*

[29] Preston, S., Griffiths, B.S. and Young, I.M. (1997) An investigation into sources of soil crack heterogeneity using fractal geometry, *European Journal of Soil Science*, **48**, 31-37.

Coupled Analysis of Electromagnetic Fields and Temperature Distributions inside the Human Body Using Microwave Therapeutic Devices

Yasuhiro Shindo

Department of Mechanical Engineering Faculty of Science and Engineering, Toyo University, Japan.

shindo060@toyo.jp

Abstract

I discuss coupled analysis of SAR distributions and temperature distributions using an anatomical simulation model reconstructed from 2D medical images. The distributions are calculated by 3D Finite Element Method (FEM) using a resonant cavity applicator for non-invasive, deep hyperthermia treatment. This applicator is made for treatment of abdominal tumors.

Some electromagnetic therapeutic devices for hyperthermia treatment are currently used in clinics. However, these applicators come with some disadvantages. The abdominal region is covered with fat tissue which is resistant to deep heat penetration. Furthermore, electromagnetic energy concentrates on the convex surfaces of the human body, such as the chests and the buttocks. However, methods capable of creating and controlling a heated area without attachments such as a bolus and loading dielectrics were insufficient.

In my previous study, I developed a new resonant cavity applicator for non-invasive hyperthermia treatment. And in these studies, in order to evaluate the effectiveness of the proposed methods, I conducted coupled analysis of specific absorption rate (SAR) distributions and the changing temperature profiles and experiment with prototype applicator.

First of all, for verification and validation (V&V) of my calculation method, the thermal properties of this proposed heating method when applied to agar phantoms were calculated with computer simulations. And the experimental results were compared with the basic heating system.

After the evaluation, I constructed an anatomical 3D calculation model from 2D medical images.

Next, to evaluate the effectiveness of the proposed methods, temperature distributions were calculated by FEM with the 3D anatomical human body model.

From these results, it was confirmed that the calculated temperatures inside the agar phantoms were in close agreement with the measured temperatures with an error margin of 10％ or less. Furthermore, the results with anatomical human body model suggest that the proposed heating method using electromagnetic field patterns generated inside of a resonant cavity is capable of non-invasive hyperthermia treatments.

Keywords: Coupled analysis, Anatomical human model, Resonant cavity, Electromagnetic, Temperature distribution.

Introduction

Hyperthermia treatment is based on the clinical fact that a tumor is weaker than healthy tissue at the temperature of 42-43^{o}C and can be eliminated by a series of approximately one-hour-long heat treatments. A variety of heating methods have already been proposed to heat deep tumors.

Some examples of heating methods are radio frequency (RF) capacitive heating applicators and microwave heating applicators. Some of these applicators have been in practical use. However, all of these heating methods have some disadvantages. An entirely advantageous heating method has not yet been realized [1], [2].
Therefore, I proposed a non-invasive heating method as shown in Fig.1. In this system, a large resonant cavity with inner electrodes was used for heating deep tumors in the abdominal region of the human body[3]-[9].

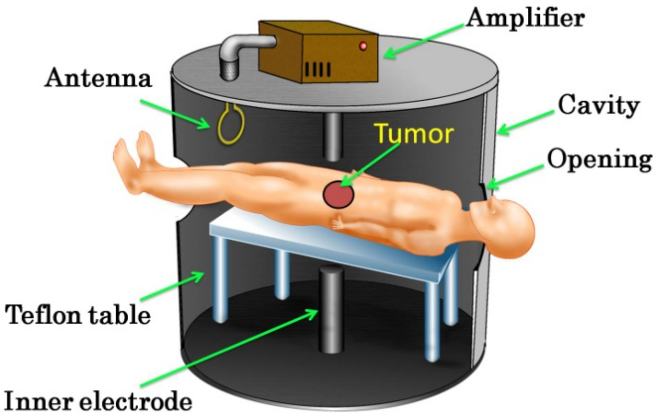

Figure 1. Illustration of the resonant cavity applicator

The human body consists of many organs that have different electrical and thermal properties and also have various shapes and sizes. Therefore, it was expected that the electromagnetic fields would concentrate on the convex parts of the human body, such as the chest and the buttocks etc.
To overcome these problems, I proposed a new heating method of using the resonant cavity applicator with cylindrical shields made of an aluminum alloy and a water bolus. In this new heating system, the human body is covered with the cylindrical shields, except for the area to be heated.
The human body is placed in the gap between the two inner electrodes. The surface of the human body is then covered with the water bolus to concentrate the electromagnetic energy on the deep-seated tumors.
Using FEM, I calculated SAR distributions of an anatomical human body model, including the bones, muscle tissue, fat tissue, lungs, liver, stomach and other internal organs.

Methods

Coupled Analysis of SAR and Temperature Distributions by 3D FEM

The SAR distribution inside the human body can be calculated by equations (1) to (4):

$$\nabla^2 E + k^2 E = 0 \quad (1)$$

$$k^2 = \omega^2 \varepsilon \mu \quad (2)$$

$$W_h = \frac{1}{2}\sigma |E|^2 \quad (3)$$

$$SAR = \frac{1}{\rho} W_h \quad (4)$$

where E is the electric field vector, ω the radial frequency, ε the dielectric constant, μ the magnetic permeability, W_h the heating power generated inside a human body, σ the electrical conductivity, and ρ the volume density of tissue. Equations (1) and (2) can be solved numerically by the FEM [6]-[11]. The electrical parameter values at 130MHz for each organ are listed in Table 1 [12]-[15].

Table 1. Identified results

Tissue	σ [S/m]	ε	ρ [kg/m³]	c [J/kg/K]	κ [W/m/K]	*F* [ml/min/gm]	Mesh size [mm]
Air	0.0	1.00	1.165	1010	0.025	-	5.0
Bladder	0.30	21.82	1000	3553	0.53	0.31	2.0
Bone	0.18	26.21	1790	2700	0.22	0.1	3.0
Colon	0.71	76.28	1000	3012	0.38	1.24	2.0
Fat	0.036	5.91	900	2524	0.24	0.21	2.0
Heart	0.77	83.89	1000	3720	0.54	3.72	1.0
Kidney	0.86	89.14	1000	1046	0.52	4.0	1.0
Liver	0.51	63.98	1000	1050	0.51	3.17	0.5
Lung	0.0	1.00	1.165	3625	0.44	1.14	2.0
Muscle	0.72	63.36	1000	3634	0.55	0.027	1.0
Small intestine	1.70	87.50	1000	3012	0.375	2.09	2.0
Spleen	0.84	82.46	1000	3603	0.54	3.60	2.0
Stomach	0.91	74.73	1000	3553	0.53	0.53	2.0
Uterus	0.96	75.19	1000	3542	0.54	0.31	2.0
Pancreas	0.80	66.67	1000	3601	0.54	0.55	2.0
Bolus	0.0	75.00	1000	4200	0.60	-	1.0
Tumor	0.6	65.00	900	3437	0.50	0.25	0.2

Using the resulting data of SAR distributions inside a human body, the tissue temperature (T) can be calculated by equations (5) to (7) [10], [11], [16]:

$$\rho c \frac{\partial T}{\partial t} = \nabla \kappa \cdot \nabla T + \rho \cdot SAR - W_C \qquad (5)$$

$$W_C = (F\rho)_{tissue} \cdot (\rho c)_{blood} \cdot (T - T_b) \qquad (6)$$

where c is the specific heat of each tissue, κ the thermal conductivity, T the temperature of tissues, t the heating time, W_c the cooling energy by blood flow, F the blood flow rate of each tissues, and T_b the temperature of blood. In this study, T_b is fixed as 37°C. The initial temperatures of each tissue set to 37°C, and that of air is 26°C. Heating time was set to 60min. Equations (1) and (5) can be solved numerically by the FEM. The thermal properties for each organ are listed in Table 1 [17]-[20].

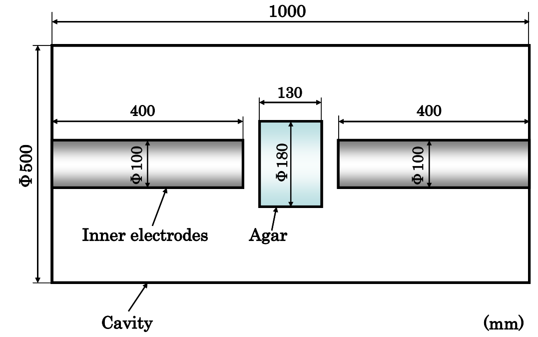

Figure 2. Cross-sectional view of the basic resonant cavity applicator

Basic Heating System

In basic evaluation, I used a basic cavity applicator shown in Fig. 2. The cavity is made of an aluminum plate, and is 500mm in diameter and 1000mm in height. To concentrate the heating energy in the center of the cavity, the inner electrodes of 100mm in diameter and 400mm in height are used. [7]

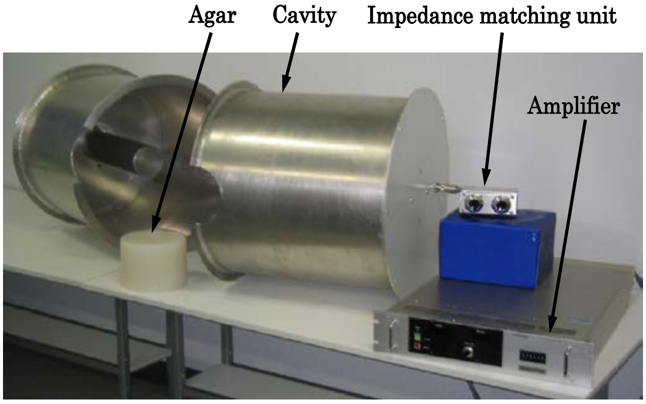

Figure 3. Setup of the heating system

Fig.3 shows a photograph of the basic heating system. It consists of a cavity, an amplifier, a looped antenna inside the cavity, and an impedance matching unit shown in Fig.3(a). The maximum input power was 150 W, and the operating frequency can be set between 50 and 400MHz. The agar phantom (agar: 4%, NaCl: 0.24%, NaN_3: 0.1 %, water: 95.66 %)used in these experiments was 13.0cm in height and 18.0cm in diameter. The impedance matching unit is connected to the cavity with coaxial cables.

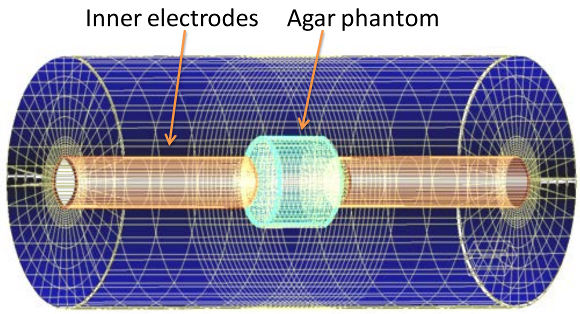

・Nodes : 34,864
・Elements : 36,448
・Initial temp.: 37[℃]
・Heating time : 60 [min]

Figure 4. Finite element mesh for calculating electromagnetic field and temperature distributions

Figure 4 shows the finite element mesh for calculating electromagnetic field and temperature distributions for basic evaluation. Here, JMAG-studio^{TM} (J-SOL co.ltd, Japan) which is FEM software was used in computer simulations. In calculating the temperature distribution of agar phantom, an initial temperature was 37°C, and the heating time was set to 60min. And the agar phantom's parameter was set to same as a muscle's one.

New heating system for an abdominal tumor

After the basic evaluation, I calculated the heating properties of the anatomical human body model using a large resonant cavity applicator. Figure 5 shows the large resonant cavity heating system for treating the abdominal tumors. In Fig. 5, a human body is placed in the center of the inner electrodes and is heated with the electromagnetic field

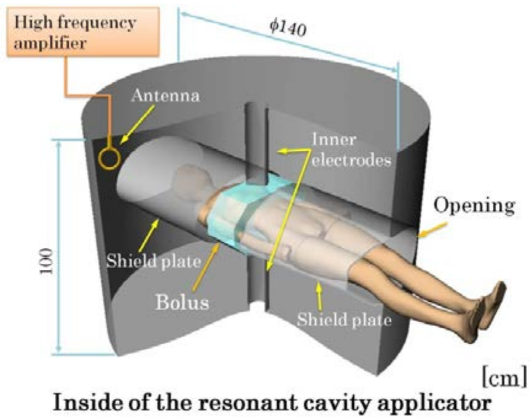

Figure 5. Illustration of the improved resonant cavity.

patterns which are generated inside the cavity. No contact is made between the human body and the applicator. The elliptic cylindrical shield is connected to the cavity wall.
This shield was designed to protect non-tumorous areas in the human body from the electromagnetic heating energy. In order to concentrate heating energy on deep tumors, the water bolus is set on the human body surface without contacting the applicator.
Figure 6 shows a cross-sectional view of the cavity. The cavity is 140 cm in diameter and 100 cm in height. To concentrate the heating energy in the center of the cavity, the inner electrodes are used. The upper inner electrode is 10 cm in diameter and 25 cm in height. The length of a lower inner electrode was adjustable. The ellipses (55 × 30 cm) are located at the head and leg regions. These allow the head and leg to rest outside of the cavity. Electromagnetic shields are 60 cm in length and are connected to the cavity wall. The water bolus, 45 cm in width, 25 cm in height and 16 cm in thickness, covers the surface of the human body. The water bolus is filled with distilled water. In order to heat the liver tumor the human body and bolus were put in a position shifted 5 cm from the center of the cavity.

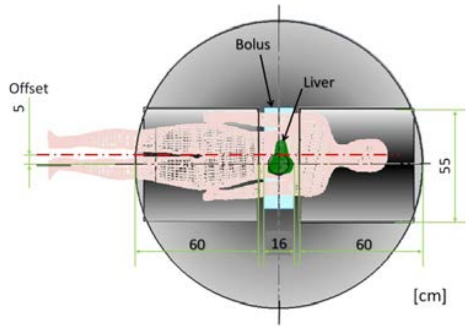

(a) Top view of the improved resonant cavity.

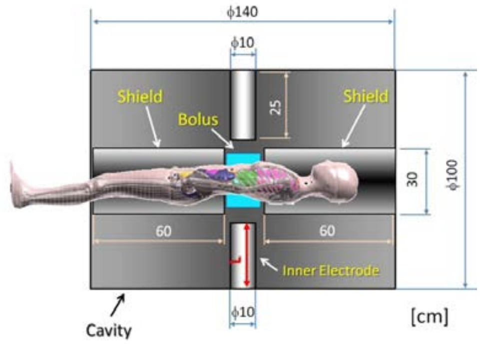

(b) Side view of the improved resonant cavity.

Figure 6. Cross-sectional view of a resonant cavity applicator for abdominal tumors.

Reconstructing the 3D anatomical human model

Figure 7 shows the process of reconstructing the 3D human body model. The proposed reconstruction method consists of 3 steps.
The first step is to collect MRI images taken at intervals of several millimeters. In this study, the 2D images of 320 sheets were used. After that, shown in Fig.7(a), I traced the outlines of all the human tissue.
The 2nd step is to collect and combine the outlines of the all the human tissue and make solid models shown in Fig. 7(b). The commercial 3D computer-aided design (CAD) software, Rhinoceros® (Robert McNeel & Associates) was used in this study.

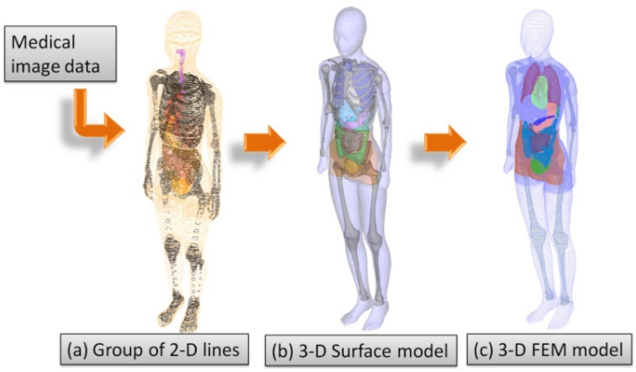

Figure 7. Process of reconstructing the 3D human body model.

The last step is to create the FEM model shown in Fig.7(c). I used the commercial pre-processor, Hyper Mesh® (Altair Engineering, LTD).

The dimensions of this anatomical human model are shown in Fig. 8. This female FEM model has 14 organs. In this study, a tumor (3 × 4 × 3 cm) set in the liver is selected as the object to be heated. The dimensions of the model are 165 cm in height, and 40.5 cm in width at the shoulders. The average mesh sizes and the electrical parameter values at 130MHz for each organ are listed in Table I.

Figure 9 shows a finite element mesh for calculating the SAR distribution. This FEM model, created by the proposed method, and consisting of nonlinear elements, is included in the analysis area (250 × 100 cm). The total number of elements is 1,898,908. We carried out FEM analysis with the 3D model using a personal computer.

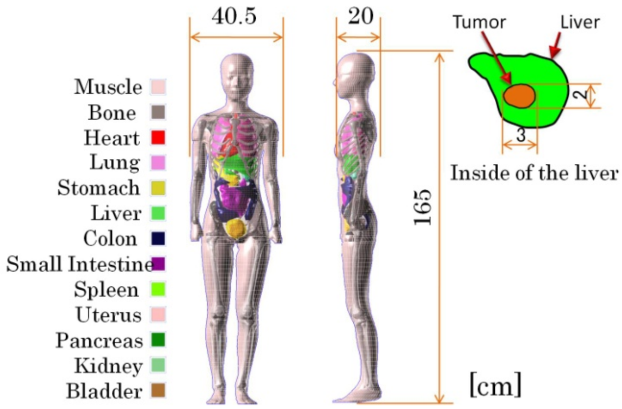

Figure 8. Dimensions of the anatomical body model.

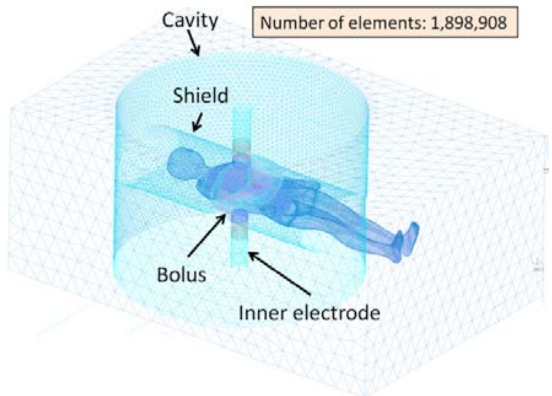

Figure 9. FEM model (Human body with the applicator)

Results and Discussions

Basic evaluation (cylindrical agar phantom)

Figure 10 shows the thermal results of the central section of the agar phantom. Fig. 10(a) is the heating result, and Fig. 10(b) is a thermal image taken by an infrared thermal camera after 60 minutes heating by the re-entrant resonant cavity. The resonant frequencies were 375.90MHz in the simulation result, and 377.55MHz in the experiment. Both of results show that the heated area of the center of the agar phantom was concentrated. From Fig. 10(b), the initial temperature of agar phantom was 22.4ºC, and the center of agar phantom is heated to maximum temperature of 27.4ºC (temperature increase: 5.0ºC) respectively

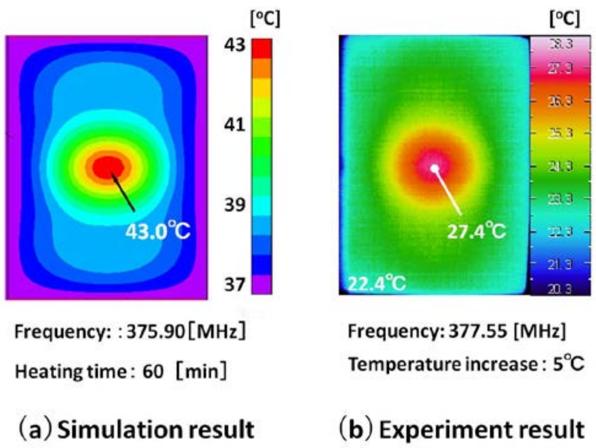

Figure 10. Temperature distributions of the central section of the cylindrical agar phantom

Fig. 11 shows the measured and estimated temperature profiles along x-axis of the both temperature results. To discuss the heating properties of our heating method in detail, the normalized temperature, T_N, is given by the following equation;

$$T_N = \frac{(T - T_0)}{(T_{\max} - T_0)} \tag{7}$$

Where T_0 is the initial temperature, T_{max} is the maximum temperature inside the agar phantom. From Fig. 11, the estimated temperature agrees with the measured temperature with an error of 5% or less on x-axes at the normalized temperature 0.8.
From this comparison of computational and experimental results showed that both were well in agreement.

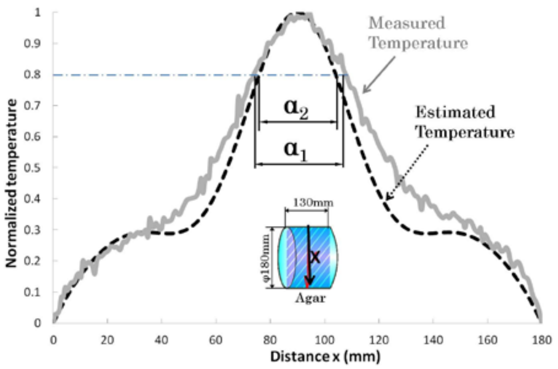

Figure 11. Temperature profiles on the X-axis

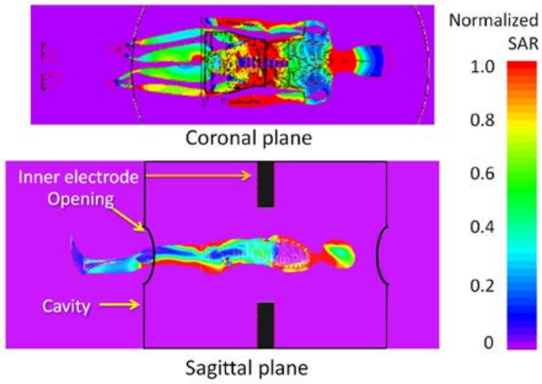

(a) Cavity before the improvement.
(Resonant Frequency: 123.0MHz.)

Calculation using anatomical human body model

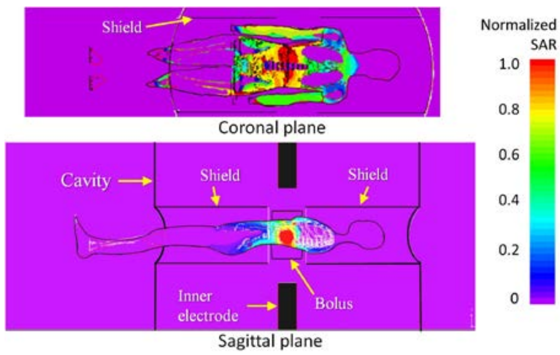

(b) Improved cavity.
(Resonant Frequency: 131.5MHz.)

Figure 12. SAR distributions of side cutting plane. (when L=250mm)

Figure 12 shows the results of normalized SAR distributions calculated by 3D FEM with two applicators, before and after the improvements. Figure 13 shows the close up view of these results. In these results, the lengths of both inner electrodes were 25cm. Figure 13(a) shows the SAR distribution with the cavity applicator before the improvement. Here, the normalized SAR is given by,

$$S_N = \frac{(S - S_{\min})}{(S_{\max} - S_{\min})} \tag{7}$$

where S_N is the normalized SAR, S_{min} is the minimum SAR, S_{max} is the maximum SAR and S is the variable SAR in the human body. The resonant frequency was 123.0 MHz. The heating energy was concentrated on the hip and the head regions. However, in Fig. 13(b), the SAR distribution was concentrated on the selected regions with the proposed applicator. The resonant frequency was 131.5 MHz. The heating power is only concentrated on the gap between the inner electrodes.

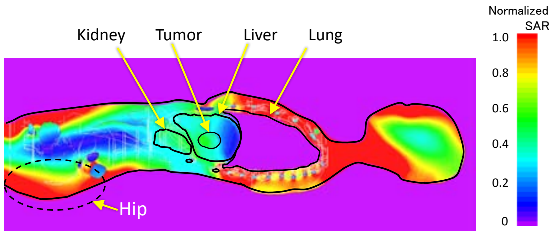

(a) Before the improvement

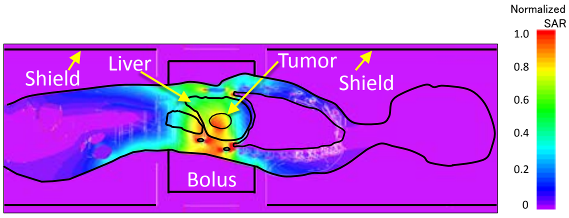

(b) After the improvement

Fig. 13. Close up view of SAR distributions.

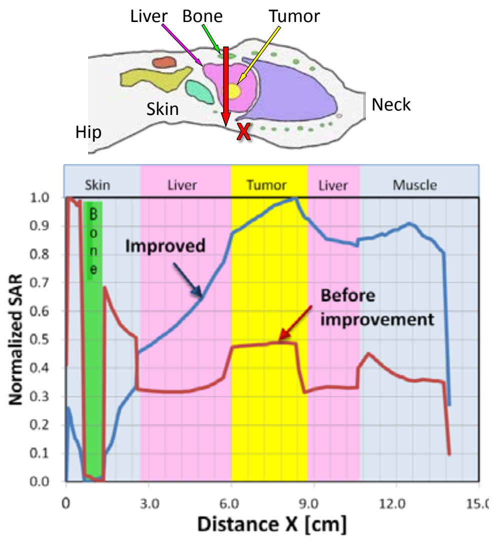

Fig. 14. Normalized SAR profiles on the X-axis.

Figure 14 shows the normalized SAR profiles along X-axis. Before the improvements, the normalized SAR value of the tumor region was half of the abdominal surface region. After the improvements, the maximum normalized SAR value is concentrated on the tumor. From these results, it was shown that the maximum heating energy was deeply concentrated on the liver tumor.

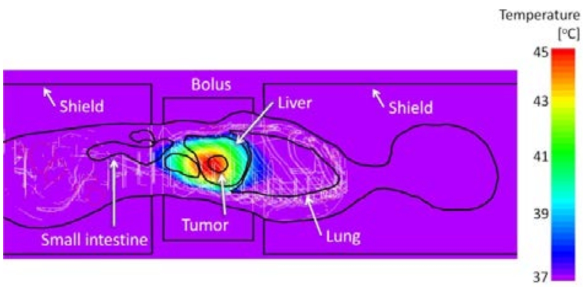

Fig. 15.Temperature distributions (Length of lower electrode: 10cm).

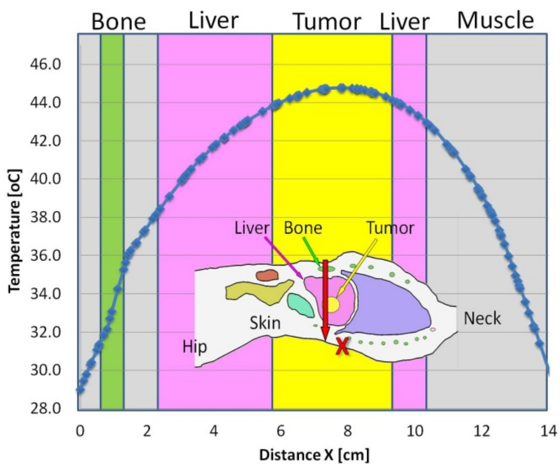

Fig. 16. Temperature profiles on the X-axis.

Fig.15 shows the results of temperature distribution when L is 10cm. From this result, it was found that the heating energy was concentrated on the targeted liver tumor. The tumor was heated to a maximum of 45°C. Coupled analysis of SAR and temperature distributions was carried out. From Fig.15, the maximum temperature inside the targeted liver tumor was 45°C. The surface of the human body was kept cool by the water bolus, which was set at a fixed temperature of 28°C.

As seen in Fig. 16, the temperature distribution results show that the tumor region was heated to a maximum of 45°C, whole of which is well over the minimum requirement for effective hyperthermia treatment (42-43°C).

From these calculations, it was shown that the improved applicator can be effective in heating targeted regions for hyperthermia treatment.

Conclusions

This paper shows the results of coupled analysis of SAR distributions and temperature distributions using an anatomical simulation model reconstructed from 2D medical images.
First of all, in order to show the validity of the proposed calculating method, the temperature distribution of agar phantom was estimated by the FEM. Based on the computer simulation results, the computer simulation and the experimental heating results were discussed. The comparison of computational and experimental results showed that both were well in agreement.
And I evaluate the improved large resonant cavity applicator for non-invasively hyperthermia treatment of deeply seated abdominal tumor. The proposed heating system was designed to protect healthy tissue from concentrated electromagnetic fields.
From SAR distributions, the electromagnetic energy was concentrated on the targeted liver tumor. Furthermore, it was found that the heating energy of the backside region can be eased by adjusting the length of the lower electrode.
And from the estimated temperature distribution, the liver tumor was able to be heated over 43^{o}C using the improved applicator. It was confirmed that the improved heating system was able to non-invasively heat abdominal deep tumors.

References

[1] Crandall CG, Brothers RM, Zhang R, "Human Cerebral Perfusion Is Reduced During Passive Heat Stress, Comments on Point: Counterpoint: Humans do/do not demonstrate selective brain cooling during hyperthermia", Appl Physiol, 2010.

[2] Mathew D White, Jesse Greiner and Patick L. McDonald, Point, "Humans do demonstrate selective brain cooling during hyperthermia", Journal of Applied Physiology vol. 110, No. 2, pp. 569-571, 2011.

[3] Y. Shindo, K. Kato, K. Tsuchiya, T. Yabuhara, T. Shigihara, R. Iwazaki, T. Uzuka, H. Takahashi, Y. Fujii, "Heating Properties of Re-entrant Resonant Applicator for Brain Tumor by Electromagnetic Heating Modes", Proc. Annual International Conference of the IEEE Engineering in Medicine and Biology Society 2007, pp. 3609-3612, 2007.

[4] E.Morita, K.Kato, Y.Shindo *et al.*, "Heating Properties of Non-invasive Hyperthermia Treatment for Abdominal Deep Tumors by 3-D FEM", Proc. of the IEEE EMBC 2009, pp.3389-3392, 2009.

[5] K. Yokoyama, K. Kato, W. Igarashi, Y. Shindo, M. Kubo, H. Takahashi, T. Uzuka, Y. Fujii, "Heating properties of a new hyperthermia system for deep tumors without contact", Proc. Annual International Conference of the IEEE Engineering in Medicine and Biology Society 2011, pp. 310-313, 2011.

[6] Y. Shindo, Y. Iseki, K. Yokoyama, J. Arakawa, K. Watanabe, K. Kato, M. Kubo, T. Uzuka, H. Takahashi, "SAR Analysis of the Improved Resonant Cavity Applicator with Electrical Shield and Water Bolus for Deep Tumors by a 3-D FEM", Proc. 34th IEEE EMBS Ann Int Conf, San diego, pp. 5679-5682, 2012.

[7] T. Yabuhara, K. Kato, Y. Kanazawa, M. Kubo, H. Takahashi, T. Uzuka, Y. Fujii, "Finite element analysis of the needle type applicator made of shape memory alloy", Proc. 30 IEEE EMBS Ann Int Conf, Vancouver, pp. 4364-4367, 2008

[8] Kubo M.,Mimoto N.,Kanazawa Y.,Shindo Y.,Kazuo K.,Takahashi H.,Uzuka T.,Fujii Y.: Heating properties of needle applicator made of shape memory alloy for brain tumor hyperthermia. Thermal Med, 25: 71-80, 2009.

[9] Y. Iseki, Y. Shindo, M. Kubo, K. Watanabe, J. Arakawa1, H. Takahashi, T. Uzuka and K. Kato "Heating Control Method for Resonant Cavity Applicator Using Divided Type of Dielectric Bolus for Effective Hyperthermia Treatment", Proc of 7th European Conference on Antennas and Propagation (EuCAP), pp. 1122-1126, 2013.

[10] Y. Shindo, Y. Iseki, K. Nakanne, N. Mimoto, M. Kubo, K. Kato *etal.* , "A Support System in Virtual Reality for Effective Hyperthermia Treatments: Heating Properties of Needle Applicator for Brain Tumors", Thermal Medicine, Vol. 27, No. 3, pp. 79-87, 2011.

[11] Y. Shindo, K. Shibafuji, Y. Iseki, K. Kato, H. Watanabe, T. Uzuka, A. Takeuchi, “Development of Coaxial Needle Applicator Made of Shape Memory Alloy” Thermal Medicine, Vol. 30, No. 3, pp. 27-40, 2014.

[12] C. Gabriel, “Compilation of the Dielectric Properties of Body Tissues at RF and Microwave Frequencies”, *King’s College London Department of Physics*, pp. 1-15, 1996.

[13] C. Gabriel, S. Gabriel, E. Corthout, “The dielectric properties of biological tissues literature survey”, *Physics in Medicine and Biology*, vol. 41, pp. 2231-2249, 1996.

[14] S. Gabriel, W. Lau, C. Gabriel, “The dielectric properties of biological tissues: II. Measurements in the frequency range 10 Hz to 20 GHz”. *Physics in Medicine and Biology*, vol. 41, pp. 2251-2269, 1996.

[15] S. Gabriel, W. Lau, C. Gabriel, “The dielectric properties of biological tissues: III. Parametric models for the dielectric spectrum of tissues”. *Physics in Medicine and Biology,* vol. 41, pp.2271-2293, 1996.

[16] Jens Lang, Bodo Erdmann, Martin Seebass, “Impact of Nonlinear Heat Transfer on Temperature Control in Regional Hyperthermia”, IEEE Transactions on Biomedical Engineering, vol. 46, No. 9, 1999.

[17] Kenneth R. Holmes "Thermal properties.", pp.1-14, 2009. http://users.ece.utexas.edu/~valvano/research/Thermal.pdf

[18] J.W. Valvano, J. R. Cochran K. R. Diller, “Thermal Conductivity and Diffusivity of Biomaterials Measured with Self-Heated Thermistors”, Journal of Thermo Physics, 6 (3), pp. 301-311, 1985.

[19] Koehler, RC, RJ Traystman and MD Jones, Jr. “Regional blood flow and O_2 transport during hypoxic and CO hypoxia in neonatal and adult sheep”. *Am. J. Physiol*., 248, pp. 118-124, 1985.

[20] Bodo Erdmann, Jans Lang, Martin Seebass, “Adaptive Solutions of Nonlinear Parabolic Equations with Application to Hyperthermia Treatments”, ICHMT DIGITAL LIBRARY ONLINE. Begel House Inc., pp. 1-9, 1997.

Hybrid Geometry/Material Monitoring Method for Microcrack Identification

Tomonari Furukawa[1]

[1]Department of Mechanical Engineering, Virginia Polytechnic Institute and State University, USA
[1]Corresponding author: tomonari@vt.edu

Keywords: Microcrack identification, Hybrid method

Introduction

The aim of this project is to establish a novel theoretical and experimental methodology that detects and localizes defects up to microscopic level. The growth and propagation of a crack, which has caused various catastrophic failures to aeronautical and aerospace structures, is rooted in the nucleation and growth of microcracks and their coalescence that results in forming a crack. Due to the inability of the existing methods in identifying defects at microscopic level, structures are traditionally designed with large margins of safety. If the structure can be rehabilitated before any visible signs of deterioration develop, the durability, reliability and survivability of the structure could significantly improve while allowing flexible design with low factor of safety. To date, the majority of structural health monitoring (SHM) methods identify defects using a single sensor with high-frequency wave analysis capability although return signals of such wave may not capture small defects due to the smallness of geometrical irregularities. Recent years have seen the use of multiple sensors accordingly where significant improvement has been made, but the accuracy is limited by the capability of sensors regardless of the number of sensors. This project uniquely adds theoretical and experimental solutions to the current sensor network setup and sees the possibility of identifying up to microcracks, which none of the existing methods can do.

The original contributions of the methodology proposed in the project that guarantees its superiority to the existing methods lie in the following new theoretical and experimental advances of science and technology:

- *Hybrid geometry irregularity and material degradation monitoring*: In addition to the geometrical irregularity measurement from high-frequency wave signals, the proposed methodology detects and localizes defects by material degradation using low-frequency loading signal. The previous work of the investigators experimentally verified that the area at which microcracks grow exhibits more strain variation under a static loading. The material degradation analysis from the displacement and strain field measurement could detect defects that the existing methods measuring geometrical irregularity are incapable of.

- *Three types of sensor network*: The geometrical irregularity and the material degradation are both measured by a network of piezoelectric (PZT) sensors and a network of piezoresistive strain gauges. The material degradation is additionally measured by a network of digital cameras and a numerical technique that extracts displacement and strain field from the camera images. The sensors have trade-offs in accuracy and field-of-view (FoV). The use of multiple types of sensors will maintain accuracy and area of coverage simultaneously.

- *Probabilistic multi-sensor observation fusion*: The multi-sensor data fusion proposed in this project fuses the locations of defects estimated by all sensors and means in terms of not scalar quantities but observation likelihoods unlike the existing deterministic sensor fusion methods. The probabilistic fusion that enables the identification in the framework of recursive Bayesian estimation (RBE) allows the uncertainty to be taken into account and thus makes the identification more reliable.

- *Element-based RBE*: The observation of defects outside the FoVs of sensors can still influence the identification if it is treated as a negative observation likelihood. Since the negative observation likelihood could however make the belief heavily non-Gaussian, the proposed methodology will extensively use the element-based method developed by the investigators for non-Gaussian RBE. The element-based method will show advantages over the other non-Gaussian RBE methods such as the grid-based method and the particle filters for defect identification as it can represent the belief over the solid structure with high-fidelity shape functions.

- *Belief fusion*: The belief fusion enables the identification of defects only by measuring geometrical irregularity or material degradation while the hybrid identification is performed. This allows the traditional defect identification in the same framework and thus sees the improvement by the direct comparison.

The project has been aimed at proving the concept of the proposed hybrid geometry/material monitoring method. More specifically, the proposed method for the proof-of-concept uses a PZT transducer to identify the geometrical irregularities caused by a defect whereas an industrial CCD camera and the Dot Centroid Tracking (DCT) method are used identify the material degradation. In order to experimentally validate its efficacy, the proposed method was applied to the measurement of geometrical irregularity and material degradation of three specimens each made of a different material. These materials identify geometrical irregularity and material degradation at different amplitudes.

The paper is organized as follows. The next section introduces the basics of the optical method or the camera-based method that includes the DCT method whereas the vibration method including a technique with a PZT transducer and the high-frequency wave analysis is described in the third section. The fourth section presents the proposed method, and the capability of the proposed method is experimentally investigated in the fifth section. The final section summarizes the conclusions made in the first-year effort.

1 Optical method

One of the key concepts of the proposed hybrid method is to measure material degradation by using an optical sensor such as a digital camera. A popular sensor used to measure the strain has been the strain gauge. While it measures even highly sensitive strain very accurately as a contact sensor, the strain gauge is not suited for the measurement of material degradation. Firstly, it is limited to the measurement at a point, so that the field strain cannot be extracted unless a number of strain gauges have been glued to the field of interest, which is highly cumbersome. Further, a strain gauge measures only longitudinal strain, so the measurement of shear strain requires at least two strain gauges at a point.

Meanwhile, a optical method has received significant attention as a non-contact displacement and strain field measurement technique in the last couple of decades. These include the holography [9], the speckle interferometry[10], the speckle photography[2], the pure grid method [17, 19], the digital image correlation (DIC) method [3, 20], and the DCT method[1]. Among these, the camera-based techniques including the pure grid method, the DIC method and the DCT method, become the lowest-cost solutions in both cost and effort. Out of the camera-based methods, the dot centroid tracking (DCT) method, in part developed by the investigators, has been found to achieve the best accuracy and speed provided that the system is properly set up.

1.1 Theory

Figure 1 illustrates the concept and function of the DCT method. The specimen in the figure is supposed to unexpectedly have a defect invisible from the front side. Both the upper and side views do not see the defect as shown in the figure. The DCT method prepares the specimen with a number of dots marked on its surface to measure the strain field. When a camera observes the specimen under a tensile force in the y direction, the location of each dot changes differently due to the deformation of the specimen; dots on the thin part of the specimen exhibits larger displacement than the dots on the thick part. Since the strain is given by the first derivative of the displacement, the extraction of the strain field sensitively identifies the existence, the location and the geometry of the defect.

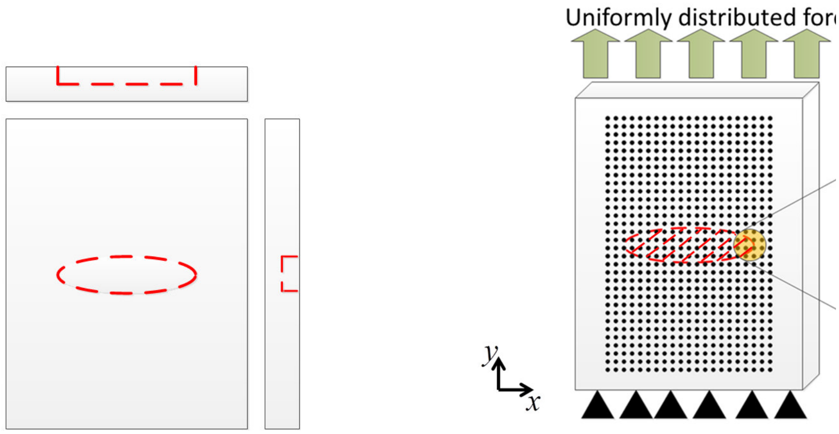

(a) Specimen (b) DCT method

Figure 1: (a) Illustration of invisible crack from the front side,(b) After applying tensile force in y-direction, full strain field is measured by meshless method. Dashed line circles represent location of dots on the undeformed material surface. Black dots represent location of dots on the deformed material surface.

Figure 2 is a simulation result by using a commercial finite element analysis tool to illustratively understand the concept. Figure 2(a) shows the front view of a specimen, Figure 2(b) shows the back view of the specimen, which sees multiple circular defects, and Figure 2(c) shows strain fields of the front and back sides after a tensile force in the y direction is applied to the specimen. Clearly the existence, the location and the geometry of the defects can be found from the front view though the defects are not visible from the front side.

Figure 3 visually explains the procedure to identify invisible defects using the DCT method. First the front surface of the specimen with invisible defects is marked with dots. A mechanical

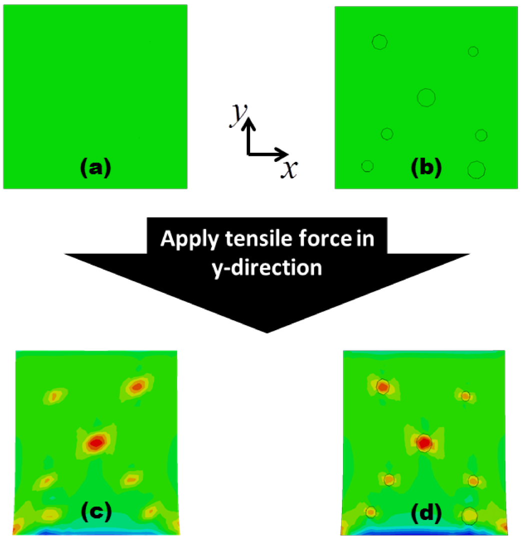

Figure 2: Result of simulation of full strain field measurement of defected specimen. (a) and (b) show front and back view of defected specimen before applying tensile force. (c) and (d) show full strain measurement after applying tensile force in y-direction.

load is then provided by a loader. By measuring a strain field using the DCT method, the existence, location and geometry of the defects can be identified from the front view.

Having understood the concept of defect identification through the strain field measurement, the next section will validate the effectiveness of the proposed material degradation measurement method by presenting experimental results.

1.2 Result

The effectiveness of the proposed material degradation measurement method was investigated with a specimen with an artificial defect. The specimen was an aluminum plate with a circular hole. Table 1 shows the parameters of the specimen. The front side of each specimen was marked with dots as shown in Figure 1.5. Figure 1.4 shows the configuration of experimental

Table 1: Mechanical properties of the aluminum specimen

Properties	Aluminum (at 25 °C)
Poisson Ration	0.33
Density(kg/m^3)	2710
Elastic Modulus(GPa)	69
Tensile Strength(MPa)	110
Yield Strength(MPa)	105

systems. Using uniformed light source, effect of light noise becomes minimized (Figure 1.4).

Figure 1.6 shows the strain fields ($\epsilon_x, \epsilon_y, \epsilon_{xy}$) identified by the DCT method. The irregular distribution around the circular hole shows the existence of the defect in the specimen clearly.

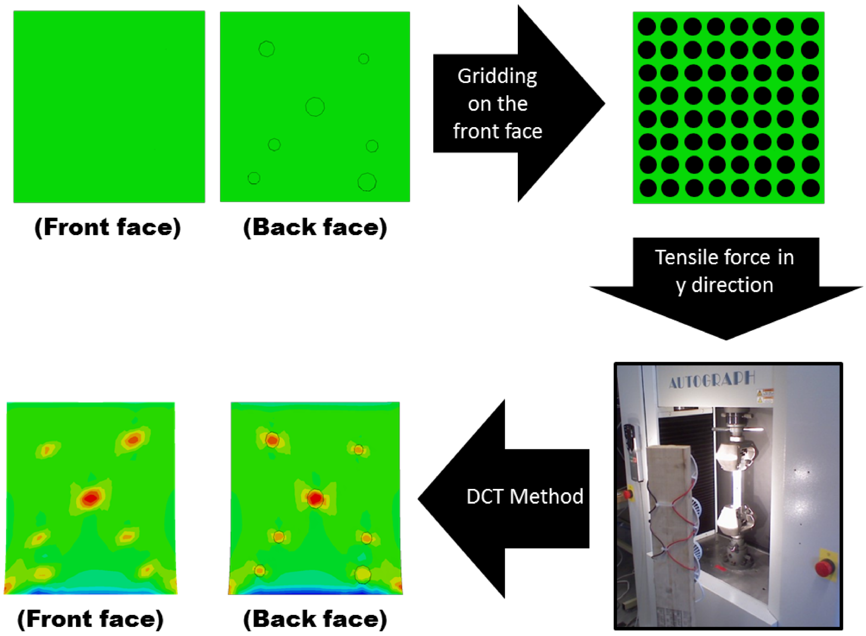

Figure 3: Procedure of full strain field measurement using DCT

2 Vibration method

Vibration methods estimate the damage by comparing the structural dynamic response (obtained by analyzing signals from transducers) with referencing baseline signals (collected from a benchmark structure supposed to be damage-free). They can be classified into active methods and passive methods based on whether the vibration is actively controlled. In active methods, the structure can be excited in an array of vibration actuators. The proposed geometrical irregularity measurement method uses piezoelectric transducers (PZT) as a vibration actuator and measures return signals of waves propagated over the structure. In the following subsections, the theory of surface waves generated by the PZT will be introduced, and the analytical solution to waves on a plate will be further formulated.

2.1 Lamb Wave

This section will introduce an important class of waves for SHM, which are guided waves. Since guided waves can travel at large distances in structures without much dissipation of energy, it can be a good candidate for SHM usage. Especially, guided waves is good for thin plate specimens. These properties allow them to apply to the ultrasonic inspection of aircraft, missiles, pressure vessels,oil tanks, pipelines, etc. In this project, lamb waves are chosen among several guided waves. Through advances in various related disciplines over the past two decades, there have been a number of studies for developing damage identification techniques using Lamb waves[13, 6, 21]. Through intensive research in this area, Lamb waves have shown their excellent properties for cost effective damage identification. Lamb waves are widely used acoustic-ultrasonic guided waves for damage identification[11].

2.1.1 Theory of Lamb Wave

Using simple plane structure such as isotropic plate, we can understand how the Lamb wave propagate in the structure. In a thin isotropic and homogeneous plate as shown in Figure 2.7,

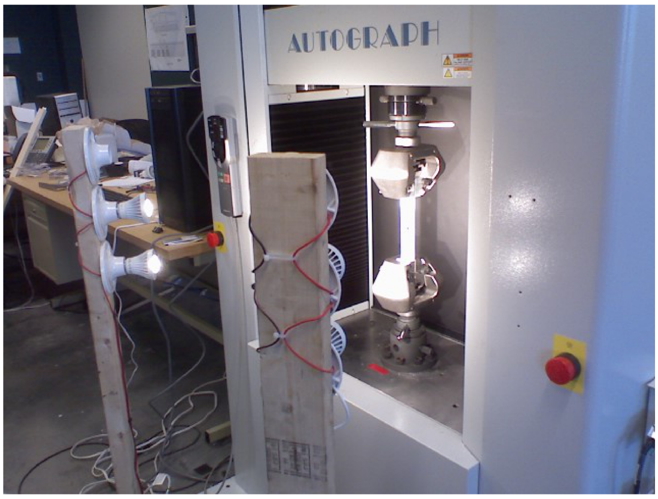

Figure 4: Experiment set-up

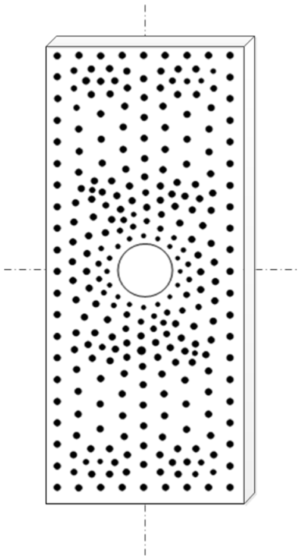

Figure 5: Illustration of dot pattern

the waves can generally be described in a form of Cartesian tensor notation as

$$\mu \cdot u_{i,jj} + (\lambda + \mu) \cdot u_{j,ji} + \rho \cdot f_i = \rho \cdot \ddot{u}_i \tag{1}$$

where u_i and f_i are the displacement and body force in the x_i direction, respectively. ρ, μ, and λ are density, shear modulus of the plate, and Lame constant, respectively[7]. The displacement potential approach based on Helmholtz decomposition is an efficient approach to decompose Equation 1 into two uncoupled parts with the condition of plane strain,

$$\frac{\partial^2 \phi}{\partial x_1^2} + \frac{\partial^2 \phi}{\partial x_1^2} = \frac{1}{c_L^2} \frac{\partial^2 \phi}{\partial t^2} \tag{2}$$

$$\frac{\partial^2 \psi}{\partial x_1^2} + \frac{\partial^2 \psi}{\partial x_1^2} = \frac{1}{c_L^2} \frac{\partial^2 \psi}{\partial t^2}, \tag{3}$$

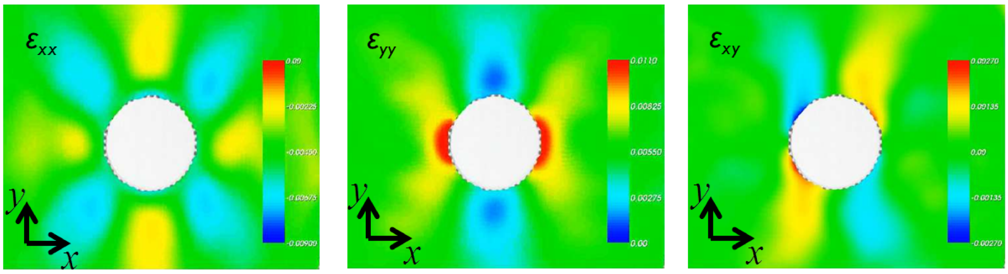

Figure 6: Full strain field measurement

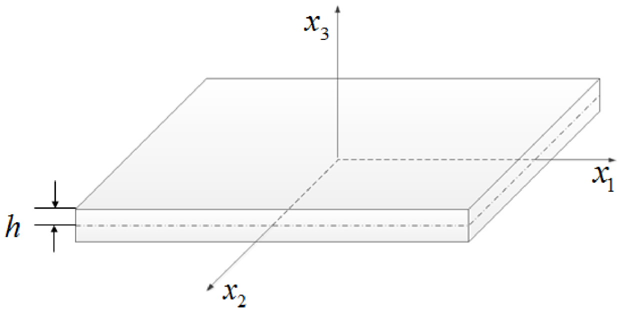

Figure 7

where

$$\phi = [A\sin(px_3) + B\cos(px_3)] \cdot e^{i(\kappa x_1 - \omega t)}, \quad (4)$$
$$\psi = [C\sin(qx_3) + D\cos(qx_3)] \cdot e^{i(\kappa x_1 - \omega t)}, \quad (5)$$

where A, B, C and D are four constants determined by the boundary conditions.

$$p^2 = \frac{\omega^2}{c_L^2} - \kappa^2, \qquad q^2 = \frac{\omega^2}{c_T^2} - \kappa^2, \qquad \kappa = \frac{2\pi}{\lambda}, \quad (6)$$

where κ, λ, and ω, and are wavenumber, wavelength, and angular velocity, respectively. c_{L} and c_{T} are the velocity of longitudinal and transverse modes, which are defined by

$$c_{\mathrm{L}} = \sqrt{\frac{E(1-\nu)}{\rho(1+\nu)(1-2\nu)}}, \quad (7)$$
$$c_{\mathrm{T}} = \sqrt{\frac{E}{2\rho(1+\nu)}}, \quad (8)$$

where E denotes elastic modulus, so-called the Young's modulus, $E = 2\mu(1+\nu)$. They are reduced to

$$c_{\mathrm{L}} = \sqrt{\frac{2\mu(1-\nu)}{\rho(1-2\nu)}}, \quad (9)$$
$$c_{\mathrm{T}} = \sqrt{\frac{\mu}{\rho}}. \quad (10)$$

Even thought there are many modes simultaneously between the upper and lower surfaces of the plate, a well behaved guided wave leads all the modes. Under the plain strain assumption, the displacement can be reduced to

$$
\begin{aligned}
u_1 &= \frac{\partial \phi}{\partial x_1} + \frac{\partial \psi}{\partial x_3}, && (11)\\
u_2 &= 0, && (12)\\
u_3 &= \frac{\partial \phi}{\partial x_3} - \frac{\partial \psi}{\partial x_1}. && (13)
\end{aligned}
$$

In addition, stress are expressed as

$$
\begin{aligned}
\sigma_{31} &= \mu\left(\frac{\partial^2 \phi}{\partial x_1 \partial x_3} - \frac{\partial^2 \psi}{\partial x_1^2} + \frac{\partial^2 \psi}{\partial x_3^2}\right), && (14)\\
\sigma_{33} &= \mu\left(\frac{\partial^2 \phi}{\partial x_1^2} + \frac{\partial^2 \phi}{\partial x_3^2}\right) + 2\mu\left(\frac{\partial^2 \phi}{\partial x_3^2} - \frac{\partial^2 \psi}{\partial x_1 \partial x_3}\right). && (15)
\end{aligned}
$$

Since the geometry of thin plate has the following boundary conditions,

$$
\begin{aligned}
u(x,t) &= u_0(x,t) && (16)\\
t_i &= \sigma_{ij} n_j && (17)\\
\sigma_{31} &= \sigma_{33} = 0 \qquad at \quad x_3 = \pm\frac{d}{2} = \pm h, && (18)
\end{aligned}
$$

the general solution of Lamb wave is expressed as

$$
\frac{\tan(qh)}{\tan(ph)} = \frac{4\kappa^2 qp\mu}{(\lambda\kappa^2 + \lambda p^2 + 2\mu p^2)(\kappa^2 - q^2)}. \qquad (19)
$$

Equation 19 can be separated into symmetric part and anti-symmetric part by substituting Equation 6 into this solution.

$$
\begin{aligned}
\frac{\tan(qh)}{\tan(ph)} &= -\frac{4\kappa^2 qp}{(\kappa^2 - q^2)^2} && (20)\\
\frac{\tan(qh)}{\tan(ph)} &= -\frac{(\kappa^2 - q^2)^2}{4\kappa^2 qp}. && (21)
\end{aligned}
$$

In addition, the speed of wave propagation is characterized into phase velocity and group velocity like,

$$
\begin{aligned}
c_{\mathrm{p}} &= \left(\frac{\omega}{2\pi}\right) \cdot \lambda, && (22)\\
c_{\mathrm{g}}(f \cdot d) &= \frac{c_{\mathrm{p}}^2}{c_{\mathrm{p}} - (f \cdot d)\frac{dc_{\mathrm{p}}}{d(f \cdot d)}}, && (23)
\end{aligned}
$$

where c_{p} is phase velocity and c_{g} is group velocity.

2.1.2 Tone burst

The wave dispersion phenomenon is most readily demonstrated during the study of the propagation of narrow band frequency wave packets, known as tone bursts. When used as a diagnostic wave, a Lamb wave mode's cycle number, frequency, and magnitude are important features that can improve the capability of damage identification, at least to a certain extent. Previous experiments using Lamb wave modes at different frequencies in plates show that a narrow bandwidth signal with a certain number of cycles can significantly prevent wave dispersion. For that reason, windowed tone bursts , rather than a single pulse or simple sinusoidal signals, are used much more often to activate diagnostic wave signals in practice, although a pulse signal may offer higher and more concentrated incident energy. Windowing techniques are used to narrow the bandwidth of a selected Lamb mode. The Hanning window is the most widely adopted window function, defined as

$$h(n) = \frac{1}{2}[1 - \cos(2\pi \frac{n}{N-1})], \qquad (n = 1, 2, \ldots, N), \tag{24}$$

where h is discretized using N sampling points. Figure 2.8 and Figure 2.9 show how the

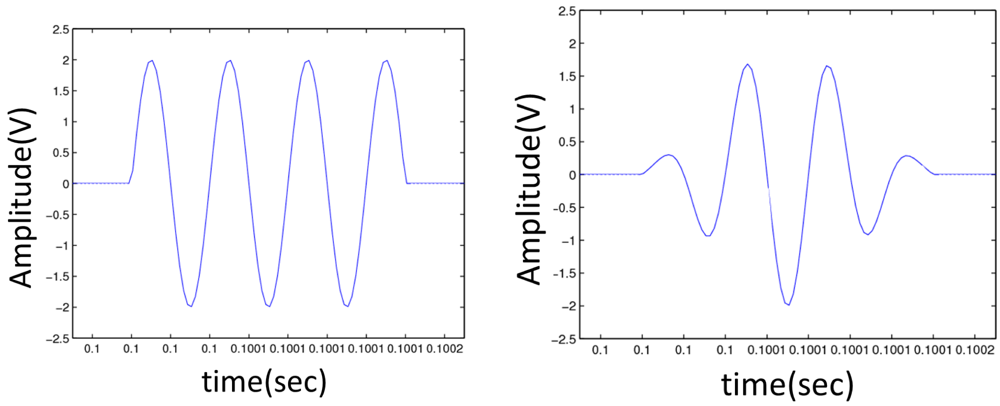

(a) (b)

Figure 8: Comparison of original sinusoid (a) and hanning window filtered wave (b)

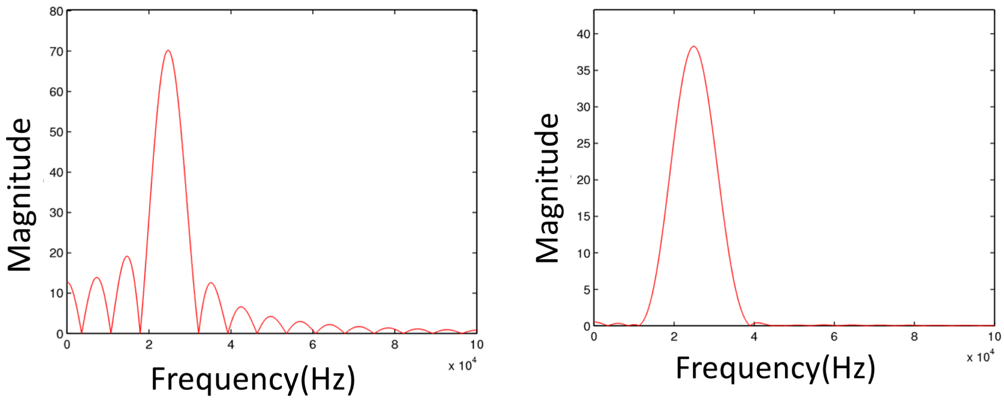

(a) (b)

Figure 9: FFT comparison of origina sinusoid (a) and hanning window filtered wave (b)

application of windowing function generates a given 3.5 cycles sinusoidal signal to tone burst signal in both time domain and frequency domain.

2.2 Result

To generate Lamb waves, Data Acquisition (DAQ) board in a personal computer is used with 1MHz sampling rate Digital Analog Convertor (DAC) It is amplified by a charge mode amplifier circuit board (Voltage range is from $-15V$ to $15V$), and then amplified voltage apply to PZT cemented on a specimen. Using matlab code, frequency and amplitude can be controlled. The excitation signals has 3.5 cycles for generating higher dispersive Lamb wave and sent to 2 PZT actuators on the specimen. To measure the reflected wave, 2 PZTs are used as sensors and they are connected to ADC of DAQ board. Matlab code can display and analyze the received data through DAQ board. Figure 2.10 shows picture of PZT used in this project and Table 2

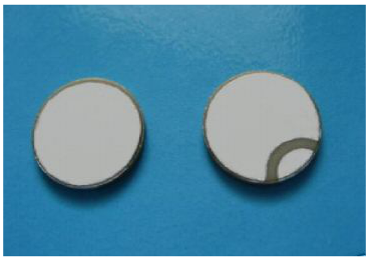

Figure 10: Picture of piezoelectric sensor/actuator

shows mechanical properties of PZT. To transfer and receive a wave of the specimen plate, these PZTs should be assembled perfectly with an adhesion. Figure 2.11 displays the architecture of PZT system. Figure 2.12 illustrates how PZTs are used for structural health monitoring. Once

Table 2: Properties of Piezoelectric Ceramic Transducer

Piezoelectric Ceramic Transducer	
Material	SM411
Dimension	7mm diameter x 0.5mm thickness
Resonant Freq	300kHz $\pm$ 10kHz
Static capacitance	1400 pF $\pm$ 15% @ 1kHz

PZT actuators generate specified signals, those signals will be propagated along the specimen. However, if there are cracks, holes, or abnormalities, the propagated signals will be attenuated scattered to ambiguous direction. It makes PZT receivers detect differences between health materials and unhealth materials. There are many methods to analyze those received signal to find exact location of defects, and there is no exact solution to defect identification by using PZTs.

Figure 2.13 shows how PZTs are assembled on the aluminum specimen. PZT transmitter is connected to amplifier which is to amplfy the tone burst signal coming from DAQ board in computer. PZT receiver is connected to DAQ board directly to measure the propagated wave from the transmitter along the specimen. Figure 2.14 plots the transmitted and received signal from PZTs. To measure time of flight, difference in time,Δt between first peaks of each waves, which is $14\mu sec$.

$$v_{wave} = \sqrt{\frac{E}{\rho(1-\nu^2)}} \tag{25}$$

where v_{wave} is velocity of wave inside of material, E is elastic modulus, ρ is density of material, and ν is possion's ration of material. Substituting the parameters of the table 3 into Equation 25,

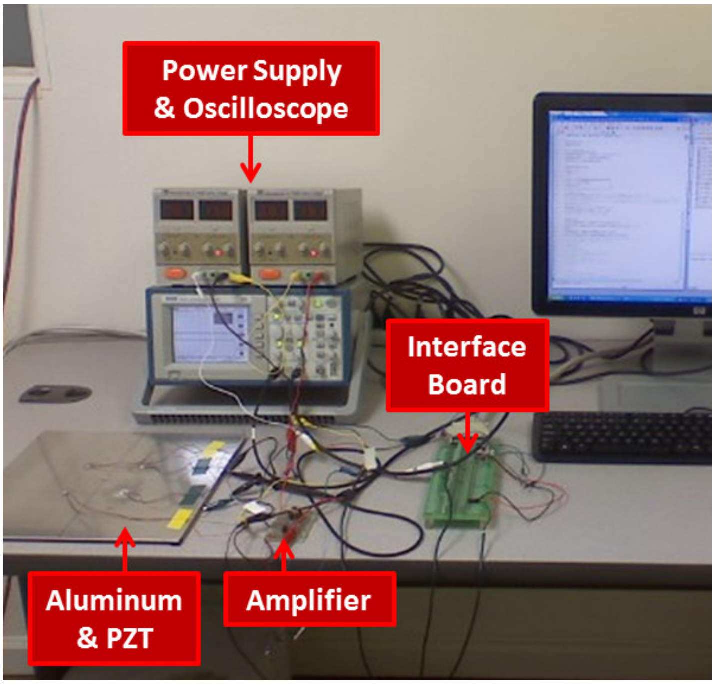

Figure 11: Experimental system for vibration method

the wave speed of aluminum plate is $5345m/sec$. calculating travel distance of wave signal by multiplying v_{wave} and Δt, it becomes $0.07483m$ which is very close to the physically measured distance by ruler, $0.0762m$. In this report, detecting a crack on the aluminum specimen with multi-PZT sensors and actuators is out of our scope. The purpose of this experiment is to show a potential to use vibration method for hybrid method which are suggested by this report. In the next section, we have presented a hybrid method and several experimental result to verifying this method.

3 Hybrid method

This section presents how optical method and vibration method are cooperated together for improving robustness of defect identification. In the preceding sections, we have a better understanding what the vibration method and optical method are. Hybrid method is a method combining those two method by using a sensor network technique. The geometrical irregularities are measured by using vibration method with high-frequency wave signals, and material degradations are measured by using optical method using low-frequency or static loading signal. The material degradation analysis from the full-field strain measurement could detect defects that the existing methods measuring geometrical irregularity are incapable of. The geometrical irregularity measured by a network of PZT and the material degradation is additionally measured by a network of digital cameras. The sensors have tradeoffs in accuracy and Field-of-View (FoV). The use of multiple types of sensors will maintain accuracy and area of coverage simul-

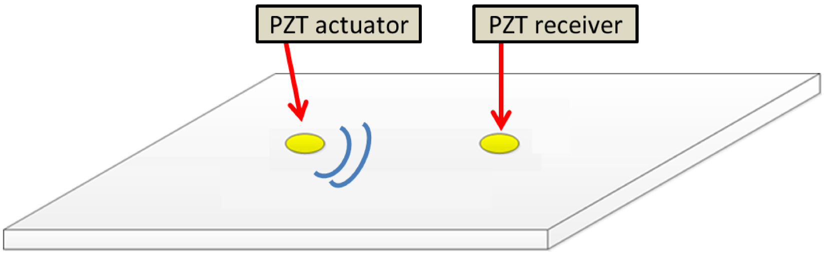

Figure 12: Schematic of vibration experiment system

Table 3: Properties of aluminum specimen

Aluminum specification (at 25 °C)	
Poisson Ration	0.33
Density	2710 kg/m^3
Elastic Modulus	69GPa
Tensile Strength	89.6 MPa
Yield Strength	34.5 MPa

taneously. The probabilistic fusion that enables the identification in the framework of Recursive Bayesian Estimation (RBE) allows the uncertainty to be taken into account and thus makes the identification more reliable. The observation of defects outside the FoVs of sensors can still influence the identification if it is treated as a negative observation likelihood.

3.1 Theory

The belief fusion enables the hybrid identification by combining the identification of defects measured from both geometrical irregularity and material degradation. Figure 3.15 shows the schematic diagram of the proposed methodology. Target motion block represents the model of defect location on the specimen. Using previous correction, new probability density function (PDF) of prediction in step 'k' is calculated. Using predicted location of defects, $\tilde{x}_k$, sensor models generate new observations, $\tilde{z}_{1:k-1}$. Those generated probability function is called likelihood, $l(x_k|\tilde{z}_{1:k-1})$. In the hybrid method, there are two sources of likelihood: PZT sensor network and camera sensor network. The geometrical irregularity is measured with networks of PZTs by generating high-frequency vibration whereas the material degradation is measured with networks of digital cameras by providing low-frequency loading input. The collected sensor measurements are fused probabilistically via observation fusion and the defect identification is maintained stochastically by the RBE. The belief fusion enables the synchronization of beliefs by the geometrical irregularity and the material degradation measurements, allowing more reliable identification than that by a single method.

3.2 Results

This report has provided a potential usage of hybrid method for defect identification by showing results getting from 3 different materials: aluminum plate, glass-fiber reinforced plate and rubber plate. Since aluminum plates have high stiffness, vibration method using PZT is very useful to measure time of flight of reflected waves from abnormal properties of materials. However, optical method is not efficient, because high stiffness requires strong tensile force to show a visible strain field. Second material is Glass-Fiber Reinforced Plate (GFRP) which is most

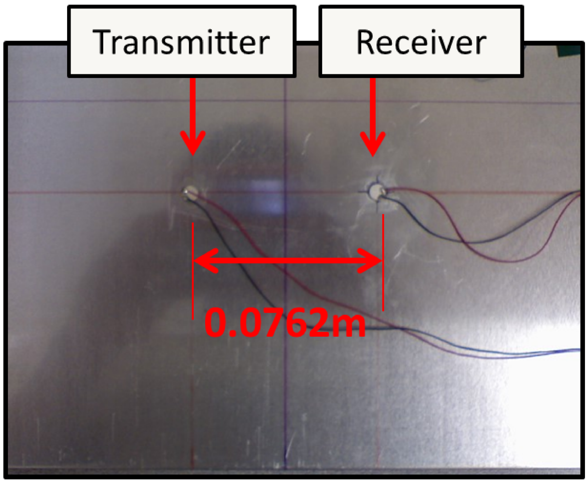

Figure 13: Installation PZT on a specimen

popular material for aerial industry. GFRP shows nonlinear behavior, so we can not use an analytical solution to wave equation which requires homogeneity of materials, whereas optical method shows a good performance for this material. Finally, rubber plate is used to show a paramount potential of this hybrid method, which existing structural health monitoring method couldn't apply to. Since rubber plate is high viscosity and high damped material, vibration method cannot be applied. However optical method can detect a class by observing a strain field. The following three subsections shows the results in detail and the Table 4 is a list of material properties.

3.2.1 Aluminum plate

Aluminum 1100 is used for this experiment. Figure 3.16(a) shows a dot pattern for applying DCT method and Figure 3.16(b) shows artificial defects which is invisible from the front side. After applying tensile force in y direction, we have observed a strain field, Figure 3.16(c). The red color distribution is too wide and too ambiguous to estimate the location of the artificial defects. However, vibration method shows a tangible potential to estimate a location of defect on the material by showing the demonstration of time of flight measurement. Figure 3.17(a) shows the installation of PZT actuator and sensor on the aluminum plate. Transmitter generates

Table 4: Properties of materials for verifying hybrid method

Properties	Al. (at 25 °C)	GPRF	Rubber
Poisson Ration	0.33	0.33	0.22
Density (kg/m^3)	2710	1500	1500
Elastic Modulus (GPa)	69	26	0.028
Shear Modulus (GPa)	26	10	0.0006
Ultimate Tensile Strength (MPa)	89.6	530	15
Yield Strength (MPa)	34.5	125	-
Breaking strain (%)	12	2	-
Thermal expansion ($10^-6/C$)	33	19	77

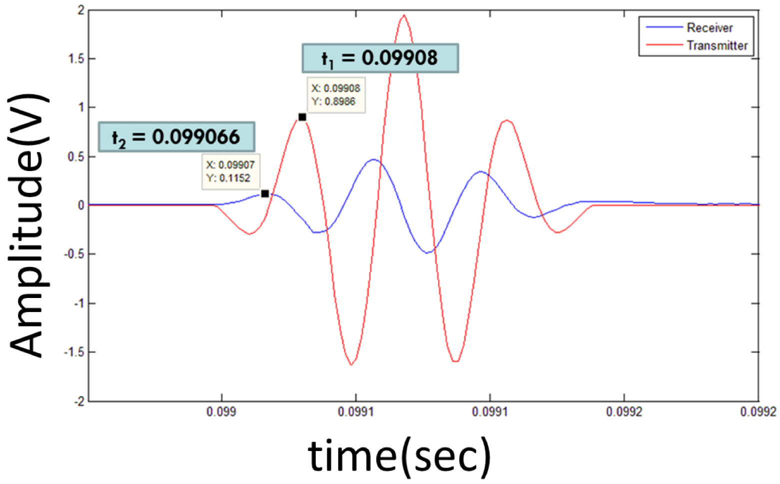

Figure 14: Time of flight measurement of aluminum plate, blue line is received signal and red line represents tone burst signal.

a vibration, and the vibration propagates through the aluminum specimen. The propagated wave is detected by the receiver and time of flight is measured as well. From the material properties in Table 4, wave speed of material is calculated by Equation 25. With this velocity and the time of flight, we can estimate a distance between the transmitter and the receiver. Substituting the parameters of the Table 3 into Equation 25, the wave speed of aluminum plate is $5345m/sec$. calculating travel distance of wave signal by multiplying v_{wave} and Δt, it becomes $0.07483m$ which is very close to the physically measured distance by ruler, $0.0762m$. The result of calculation shows that there is almost zero error between estimated distance and physically measured distance. In this experiment, even thought we didn't use this vibration method for a damaged aluminum plate, this demonstration shows a possibility to use vibration method to detect defections for aluminum plate.

3.2.2 Glass-Fiber Reinforced Plate (GFRP)

GFRP is a composite material which is popularly used in aerial industry, because it has light weight and strong strength. However, since shows very weak performance in the transverse direction, crack propagation in that direction will be particularly fatal. To prevent this kind of accidents, it is very important to detect invisible defects. Figure 18(a) shows a regular dot pattern, which means that there are unknown defects. Figure 18(b) shows an artificial defects which is not observable from the front side. After applying optical method, we can see the strain field of the GFRP and we can estimate a location of invisible defects (Figure 18(c)). In addition, to check the availability of vibration method, we install two PZT on the GFRP (Figure 19(a)). From both the GFRP properties and Equation 25, we can get $3958m/sec$ as a speed of wave in GFRP. Multiplying the time of flight from the Figure 3.19(b) with the speed of wave, the calculated distance is $0.03958m$ which is not close to physically measured distance, $0.0762m$. This result has presented that hybrid method can complement classical vibration method which is popular in structural health monitoring field by using optical method.

3.2.3 Rubber plate

This section shows the specialty of this hybrid method by applying this method to rubber which most of existing structural health monitoring technique can be applicable. Figure 3.20 (a) shows

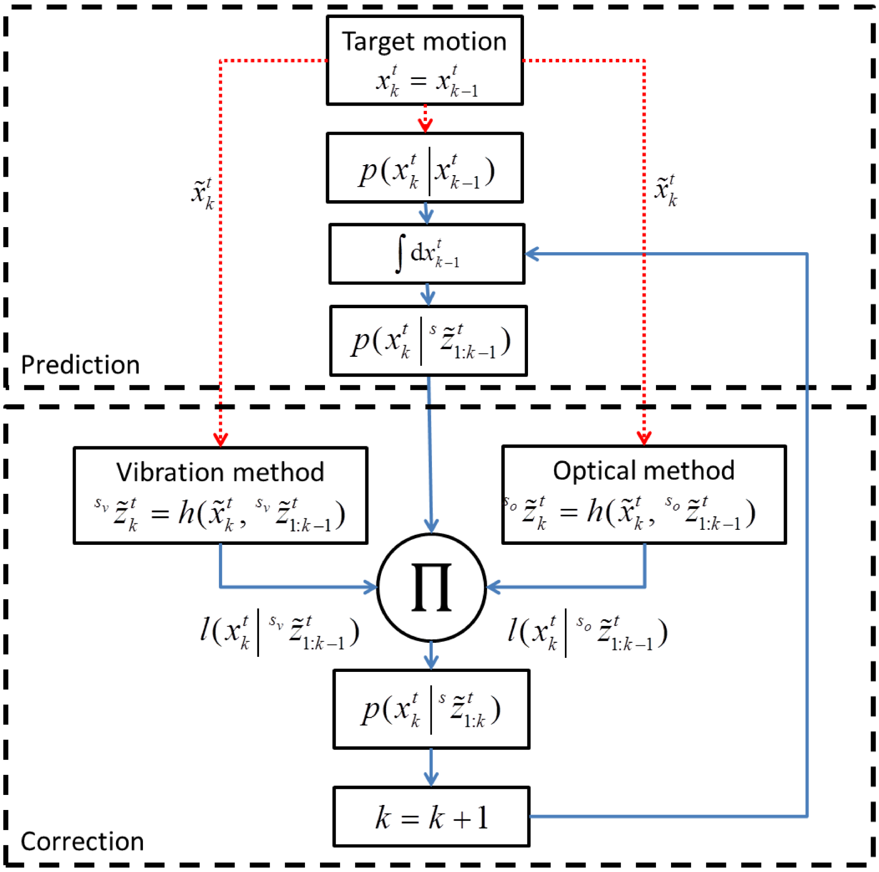

Figure 15: Schematic of hybrid method

a doc pattern for optical method and Figure 3.20 (b) shows a crack which is invisible from the front side. After applying optical method, we can obtain a strain field, Figure 3.21(b). It allows us to estimate a location of invisible defects intuitively. To show the inapplicability of vibration method, we have added a result below. From the Table 4 and Equation 25, we can obtain the wave speed inside of rubber, $333m/sec$. Since Figure 3.22(b) tells the time of flight is $10\mu sec$, the calculated distance becomes $0.0033m$ which is not close to the physically measured distance. The fail of vibration method for rubber is very obvious, because rubber has high viscosity which make wave propagation hard and attenuated easily.

(a) (b) (c)

Figure 16: Full strain field measurement of aluminum plate, (a) dot pattern, (b) artificial defects on the back side of the specimen, and (c) result of full strain field measurement using DCT.

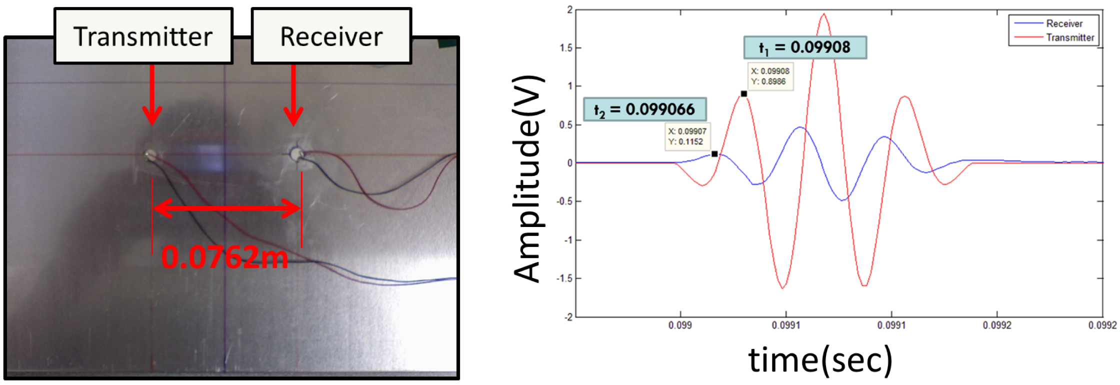

(a) (b)

Figure 17: Time of flight measurement of aluminum plate

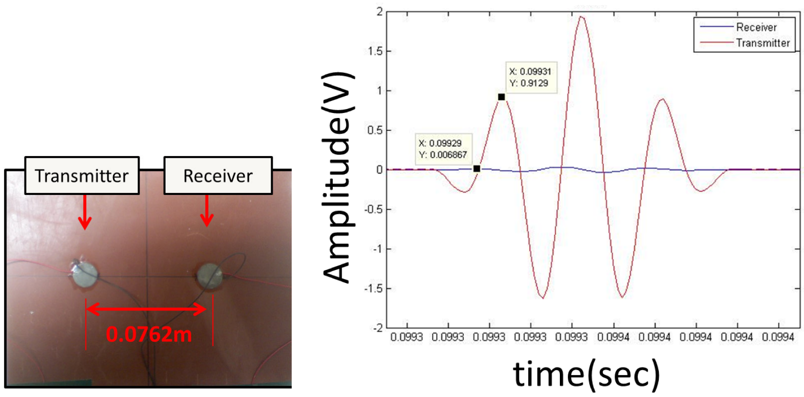

(a) (b)

Figure 22: Time of flight measurement of rubber plate

(a) (b) (c)

Figure 18: Full strain field measurement of glass-fiber reinforced plate, (a) dot pattern, (b) artificial defects on the back side of the specimen, and (c) result of full strain field measurement using DCT.

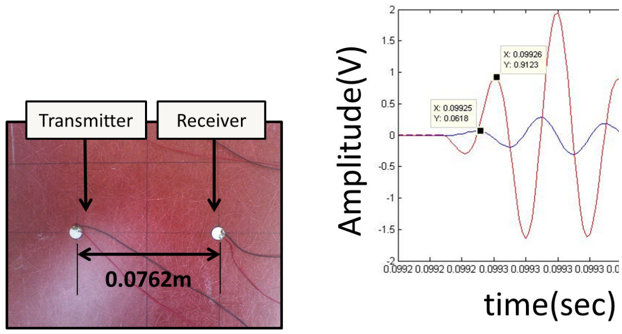

(a) (b)

Figure 19: Time of flight measurement of glass-fiber reinforced plate

However, since hybrid method can use both optical method and vibration method, they complement each other and the result have a potential to use in practical for monitoring rubber structure.

4 Conclusion

This paper has presented the first-year outcomes of the three-year project developing the hybrid geometry/material monitoring method for microcrack identification. The geometrical irregularity measurement method has been developed with a PZT transducer and associated wave analysis techniques whereas a digital camera and the novel DCT method has been implemented for material degradation measurement. The specimens or structures are specified by geometrical and material properties. By measuring both properties and identifying defects, the proposed method has the potential for identifying a variety of defects including microcracks.

The proposed method was tested for the identification of defects on different specimens. The application of the material degradation measurement method to the holed specimen with a tensile load has shown its capability for measuring the strain field and identifying defects whereas the

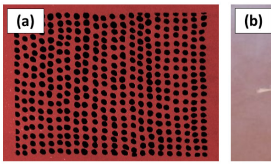

Figure 20: (a) The front face of rubber plate with dot pattern, (b) the back face of rubber plate with a crack which is not through the rubber plate.

(a) (b)

Figure 21: Full strain field measurement of rubber, (a) artificial crack named kissing bond and (b) result of full strain field measurement using DCT.

potential for detecting the location of defects using the proposed geometrical irregularity measurement method has been demonstrated using an aluminum plate. The proposed hybrid method was further used to identify invisible defects in the aluminum, GFRP and rubber specimens, each of which has different elastic modulus. In the aluminum specimen, the proposed hybrid method was able to find defects using the geometrical irregularity measurement method. The material degradation measurement method did not work since the deformation of aluminum, with high Young's modulus, is generally small. Defects in the GFRP specimen was, meanwhile, identified by both the geometrical irregularity and material degradation measurement methods. Lastly, the material degradation measurement method greatly found defects in the rubber specimen whereas they were not at all detected by the geometrical irregularity method due to high viscosity of the rubber specimen. The result of the rubber specimen is particularly important for this project since the rubber specimen grows a number of microcracks. The proposed hybrid method has the capability of identifying microcracks using the material degradation measurement method whilst it is also able to identify macrocracks using the standard geometrical irregularity measurement method. Due to the hybrid implementation, the proposed method could also identify other challenging defects such as a kissing bond or scar which a number of methods failed in the past.

The goal of the first year, which is the proof-of-concept of the proposed hybrid method has been accomplished. The project, if continuously funded for the second and the third year, will investigate the capabilities and limitations of the proposed method in detail and, together with probabilistic formulation, improve the identification accuracy so that the identification of microscopic or semi-microscopic cracks can be possible.

References

[1] Andrianopoulos, N. Full-Field Displacement Measurement of a Speckle Grid by using a Mesh-Free Deformation Function Strain, Wiley Online Library, 2006, 42, 265-271

[2] Archbold, E.; Ennos, A. & Virdee, M. Speckle photography for strain measurement?a critical assessment First European Congress on Optics Applied to Metrology, Strasbourg, 1977, 136, 258-264

[3] Bruck, H.; McNeill, S.; Sutton, M. & Peters, W. Digital image correlation using Newton-Raphson method of partial differential correction Experimental Mechanics, Springer, 1989, 29, 261-267

[4] Cheng, P.; Sutton, M.; Schreier, H. & McNeill, S. Full-field speckle pattern image correlation with B-spline deformation function Experimental mechanics, Springer, 2002, 42, 344-352

[5] Gazis, D. Three-Dimensional Investigation of the Propagation of Waves in Hollow Circular Cylinders. I. Analytical Foundation The journal of the Acoustical Society of America, Acoustical Society of America, 1959, 31, 568-573

[6] Gazis, D. Exact Analysis of the Plane-Strain Vibrations of Thick-Walled Hollow Cylinders The Journal of the Acoustical Society of America, Acoustical Society of America, 1958, 30, 786-794

[7] Giurgiutiu, V. Structural health monitoring with piezoelectric wafer active sensors Academic Press, 2008

[8] Goldrein, H.; Palmer, S. & Huntley, J. Automated fine grid technique for measurement of large-strain deformation maps Optics and lasers in engineering, Elsevier, 1995, 23, 305-318

[9] Gottenberg, W. Some applications of holographic interferometry Experimental Mechanics, Springer, 1968, 8, 405-410

[10] Hung, Y. Shearography: a new optical method for strain measurement and nondestructive testing Optical Engineering, International Society for Optics and Photonics, 1982, 21, 213391-213391

[11] Lee, B. & Staszewski, W. Modelling of Lamb waves for damage detection in metallic structures: Part I. Wave propagation Smart Materials and Structures, IOP Publishing, 2003, 12, 804

[12] Raghavan, A. & Cesnik, C. Modeling of piezoelectric-based Lamb-wave generation and sensing for structural health monitoring Proceedings of SPIE, 2004, 5391, 419-430

[13] Rayleigh, L. On waves propagated along the plane surface of an elastic solid Proceedings of the London Mathematical Society, Oxford University Press, 1885, 1, 4-11

[14] Reddy, P. & Tajuddin, M. Exact analysis of the plane-strain vibrations of thick-walled hollow poroelastic cylinders International journal of solids and structures, Elsevier, 2000, 37, 3439-3456

[15] Rockett, I. & Smith, G. Homicide, suicide, motor vehicle crash, and fall mortality: United States' experience in comparative perspective. American Journal of Public Health, American Public Health Association, 1989, 79, 1396-1400

[16] Rose, J. Ultrasonic waves in solid media Cambridge university press, 2004

[17] Sevenhuijsen, P. The photonical, pure grid method Optics and lasers in engineering, Elsevier, 1993, 18, 173-194

[18] Shapiro, R. & Haralick, R. Computer and robot vision Reading: Addison-Wesley, 1992

[19] Sirkis, J. & Lim, T. Displacement and strain measurement with automated grid methods Experimental mechanics, Springer, 1991, 31, 382-388

[20] Sutton, M.; Wolters, W.; Peters, W.; Ranson, W. & McNeill, S. Determination of displacements using an improved digital correlation method Image and vision computing, Elsevier, 1983, 1, 133-139

[21] Worlton, D. Experimental confirmation of Lamb waves at megacycle frequencies Journal of Applied Physics, AIP, 1961, 32, 967-971

4.5.その他

・TV 出演

2015 年 6 月 13 日（土）TBS 系列放送「報道 LIVE あさチャン！サタデー」において，田村センター長が，マンションの 10 階相当から水の入った 2 リットルのペットボトルが落とされた事件に関連して，その威力をシミュレーションの結果に基づき解説した。

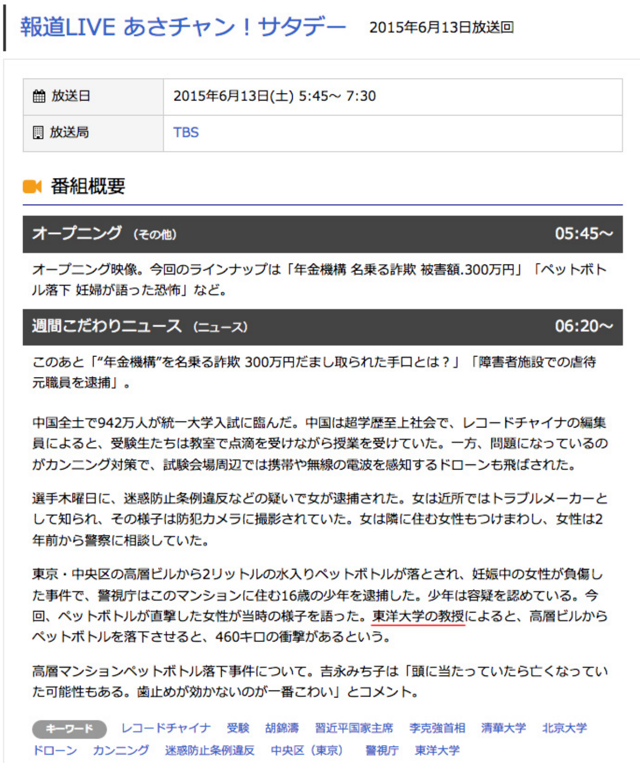

報道LIVE あさチャン！サタデー　2015年6月13日放送回

放送日	2015年6月13日(土) 5:45～ 7:30
放送局	TBS

番組概要

オープニング（その他）　05:45～

オープニング映像。今回のラインナップは「年金機構 名乗る詐欺 被害額.300万円」「ペットボトル落下 妊婦が語った恐怖」など。

週間こだわりニュース（ニュース）　06:20～

このあと「"年金機構"を名乗る詐欺 300万円だまし取られた手口とは？」「障害者施設での虐待 元職員を逮捕」。

中国全土で942万人が統一大学入試に臨んだ。中国は超学歴至上社会で、レコードチャイナの編集員によると、受験生たちは教室で点滴を受けながら授業を受けていた。一方、問題になっているのがカンニング対策で、試験会場周辺では携帯や無線の電波を感知するドローンも飛ばされた。

選手木曜日に、迷惑防止条例違反などの疑いで女が逮捕された。女は近所ではトラブルメーカーとして知られ、その様子は防犯カメラに撮影されていた。女は隣に住む女性もつけまわし、女性は2年前から警察に相談していた。

東京・中央区の高層ビルから2リットルの水入りペットボトルが落とされ、妊娠中の女性が負傷した事件で、警視庁はこのマンションに住む16歳の少年を逮捕した。少年は容疑を認めている。今回、ペットボトルが直撃した女性が当時の様子を語った。東洋大学の教授によると、高層ビルからペットボトルを落下させると、460キロの衝撃があるという。

高層マンションペットボトル落下事件について。吉永みち子は「頭に当たっていたら亡くなっていた可能性もある。歯止めが効かないのが一番こわい」とコメント。

キーワード　レコードチャイナ　受験　胡錦濤　習近平国家主席　李克強首相　清華大学　北京大学　ドローン　カンニング　迷惑防止条例違反　中央区（東京）　警視庁　東洋大学

番組内容

映像の 1 コマ